ABSTRACT

Title of Dissertation: Correlating Chemical Activity and
Structure in Mesoporous Metal Oxides for
Nerve Agent Decomposition

Tianyu Li
Doctor of Philosophy, 2022

Dissertation Directed by: Efrain E. Rodriguez
Department of Chemistry and Biochemistry

GB (sarin), a chemical ware fare agent (CWA), due to its extreme fatal toxicity and its involvement in a few terrorist and battle attacks, has become an increasing concern for the national public and military safety. Developing filter materials that can strongly adsorb and effectively decompose GB thus attracts growing research interest. The great diversity of metal oxides and their abundant surface chemistry suggest an opportunity to realize their potential as filter materials. This dissertation outlines our effort to gain fundamental understanding of the interaction between GB (also its simulant DMMP) and metal oxides. We aim to determine the structural factors that influence the performance of metal oxides on adsorbing and decomposing GB, and to ultimately predict the behavior of a given metal oxide. We used two mesoporous metal oxides (TiO_2 and CeO_2) as two model systems and performed systematic studies on their interaction with GB and its simulant DMMP. We utilized multiple techniques to fully characterize the crystal and surface characters of the mesoporous metal oxides. The interactions between

GB/DMMP and metal oxides were explored by different spectroscopic techniques (majorly infrared techniques). Combining the experimental observations and DFT calculations on two different metal oxides, we propose several governing parameters of the metal oxides to impact their reactivity for decomposing GB. We also derive a simplified and qualitative model to predict the reaction behavior and activity of metal oxides when interacting with GB.

Correlating Chemical Activity and Structure in Mesoporous Metal Oxides for Nerve Agent Decomposition

by

Tianyu Li

Dissertation submitted to the Faculty of the Graduate School of the
University of Maryland, College Park in partial fulfillment
of the requirements for the degree of
Doctor of Philosophy
2022

Advisory Committee:
  Professor Efrain E. Rodriguez, Chair/Advisor
  Professor Andrei Vedernikov
  Professor Dongxia Liu
  Professor Janice Reutt-Robey
  Professor Mercedes Taylor

Acknowledgments

First I would like to thank Professor Efrain Rodriguez for his patient guidance and support. I am so lucky to work with such a nice person. I appreciate the opportunities he has offered to me to travel to national labs and different conferences to meet and learn from other amazing scientists. I also want to thank past and present members of the Rodriguez Group. Their helps contribute to what I have achieved in my Ph.D career. I extremely appreciate the help from Dan Taylor, Rishvi Jayathilake and Xiuquan Zhou.

Second I want to thank all the collaborators for my project, including Will Gibbons, Lucas Algrim, Monica Mcentee, Roman Tsyshevsky, Mathew Leonard, Erin Durke, Majia Kuklja, Michael Zachariah, and Bryan Eichhorn. I especially Want to thank the tremendous support from Dr. Roman Tsyshevsky and Professor Majia Kuklja in helping me to understand my materials with DFT modeling. I really appreciate Professor Michael Zachariah for providing lab spaces and instruments for my experiments. I am grateful for Professor Bryan Eichhorn's early advice on the research. I would also like to thank Professors Andrei Vedernikov, Dongxia Liu, Janice Reutt-Robey, Mercedes Taylor for sparing their time to serve on my thesis committee and review this manuscript. I appreciate the financial support from Ann G. Wylie Semester Dissertation Fellowship.

Thirdly, as a foreigner student, I really appreciate that the United States and University of Maryland offered me such a friendly environment to learn and conduct research.

In the end, I really could not find any words to describe my love and gratitude to my family. I could not have achieved this without the emotional and financial support from my parents all over the years. And my grandmother, I miss you, I wish I made you proud and you witness this in the heaven.

Table of Contents

List of Tables

List of Figures

List of Abbreviations

ACh	Acetylcholine
AChE	Acetylcholinesteras
BET	Brunauer–Emmett–Teller
CWA	Chemical warfare agent
DFT	Density-Functional Theory
DMMP	Methylphosphonate
DRIFTS	Diffuse Reflectance Infrared Fourier Transform Spectroscopy
EDS	Energy-dispersive X-ray Spectroscopy
EELS	Electron Energy Loss Spectroscopy
GB	Sarin
HER	Hydrogen evolution reaction
HOMO	Highest Occupied Molecular Orbital
LUMO	Lowest Unoccupied Molecular Orbital
MO	Molecular Orbital
SAXS	X-ray Small angle scattering
SEM	Scanning Electron Microscope
TEM	Transmission Electron Microscope
TGA	Thermogravimetric Analysis
XPS	X-ray Photo-electron Spectroscopy
XRD	X-Ray Diffraction

Chapter 1: Introduction

1.1 Chemical Warfare agents

Chemical warfare agent (CWA) is one of most effective weapons of mass destruction. The CWAs are lethal synthetic chemicals that can be easily dispersed through air and water and then kill lives with very small amount of dosing[5].

The expansion of chemical industry in the 19th century made it possible for the mass production and deployment of CWAs[6]. The first documented attack of CWAs happened during the World War I, when German army released chlorine gas in the battlefield at Ypres, Belgium[7]. Other CWAs such as phosgene, sulfur mustard and lewisites were later used also by German army, and they caused 100,000 deaths in World War I. The usage of CWAs was expanded during the World War II. The Nazis Axis power Countries (German and Japan) tested the CWAs on innocent civilians and also used the CWAs in the battlefield, causing more than 1 million deaths[7]. Both World Wars proved the usage of CWAs are extremely dangerous and always cause mass killings on the innocent due to their uncontrolled dispersion once released. Even if not killed, the consequences of contacting those CWAs usually lead to severe long-term health conditions. Some of the CWAs (released or wasted) will remain on the land for very long time, causing potential damage to the future generations. There are multiple reports that Chinese farmers were intoxicated after contacting unknown wasted cans, which are the containers of CWAs left by

Japanese army during World War II[8]. In the Vietnam, the US army deployed Agent Orange in the battle ground. Though Agent Orange is not deadly enough to be categorized into CWAs, it remains on the battleground even after 50 years of usage, causing damage on the local people[9]. Due to their extreme hazard, more than 130 countries signed the Chemical Weapon Convention to prohibit the use, development, production, stockpiling and transferring of chemical weapons in 1993[10]. However, there are still scattered events where CWAs are used by the terrorists. Furthermore, some governments might still store large amounts of CWAs. Thus, the threat of CWAs remains, and might increase due to the current international tensions. The development of materials for effective protection against CWAs exposure has thus increased in need for both military personnel and for civilians.

1.2 Nerve Agent and Sarin (GB)

Nerve agents are currently the most dangerous CWAs. They are a group of organophosphorus compounds. Nerve agents are highly toxic and can cause death within a few minutes to a few hours after exposure. Their structures are shown in Figure 1.1. They are colorless and have very light or even no odor, making them very hard to be detected and distinguished. The nerve agents have very similar structures with some phosphorus containing agricultural insecticides. Thus, their production only requires similar chemical technologies used for production of agricultural insecticides. Because of that, there is always a worry about the proliferation of the nerve agent. Nerve agents do not occur naturally. The first known nerve agent, Tabun (GA), was first developed by the German chemist, Gerhard Schrader, in the 1930s during his research in the development of new OP insecticides. Later, a series of nerve agents known as the G-agents, which include Sarin

(GB) and Soman (GD), were developed in Germany during the World War II. Though Germany had the stockpile of the nerve agent, they did not use them in battles. The only usage of nerve agents in the war was during the Iraq–Iran conflict in the 1980s war, where sarin (GB) was used against Iranian troops and later against the Kurdish population. There are several terrorist attacks and assassinations that involve the usage of the nerve agent.

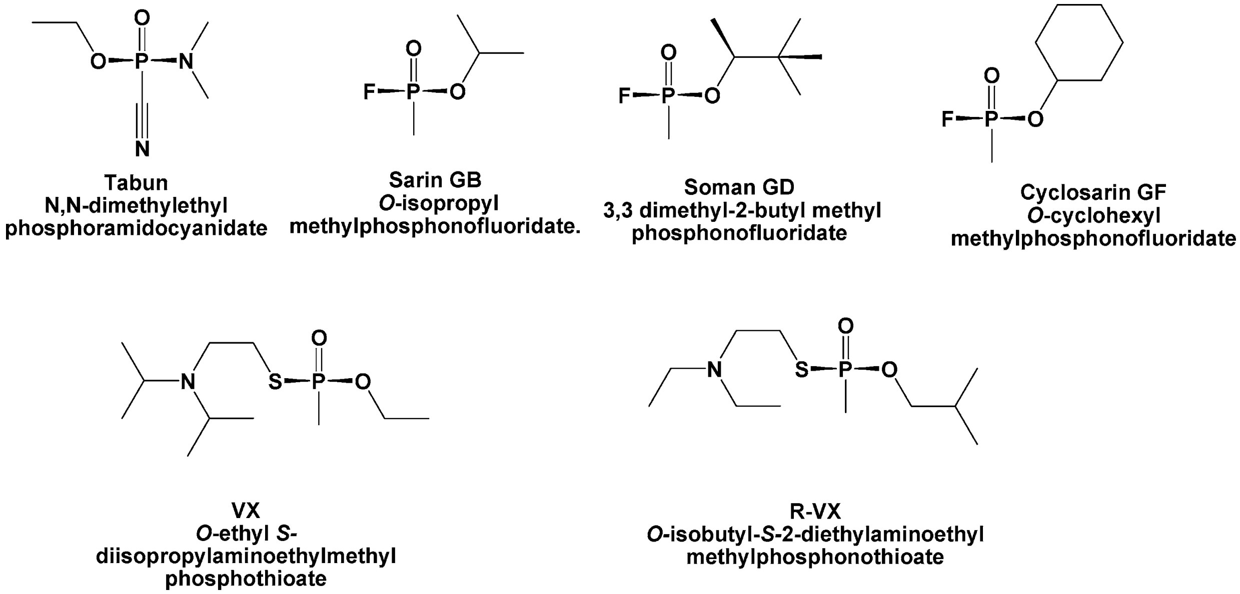

Figure 1.1: Structures and names of nerve agents, figure adapted from ref[1]

The toxicology of the nerve agents are very similar to each other. The most well-known mode of action of nerve agents is through Acetylcholinesterase (AChE) inhibition[11]. The enzyme AChE hydrolyzes the neurotransmitter acetylcholine (ACh) in postsynaptic membranes and neuromuscular junctions in the human nerve system. Once nerve impulses reach a nerve ending, the terminals of presynaptic nerves will release acetylcholine (ACh) into the synaptic or neuromuscular junction and then binds to the ACh receptor site located on the postsynaptic membrane, triggering stimulation of the nerve fibers or muscles. AChE are crucial in this neurotransmission process as it can control the concentration of neurotransmitter ACh by catalytic hydrolysis of ACh. The catalytic cycle is presented in Figure 1.2.

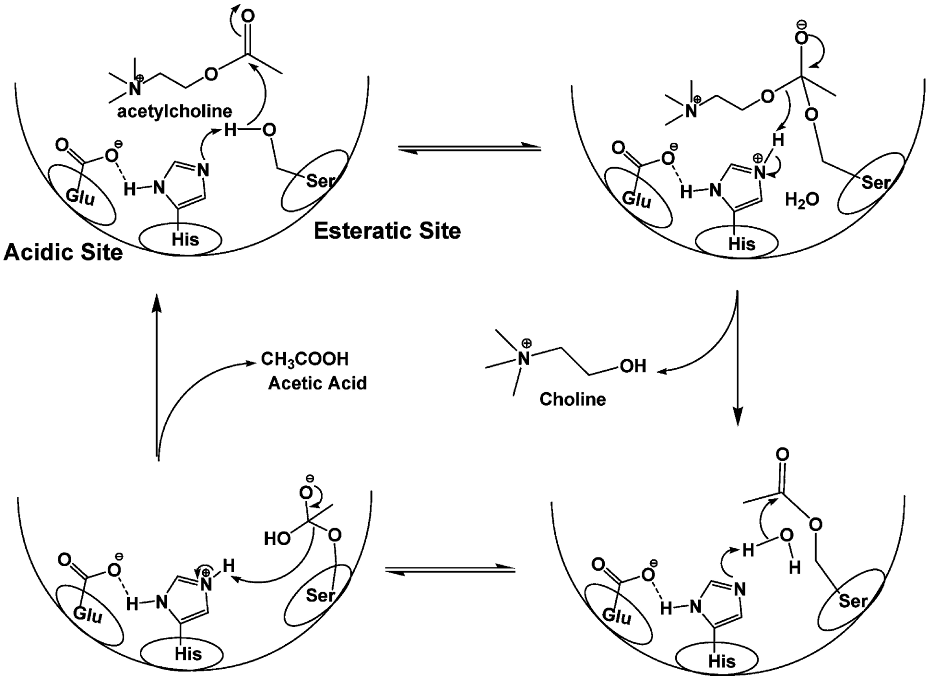

Figure 1.2: Acetylcholinesterase Hydrolysis of Acetylcholine, figure adapted from ref[2]

The nerve agent can also effectively bind to the AChE enzyme, however irreversibly. Figure 1.3 show the binding mechanism between the nerve agent and AChE. Once binded with the nerve agent, the active site of AChE becomes unavailable to hydrolyze ACh, leading to an accumulation of ACh in cholinergic receptors. In this way, the neurotransmission process will be disrupted, and the nerve system will lose function[2]. The AChE enzyme is highly effective in catalyzing the hydrolysis of ACh, thus the concentration of AChE is very low in human body. Also because of that, a small amount of nerve agent is enough to deactivate most of the AChE in the human body, causing lethal consequences.

The structure of sarin (GB) is shown in Figure 1.4a. GB is a colorless and odorless liquid. The vapor pressure of GB is relatively high thus it can be easily dispersed through air. By far, sarin is the most used nerve agent and attracts most the attention.

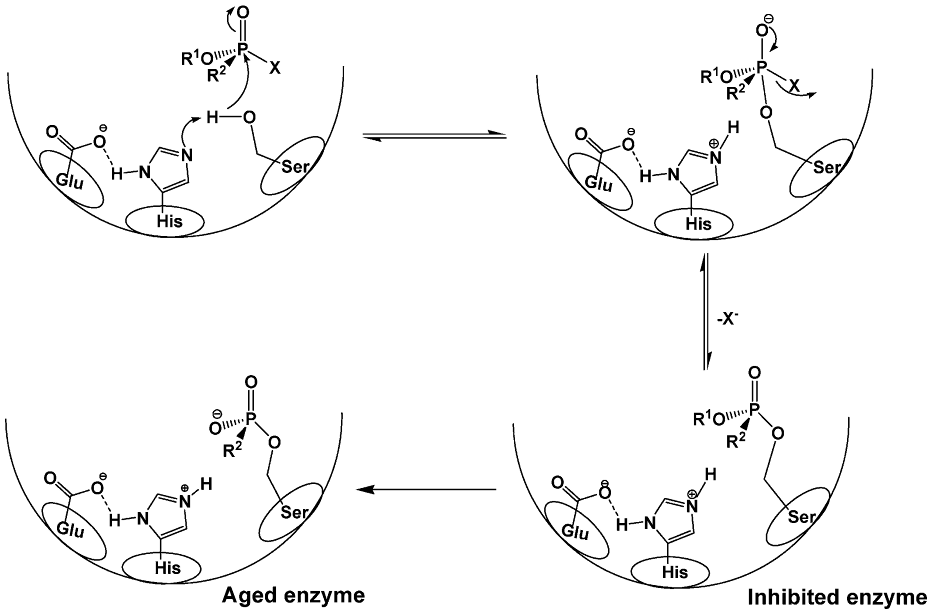

Figure 1.3: Inhibition of AChE with Organophosphates, figure adapted from ref[2]

1.3 Research Motivation

As mentioned earlier, due to the extreme fatal toxicity and the involvement in a few terrorist and battle attacks, the use of chemical warfare agents especially GB has become an increasing concern for the national public and military safety. Developing filter materials that can strongly adsorb and effectively decompose sarin thus attract growing research interest[6, 12, 13, 1, 14]. Several categories of materials have been proposed and studied for the application of combating GB including carbon-based materials[15] , MOFs[16, 17, 18, 19, 20] , polymer fibers[21], metal oxides[22, 23, 24, 25, 3, 26, 27, 28] and their composites[29, 17, 30, 31]. At the same time, a variety of characterization techniques have been developed to evaluate the performance of materials for the adsorption and decomposition of CWAs[32]. The great diversity of metal oxides and their abundant surface chemistry suggest a huge opportunity and possibility to find the potential filter materials among metal oxides. In addition, fabrication of the mesoporous

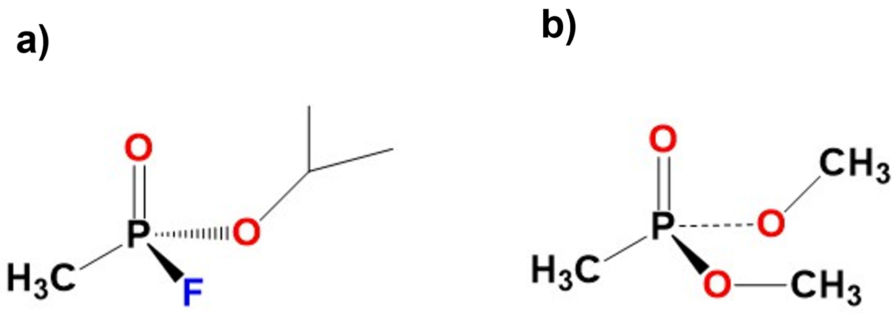

Sarin (GB)

DMMP

Figure 1.4: Structure of a) Sarin (GB) and its simulant b) dimethyl methylphosphonate (DMMP).

metal oxides can overcome the low-surface-area nature of conventional metal oxides materials as adsorbers.

My research is focused on understanding the interaction between the mesoporous metal oxides and GB molecules. By understanding the interaction process, I hope to determine the structural factors that influence the performance of metal oxides on adsorbing and decomposing GB and ultimately predict behavior of given metal oxides and locate the good performing candidate materials. In my research, I focused majorly on two mesoporous metal oxide systems, CeO_2 and TiO_2. CeO_2 and TiO_2 have significant differences on the crystal and surface structures. I used these two metal oxides as model systems to study their interaction with GB. Based on what I have learned on these two oxides, I proposed a simplified and qualitative model that is used to predict the interaction behavior between a certain metal oxide and GB. It should be noted, due to the extreme danger of GB, most of the research related to GB in academia is performed with its simulant DMMP, whose structure is presented in Figure 1.4b. The vapor pressures of GB and DMMP are similar, so DMMP is a good simulant for the study of adsorption of GB. GB and DMMP also bare some structural similarities. However, DMMP lacks the P-F bond, which is believed to be the most reactive part of GB. Some researchers remain skeptical on the suitability of DMMP as a simulant to study the GB decomposition. Here we argue that DMMP is a good simulant of GB to study the decomposition behavior, at least on the metal oxides, as the dissociation pathways and products of GB and DMMP are highly similar. We will discuss it in detail in the main text. The DMMP is more stable than GB. Generally speaking, a material that is reactive towards DMMP is always reactive towards GB. Because of the limit of GB, some of my research is based on DMMP, which I performed the experiment myself. And other is based on GB. The GB experiment was performed by the staff scientists from US Army Combat Capabilities Development Command Chemical Biological Center.

1.4 Thesis outline

This dissertation outlines our effort to gain fundamental understanding of the interaction behavior between the GB (also its simulant DMMP) and mesoporous metal oxides. Mesoporous CeO_2 and TiO_2 are systematically studied. Based on what we have learned from CeO_2 and TiO_2, as well as the studies on other metal oxides from previous research, a simplified and qualitative model that is used to predict the interaction behavior between a certain metal oxide and GB is proposed.

In Chapter 2, we briefly present the techniques that were used in the research, which include the material synthetic methods, the characterization techniques on the bulk and surface structure of metal oxides, and finally the techniques that were employed to understand the interaction between the metal oxides and GB/DMMP.

In Chapter 3, we present the proposed the qualitative model to understand the interaction behavior of metal oxides with GB/DMMP. Such a model was conceived based on our studies on the CeO_2 and TiO_2, as well as the studies on other metal oxides from previous research. We present the model before our experimental studies so that the readers can compare the model and experimental observations when they reach the experimental parts and evaluate the validity of this oversimplified model. We also discuss the aspect catalytic decomposition of GB on metal oxides at the end of this chapter.

Chapter 4 presents our original work on understanding the interaction between DMMP/GB and mesoporous CeO_2. Both GB and DMMP are studied in terms of the interaction with mesoporous CeO_2. Experimentally, we observed a high activity of mesoporous CeO_2 in degrading DMMP. Different reaction pathways between DMMP and CeO_2 are also observed. Theoretically, we build several surface models of CeO_2 based on the experimental surface characterizations and perform the DFT modeling to understand the reaction mechanism between the surfaces and DMMP. The modelling reveals that the exposed surface and hydroxylation play a critical role in the reactivity and reaction pathways in terms of interaction between DMMP and CeO_2. Similar study is performed to understand the interaction between GB and mesoporous CeO_2.

In Chapter 5 we aim at understanding how a general alio-doping (low valence doping) influences the interaction between CeO_2 and DMMP. Thus, we synthesize mesoporous CeO_2 doped with various amounts of Y^{3+}, Gd^{3+}, and La^{3+}. Y, Gd, and La are neighboring Ce in the periodic table thus Y^{3+}, Gd^{3+}, and La^{3+} show similar ionic radius and chemical activity to Ce^{4+}. All measurements consistently indicate Y^{3+} doping decreases the activity of DMMP decomposition compared with pure mesoporous CeO_2. Similarly, we also observed such a trend for Gd^{3+} and La^{3+} doped mesoporous CeO_2. The consistency on Y^{3+}, Gd^{3+}, and La^{3+} doped CeO_2 implies a relatively general effect of alio-doping of CeO_2 on DMMP decomposition activity.

Based on the structure and surface characterization, we attribute the reactivity difference of alio-doped mesoporous CeO_2 to the surface hydroxylation and preferred surface exposure.

In Chapter 6, we perform joint experimental and theoretical study of interactions between GB and three different TiO_2 nanomaterials. Experimentally, we study the adsorption and decomposition of sarin on commercial P25, anatase TiO_2 nanoparticles and synthesized mesoporous anatase TiO_2 at room temperature. We found the as-synthesized mesoporous anatase TiO_2 exhibits the highest activity towards GB decomposition despite it has the same crystal structure and similar surface area with anatase TiO_2 nanopowder. We then turn to DFT calculations and further explore mechanisms of adsorption and decomposition of GB on a pristine TiO_2 surface and surface with defects to reveal factors that govern high reactivity of mesoporous TiO_2. A comparison of experimental data with results of density functional theory (DFT) modeling suggests that high reactivity of mesoporous materials is correlated with surface hydroxylation. We find that mesoporous TiO_2 adsorbs more water than P25 and anatase nanoparticles, and that the water and OH groups facilitate the P—F bond cleavage of sarin on the surfaces of TiO_2.

Chapter 2: Experimental Methods

2.1 Synthesis of Mesoporous Metal Oxides

Since Prof. Galen Stucky developed the method to synthesize ordered mesoporous silica[33], the research on synthesizing ordered mesoporous metal oxides has increased explosively. Because of the high surface area and favored mass transport, ordered mesoporous metal oxides attract great interest in the field of catalysis and energy conversions. For the fundamental study, the ordered porous materials are also significant. The universal pore size and structure of countless pores in the materials will respond collectively and thus can 'magnify' an event happening in the nanoscale. We can therefore characterize a nano-scale event with statistical scattering and spectroscopic measurements. The high surface area nature of ordered mesoporous metal oxides also makes them good candidates for filter materials. For the fundamental research, the high surface area of those mesoporous metal oxides allows for maximizing the interaction between the metal oxides and molecules of interest, which will benefit the signal strength of spectroscopic characterizations such as IR and Solid-State NMR. The ordered nature also makes it easier to control the pore structures and surface areas. In cases where we are only interested in comparing the surface activities of the materials, the control of the surface area and pore structures are very important. Thus, in our study on the interaction between the metal oxides and sarin/DMMP, ordered mesoporous metal oxides are primarily used in order to get better spectroscopic signal and better control on surface and pore parameters.

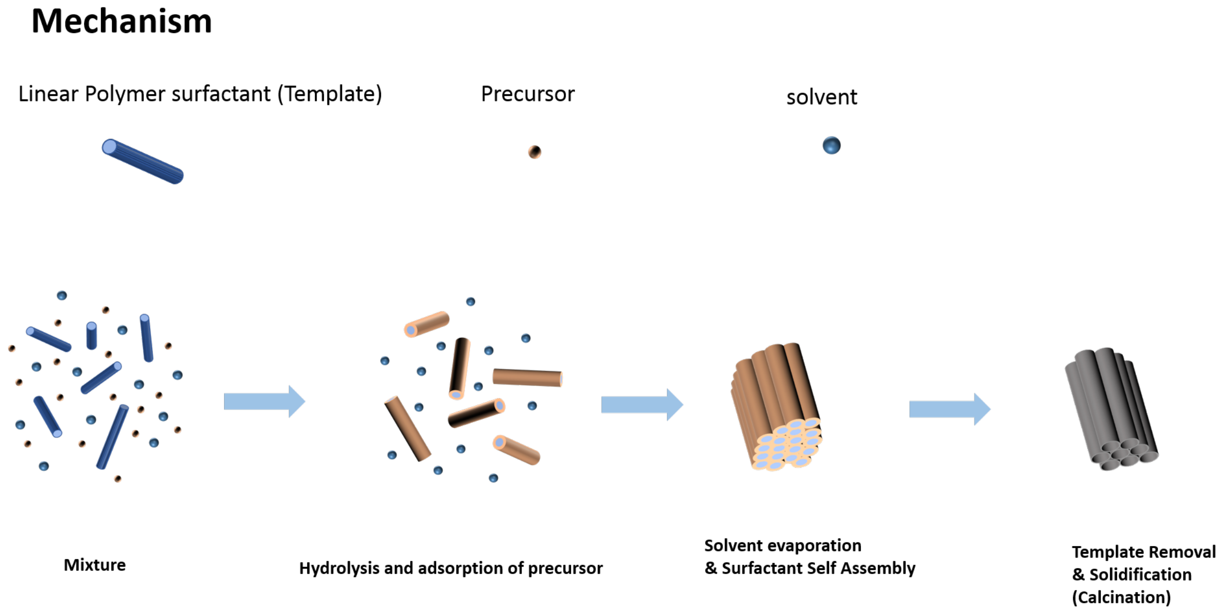

Figure 2.1: Illustration of soft template method for mesoporous materials synthesis.

To synthesize an ordered mesoporous material, templates (soft and hard) are usually required during the synthesis to create pore structures[34]. Prof. Galen Stucky developed the soft template method[33]. The soft templates are copolymers with hydrophobic and hydrophilic end. At proper pH in the solution, the copolymer will self-assembly into ordered micelle structures, serving as a template for pore structures when oxides precipitate, as shown in Figure 2.1. After the consolidation of the metal oxides and removal of the copolymer, ordered pore structure can form. Based on the types of polymers and pH of the solutions, different pore structure might be created. Ordered mesoporous SiO_2, C, TiO_2, ZrO_2 and CeO_2 can be synthesized through such procedure.

A hard template method usually utilizes the as synthesized ordered mesoporous SiO_2 or carbon as precursor. In a typical synthesis, the metal salts are first filled into the mesopores of the ordered mesoporous SiO_2 or carbon. Then the mixtures are heated so that the metal salts decompose into metal oxides inside the mesopores. Finally the hard template SiO_2 or carbon are etched away. The procedure is illustraed in Figure 2.2.

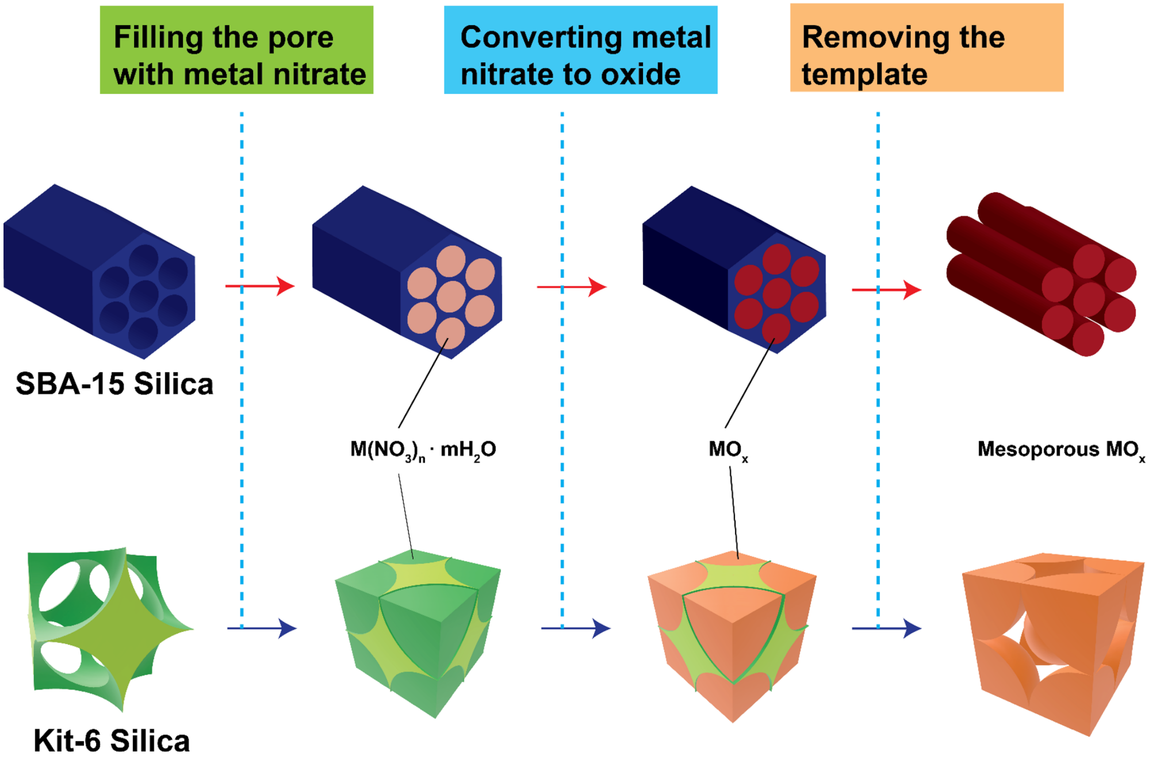

Figure 2.2: Illustration of hard template method for mesoporous materials synthesis.

2.2 X-ray and Neutron Diffraction

Most of metal oxides are in the crystalline state where the individual atoms are arranged in a highly ordered manner. The smallest repeating unit in the crystalline materials is called the unit cell. The ordered atoms also form different planes in the unit cell. The equally spaced planes can interact with the light (photon) when the spacing of the planes and wavelength of the light are in the similar scale, resulting in the diffraction phenomenon. Bragg came up with a simple model to explain this phenomenon, which is now known as Bragg's law. It states that the diffraction will appear when the spacing of the crystal planes d, the wavelength of the light λ and angle of incident light θ should have the relation: $n\lambda=2d\sin\theta$, as shown in Figure 2.3.

Different materials have different atomic arrangement, leading to different θ when diffraction appears (diffraction peaks appears at different locations). Thus, the diffraction patterns can be used as a fingerprint for the materials. The wavelength of neutron and X-ray have similar scale with the lattice, so they are optimal for the diffraction experiment on the solids to understand the atomic structures of the materials. X-rays mainly interact with the electron clouds of the atoms while neutrons interact with the nuclei, thus they have different sensitivity on different atoms and isotopes, respectively. Specifically, neutron is much more sensitive towards light atoms such as H, Li, O. A more fundamental explannation on the diffraction is referred to Kittel's Introduction to Solid State Physics (Chapter 2)[35].

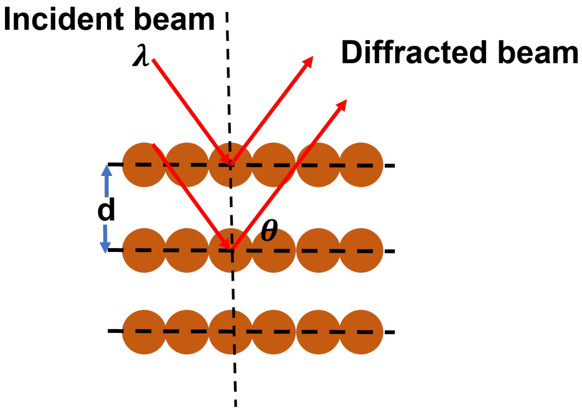

Figure 2.3: Illustration of Bragg Diffraction

2.3 Electron Microscope

The particle size of mesoporous materials ranges from hundreds of nanometers to hundreds of micrometers. And the pore size of mesoporous materials is typically below 10 nanometers. To understand the morphology and size of particles and pores of the as-synthesized mesoporous materials, electron microscope is used in our studies. Electron microscopes use electrons to

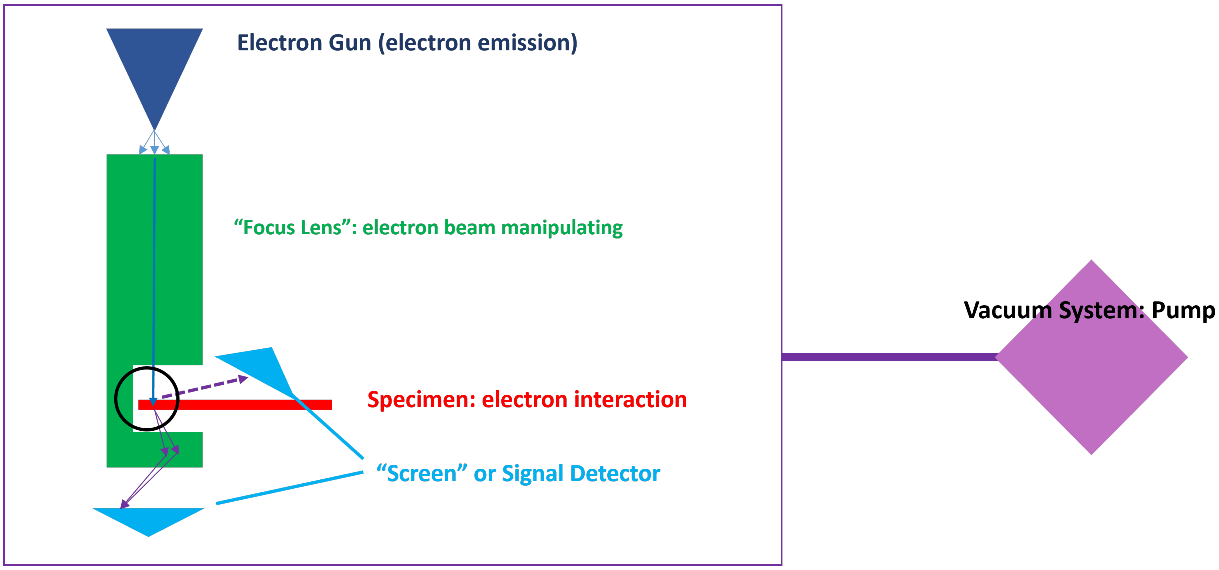

Figure 2.4: Illustration of the electron microscope

image rather than light. Hight energy electrons (10 kev) have a wavelength at the nanometer scale, so they are ideal for imaging nanoscale objects. In a typical electron microscope set up, as is displayed in Figure 2.4., electrons are first emitted from the electron gun and accelerated by an electric filed. Then another electric field and several magnetic fields behave as "focus lenses" to focus and manipulate the emitted electrons. The focused electrons reach and interact with the different parts of specimen and then was scattered by the specimen. The detectors finally collect different parts of scattered electrons for imaging and spectroscopic analysis. For one object, due to different compositions, morphology and thickness at different parts, the electron scattering behaviors will vary, leading to different scattering cross sections. The different cross sections of the electron scattering result in the contrast of the image. Depending on which part of electrons was collected for the imaging, there are mainly two types of electron microscopes. The transmission electron microscope (TEM) utilizes the elastic scattered electrons to image. While the scanning electron microscope (SEM) utilizes the secondary excited electrons (electrons emitted from sample after being hit by electrons) to image. Besides imaging, electrons can interact and exchange energy with the individual atoms. The high energy electrons can give energy to orbital electron of the atoms. The energy given to the orbital electron follows the quantum principle and thus is quantized. Apparently, different elements with different valences will have different energy levels of the electron orbitals, thus the value of given energy can behave as a fingerprint for elements or oxidation state. One can analyze how much energy is lost from the electron (electron energy loss spectroscopy (EELS)) or the energy of X-ray emitted from the relaxation of excited electrons (Energy-dispersive X-ray spectroscopy (EDS)) to gain elemental and atomic information (Figure 2.5.).

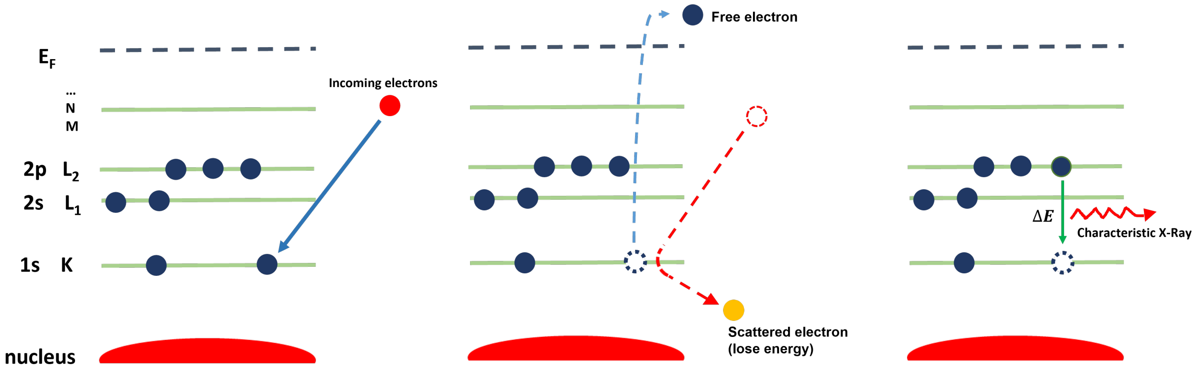

Figure 2.5: Illustration of inelastic electron scattering

2.4 Thermogravimetric Analysis

In thermogravimetry the weight of the sample is recorded as a function of time under the heating conditions. In this research TGA was mainly used for determining the water or hydroxylation level of the mesoporous metal oxides. The TGA instrument consists of two balances, one for the sample and the other for the reference. Via monitoring the weight change from both balances simultaneously, weight changes in the sample can be detected and recorded. Water and hydroxylation from the metal oxides typically leave from the materials at 100-200 °C.

Thus, by recording the weight loss of the materials between 100-200 °C, the amount the water and hydroxylation in the materials can be calculated.

2.5 Nitrogen Adsorption Isotherm

Nitrogen adsorption measures the isotherm adsorption and desorption of the nitrogen gas of solid-state materials at different pressures. In the single layer adsorption model, the amount of the nitrogen gas adsorbed is related to the adsorption strength, pressure, temperature, and surface area. By applying the Brunauer–Emmett–Teller (BET) model at certain range of the nitrogen adsorption isotherm data, the surface area of the material can be extracted. In our study we measure the nitrogen adsorption isotherm for the mesoporous materials to understand their surface area.

2.6 X-ray photoelectron spectroscopy (XPS)

XPS is a technique to analyze the elements and oxidation state of the materials. When a monochromatic X-ray source hit the specimen, one X-ray photon can give its energy to one core electron of the atom. Then the electron will be excited and kicked out from the sample. The kicked-out electron carries the kinetic energy and can be analyzed by electron detectors. The kinetic energy of the kicked-out electron can be expressed as: Ek=Ep-Eb. Where Ek is the kinetic energy, Ep is the energy of the X-ray, and Eb is the binding energy of the core electron in the atom. When Ep is fixed, Eb can be back calculated from Ek. And the binding energy describe the attractive force between the certain core electron and nuclear. This attractive force is very sensitive to the type of atoms and oxidation of the atoms. Thus, Eb can be used for identifying the elements, their chemical environment and their oxidation states. Because electrons have a mean free path of several nanometers within the solid, the analyzed electron on mainly from the surface of the sample. Thus, XPS is a surface sensitive technique. In our study, we use XPS to identify the oxidation states of metal element as well as to distinguish the lattice oxygen and surface oxygen (oxygen in OH group) on the surfaces of mesoporous materials.

2.7 IR Spectroscopy

Molecules and solids can absorb infra-red (IR) light to excite their vibrations. Different molecules and solid have different geometry and bond strength, and thus their vibrations vary in energy. Thus, IR absorption can be used to identify the bonds or molecular species. Here we use the IR to identify the decomposition species when Sarin/DMMP interact with metal oxide surfaces.

2.8 Solid State NMR

NMR is a technique to understand the local chemical environment of the certain atoms in the molecules or solids. For certain elements, their nuclei carry spins. Under the magnetic field, the energy of the spins will split into different levels. The surrounding electrons of the nuclei provide a local magnetic field, and this magnetic field is very sensitive towards the chemical environment such as coordination number, bond distance and bond angle. Thus, the energy splitting of the spins provides the information of the local environments of the atoms (Figure 2.6). By applying an external magnetic field, the local magnetic field created by electrons will shield the external magnetic field, and NMR can analyze this magnetic field shielding effect. The shielding effect is anisotropic. However, in the liquid sate, the molecules undergo rotation with extremely high frequency (300 GHz). Thus, the anisotropic effect will be averaged out. In the solid-state, the crystal cannot rote itself, so anisotropic shielding will be observed. Magic angle spinning thus is utilized to average out the anisotropic shielding of the solid materials during the measurement. In our study, Sarin/DMMP contains phosphorus atoms (31P S=1/2, NMR active), which can be detected by solid sate NMR once they are adsorbed on the surfaces of solid mesoporous metal oxides. If Sarin/DMMP decompose on the metal oxides, the chemical environment of phosphorus atoms will change and can be detected by solid-Sate NMR. Thus, we use the solid-state NMR to detect the reactivity of mesoporous materials towards the Sarin/DMMP decomposition.

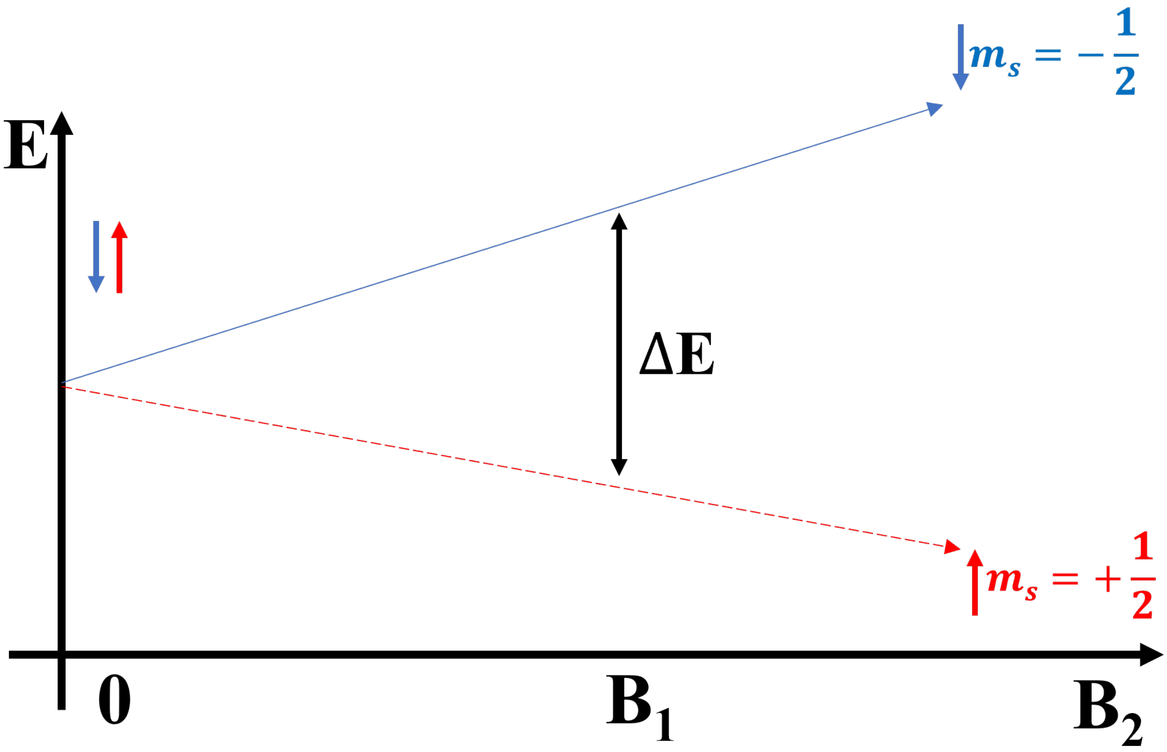

Figure 2.6: Illustration of splitting of the energy of nuclear spin under magnetic field

2.9 Mass Spectrometry

Mass spectrometry is an analytical technique used to identify or quantify the volatile species. In our study, the mass spectrometry is used for detecting the reaction product from a packed-bed reactor. All molecules are first ionized as they enter the instrument, then, by investigating the species for specific mass-to-charge ratios, one can accurately identify and quantify the given molecule. In our experiment, a quadrupole mass spectrometer was used to monitor some of the decomposition product of DMMP, such as methanol.

2.10 DFT Modelling

Density-functional theory (DFT) is a computational quantum mechanical modelling method used to primarily investigate the ground sate of electronic structure of many-body systems, such as atoms, molecules, and the condensed phases. In our study, we utilize the DFT modeling to calculate the activation energy and relative energy of the transitional states of the molecule-surface system to understand the reaction mechanism for the Sarin/DMMP decomposition on the metal oxides. The DFT calculations in this study were performed by Dr. Roman Tsyshevskiy from Dr. Maija Kukla's Group.

Chapter 3: An Attempt to Understand the Interaction of Metal Oxides and CWAs from the Fundamental Solid Chemistry

The great diversity of metal oxides and their abundant surface chemistry suggest a huge opportunity and possibility to find the next-generation filter materials among metal oxides. However, such a diversity also leads to a great difficulty in searching for an optimal one as it seems there are countless possible metal oxides to be tested. For material scientists or chemists, there is a strong belief that gaining fundamental understanding of the interaction between surface of metal oxides and CWA molecules allows us to make reasonable predictions on the behavior of the materials, and even further to predict the candidate materials based on fundamental scientific principles. Together with the experimental measurements in the past decades, recent effort in DFT modeling does help us to make a great progress in understanding interaction mechanisms between different metal oxides and CWAs[36, 37, 38, 39, 40, 41, 42, 43, 44, 45, 3, 46, 47]. Despite the progress, it remains challenging to exactly predict a candidate metal oxide (this holds true for other categories of materials too). The reason again lies on the diversity of metal oxides. Different metal oxides have different crystal and surface structures, so a specific model has to be developed and optimized for each metal oxide or even each surface. DFT modeling is costly in time and money thus it is not realistic to perform thousands of calculations on different metal oxides given the current limitation on computing power. Machine learning seems to be an intriguing direction in terms of high-through-put prediction. While the current size of the collected data does not meet the threshold to make a reasonable machine learning model and it remains challenging on formatting the experimental and computational data.

To be able to predict a candidate oxide, we need to build a universal model in terms of the interaction between the metal oxides and Sarin. Qualitatively, a traditional way to develop a model is through the summarization and classification. One has to admit this traditional way still plays an important role in the current research especially when a quantitative model is difficult to build. In this review, we present our attempt to build a universal model for the interaction between the metal oxides and sarin based on the summarization and classification of the metal oxides that have been studied experimentally and computationally in the past. Our initial is to make qualitative predictions based on the fundamental chemical and physical principles. Our most important goal here is to provide a different hypothesis to test when approaching this practical problem.

As mentioned earlier, a good filter material for combating CWAs should possess two key features: The CWAs molecule can strongly bind to its surface (strong adsorption) and readily dissociate upon interacting with it (active towards decomposition). To simplify the problem, we will treat the adsorption and dissociation on the metal oxides separately. We will focus on sarin and its simulant DMMP in the discussion.

3.1 Adsorption on the Metal Oxides

3.1.1 Covalent Interactions

When we say the molecule can strongly adsorb on the surface, it means there is a strong attractive force between the two subjects. In the atomic or molecular level, the attractive forces can be put into several categories: (1) London Force (2) Dipole-dipole interaction (3) Hydrogen Bond (4) Covalent Bond. The magnitudes of the forces are presented in the Figure 3.1 . The strength of London forces is the weakest, followed by the dipole-dipole interaction and then hydrogen bond. And generally, the strength of covalent bond is largest. By simply comparing the strength of different categories of attractive forces, we can easily draw a conclusion: A potential metal oxide that can strongly adsorb the DMMP or Sarin should be able to form covalent bonds with these molecules.

Can we predict which attractive force dominate a certain metal oxide in terms of interacting with DMMP and GB? Or which metal oxide can display a stronger covalent interaction with these molecules? Covalent bonds are essentially electron orbital interactions. For the metal oxides in the solid state, bands are used to describe the collective behavior of the electron and orbitals within the solid, while molecular orbital is applied for the molecules. When a solid surface forms covalent interactions with molecules, this process can be treated as an interaction between the bands and molecular orbitals in reciprocal space[48]. For the solid-state surface, we may just take the conduction band and valence band near the Fermi level into consideration as electrons are most active near the Fermi level. The molecular orbitals of DMMP or GB are surely complicated since they are relatively large molecules. However, some simplifications can be made based

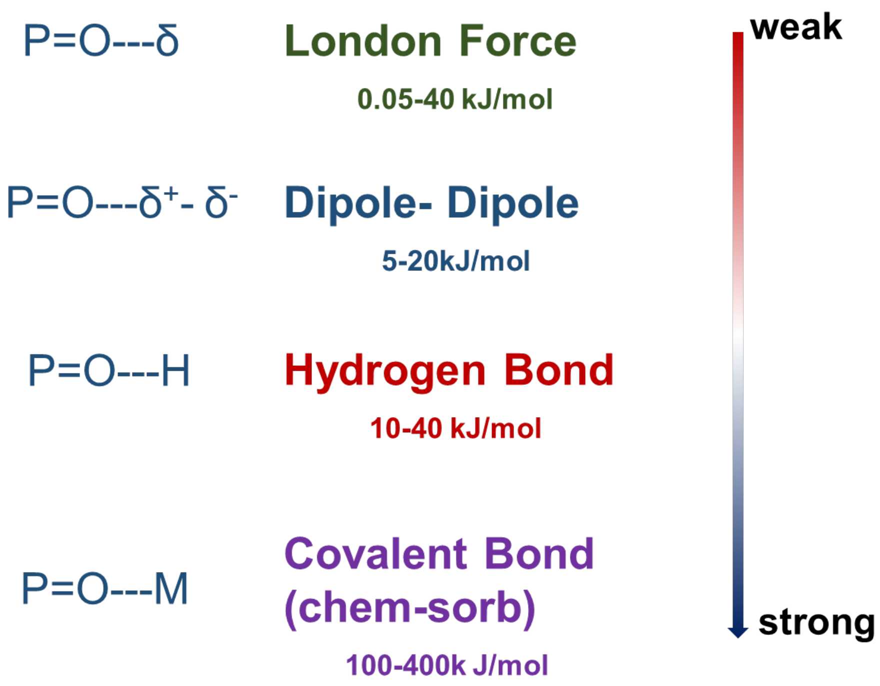

Figure 3.1: Classification and comparison of attractive force between molecules and surfaces of solid materials.

on the experimental observations: the IR spectroscopic studies found when DMMP/GB interact with materials, a significant red shift of stretching mode of the P=O bond is generally observed, implying a weakening of the P=O bond[20, 23, 49, 22]. The weakening of the P=O bond is a strong indication that DMMP/GB interact with solid materials through the P=O double bond. Thus, in this specific case, we may only take MOs from P=O bond part of the molecules into considerations.

So we can now draw diagrams of bands and MOs. For most of insulating or semiconducting oxides, the valence band is dominantly composed of the O 2p orbitals and electrons, while the major components of conduction band are the d (if not fully filled) and s orbitals and electrons[50, 51, 52], as presented in the Figure 3.2. For P=O from DMMP or sarin, the HOMOs are mainly the non-bonding p-orbital with lone pair electrons while the LUMO is the π^* antibonding orbital

(Figure 3.2). For the band-MO interaction, another important concern is the relative energy level. Of course, DFT calculation can easily help us to determine the energy levels of bands and MOs. We can still qualitatively approximate them based on some simple chemical and physical principles. Since the σ bond and π bond MO of P=O has O 2p components, and valence bands of most of the metal oxides are formed also by O 2p orbitals and electrons, it is reasonable to assume that the σ bond and π bond MO from P=O has a similar energy with the valence band, as shown on Figure 3.2.

In MO theory, to form a chemical bond, two orbitals from different atoms need to overlap to form the bonding and antibonding MOs with electrons filled in the bonding MO. The overlap of the atomic orbitals requires symmetry match and similar energy levels between two orbitals. Here we can apply this principle when considering the covalent interactions between the DMMP/GB and surfaces of metal oxides. A covalent bonding can be expected when the conduction band of the metal oxide have similar energy level with the HOMO (where lone pair electrons fills) of the P=O MOs, as indicated in Figure 3.2 a. A too low or too high energy level of the conduction bands will cause a larger gap between the HOMO and conduction band, leading none covalent interactions, where the dipole-dipole interactions will dominate between the molecules and metal oxides, as is displayed in Figure 3.2 b and c.

From the point of view of chemistry, we can predict the adsorption strength of oxides towards DMMP/GB based on the degrees of energy match between the bands and MOs. In the DFT modellings, Density of States(DOS) diagrams of solids and molecules are calculated to make comparisons[53, 54]. Qualitatively, in the valence bands, the energy of s band is higher than d band, so the s band is further away from the HOMO of DMMP/GB (Figure 3.2 a). Thus, it can be expected the covalent interactions on the metal oxides with d band is stronger than the one with only s band. DFT calculations does exactly show pristine surfaces of s band oxides like MgO[39], Al_2O_3[37], SiO_2 [55, 38], and ZnO[44] have a lower adsorption energy towards DMMP or GB compared with the d band oxides like TiO_2[56, 57, 47, 58], CuO[59], CeO_2[60] and Fe_3O_4[61]. It can be predicted transition metal oxides (with available d orbitals) should be good candidates to achieve strong adsorptions towards DMMP and Sarin. And the smaller the energy difference between the d-band and HOMO of DMMP/Sarin, the stronger the adoption should be. Besides the HOMO-d band interaction, d-π* interactions might also be expected when there is a good energy and symmetry match between d-band of the oxides and π* MO of the molecules. If there are available d- electrons, a feedback bond can be formed, leading to a stronger covalent interaction. With the help of the DFT calculations, we can get much more quantitative comparisons between bands and MOs, which can assist us to determine best oxides that strongly adsorb DMMP/Sarin.

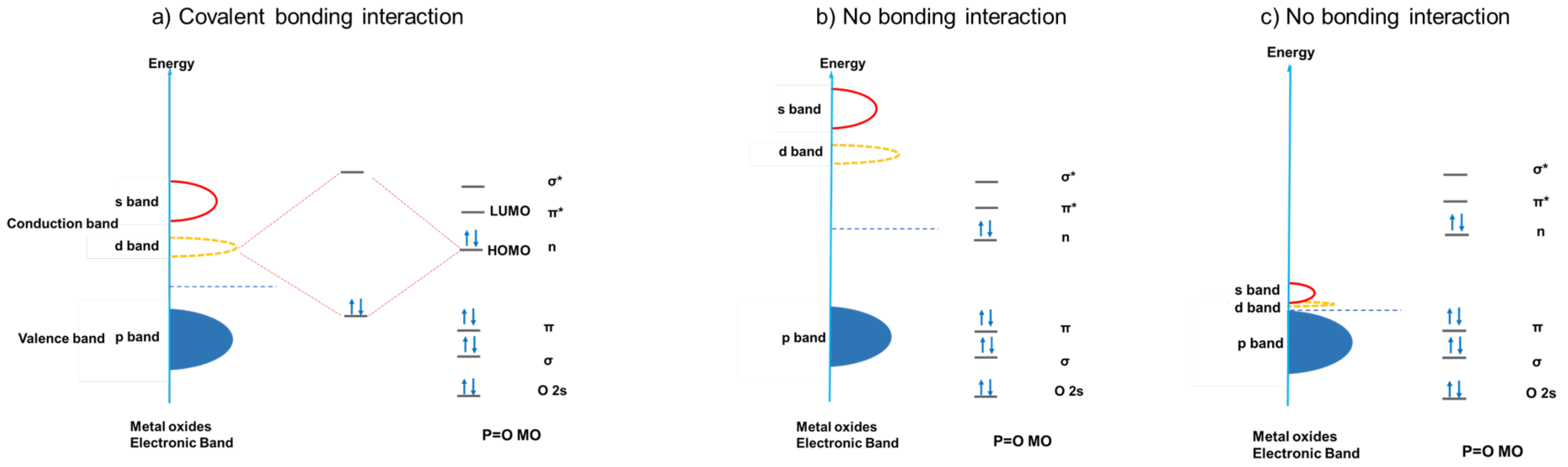

Figure 3.2: Diagrams of interaction between bands of metal oxides and molecular orbitals (MOs) of P=O from GB/DMMP.

3.1.2 Hydroxylation

In the practical situation, filter materials are always applied in the ambient conditions where moisture cannot be avoided. That means the surfaces of the metal oxides are more or less hydroxylated. Thus, it is important to understand and to be able to predict how the hydroxylation will influence the adsorption strength of oxides towards DMMP/Sarin. When the hydroxylation (OH termination) exists on the surface, DMMP/Sarin tends to form hydrogen bond with the metal oxides, as is displayed in Figure 3.3, structure 2, which is also evidenced through the experimental observations [62, 22, 25]. As mentioned previously, the strength of hydrogen bond is between the dipole-dipole interaction and covalent bond. Thus, whether the hydroxylation of metal oxides will lead to a stronger or weaker adsorption, depends on what is the initial dominant attractive force on the pristine surface. Oxides with the energy level of conduction band far away from HOMO of DMMP/Sarin, the dipole-dipole interaction is the major attractive force. Hydrogen bond on the hydroxylated surfaces is expected be stronger than the dipole-dipole interaction. In such a case, the hydroxylation should benefit the stronger adsorption. Oxides like SiO_2 fall onto this category, where the hydroxylated surface has a stronger adsorption energy towards DMMP/Sarin than pristine surface[55, 38]. On the other hand, d-band metal oxides interact with DMMP/Sarin through covalent bonding. The hydrogen bond on the hydroxylated surfaces is weaker than the covalent interactions. Hydroxylation on this type of metal oxides will therefore lower the adsorption strength significantly. Such behavior is commonly observed on the transition metal oxides like TiO_2[56] and CeO_2[60]. For s-band metal oxides, the covalent interaction is much weaker, so a smaller difference of adsorption strength between pristine and hydroxylated surfaces should be expected such as Al_2O_3 and ZnO.

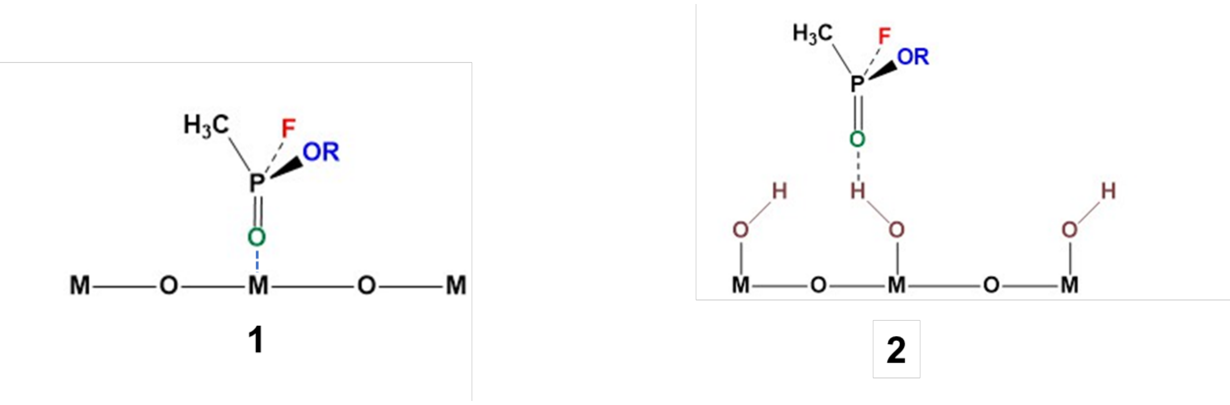

Figure 3.3: Adsorption configuration of GB on pristine metal oxide surface (structure 1) and hydroxylated metal oxide surface (structure 2).

3.1.3 Real Space Concern

The above-mentioned model can help predict the adsorption behavior of DMMP/Sarin based on the energy of molecular orbitals and bands. However, to form a bond, the "physical contact" between the atoms is necessary. The d and s conduction bands of the metal oxides are mostly contributed by the metal atoms. The HOMO of P=O lie on the lone pair electrons of oxygen atom. Therefore, the covalent interaction requires the metal atoms sites of the oxides are close enough to oxygen atoms from P=O in the real space, shown in Figure 3.3, structure 1. The atoms can arrange in different manners on the surfaces of metal oxides. Some surfaces can have more metal atoms exposed while other surfaces might have metal atoms embedded below the surfaces. In the latter case, even if there is good energy and symmetry match between conduction bands of metal oxides and HOMO of DMMP/Sarin, the covalent interactions will not be expected as there is no physical pathway to connect metal sites and P=O. Instead, a weak dipole-dipole interaction will dominate. A good example would be the case of MoO_3. MoO_3 is transitional metal oxides with available non-filled d-bands. Based on the orbital electron energy consideration, a strong adsorption towards DMMP /Sarin should be expected. However, the real stable surface of MoO_3 is nearly entirely terminated with O, leaving no metal sites to have contacts with molecules, resulting in the dominance of dipole-dipole interaction, as is displayed in Figure 3.4. Experimentally and computationally, the adsorption strength of MoO_3 towards DMMP is relatively weak compared with other transition metal oxides[3], which is around -20 kJ/mol and falls onto the dipole-dipole interaction range. And the hydroxylation of the surface leads to a stronger adsorption as the hydrogen bond is replacing the dipole-dipole interaction.

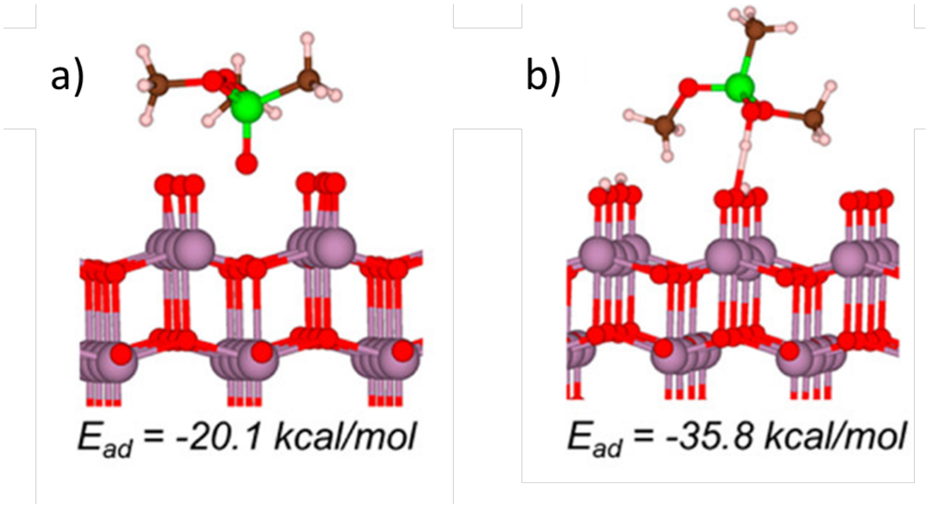

Figure 3.4: a) calculated structure of DMMP adsorbed on the oxygen terminated (010) MoO_3 surface and adsorption energy. b) calculated structure of DMMP adsorbed on the hydroxylated (010) MoO_3 surface and adsorption energy. Figure modified from [3]

3.2 Dissociation on Metal Oxides

The dissociation of GB or DMMP on metal oxides are generally regarded as a multiple-step process. DFT modelling usually takes several transition states into considerations and calculates the activation energy barrier to reach each transition state and the free energy of these states. An ideal metal oxide to degrade Sarin/DMMP should allow the molecules to dissociate with a relatively low activation energy barrier (kinetic consideration). In addition, the final products should be as stable as possible (low free energy, exothermic process, thermodynamic consideration). It is true that Sarin/DMMP dissociate through different mechanisms on different metal oxides, there are several key steps that Sarin/DMMP has to go through on most metal oxides.

3.2.1 Structure of Dissociation Products

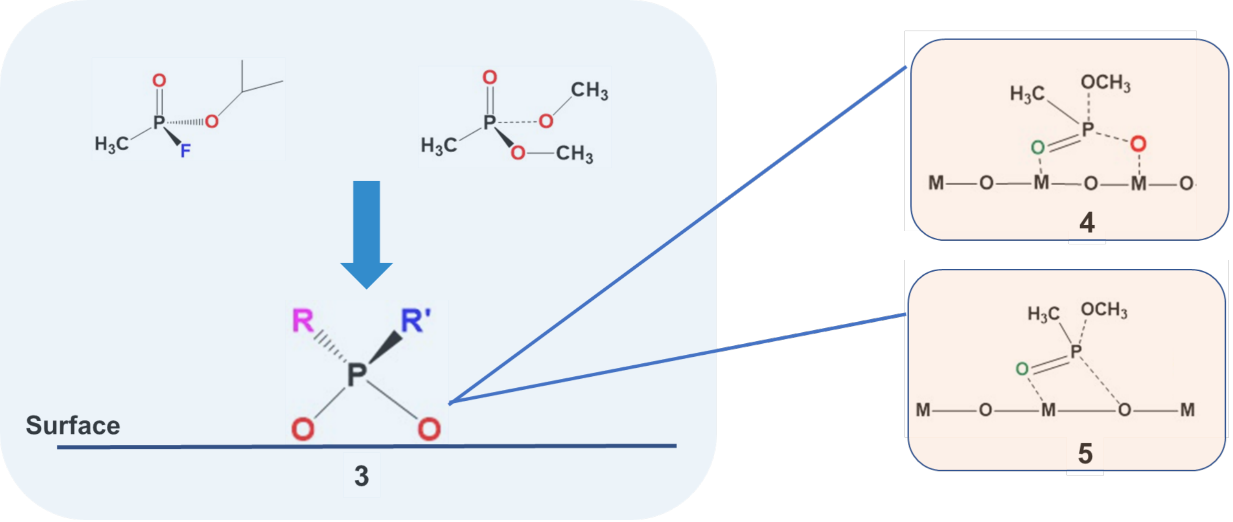

Figure 3.5: Decomposition product of sarin/DMMP on metal oxide surface.

First, let us only look at initial molecules and the final dissociation products. Spectroscopic studies on surfaces have proven, upon the dissociation of DMMP/Sarin on metal oxides, vibration modes of O-P-O arise in the spectrum[63, 49, 62, 64] and these modes are frequently used as the indication of highly reactive surface toward Sarin/DMMP. It is widely believed that sarin/DMMP lose -OR group or F group and form two P-O bonds with the oxygen atoms shared by the surface (structure 3 in Figure 3.5). Now let us consider a very simple surface model of metal oxides, where metal and oxygen atoms neighbor each other to form a flat surface (O-M-O-M-O…). To achieve structure 3 on such a surface, there are two possibilities: (1) the oxygen atoms from two P-O bonds are both above the O-M-O-M flat surface and form covalent interactions with two metal sites (structure 4). (2) one oxygen atom from P-O bonds is above the O-M-O-M flat surface and another oxygen atom is within the flat surface (structure 5). Which structure should be the dissociation product of Sarin/DMMP on different metal oxides? Due to the extremely broad feature of O-P-O stretching mode in the spectroscopy, the exact structure is not yet determined. However, DFT modeling can calculate the free energy of the structure and predict the most possible and stable structures.

While qualitatively, we can also evaluate the relative energy of each structure based on simple chemical principles. If we regard P atom as the center of the Sarin/DMMP molecules, the molecules have a tetrahedral geometry. At the most stable state of the molecules, the bonds connecting P should have a bond angle close to 109°. A significant smaller or larger bond angle will raise the energy of molecule. When the molecules dissociate on the surfaces of metal oxides to form structure 3, the tetrahedra geometry does not change. So it is reasonable to assume that stability (energy) of the structure 3 strongly correlates to the bond angle between two P-O bonds.

Whether structure 4 or structure 5 are the dissociation product on the metal oxides should depend on which structure has a O-P-O bond angle closer to 109°. It is more convenient to use distance instead of angle to describe here. P-O bond distance in molecules is around 1.62Å and P=O bond distance is 1.48Å[65, 66]. We can assume the P-O bond in structure 3 is in between P-O and P=O, so the distance should be close to their average 1.55 Å. With O-P-O bond angle of 109°, the most stable distance between two oxygen atoms from O-P-O should be around 2.54 Å. In structure 4, the distance between O atoms from O-P-O is similar to the distance between closet metal sites. While in structure 5, the distance between O atoms from O-P-O is similar to or slightly larger than closet metal and oxygen sites on the surface. Thus, we believe that how the atoms arrange on the surfaces (distance between atoms) will have a strong impact on the stability of structure 4 and structure 5. If the distance between the metal and metal is close enough to the optimized oxygen-oxygen distance from O-P-O (2.54 Å), structure 4 should be adapted. Similarly, If the distance between metal and oxygen is close enough to 2.54 Å, structure 5 will be preferred. Of course, it is not likely that we find the exact distance on the metal oxides, but we can set an optimal range. If we set the bond angle range at 95∼130° (109° is the optimal) as a suitable angle, the oxygen-oxygen distance should be 2.2 Å∼ 2.94 Å. So we can roughly predict which structure should be adapted based on whether it is the metal-oxygen or metal-metal atomic distances that fall into 2.2 Å∼2.94 Å range.

Here we list metal-oxygen and metal-metal atomic distances of several metal oxides, which is generated from ICSD, as shown in Table 3.1. Based on the argument we just established, we can make reasonable predictions on the structure of the decomposed product. The prediction agrees well with our calculation results on TiO_2[58], MoO_2 [67], MoO_3[3], CeO_2[60].

3.2.2 Activity for Dissociation

Once the structure of the product is determined, we can now consider reactivity of the surface. We can still use the above-mentioned argument here. From the point of view of kinetics, being active mean the activation energy for the dissociation of sarin/DMMP is low. As mentioned earlier, from the intact molecules of sarin/DMMP to the dissociate into structure 4 or structure 5, except breaking bond of P-F or P-O-R, the molecules have to adjust their configurations so that the decomposition products can fit on the surface of metal oxides. This configuration adjustment mainly involves the stretching or bending the bond angle to deviate the original stable state, which

Metal oxides	M-O distance (Å)	M-M distance (Å)
SnO_2	2.052/ 2.058	3.187/ 3.71
α-Al_2O_3	1.856/ 1.971	2.792
γ-Al_2O_3	1.642/ 1.69/ 1.71	1.71/ 2.78/ 3.27
MgO	2.109	2.982/ 4.217
Y_2O_3	2.248/ 2.262/ 2.28/ 2.345	3.512/ 3.529
CeO_2	2.387	3.898
ZnO	1.974/ 1.973/ 1.992	3.209/ 3.25
MoO_3	1.955/ 2.291/ 1.738/ 1.682/ 2.24	3.42/ 3.699/ 3.956
MoO_2	1.956/ 2.069	2.814 3.705
r-TiO_2	1.945/ 1.986/ 3.485	2.959 3.57
a-TiO_2	1.934/ 1.98/ 1.98/ 3.857	3.039/ 3.784
CuO	1.951/ 2.784/ 3.408/ 1.961	2.9 (111), (101)/ 3.083/ 3.173
Cu_2O	1.848/ 3.538	3.017
NiO	2.089/ 3.618	2.954
CoO	1.943/ 1.912/ 3.386/ 3.3	3.495/ 2.854
h-Fe_2O_3	1.944/ 2.114	2.899/ 3.361/ 3.702
m-Fe_2O_3	2.091/ 1.837/ 3.488	2.972/ 3.485
Fe_3O_4	1.889/ 2.058/ 3.493	2.968/ 3.48
MnO	2.223/ 3.85	3.144
Mn_3O_4	2.275/ 2.361/ 1.909/ 2.61	2.969/ 2.877/ 3.026
α-MnO_2	1.882/ 1.901/ 3.416	2.847/ 2.889/ 3.454
β-MnO_2	1.879/ 3.338/ 1.898	2.873/ 3.426
γ-MnO_2	1.821/ 1.917/ 2.267/ 1.975/ 3.054	2.859/ 2.957/ 3.371
δ-MnO_2	1.916/ 3.309/ 3.555	2.85
ZrO_2	2.005/ 2.208/ 2.149/ 2.232/ 2.276	3.332/ 3.438/ 3.617

Table 3.1: Table of distances of M-O and M-M in common binary metal oxides .

will cost energy. Such a process is illustrated in Figure 3.6. The energy cost here is one of major contributions to the activation energy barrier. Thus, the smaller degree that the molecules stretch or bend themselves, the more reactive of the surfaces for the molecules to dissociate. Then it is obvious, the distance of the metal-oxygen and metal-metal atoms will have an influence on the reactivity of the surfaces. Once the decomposition structure is determined, we can qualitatively predict the reactivity of the surface based on how much metal-oxygen/metal-metal distance is close to the optimized distance of 2.54 Å, where the molecule undergoes minimum configuration change to fit the surface. On Table 3.1, we also indicate our predictions on which material is reactive based on atomic distance arguments. CeO_2, ZrO_2, Y_2O_3 are experimentally proven to be reactive towards DMMP or sarin dissociation at room temperature[63, 60, 68, 49], and the M-O distances are very close (smaller) to the optimal distance 2.54 Å compared with other metal oxides. For ZnO and TiO_2, neither the M-O nor M-M distance is close to 2.54 Å, and both modelling and experiment indicates the dry TiO_2 and ZnO can hardly decompose DMMP or sarin at room temperature[22, 58].

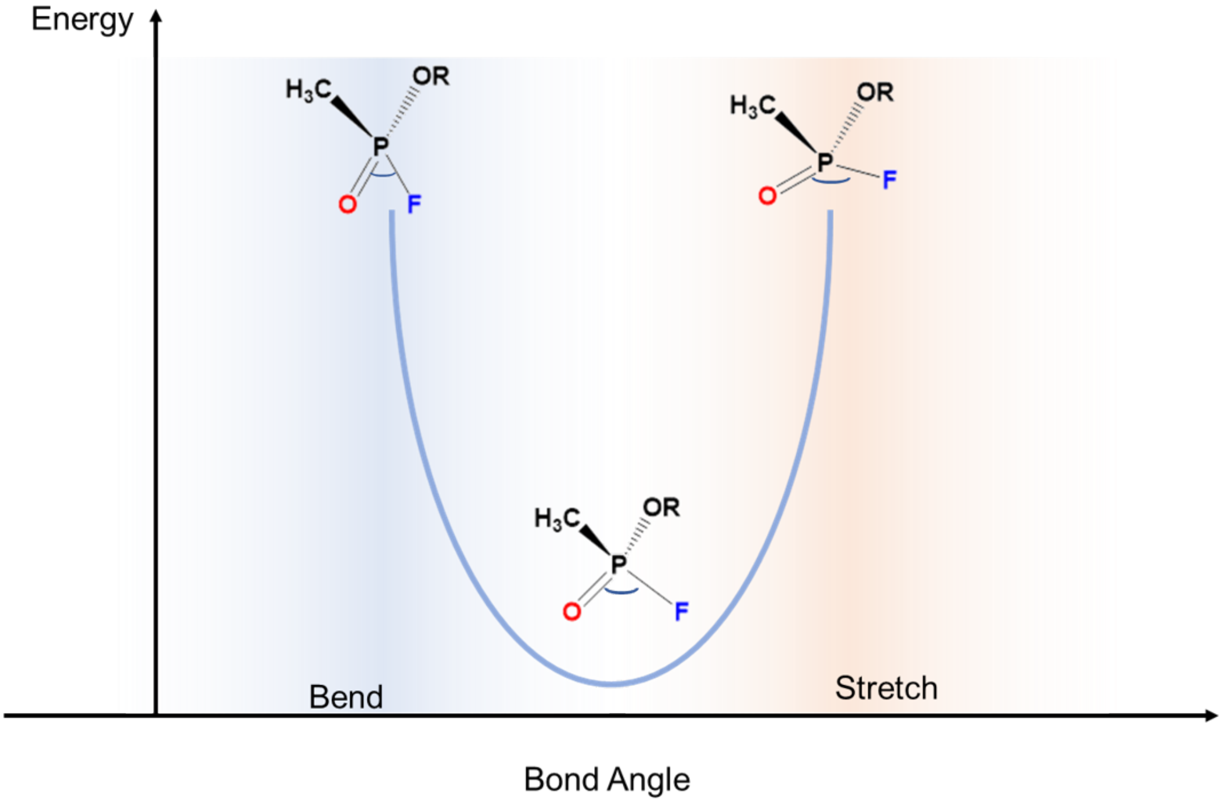

Figure 3.6: Energy diagram of the sarin molecule depending on O-P-O bond angle.

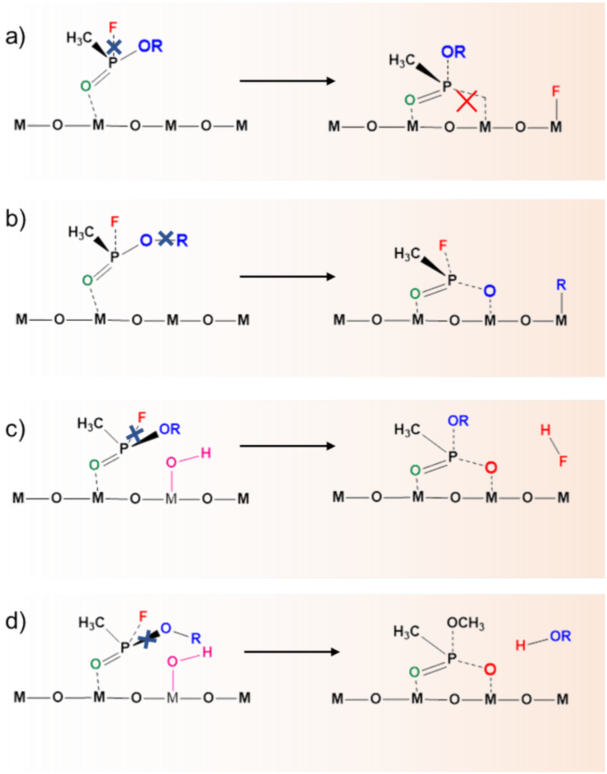

Figure 3.7: a) and b) Proposed pathways for formation of Structure 4 on the dry surfaces of meta oxides. c) and d) Proposed pathway for formation of Structure 4 on the hydroxylated surfaces of meta oxides.

3.2.3 Influence of Hydroxylation on the Surface

Again, there is always moisture and hydroxylation in practical situations so it is important to be able to predict how the surface hydroxylation will influence the dissociation behaviors of sarin/DMMP. We will evaluate the case of structure 4 and the case of structure 5 separately.

Let us first consider that sarin/DMMP dissociate to form structure 4 on pristine dry surfaces. For sarin, P-F bond breaking in this situation seems to be not preferred, as there no is favored oxygen sites to form bond with under-bonded P atom after P-F bond breaking, as shown in Figure 3.7a. P-O-R bonding breaking is possible for sarin and DMMP. To form the stable structure 4, O-R bond breaking is necessary instead of P-O bond breaking, as illustrated in Figure 3.7b.

Generally, P-O breaking is easier than O-R breaking, as P-O has larger polarity (larger difference in electronegativities). Thus O-R breaking will raise activation energy barrier. Plus, the leaving alkyl group (R) is usually not stable on the metal oxide surfaces or in the atmosphere, which lead to the significant increase of the free energy of the final dissociation products. We conclude here dissociation to form structure 4 on pristine oxide surface is not an energy favored process even M-M distance is close to optimal. The lack of low-energy path to form O-P-O species in the surfaces might be one of the reasons why dry TiO_2 and Al_2O_3 are barely reactive to sarin and DMMP and why most reactive metal oxides reported are the cases of structure 5 instead of structure 4.

With hydroxylation, surface -OH can provide oxygen sites to form bonds with under-bonded P atom after P-F bond breaking (Figure 3.7c), leading to an energy -favored stable structure. On the cases where P-O-R breaking, now P-O bond become possible due to oxygen sites provided by OH group (Figure 3.7d). The energy cost to break the P-O is less than to break O-R. Besides, the leaving group -OR is much more stable on the metal oxides or in the atmosphere in the form of methanol. Obviously, the activation energy barrier of the dissociation reaction as well as the free energy of the final products for sarin/DMMP dissociation on hydroxylated surfaces are lower than on the pristine surfaces. Thus, in cases where structure 4 is formed, hydrogen will promote the degrading of DMMP/sarin. Experimentally and computationally, we found that sarin will decompose on hydroxylated TiO_2 surfaces at room temperature[69], which agrees well with the predictions here.

In the case where sarin/DMMP dissociate to form structure 5 on pristine dry surfaces, P-F or P-O can break to form stable structures (Figure 3.8a and b). It is also worth noting here, the oxygen atom from the surface lattice of metal oxides participates in the formation

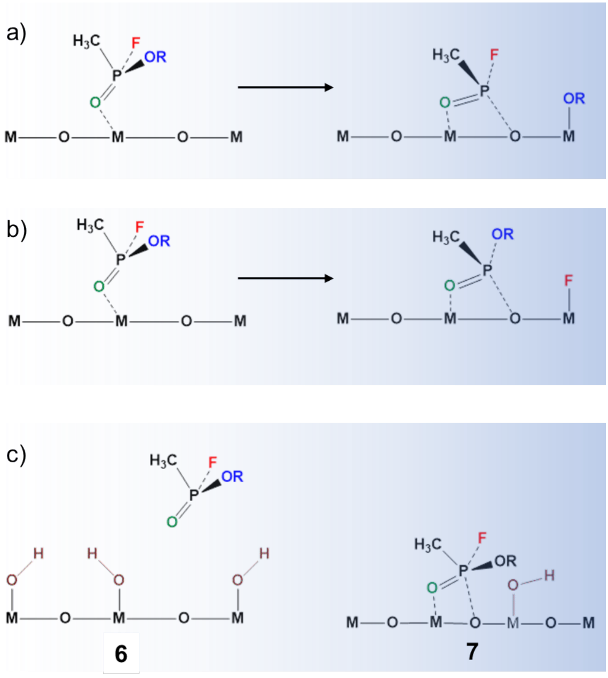

Figure 3.8: a) and b) Proposed pathway for formation of Structure 5 on the dry surfaces of metal oxides. c) Effect of hydroxylation to form Structure 5 on the surfaces metal oxides.

of structure 5. Thus, we might expect the activity of the lattice oxygen of metal oxides will have an impact on the surface activity in this case. As mentioned earlier, fluorite CeO_2, whose lattice oxygen are known to be active[70, 71], is one of most reactive metal oxides reported to dissociate DMMP[60, 26, 63]. When the surface is hydroxylated, unlike the case of structure 4, the OH group seems to impede the formation of structure 5. On one hand, since lots of the metal sites will be OH terminated after hydroxylation, it will stop the sarin/DMMP to get intact with the metal sites through their P=O bond (Figure 3.8c, structure 6). On the other hand, the neighboring OH group not only might have a steric effect when the P atom tries to approach the oxygen within the surface, but also can block the dissociated -OR or F group to attached on the neighboring metal sites (Figure 3.8c, structure 7). Based on this argument, we may predict hydroxylation should have a negative impact on the dissociation of sarin/DMMP. DFT results do show that hydroxylation on the CeO_2 will greatly increase the activation energy barrier for DMMP dissociation[60]. Experimentally, increase of the hydroxylation level decreased the surface activity of CeO_2 for DMMP dissociation.

3.2.4 Other considerations

3.2.4.1 Exposed surfaces(facets)

The atomic structure especially the interatomic distance plays a significant role in the activity of metal oxides towards sarin/DMMP dissociation. When evaluating the atomic distance, we have to realize there are usually more than one M-M or M-O distances existing in the structure of metal oxides, as listed in the Table 1. As the dissociation of sarin/DMMP relies on the direct physical interaction with the surface, it is the atomic distance on the exposed surface that matters. For example, we may find CuO structure have a favored M-O distance (2.784 Å) to form Structure 5. However, such a M-O distance exists on the surface with high lattice indices, which is not usually exposed on CuO materials. Surfaces of (111) or (101) are much more commonly exposed to environment[72, 73]. When attempting to link the atomic distance to the activity, we must use the distances on the practically exposed surfaces to get a better prediction.

3.2.4.2 Surface structures and defects

Till now, our qualitative model and prediction are based on flat surface of metal oxides. While the real structures of the surfaces are much more complicated. The difference between the structures in the model and real surface structure are usually the reason the prediction fails. One situation we might need to consider is surface reconstruction. For example, the surface of MoO_3 is terminated with O in practice after surface reconstruction. We may predict MoO_3 has some activity to decompose DMMP/sarin purely based on atomic distance argument. But when we take the real surface structure into consideration, we will realize the O termination on the surface will stop the direct interaction between metal site and molecules, leading the low activity of the surface. Another case worth noting is the zigzag surface structure shown on Scheme 8. Such surface structure might lead to favored dissociation sites (Figure 3.9, Structure 8) and or cause steric effect to impede the formation the dissociation structure (Figure 3.9, Structure 9).

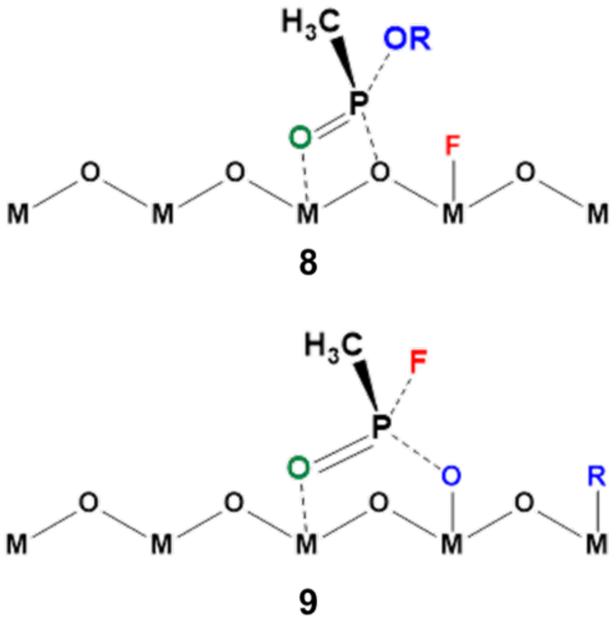

Figure 3.9: Proposed configuration of dissociated GB on the metal oxides with a zigzag surface structure.

3.2.4.3 Other Interfering Molecules

In practice, the interaction between sarin/DMMP and filter materials happens mostly in atmospheric conditions, which can involve the participation of other species from the atmosphere. Some of the species might simply compete with sarin/DMMP to occupy the available sites of metal oxides. Other species can even significantly change the surfaces of metal oxides, leading to different interaction behavior between surfaces and sarin/DMMP. We have already discussed the potential impact from moisture(water).

Another common interfering molecule is CO_2. In the short period, CO_2 seems to be a weak competitor to occupy the active sites of filter materials, which has been explored in some studies. However, for the longtime exposure of CO_2, which can happen to the filter material in practical situations, might be a different story. It is known carbonates can form on quite a few metal oxides after being exposed in atmosphere for a period. When such materials are tested to interact with sarin/DMMP, it is actually the carbonates that are interacting with molecules. The formation of carbonates and its influence on the reactivity is rarely mentioned when evaluating the performance of metal oxides as filter materials, which should be addressed in the future studies.

3.3 Potential for Catalysis?

In the above discussion, we treat the dissociation of CWAs as an irreversible chemical reaction between the metal oxide surfaces and CWA molecules. In the practice, besides the filter materials used for individual protection equipment, developing materials that can effectively detoxify the CWAs in the environment is necessary to fight against the threat from CWAs. For the application of detoxification, one important feature of the candidate materials is that they can catalytically decompose CWAs at mild conditions (e.g., room temperature), which allows the materials to function repeatedly. Searching for the materials that are catalytically reactive towards CWAs degradation is a popular trend.

Here the question is: Can metal oxides also serve as catalysts to repeatedly degrade CWAs? And what feature should a metal oxide have to be a good candidate? First, after reviewing wide range of literature, we have to acknowledge, the dissociation of CWAs on most oxides are found to be non-catalytic reactions. Multiple studies used mass spectrometry to analyze the waste after the reaction between DMMP and metal oxides, only methanol was detected as the product, meaning the leaving phosphorus species has stuck to the surface. XPS, IR characterization also shows that the phosphorus species remain on the surface even after the heating and long period of evacuation[63]. Quite a few studies show the metal oxides gradually deactivate after dosing excessive DMNP[49]. Such observations are not surprising to us. If we look back on our previous discussion on the dissociation of sarin/DMMP on metal oxides, the products always form some covalent interaction with the surface atoms (shown on Figure 3.5), making it extremely difficult for them to leave the surface.

With the moisture or hydroxylation, fluoride or alkyl group on the surface might undergo hydrolysis to form HF and alcohol and then leave the surface with relatively low activation energy barrier. However, it does not help the leaving of phosphorus containing part as its interaction with the surface is too strong. MOFs seem to encounter similar problems as most of studies apply special solvents to prevent the active center being poisoned[19].

Based on what we have mentioned, we cautiously think it is extremely challenging to develop a catalyst based on metal oxides in this field. However, theoretically, it is possible. And the metal oxides that have been explored in this field are still very limited. So we remain hopeful that some unexplored metal oxides can stand out in the future.

From the theoretical perspective, we can also predict some features that a metal oxide should have to be a catalyst to degrade CWAs. Here we use one of the simplest heterogeneous catalytic reactions, the hydrogen evolution reaction (HER), as an analogy. The HER on the electrode mainly involves three steps[74, 75]: (1) adsorption of H+ on the electrode surface (2) conversion of H^+ to H on the surface (3) desorption of H from the surface to form H_2. The process is presented in Figure 3.10a. It is well recognized that the adsorption in the first step and desorption in the third step contribute to a major part of the activation energy barrier of this reaction. A close to zero adsorption/desorption energy will be ideal for such reactions.

Though sarin/DMMP catalytical dissociation is more complicated, we can also separate it into several parts: (1) adsorption of DMMP/sarin on the surface (2) modify the configuration of DMMP and sarin on the surface to allow the match between molecules and lattice (3) dissociation (4) desorption from the surface with help of moisture, as displayed in Figure 3.10b. (1)(3)(4) are similar processes with HER. Step (2) are unique as dissociation of sarin/DMMP involves multiple sites on the surface as we have mentioned previously. We can see that the activation energy barrier now comes from the adsorption in the first step, desorption in the fourth step, and the configuration adjustment of the molecule in the second step. Based on that, we can conclude low adsorption/ desorption energy and a minimum configuration adjustment are necessary to achieve high catalytic activities. As we can see, same as filter materials, optimized atomic distances on the surfaces are necessary to achieve minimum configuration adjustment of the molecule. While contrary to filter materials, catalysts “hate” strongly adsorbed molecules. Thus, when screening possible metal oxides as catalysts, we might pay attention to those who have a relative high-energy conduction band (far away from the LUMO of P=O). In the existing theoretical studies, very few did calculation to understand the desorption of the decomposition species. Future studies should address the desorption for the catalysis applications.

There are other possible strategies to avoid the problem of the surface deactivation when applying them as catalysts to degrade CWAs. For example, instead of utilizing a thermally activated catalytic reaction, exploring the possibility of electron activated catalytic reaction such as photocatalytic[76, 77, 78] and surface-plasmon catalytic reaction[79] might be a good solution as they are less sensitive to the surfaces. Besides, surface modification of the metal oxides with functional groups to totally change the reaction pathways might also be an intriguing direction.

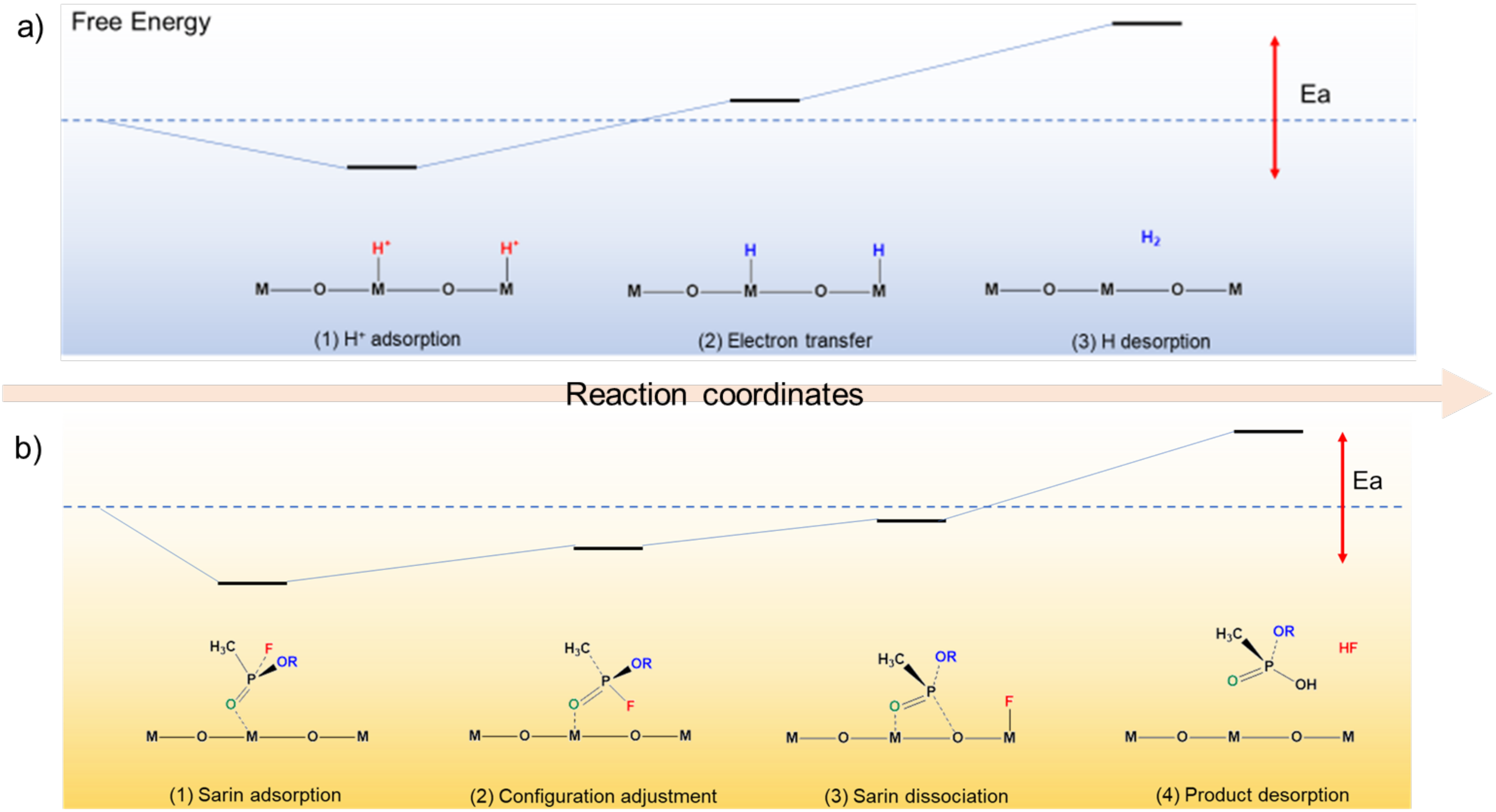

Figure 3.10: Free Energy diagram of a) catalytic Hydrogen Evolution Reaction and b) catalytic sarin dissociation.

3.4 Summery

We admit that interaction between CWAs and metal oxides is a very complicated process. The complexity of the molecules and the surface structures can make the experimental data interpretation and DFT simulation difficult and time-consuming. Despite the difficulty, however we demonstrate that we can build a simplified universal model to qualitatively understand and predict the interaction behavior based on the fundamental chemical principles. From this simple model, we argue that evaluating the energy of the valence band and the interatomic distance on the surfaces are crucial to efficiently locate potential metal oxides which can strongly adsorb and effectively dissociate CWAs. Once we start taking more factors such as surface hydroxylation and surface structure into consideration, the prediction will be more accurate. But on the other hand, it also adds significant difficulties to evaluate the overall effect without DFT modeling. still, In the practical search of candidate metal oxides, having such simple model as guidance can reduce some unnecessary attempts, given that both experiments and modelling are both costly.

The oversimplified model we present in this review is far from perfect. However, the main goal here is to present a different approach to this practical problem: to build a universal model based on fundamental scientific principles and current data/observation we have. As more binary or even ternary oxides are experimentally and computationally measured, we will gain better understanding on the details of the interaction mechanisms, so that a more accurate universal model can be developed.

Chapter 4: Interaction of Sarin and its Simulant DMMP with Mesoporous CeO_2

The research described in Part 1 was published in *ACS Appl. Mater. Interfaces*. 2021, 13 (45). Tsyshevsky, R.; Algrim, L.; McEntee, M.; Durke, E. M.; Eichhorn, B.; Karwacki, C.; Zachariah, M. R.; Kuklja, M. M. and Rodriguez, E. E. were contributing authors on the manuscript. I designed experiments, synthesized and characterized the materials, performed the DMMP dosing DRIFTS experiments, and wrote the manuscript draft.

The research described in Part 2 has been submitted for publication. Leonard, M.; Tsyshevsky, R.; M.; Durke, E. M.; Karwacki, C.; Kuklja, M. M. and Rodriguez, E. E. were contributing authors on the manuscript. I designed experiments, synthesized and characterized the materials, performed the data analysis and interpretation, and wrote the manuscript draft.

4.1 Part 1: Investigation of DMMP interaction with mesoporous CeO_2

4.1.1 Introduction

DMMP interaction on different binary metal oxides, such as $Al_2O_3$16, TiO_2[80, 23, 62], CuO[59, 45], MoO_3[3, 81], Fe_2O_3[82], ZnO[22],Y_2O_3[68] and CeO_2[63], has been studied experimentally and theoretically. DMMP reactivity on TiO_2, CuO, Y_2O_3 and CeO_2 has been reported, with DMMP dissociation observed at room temperature. Fluorite CeO_2 draws extensive attention in many fields of catalysis and surface reaction such as photocatalytic dye degradation, electrocatalytic water splitting/ CO reduction, fuel/CO conversion and oxidation[83, 84]. CeO_2 demonstrates high reactivity in many catalytic and noncatalytic reactions due to its unique surface structure and the high reactivity of Ce_{4+}. Several studies on the decontamination of phosphorus containing compound with CeO_2 materials show high activity of CeO_2 towards dephosphorylation-[63, 85, 86, 87, 26]. DMMP dissociation is no exception. Chen et al. 24studied the interaction of DMMP on the CeO_2 (111) single crystal surface. They concluded based on observed DMMP dissociation that CeO_2 can be used as the potential filter material for the protection against CWAs[63]. However, results obtained from single crystal surface experiments are far from the practical applications due to the low surface area of samples and experimental conditions that are significantly different from atmospheric conditions. Additionally, a fundamental understanding of why CeO_2 is reactive towards DMMP and how DMMP dissociates on the CeO_2 is still lacking.

In this Study, we report the results of the most comprehensive (thus far) joint experimental and theoretical study of DMMP adsorption and decomposition on mesoporous CeO_2.To study the interaction of DMMP with CeO_2, we synthesized mesoporous CeO_2 with a reported nanocasting method[88, 89]. The as-synthesized mesoporous CeO_2 has a relatively large surface area, making it practical for the application as an adsorber. Adsorption and decomposition of DMMP on mesoporous CeO_2 were studied using mass spectroscopy and in situ Diffuse Reflectance Infrared Fourier Transform Spectroscopy (DRIFTS). DFT modeling of DMMP interactions with pristine and hydroxylated CeO_2 (110) and (111) surfaces was conducted to interpret experimental measurements. We observed the DMMP decomposition through both mass spectroscopy and DRIFTS measurement at room temperature. DFT modeling shows that although both pristine and hydroxylated CeO_2 surfaces decompose DMMP, it is the pristine surfaces that are more reactive than the hydroxylated ones. Our combined experimental and theoretical studies provide fundamental insights on the key parameters for designing CeO_2 -based materials to defeat chemical agents similar to DMMP such as GB.

4.1.2 Experimental Section

4.1.2.1 Synthesis of Templated Mesoporous CeO_2

Mesoporous CeO_2 was synthesized via a nanocasting method similar to the previously reported approach[88, 89]. The silica template KIT-6 was first prepared via a reported method34, for which 85 °C was used as the aging temperature during the KIT-6 synthesis. In our typical synthesis of mesoporous CeO_2, 0.5000g as-prepared KIT-6 silica was initially dispersed in 20.0 mL 95% ethanol. Then 1.362g $Ce(NO_3)_36H_2O$ was also dissolved in the same solution. The mixture was stirred at room temperature until all solvents evaporated and the mixture became a dry powder. The powder was later transferred to a glass vial (diameter $\sim$ 5 mm) and under calcination at 560 °C for 6h (ramping rate 1°C/min). During the calcination step $Ce(NO_3)_3 \cdot\cdot 6H_2O$ decompose and oxidizes to pure CeO_2. To fully remove the silica template, the CeO_2/KIT-6 composite was soaked in 2M NaOH solution at 80 °C overnight; this step was repeated three times. After washing 3 times with distilled water and twice with ethanol, the final mesoporous CeO_2 product was dried in air at 80°C overnight and then at 150°C for an additional 24h.

4.1.2.2 Surface and Structural Characterization of Mesoporous CeO_2

Transmission electron microscopy (TEM) image was taken using a JEOL JEM 2100 LaB6 TEM system. Powder X-ray diffraction (XRD) pattern was recorded on the Bruker D8 Advance diffractometer, with Cu Kα/Kβ radiation. Rietveld refinements were performed using TOPAS 535. X-ray Small angle scattering (SAXS) patterns were collected with a Xenocs Xeuss SAXS/-WAXS/GISAXS system. The nitrogen adsorption isotherms were measured with a Micromeritics ASAP 2020 Porosimeter Test Station, and the surface area was calculated by applying the Brunauer-Emmett-Teller (BET) equation on adsorption data obtained at P/P0 between 0.05 and 0.35. The pore size distributions were calculated by analyzing the adsorption branch of the N_2 sorption isotherm using the Barret-Joyner-Halenda (BJH) method. Raman spectroscopy was obtained with Yvon Jobin LabRam ARAMIS using 532 nm laser source. Ce 3d and O 1s spectra were collected on a Kratos Axis 165 X-ray photoelectron spectrometer (XPS) operating in hybrid mode using Al Kα monochromatic X-rays at 280 W. All XPS spectra were calibrated to the C 1s peak at 284.80 eV, and fits were performed using CasaXPS. Shirley background was used for background subtraction, and the peaks fit with a 30% Gaussian +70% Lorentzian peak shape profile.

4.1.2.3 CO Adsorption IR Spectroscopy on CeO_2

CO adsorption studies on CeO_2 were performed in a high vacuum chamber with a base pressure at $3x10^{-9}$ Torr. A more detailed description of the vacuum chamber is provided elsewhere [20]. The CeO_2 was pressed into a 0.004" thick W-grid and attached to the sample mount via stainless steel clamps connected to copper rods. The copper rods were attached to a power supply allowing for resistive heating of the sample up to $\sim$1000 K at a resolution of ±0.1 K. Before introducing CO into the vacuum chamber, the sample was heated up to 450 K for 30 minutes in order to remove H_2O and hydrocarbon impurities. After heating, the surface was cooled down with LN2 (∼140 K) and an IR spectrum was taken of the CeO_2 sample. An IR spectrum was taken of the W-grid without any CeO_2 powder and used as the background. Each IR spectrum contains an average of 256 interferograms at a resolution of 2 cm^{-1}.

Subsequently, 10^{-2} Torr of CO vapor was introduced into the vacuum chamber. An IR spectrum was taken and was subtracted from the IR spectrum of CeO_2 prior to CO exposure. The subtracted spectrum represents a difference spectrum showing the CO adsorption on the CeO_2 surface.

4.1.2.4 Detection of DMMP Decomposition on Mesoporous CeO_2 via Mass Spectrometry

Mass spectrometry was used to detect any reaction products from the interaction of mesoporous CeO_2 and DMMP. The measurements made with a mass spectrometer used an experimental setup described in the previous work[90], but again briefly described here. Before analysis with the mass spectrometer, the CeO_2 sample was heated to 200°C to remove any potential surface contaminants. Three mass flow controllers regulate the flow of dry argon, argon saturated with water, and DMMP, all of which are combined to produce a 35 mL/ min total flow that is 0.4 P/P_0 DMMP and 4% relative humidity at room temperature. The combined flow is passed into a 4.7625 mm (3/16”) ID quartz tube which holds the CeO_2 sample, supported by inert glass wool. The quartz tube is heated at 10 °C/min to 325 °C and held for 3 hours before cooling to room temperature, where it dwells for approximately 7 hours before heating again. This temperature cycle was repeated multiple times. Downstream from the material, a capillary line samples the gas mixture into the Quadrupole Mass Spectrometer, which collects full mass scans up to m/z

125. All-time traces are normalized to m/z 36 (an isotope of Argon) to minimize the effects of signal drift.

4.1.2.5 In situ DRIFTS of DMMP Adsorption/Decomposition on Mesoporous CeO_2

For the diffuse reflectance infrared Fourier transform spectroscopy (DRIFTS) measurements, a Harrick Scientific Praying Mantis DRA optical accessory was used with an associated Harrick Scientific high-temperature reaction chamber HVC-DRP-5 and temperature controller unit (110 V, ATC-024-3). Prior to DMMP exposure, mesoporous CeO_2 powder was heated under the 25 mL/min Ar flow at 200°C for 2 hours to remove as much physisorbed water as possible and then cooled to room temperature. We were mainly interested in the interaction between mesoporous CeO_2 and strongly adsorbed DMMP molecules. Additionally, we wanted to minimize the DMMP contamination in our DRIFTS system. Thus, a swift injection approach was employed to introduce DMMP into the DRIFTS cell containing mesoporous CeO_2 powder. In a typical experiment, mesoporous CeO_2 powder in the cell was under constant 25 mL/min Ar flow. Then 2 mL saturated DMMP vapor carried by N_2 was quickly injected into the system using a delay-controlled electronic injector. The illustration of such a system is provided in the Appenidx A (Figure A.1). The injections occurred every 20 min. Between injections, DRIFTS spectra were collected every 30 s, allowing for the observation of strong interaction between the substrate (CeO_2) and the molecule of interest (DMMP). In total, 10 DMMP injections were performed. Instrument setup is presented in the supplementary information.

4.1.2.6 DFT Modeling of DMMP interacting with CeO_2 surfaces

Solid state periodic calculations were performed with DFT[91, 92] using GGA PBE[93] functional and projector augmented-wave (PAW) pseudo-potentials[94], as implemented in the VASP code[95, 96, 97, 98]. Hubbard's parameter U44 was introduced to account for Ce 4f orbitals and was set to 4.0 eV in accordance with reported literature[99]. Grimme's D246 corrections were added to account for weak van der Waals interactions. In simulating ideal bulk crystals, atomic coordinates and lattice constants were allowed to relax simultaneously without any symmetry constraints. The convergence criterion for electronic steps was set to 10^{-5} eV, and the maximum force acting on any atom was set not to exceed 0.01 eV/Å. Kinetic energy cut-off was set to 520 eV. In modeling CeO_2 crystal, an 8×8×8 Monkhorst-Pack k-point mesh was used. The calculated lattice parameters of the CeO_2 cubic unit cell (Figure 1a) with Fm-3m space group, a=5.37 Å, agree with the experimental lattice vectors (a= 5.41 Å) within $\sim$1 %.

Our calculations of DMMP adsorption and decomposition were limited to modeling reactions on the most stable surfaces, including (110) and (111) surfaces (Figure 1 b and c), observed in our experiments. The model slab of (110) surface contained 252 atoms with the supercell lattice vectors of a = 16.23 Å, b = 14.92 Å, and c =31.61 Å. The model slab of (111) surface contained 240 atoms with the supercell lattice vectors of a = b = 15.03 Å, and c =34.37 Å. A vacuum layer of 20 Å placed on top of the CeO_2 surfaces served to minimize interactions between the supercells in the z-direction and to avoid any significant overlap between wave functions of periodically translated cells. All surface calculations were performed at G-point only. Kinetic energy cut-offs in modeling CeO_2 (110) and (111) surfaces were set to 520 eV. The convergence criterion for electronic steps was set to 10^{-5} eV, and the maximum force acting on any atom was set not to

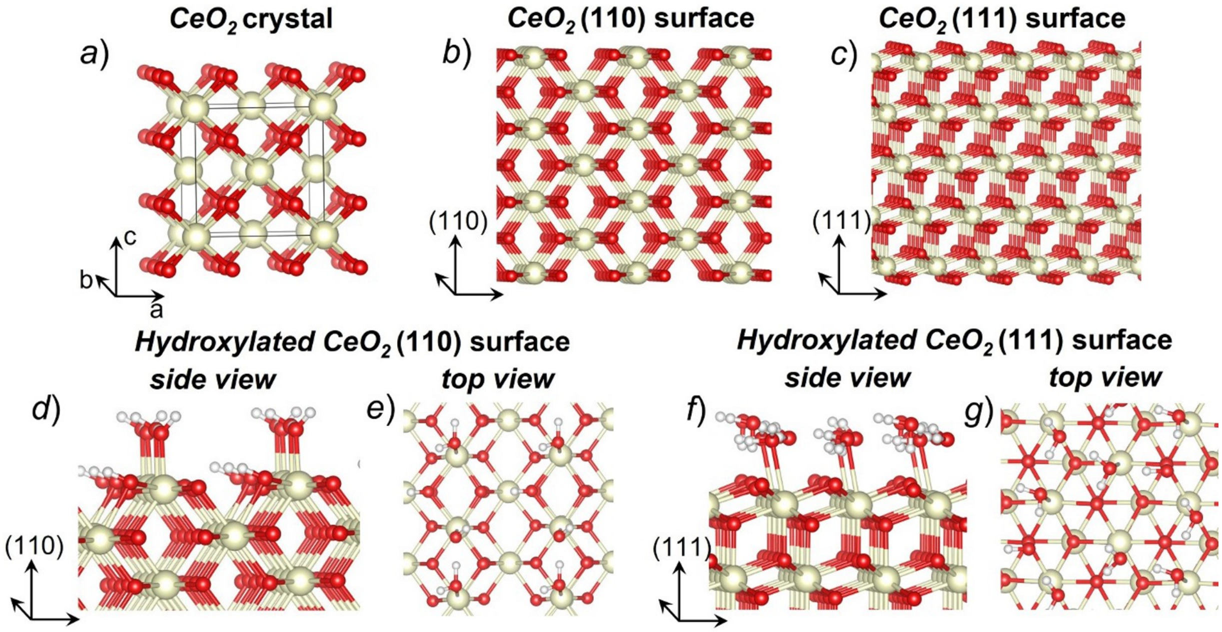

Figure 4.1: a) Structure of CeO_2 crystal; Structures of CeO_2 b) (110) and c) (111) surfaces; d) side and e) top views of hydroxylated CeO_2 (110) surface; f) side and g) top views of hydroxylated CeO_2 (111) surface.

exceed 0.03 eV/Å.

In modeling DMMP interactions with hydroxylated CeO_2 surfaces, a monolayer of water was added on CeO_2 (110) and (111) surfaces. Our calculations show that the monolayer of water containing intact and dissociated water (OH group) molecules is the most energetically favorable configuration for CeO_2 (110) surface (Figure 4.1 d and e), whereas for CeO_2 (111) surface the monolayer of water containing only intact water molecules corresponds to the most energetically favorable configuration (Figure 4.1 f and g).

Minimal energy paths in the VASP periodic calculations were obtained with the standard nudged elastic band method[100] . Atomic positions were relaxed using conjugate gradient and quasi-Newtonian methods within a force tolerance of 0.05 Å/eV. The convergence criterion for electronic steps was set to 10^{-5} eV.

4.1.3 Results

4.1.3.1 Bulk and Surface Properties of Mesoporous CeO_2

Characterization of the structure and surface of synthesized mesoporous CeO_2 is presented in Figure 4.2. The resulting mesporous morphology and structure resemble results previously reported for mesoporous ceria[89, 101]. An ordered mesoporous structural property is visible from the TEM image (Figure 4.2a). Diffraction peaks for the (211), (220) and (420) reflections of structure are observed in the SAXS pattern (Figure 4.2b), which confirm the ordered porous structure of a body-centered cubic structure (space group Ia-3d). Nitrogen adsorption isotherms and the corresponding pore size distribution curve (inset) are displayed in Figure 4.2d. The extracted BET surface area is 130.4 m^2/g and the mean pore size is approximately 3.6 nm. XRD patterns (Figure 4.2e) confirm the pure phase of cubic CeO_2 with the fluorite-type structure (space group Fm-3m). We note that the diffraction peaks in the XRD pattern severely broaden due to the nanocrystalline nature of the mesoporous CeO_2. The Rietveld refinement indicates that the lattice parameter is 5.4138(8) Å and the average crystallite size 11.8(1) nm. Raman spectroscopy (Figure 4.2c) shows a major F2g vibration mode, also indicative of phase-pure CeO_2 with the fluorite-type structure. Similar to the XRD patterns, the pronounced peak broadening in the Raman spectrum arises from quantum size confinement of nanocrystalline CeO_2[100]. The asymmetric peak shape is largely due to the surface states[102] because of the high surface area of the mesoporous CeO_2.

Ce 3d XPS is displayed in Figure 4.3a. The spectra are fit by employing previously reported parameters[103] . Appling only Ce^{4+} components affords a good fit to the spectrum, which implies that Ce^{4+} predominates as the Ce species on the surface. O 1s XPS (Figure 3b) suggests

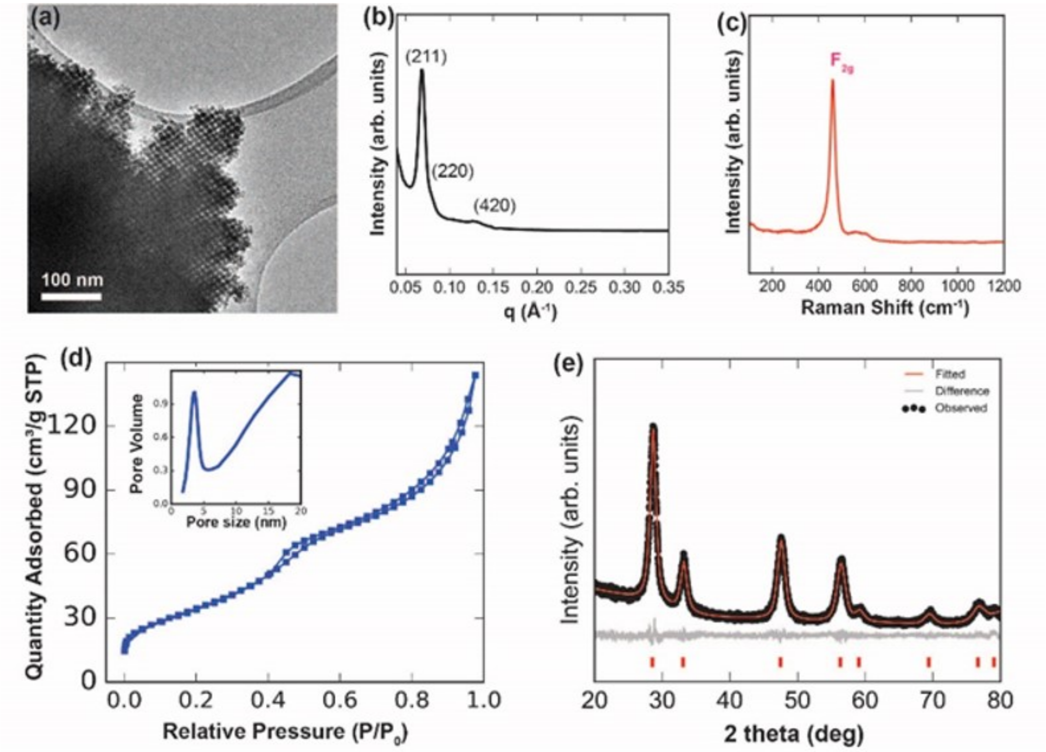

Figure 4.2: Structural and surface characterization of as synthesized mesoporous CeO_2: (a) TEM. (b) SAXS. (c) Raman Spectroscopy. (d) Nitrogen adsorption isotherm and pore size distribution(inset). (e) XRD pattern and Rietveld refinement fit.

the presence of two major types of oxygen, namely 40% lattice oxygen (O^{2-}) at 529.3 eV and 60% surface oxygen(-OH) at 531.5 eV. The O 1s XPS also indicates that a large fraction of the surfaces of mesoporous CeO_2 is hydroxylated (-OH terminated), which is common for metal oxides under ambient conditions.

For a crystalline material, its chemical reactivity can vary greatly depending on which crystalline surfaces are exposed, since surface properties (such as polarity, surface energy, hydrophilicity, coordination configuration of surface atoms) differ considerably from surface to surface. Thus, the determination of the exposed surfaces (facets) is crucial to understand the surface chemistry of certain materials. For a material with a single crystal surface (film), the exposed surface can be determined by surface diffraction methods or Scanning Tunneling Microscopy

(STM). High-resolution TEM is normally applied to visualize the exposed surface of nanocrystals. However, it is challenging to use the above-mentioned techniques for the determination of exposed surfaces in mesoporous materials. On one hand, the 3-dimensional pore structure makes it impossible to obtain information about the interior of pores with STM and TEM. On the other hand, TEM only gives very localized information instead of statistical information of the exposed surface if more than one surface is exposed. Therefore, we followed well-established studies whereby CO molecules adsorb on the different surfaces of CeO_2; since the C-O stretching frequencies correlate to coordination strength and degree of back bonding between CO and Ce atoms on the surface, then one can learn about the nature of the exposed ceria surface[104, 105]. Infrared spectroscopy (IR) can detect C-O stretching frequencies, and the large penetration depth of the IR beam (hundreds of nanometers to tens of microns) makes it ideal to gain information inside the pores of mesoporous materials.

Here, we applied an indirect method to gain statistical information on exposed surfaces of the mesoporous CeO_2. As a probe molecule, CO is first dosed into mesoporous CeO_2, followed by the detection of C-O stretching with transmission IR. The results are displayed in Figure 4.3c. Two major CO stretching frequencies are visible. The peak around 2178 cm^{-1} corresponds to CO adsorbed on the (110) CeO_2 surface. 2159 cm^{-1} corresponds to CO adsorbed on the (111) CeO_2 surface[104, 105]. A Gaussian peak profile is used to fit the peaks within the spectrum. The fitting implies (110) surface accounts for 56% of the exposed surface of the mesoporous CeO_2 system and (111) surface the remaining 44% of the exposed surface. It is worth noting CO adsorbs on the surface of CeO_2 through the coordination between CO and exposed Ce metal sites[105]. The observation of CO stretching modes in the IR spectrum indicates considerable amounts of exposed (or undercoordinated) Ce atoms on the surface of mesoporous CeO_2 despite the fact that our XPS results show a large part of the surface is hydroxylated (-OH terminated).

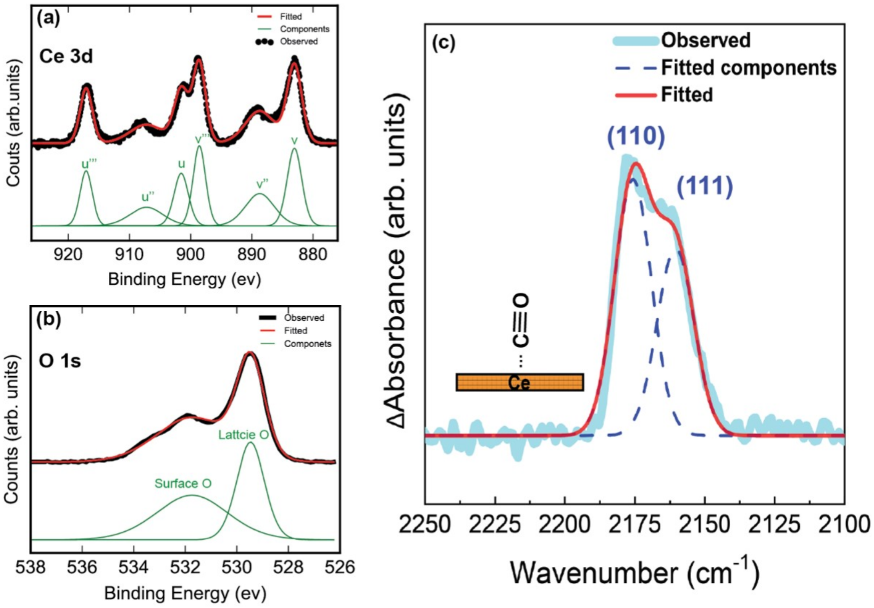

Figure 4.3: (a) Ce 3d XPS spectra and fitting of mesoporous CeO_2. (b)O 1s XPS spectra and fitting of mesoporous CeO_2. (c) IR spectra of CO stretching when CO is adsorbed onto mesoporous CeO_2.

4.1.3.2 DMMP Decomposition Product at Elevated Temperatures

Time traces of common product ions from DMMP dosing onto mesoporous CeO_2 are plotted in Figure 4.4. Each m/z trace is plotted against temperature and is colored according to the number of heat ramps. Across the entire measured temperature range in the first heat ramp, methanol is observed as a major product (m/z 31 signal in Figure 4.4A), which is a common decomposition product of DMMP[22, 106]. It is noticeable that the methanol signal is first observed near room temperature (∼40°C), implying high reactivity of mesoporous CeO_2 towards DMMP dissociation. In the methanol production trace plot (Figure 4.4A), a bimodal peak is observed at 200 °C and a small shoulder appears at 100 °C, implying there are possibly two reaction pathways for DMMP decomposition on mesoporous CeO_2 to produce methanol.

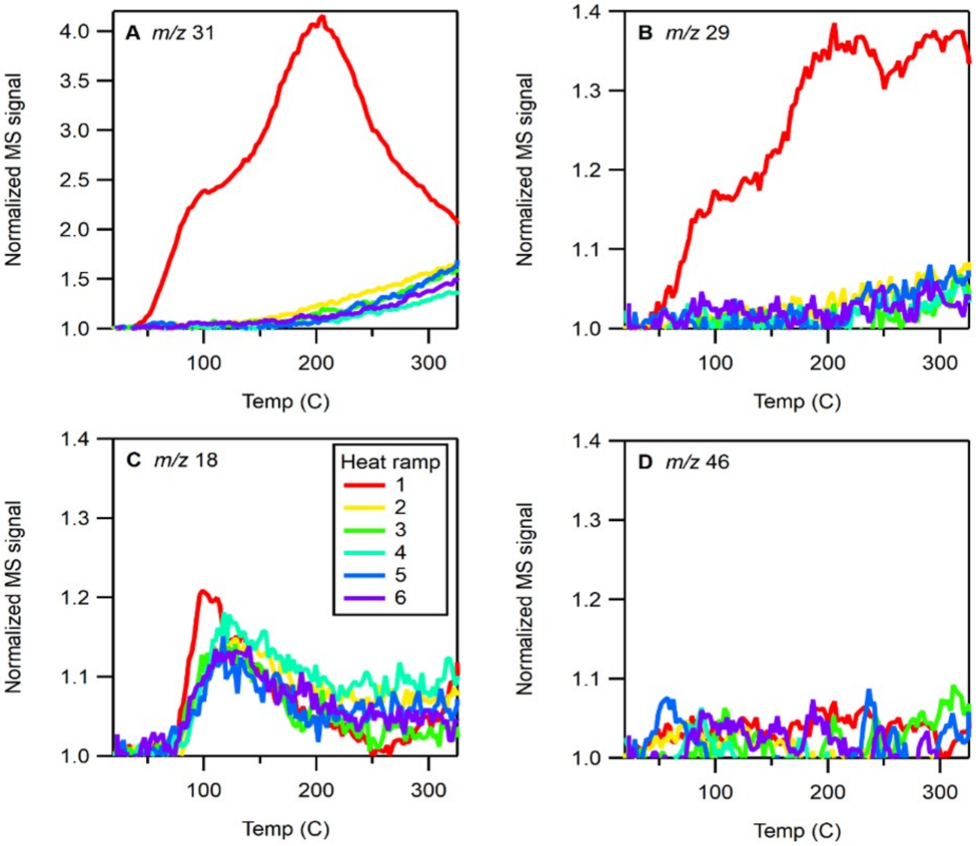

Figure 4.4: Mass spec signal from water and DMMP decomposition products as Ceria was heated. The panels show traces of m/z 31 (A) for methanol product, m/z 29 (B) which can be from methanol or formaldehyde. Panel C is m/z 18 which is water, and panel D is m/z 46 which is from dimethyl ether product.

Two different peak temperatures of methanol production suggest that the two pathways of DMMP decomposition have different activation barriers. The mass spectra alone is insufficient to determine whether the methanol observed near 100 °C is generated at that point, or whether it readily forms through decompositions at room temperature followed by desporbtion at higher temperatures. In the subsequent heat ramps, a dramatic decrease in methanol production was noted and the methanol signal curve is very different from the first ramp (i. e. peaks disappear). Such phenomena reveal that the DMMP decomposition on the CeO_2 is a surface reaction instead of a hetero-catalytic reaction. After the first cycle of DMMP interacting with mesoporous CeO_2, the surface of CeO_2 is changed and is shown to be deactivated towards DMMP decomposition. The changing of the CeO_2 surface after the first ramp can also be confirmed by looking at the water trace. Moisture is always present in the system. As shown in Figure 4.4C, we observed a water signal peak after 100 °C for every heating ramp, which we attribute to the thermal desorption of the water molecules on the CeO_2 surface. However, the water desorption peak appears at 100 °C in the first heat ramp, but in all successive ramps, the temperature slightly elevates to 125 °C, confirming a change of the surface after the first ramp of DMMP reaction.

Figure 4.4B shows the time traces for m/z 29, which can be attributed to methanol or formaldehyde. It can be seen that the m/z 29 trace mostly mimics that of m/z 31 due to the majority of the m/z 29 signal coming from MeOH. However, one difference is observed in heat ramp 1 above 250 °C. Because m/z 29, and not m/z 31, rises to form a third mode at high temperature($>$250 °C), this third mode can be reasonably assigned to formaldehyde which has been observed as a DMMP decomposition product from CeO_2[63] . The trace of m/z 46 (Figure 4.4D) is the molecular ion of dimethyl ether, another common DMMP decomposition product that has been observed from CeO_2 in the air as well as from other metal oxides[25] at high temperatures. However, we observe none in our measurements here possibly because our experiments were performed in the Ar environment instead of air. Since we are mainly interested in the near-room-temperature behavior of DMMP interacting CeO_2 for practical applications, the decomposition products at high temperatures are only briefly mentioned here.

We also monitored the fraction of DMMP that desorbs from the CeO_2, as is presented in Figure 4.5. the DMMP signal is integrated on each valley below and above the baseline separately to obtain total adsorbed and desorbed DMMP in the mesoporous CeO_2 during each heat cycle, as is displayed in Figure 4.5a. The fraction of sorbed DMMP is plotted in Figure 4.5b.

A lower desorb/adsorb ratio is observed in the first heat cycle, but subsequent cycles give ratios that average about 0.4. Less DMMP is desorbing off the surface in the first cycle aligns with the increased product, such as methanol, observed in that cycle. After the surface is altered in the first heat cycle the sorption/desorption ratio remains relatively constant, which is consistent with the observation that methanol production remains similar in subsequent cycles.

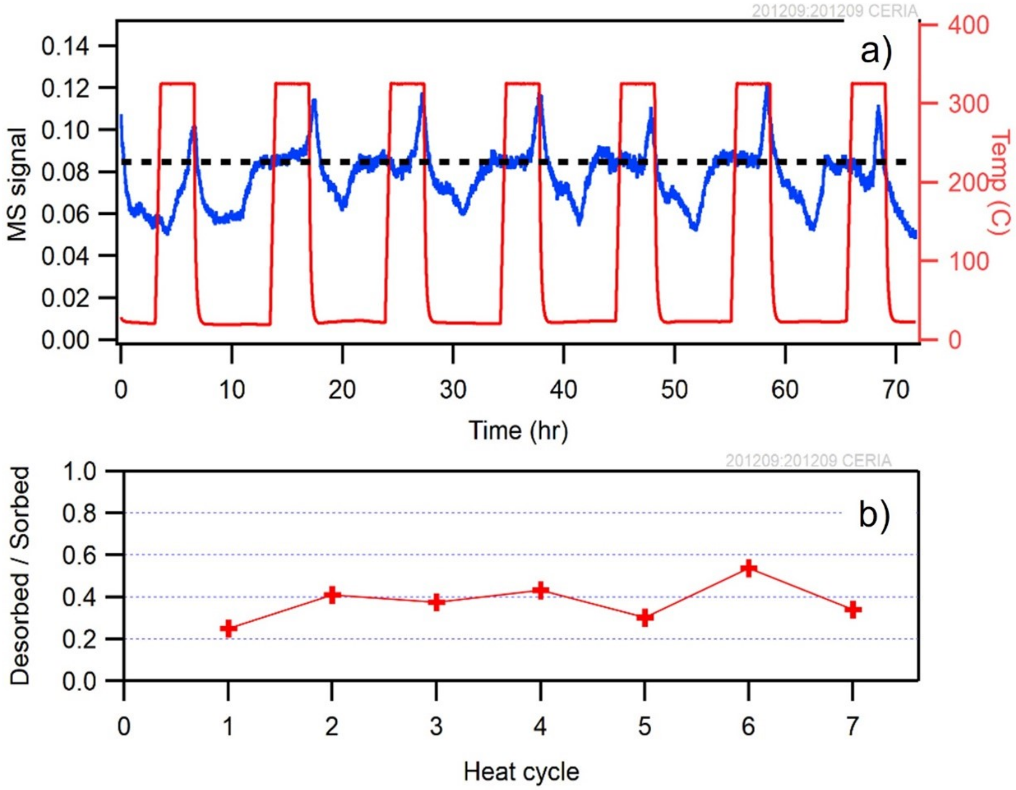

Figure 4.5: a) DMMP Mass Spectrometry signal in the heating cycle when flowing DMMP to the mesoporous CeO_2. b) Ratio of desorbed/adsorbed DMMP during the heating cycles.

4.1.3.3 DMMP Adsorption and Decomposition on Mesoporous CeO_2 at Room Temperature

Our mass spectrometry measurements indicate the as-synthesized mesoporous CeO_2 is active towards DMMP decomposition near room temperature. However, mass spectrometry cannot detect methanol production until MeOH has been desorbed from the CeO_2 surface. Thus, we perform DRIFTS measurement to understand how DMMP would interact with the surface of mesoporous CeO_2 at room temperature. Figure 4.6a shows the in situ DRIFTS spectra taken upon the first injection of DMMP onto mesoporous CeO_2. The scan right before the first injection is used as a baseline background. The vibration modes corresponding to IR adsorption peaks are assigned based on literatures[62, 23, 63] and listed in Table 4.1. Bands 1-4,6-10,12-13 belong to the different vibration modes of intact DMMP, which was also reported in the study DMMP on CeO_2 single crystal surface[63] and other metal oxide systems[62, 22]. Spectra in between 3100-3900cm^{-1} are the characteristic region for O-H vibration mode. Bands between 3600-3800 cm^{-1} (region A) are typically associated with “free” OH groups while modes between 3300-3600 cm^{-1} (region B) with OH groups that are hydrogen bonded[62, 22].

Position	Wavenumber (cm^{-1})	vibration	Assignment
1	3003	$v_a(PCH_3)$	Intact DMMP
2	2960	$v_a(OCH_3)$	Intact DMMP
3	2928	$v_s(PCH_3)$	Intact DMMP
4	2858	$v_s(OCH_3)$	Intact DMMP
5	2811	$v_s(MOCH_3)$	Methyl (DMMP dissociation)
6	1467	$\sigma_a(OCH_3)$ and $\sigma_s(OCH_3)$	Intact DMMP
7	1421	$\sigma_a(P–CH_3)$	Intact DMMP
8	1314	$\sigma_s(P–CH_3)$	Intact DMMP
9	1204	v(P=O)	Intact DMMP
10	1188	$\rho(OCH_3)$	Intact DMMP
11	1096	v(O–P-O)	DMMP dissociation
12	1070	v_a(C–O))	Methyl as well as DMMP
13	1047	v_s(C–O))	Methyl as well as DMMP
14	1116-1170	v(O–P-O)	DMMP dissociation

Table 4.1: Assignment of IR peaks upon DMMP dosing onto mesoporous CeO_2 from DRIFTS characterization.

As is displayed in Figure 4.6a, upon dosing the DMMP, there is a dramatic decrease of the “free” OH groups and an increase of hydrogen-bonded OH groups, which indicates that

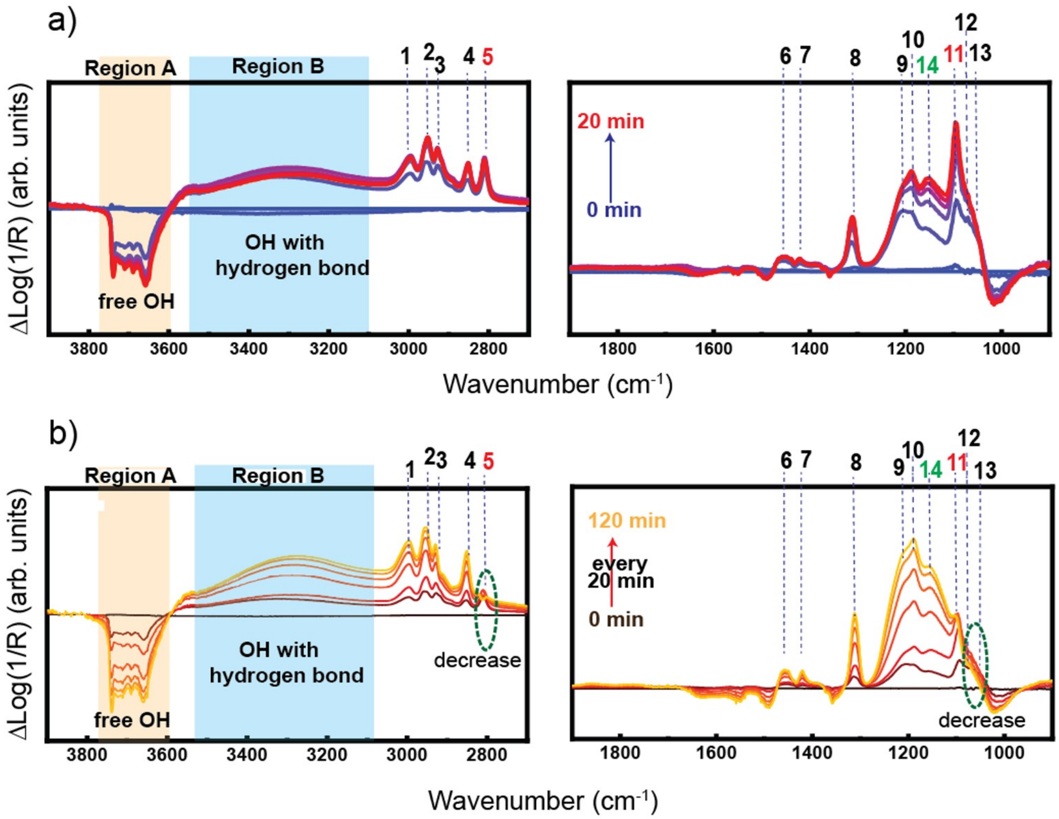

Figure 4.6: (a) in-situ DRIFTS spectra taken instantly following the first injection of DMMP onto mesoporous CeO_2. (b) in- situ DRIFTS spectra taken during the multiple injections of DMMP.

hydroxylated (-OH terminated) CeO_2 surfaces interact with DMMP via hydrogen bonds. Previous studies[62, 68] propose structure 1 as a major pathway for DMMP to interact with hydroxylated surfaces, as shown in 4.7a. Band 5 at 2811 cm^{-1} is the C-H modes of the OCH_3 group when OCH_3 group directly bonds to a metal center. A clear intensity increase of such mode indicates the existence of Ce-OCH_3, resulting from the breaking of the P-OCH_3 bond of DMMP, shown in structure 3 in 4.7b. The strong band 11 at 1096cm^{-1} is from vs(O-P-O) vibration when the species has a similar form of structure 4[62]. The observation of clear $CeOCH_3$ and OPO vibration modes is a strong indication of dissociation of DMMP on the mesoporous CeO_2 surface at room temperature. Apparently, the dissociation species remains adsorbed to the surface. The broad band(s) 14 observed at 1116-1170 cm^{-1} is a mixture of several bands. Part of this region is reported to belong to the va(O-P-O) as the result of the dissociation of DMMP[62, 22].

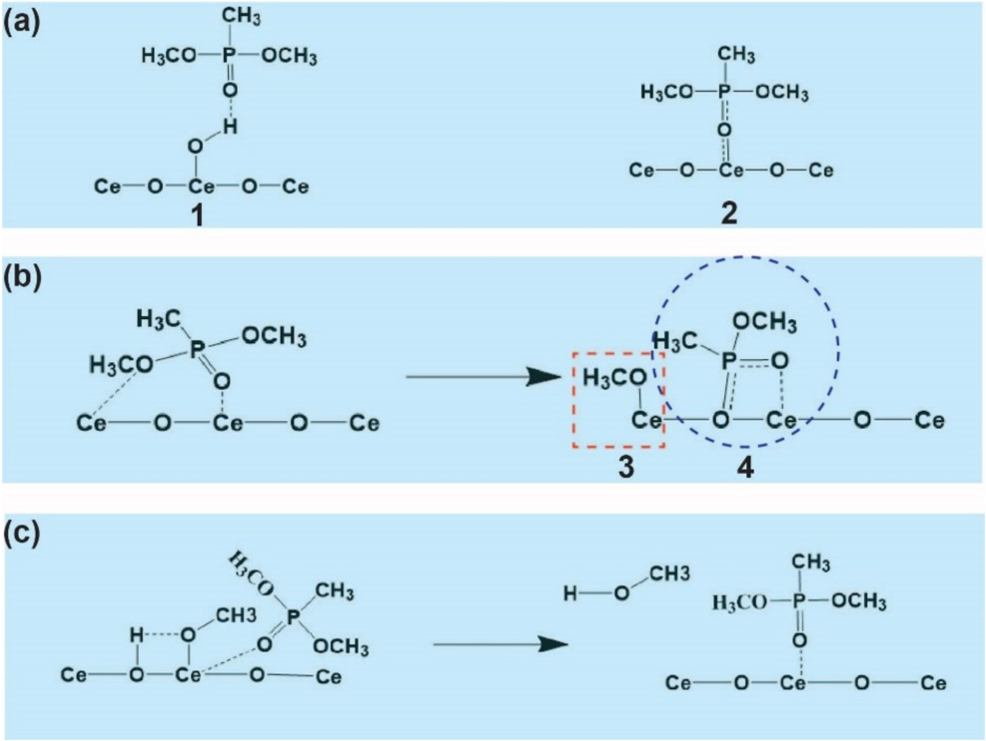

Figure 4.7: Proposed configurations after DMMP interact with CeO_2 surfaces: (a) DMMP adsorption configuration on the surface of CeO_2. (b) Cleavage of -OCH_3 from DMMP. (c) Surface methoxy group replaced by DMMP and leave in the form of methanol.

Following the first injection of DMMP, multiple injections also proceeded every 20 min. Figure 4.6b displays the in situ DRIFTS spectra taken during the multiple injections of DMMP. Each scan shown in the figure was taken right before the start of each injection. The spectral evolution is very similar to that during the first injection. The continued increase of intensity of bands 1-4,6-10,12-13 indicates that intact DMMP continues to adsorb on the hydroxylated CeO_2 surface, consuming free surface OH (decrease in region A) and forming hydrogen bonds (increase in region B). This process occurs until the surface reaches saturation. Interestingly, the C-H stretching mode from $CeOCH_3$ (band 5 at 2811cm^{-1}) increases in intensity during the initial injections, and the intensity decreases in subsequent injections. We attribute the decrease of $CeOCH_3$ stretching mode to the decrease of the -OCH_3 group attached to the surface. Band 12 at 1047 cm^{-1} and band 13 at 1070 cm^{-1} correspond to C-O stretching modes[107]. These two bands also decrease with subsequent injections, further confirming the decrease of the -OCH_3 group attached to the surface. Since we observe the methanol production in our mass spectrometry measurements on DMMP dosing on mesoporous CeO_2, we conclude that -OCH_3 leaves the CeO_2 surface to form methanol. Also, the replacement of -OCH_3 by the DMMP drives the leaving of the -OCH_3 group from the CeO_2 surface. Upon leaving the surface, -OCH_3 groups could take hydrogen from surrounding OH and form the methanol as a product. This mechanism, described in a previous study[62], is illustrated in Figures 4.7c. While the $CeOCH_3$ stretching mode continues to degrade, we observed O-P-O vibration modes (band 11 and 14) grow) grow, implying the DMMP is still dissociating on the surfaces. Such phenomenon indicates that DMMP dissociation, which occurs in later injections, does not involve the step whereby OCH_3 binds onto Ce sites (Figure 4.7). Obviously, two different DMMP dissociation pathways happen respectively in the DMMP initial injections and subsequent injections.

4.1.3.4 DFT modeling of DMMP Adsorption and Decomposition on CeO_2

We constructed model CeO_2 surfaces based on our characterization of the mesoporous CeO_2 samples. Our CO adsorption IR characterization indicates that the as-synthesized mesoporous CeO_2 possesses both (110) and (111) surfaces. The XPS and CO adsorption IR measurement show that there exist hydroxylated (OH terminated) surfaces as well as pristine-like (with exposed under-coordinated Ce atom) surfaces. Thus, we modeled the DMMP interactions with the (110) and (111) CeO_2 surfaces to better understand our experimental observations. For both (110) and

(111) surfaces, we also investigated pristine and hydroxylated situations separately to simplify the calculations, although the pristine and hydroxylated surfaces do not exist separately in our mesoporous CeO_2 system.

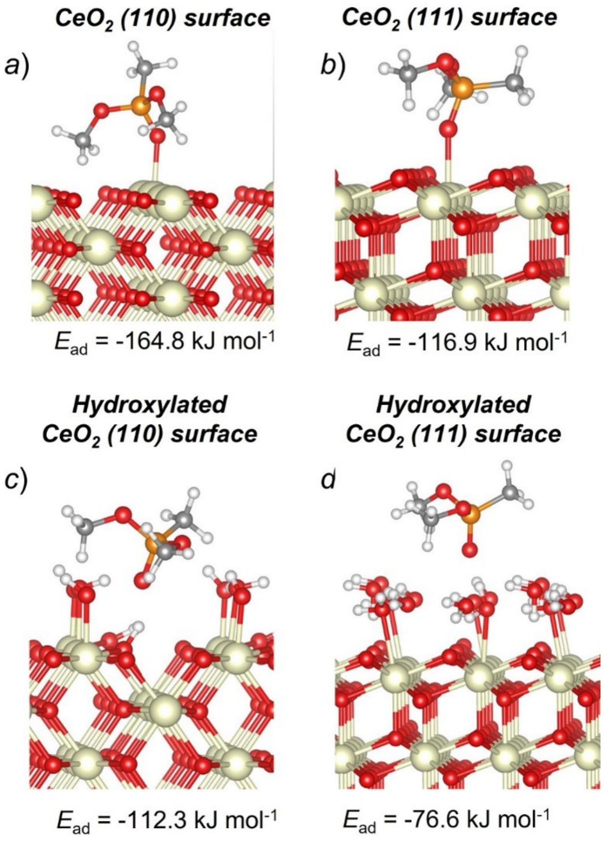

Figure 4.8: Adsorption of DMMP on pristine CeO_2 (a) (110) and (b) (111) surfaces; Adsorption of DMMP on hydroxylated CeO_2 (c) (101) and (d) (111) surface.

Adsorption of DMMP on CeO_2 (110) and (111) surfaces is a straightforward process. Similar to other metal oxides[59, 22, 99, 46, 56, 61], DMMP is adsorbed on the Ce atom via its phosphoryl oxygen, as depicted in Figures 4.8a and b. The calculated energy of DMMP adsorption on CeO_2 (110) surface (-164.8 kJ mol^{-1}) is considerably higher than that on (111) surface (-116.9 kJ mol^{-1}), which is, most likely, explained by a stronger electrostatic repulsion between phosphoryl oxygen of DMMP and a surface oxygen atom on the CeO_2 (111) surface.

DMMP interacting with hydroxylated CeO_2 (110) surface forms a hydrogen bond with one of surface hydroxyls, as shown in Figure 4.8c. The calculated energy of DMMP adsorption is -112.3 kJ mol^{-1}. Once DMMP is adsorbed on the hydroxylated CeO_2 (111) surface, it interacts with a water molecule via its phosphoryl oxygen as depicted in Figure 4.8d. The calculated energy of DMMP adsorption on CeO_2 (111) surface is -76.6 kJ mol^{-1}.

For DMMP decomposition on CeO_2 (110) and (111) surfaces, we considered two channels associated with the formation of surface methoxy group. The first channel involves a O-CH_3 bond breaking and a subsequent coordination of the methyl group to the nearest surface oxygen. The second mechanism involves a cleavage of the P-OCH_3 bond. After losing the methoxy group, a new bond is formed between the phosphorus atom and one of the surface oxygen atoms. The methoxy group remains on the surface and forms a bond with a surface Ce atom.

A formation of the methoxy group via the O-CH_3 bond breaking (A1-A2, Figure 4.9a) on (110) surface requires 180.9 kJ mol^{-1}. The reaction is exothermic with the calculated reaction energy of -147.3 kJ mol^{-1}. A similar mechanism on CeO_2 (111) surface (B1-B2, Figure 4.9b) requires 221.0 kJ mol^{-1}. More energetically demanding the O-CH_3 bond breaking on the (111) surface is less exothermic (-81.7 kJ mol^{-1}) as compared to the (110) surface (-147.3 kJ mol^{-1}). The methoxy group formation via the P-OCH_3 bond cleavage on (110) surface (A1-A3, Figure 4.9a) requires 75.7 kJ mol^{-1}, which is considerably lower than the activation barrier of the process proceeding via the O-CH_3 bond breaking (180.9 kJ mol^{-1}). The calculated reaction energy of the A1-A3 step is -97.5 kJ mol^{-1}, which reflects a relatively high exothermicity of the reaction. Breaking of the P-OCH_3 bond on the CeO_2 (111) surface (B1-B3-B4) requires surprisingly low energy of 24.1 kJ mol^{-1} (Figure 4.9b). The reaction proceeds in two steps. The first step (B1-B3) requires 17.8 kJ mol^{-1} and involves the formation of a reaction intermediate with 5-coordinated phosphorus atom. An intermediate B3 lies 19.2 kJ mol^{-1} lower than the reagent structure. The subsequent decomposition of the intermediate B3 via a cleavage of one of the P-OCH$_3$ bonds requires 24.1 kJ mol^{-1}. The overall reaction energy of the mechanism B1-B4 is -22.2 kJ mol^{-1}.

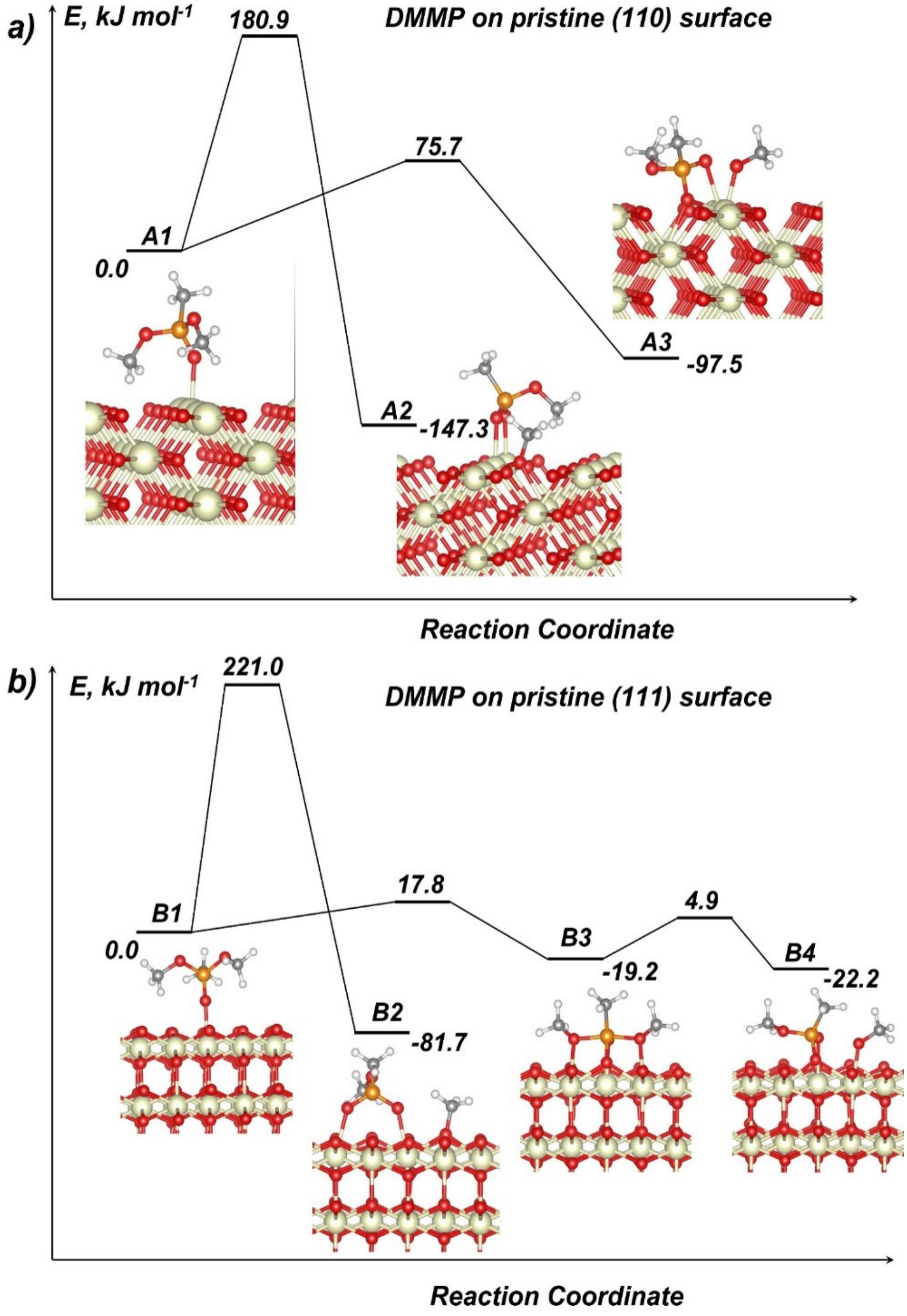

Figure 4.9: Decomposition of DMMP on pristine CeO_2 a) (110) and b) (111) surface

Decomposition of DMMP on hydroxylated CeO_2 (110) surface yields methanol and can proceed via several plausible channels, which require close activation energies. The most favorable mechanism, i.e. mechanism with the lowest activation energy is depicted in Figure 4.10a. An elimination of methanol on hydroxylated CeO_2 (101) surface proceeds in two steps. The first step (C1-C2) involves a formation of the reaction intermediate C2 with a 5-coordinated phosphorus atom. The activation barrier of this step is 110.2 kJ mol^{-1}. The intermediate structure C2 corresponds to a shallow minimum on the potential energy surface and lies 100.9 kJ mol^{-1} above C1. Breaking of the P-OCH_3 bond in C2 and a subsequent elimination of methanol (C2-C3) requires only 4.6 kJ mol^{-1}. The overall reaction energy of mechanism C1-C2-C3 is -93.5 kJ mol^{-1}.

Decomposition of DMMP on hydroxylated CeO_2 (111) surface also proceeds via an elimination of methanol. Similar to decomposition on hydroxylated CeO_2 (110), elimination of methanol on CeO_2 (111) proceeds in two stepsteps (Figure 4.10b). The formation of the reaction intermediate with coordinated phosphorus atom (D1-D2) on hydroxylated CeO_2 (111) requires 121.1 kJ mol^{-1}, which is slightly higher than that on hydroxylated CeO_2 (110) surface (110.2 kJ mol^{-1}). An intermediate D2 lies 63.8 kJ mol^{-1} higher than D1. The activation barrier of the subsequent methanol elimination from D2 is 10 kJ mol^{-1}. The calculated reaction energy of methanol elimination on the CeO_2 (111) surface is -31.7 kJ mol^{-1}.

We also modeled amodeled a reaction of methanol elimination from DMMP on a hydrated CeO_2 (111) surface proceeding via a water molecule displacement. According to our calculations, this mechanism requires significantly higher activation energy (207.8 kJ mol^{-1}) than the methanol elimination mechanism depicted in Figure 8 and therefore can notcannot compete with other reactions.

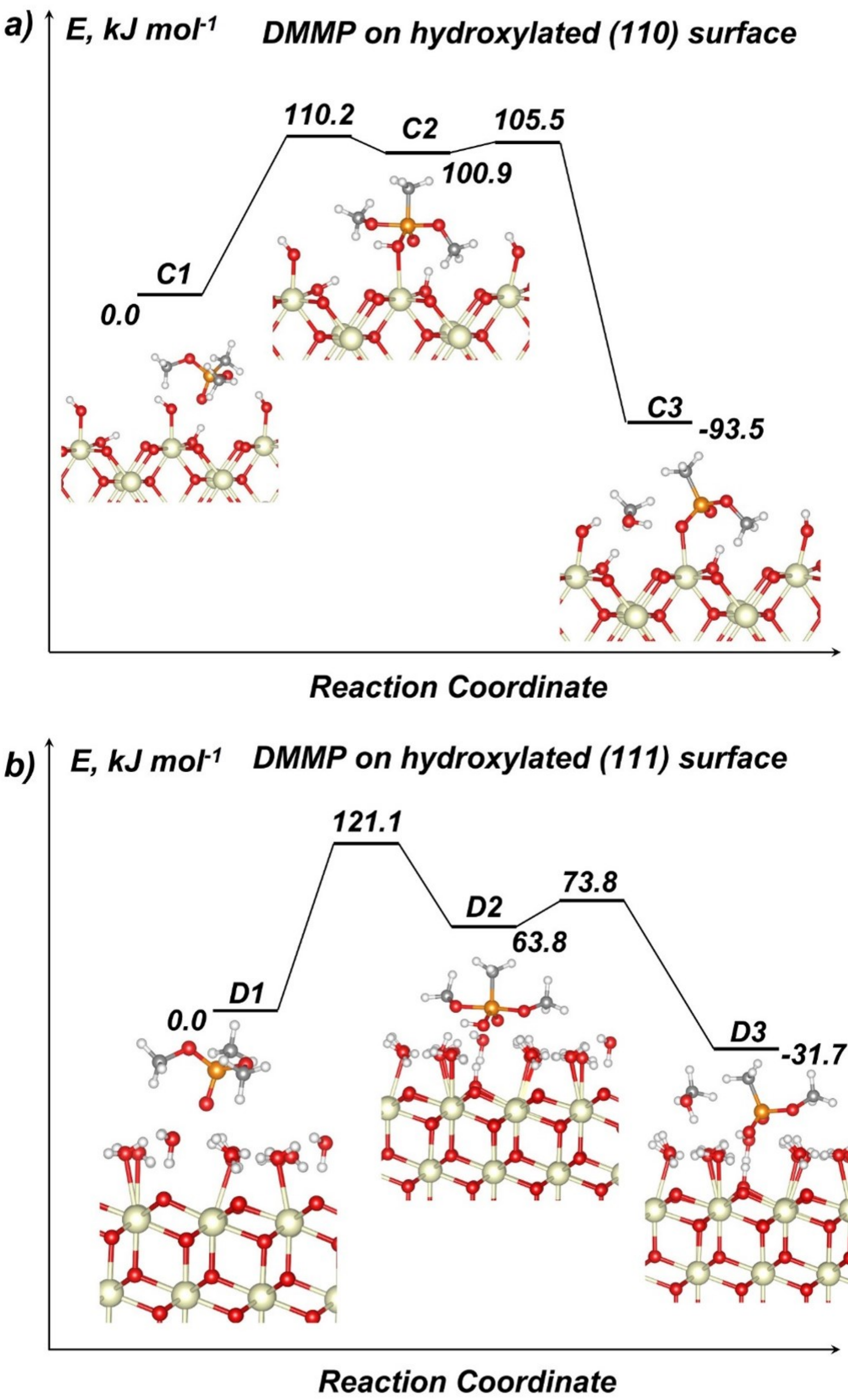

Figure 4.10: Decomposition of DMMP on hydroxylated CeO_2 a) (110) and b) (111) surfaces

4.1.4 Discussion

4.1.4.1 DMMP Adsorption through Hydrogen Bonding and Coordinate Covalent Bonding

Under ambient conditions, as-synthesized mesoporous CeO_2 has both hydroxylated and pristine-like surfaces, as is implied by the XPS and CO adsorption measurements. Thus, DMMP adsorption occurs on both hydroxylated and pristine-like surfaces of mesoporous CeO_2. Our calculations of both (110) and (111) surfaces show that adsorption of DMMP on pristine surfaces is stronger than on hydroxylated surfaces, as the energy released through DMMP adsorption (E_{ad}) on pristine surfaces is significantly larger than the hydroxylated surfaces (-164.8 kJ mol^{-1} vs.-112.3 kJ mol^{-1} for (110), and -116.9 kJ mol^{-1} vs.-76.6 kJ mol^{-1} for (111) surface). Such a difference in adsorption strength on hydroxylated and pristine surfaces originates from the different adsorption mechanisms. As mentioned previously, the DMMP adsorption on the pristine CeO_2 surfaces proceeds through P=O group coordination to Ce^{4+} through oxygen atoms. Ce^{4+} has empty f- and d-orbitals. Electron transfer from the P=O group to the empty f- and d-orbitals of Ce^{4+} forms a strong covalent coordinative Ce–O=P bond. Alternatively, on the hydroxylated CeO_2 surfaces, the DMMP adsorbs through hydrogen bonds of the type P=O$\cdot\cdot\cdot$H—O. Thus, the adsorption through hydrogen bonding is weaker. These results are consistent with the results of other theoretical studies. For example, we have recently shown that the energy of DMMP adsorption on pristine ZnO (101) surface is 71 kJ mol^{-1}, stronger than on hydroxylated surface (-142 kJ mol^{-1} vs 71 kJ mol^{-1})[81]. Bermudez observed similar trends of DMMP adsorption on pristine and hydroxylated γ-Al_2O_3 (222 kJ mol^{-1} vs 97 kJ mol^{-1})[46]. Typically, the presence of water and hydroxyl groups reduces the energy of DMMP adsorption, making the binding with the surface weaker. Opposite trends were observed for DMMP adsorption on MoO_3. Our recent study[3] showed that the presence of water is essential for DMMP adsorption on oxygen terminated MoO_3 (010) surface.

4.1.4.2 Decomposition of DMMP

Our DRIFTS measurements during the initial DMMP dosing revealed that DMMP decomposition involves the formation of surface methoxy groups. With more dosing, the DMMP continuously decomposes while the signal for surface methoxy groups on the surface decreases. In the mass spectroscopy experiments, two methanol production peaks are observed at different temperatures.

Our DFT modeling shows that the formation of surface methoxy groups corresponds to DMMP decomposition on pristine CeO_2 (110) and (111) surfaces. Decomposition on both hydroxylated (110) and (111) surfaces proceeds via methanol elimination. Although the formation of surface methoxy groups on pristine CeO_2 (110) and (111) surfaces can take place via breaking of either O-CH_3 and P-OCH_3 bonds as shown in Figure 4.9 (a and b), surface-enhanced rupture of P-OCH_3 bond is the considerably more favorable mechanism on both surfaces. The lower activation energy barrier for P-OCH_3 bond breaking rather than PO-CH_3 bond breaking (75.7 vs.180.9 kJ mol^{-1} for (110), and 22.7 vs.221 kJ mol^{-1} for (111)) can be attributed to the different polarity of the P-O and C-O bonds. The electronegativity of P, C and O is 2.2, 2.6, and 3.5, respectively. The difference of electronegativity between O and P is significantly higher, leading to a larger polarity and more ionic nature of the P-O bond than the C-O bond. Less covalency of the P-O bond makes it easier to break. The dissociation of para-Nitrophenylphosphate on CeO_2 surface is reported to proceed through P-OR breaking instead of PO-R breaking[54], which is similar to the DMMP case here. While for phosphoric acid where POH group instead of POR group exists in the structure, the favored dissociation path is through the deprotonation (PO-H breaking) rather than P-OH bond breaking[53]. The different dissociation mechanism for POR and POH group on CeO_2 surface might come from a weaker bond strength of PO-H than PO-R. Different stabilities of dissociation species (-OR and -R for POR group, H^+ and -OH for POH group) on the surfaces also contribute to the varied dissociation mechanism.

Thus, The cleavage of P-OCH_3 bond on CeO_2 (110) surface requires 75.7 kJ mol^{-1}, which is significantly lower than activation energies of P-OCH_3 bond cleavage on ZnO (101) surface (170.6 kJ mol^{-1})22 and MoO_2 (011) surface (149.2 kJ mo^{-1}1)[67]. Decomposition of DMMP on CeO_2 (111) surface via P-OCH_3 bond cleavage requires even low activation energy (22.7 kJ mol^{-1}, Figure 7b). The low activation energy barrier for cleavage of P-OCH_3 bond on CeO_2 surfaces explained the observed high activity of mesoporous CeO_2 in the spectroscopic measurements.

The difference in activation energies of P-OCH_3 bond cleave on CeO_2 (110) and (111) surface is most likely due to different surface structures. Figure 4.11 shows that in the transition state structure of the P-OCH_3 bond cleavage reaction on CeO_2 (110) surface, DMMP coordinates to Ce atoms via its phosphoryl oxygen and one of the methoxy oxygens (Figure 4.11a). In addition, phosphorus atom is coordinated to lattice oxygen which leads to breaking the bond between lattice oxygen and cerium atom on the surface. In the transition state localized for P-OCH_3 bond scission on CeO_2 (111) surface (Figure 4.11b), DMMP is coordinated to cerium atoms via its phosphoryl and both methoxy oxygen atoms. There is no bond formed between phosphorus and lattice oxygen atoms. As a result, there is no additional perturbation in the system leading to breaking of bonds between cerium and lattice oxygen atoms.

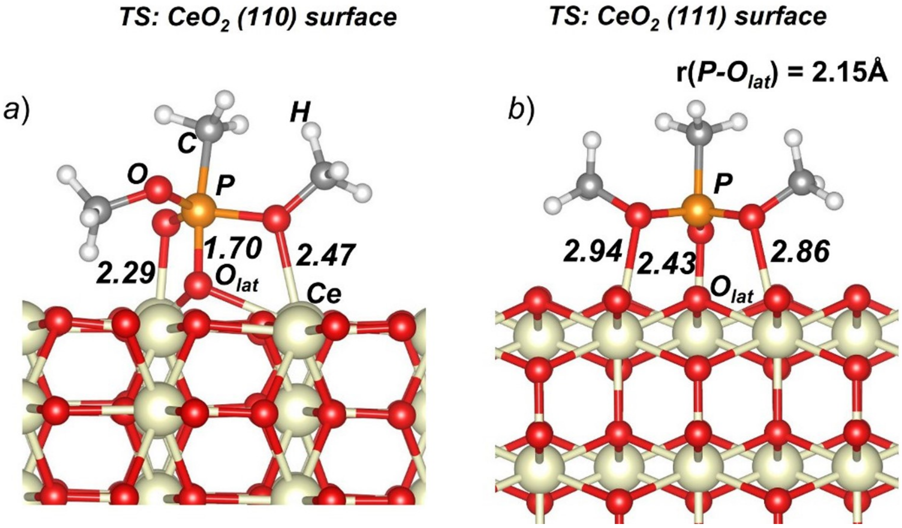

Figure 4.11: Transition state structures of P-OCH_3 bond cleavage reaction on CeO_2 (a) (110) and (b) (111) surface

We found no pathways to form surface methoxy groups upon DMMP decomposition on hydroxylated CeO_2 (110) and (111) surfaces. On the hydroxylated CeO_2 surfaces, decomposition of DMMP proceeds via methanol elimination and requires about 110-120 kJ mol^{-1} (Figure 4.10), which is higher than the energy required for DMMP dissociation on the pristine (110) and (111) surfaces.

Based on the comparison of results obtained from DRIFTS, mass spectrometry, and DFT modeling, we conclude that DMMP decomposition on mesoporous CeO_2 proceeds in two steps. The first step corresponds to DMMP decomposition on dry CeO_2 surface via P-OCH_3 bond cleavage. This mechanism requires relatively low activation energy 25-75 kJ mol^{-1} (Figure 4.9). Methoxy groups, which are the main products of DMMP decomposition on pristine surfaces, remain on the surface. This conclusion is consistent with the increased intensity of the corresponding C-H stretching band from M-OCH_3 groups observed in DRIFTS measurements and the absence of methanol signal in mass spectra at room temperature. After areas of the pristine surface are saturated with DMMP and decomposition products, DMMP begins interacting with hydroxylated parts of CeO_2 because the elimination of methanol from DMMP on the hydroxylated surface requires a noticeably higher energy than decomposition on the pristine surface (110-120 vs 25-75 kJ mol^{-1}, Figure 4.9 and Figure 4.10). This second step likely corresponds to the DMMP dissociation observed in the later injections of DMMP from the DRIFTS measurement, where the surface M-OCH_3 group does not form in this dissociation process. A higher activation energy also means elimination methanol is favored at elevated temperatures, which is consistent with mass spectrometry measurements. It is also worth noting that methanol formation may also come from the methoxy groups (from DMMP decomposition on pristine CeO_2 surfaces) interacting with hydroxylated parts of CeO_2 surfaces. Such a process as well as the elimination of methanol from DMMP on the hydroxylated surface might contribute to the two methanol production peaks observed in the mass spectrometry measurements.

4.1.5 Conclusion

The as-synthesized high-surface-area mesoporous CeO_2 is proved experimentally to have high reactivity towards DMMP decomposition at room temperature. Our DFT calculations indicate the activation energy barrier for DMMP dissociation on the pristine (111) surface is the lowest among the metal oxides ever studied[3, 56, 37, 22]. Both experiments and DFT modeling show the potential of mesoporous CeO_2 to be applied in the protection against CWAs. We note that sarin is different from DMMP in terms of the chemical structure. Thus, investigations on sarin interactions with CeO_2 materials should be performed in the future to get a true understanding and verification on the activity of CeO_2 towards sarin.

As for the materials design perspective, our DFT modeling provides significant insights on future directions of improving CeO_2 materials for better DMMP adsorption and decomposition. Mesoporous CeO_2 materials should be designed and synthesized to expose more (111) surfaces as this surface displays a lower activation energy barrier for DMMP decomposition. In addition, CeO_2 materials might need to be modified to be less hydrophilic so that there will be more dry pristine surfaces available at ambient conditions, providing stronger DMMP adsorption and higher DMMP decomposition activity on the surface. Such materials design parameters may be achieved through exploration of different CeO_2 syntheses, post-synthetic modification of the surfaces, or chemical modification of CeO_2 such as isovalent or aliovalent doping.

4.2 Part 2: Investigation of sarin(GB) interaction with mesoporous CeO_2

4.2.1 Introduction

After several tests with GB simulant molecules on CeO_2 materials from different research groups[107, 60, 85, 108, 63], to verify the activity of CeO_2 on GB dissociation, we performed surface characterizations on the dry mesoporous CeO_2 under the exposure of GB for the first time. Our observations are encouraging. We found the as synthesized mesoporous CeO_2 displays extraordinary activity on GB dissociation at room temperature. Such a reaction happens under vacuum without any assistance of moisture or photo excitement. We also performed DFT calculations, which again implies relatively low activation energy barrier for GB to dissociate on the CeO_2. With the spectroscopic measurement and DFT calculations we reveal possible reaction pathways. Our study suggests a strong potential of CeO_2 to be applied in combating CWAs.

4.2.2 Experimental Section

4.2.2.1 Synthesis and Characterization of of Templated Mesoporous CeO_2

The material used here is from the same batch of mesoporous CeO_2 that we used for the DMMP study in Part 1.

4.2.2.2 IR Characterization of GB interaction with dry mesoporous CeO_2 under high vacuum

(CAUTION! Experiments performed with ultra-toxic CWAs require highly trained operators, extreme safety protocol and approved facilities.) Chemical Agent Standard Analytical Reference (CASARM)-grade sarin (95+% by NMR) was used for all experiments. Prior to dosing, the GB was purified through a freeze-pump-thaw cycle.

IR Experiments of mesoporous CeO_2 interacting with GB were done in an ultra-high vacuum chamber with a base pressure of 9.3×10^{-9} Torr. The mesoporous CeO_2 was pressed into a 0.004” thick tungsten grid and attached to the sample mount with stainless steel clamps connected to copper rods. An IR spectrum was taken of the W grid without CeO_2 at each step and used to subtract any background interactions. Before the experiments, the sample was placed in vacuum for 24 h and then heated to 300 °C in the presence of O_2 for 1.5 h to remove any environmental gases (i.e., H_2O, carbonates, CO_2, NO_x, ect.). Subsequently, 10^{-4} Torr of GB vapor was introduced into the vacuum chamber to interact with the mesoporous CeO_2 sample. IR scans of the sample were taken every couple of minutes for total 60 min. After the experiment, the chamber with sample was under vacuum for 10 days to examine how strong the GB is adsorbed on the surfaces of mesoporous CeO_2. The IR spectrum was also collected after the evacuation. Each IR spectrum includes 256 interferograms at a resolution of 2cm^{-1}. After final dosing, the sample was evacuated and returned to a pressure of 10^{-9} Torr to determine what remained on the surface. The scan prior to GB exposure was used as a background to create difference spectrum

4.2.2.3 Ambient diffuse reflectance infrared Fourier transform spectroscopy (DRIFTS)

(CAUTION! Ultra-toxic CWAs were used in the experiment. Such an experiment requires extreme care, highly trained staff, and a secure government-regulated facility.) The activity of mesoporous CeO_2 for GB degradation under ambient conditions was characterized in an in-situ environmental DRIFTS reaction cell maintained at 25 °C. A 6 mm porous ceramic cup was used as a sample holder. Approximately 20 mg of the sample was used.

A detailed instrument set-up is described elsewhere[109]. Helium (Airgas, 99.999% purity) was used as the carrier gas to carry GB vapor. The carrier gas first flew (10 mL/min) through a microsaturator cell containing a liquid reservoir of GB (maintained at 20 °C) before entering the sample cell. GB flow was maintained for 90 min and DRIFTS IR spectra were in-situ recorded with a Thermo Fisher Scientific 6700 FTIR spectrometer. A background scan was collected prior to beginning the dosing experiment. During the dose, collected spectra were averaged over ~ 2 min with a 2 cm^{-1} resolution.

4.2.2.4 DFT Modeling of DMMP interacting with pristine CeO_2 surfaces

Solid state periodic calculations were performed with DFT[91, 92] using GGA PBE[93] functional and projector augmented-wave (PAW) pseudo-potentials[94], as implemented in the VASP code[95, 96, 97, 98]. Hubbard's parameter U44 was introduced to account for Ce 4f orbitals and was set to 4.0 eV in accordance with reported literature[99]. Grimme's D246 corrections were added to account for weak van der Waals interactions. In simulating ideal bulk crystals, atomic coordinates and lattice constants were allowed to relax simultaneously without any symmetry constraints. The convergence criterion for electronic steps was set to 10^{-5} eV, and the maximum force acting on any atom was set not to exceed 0.01 eV/Å. Kinetic energy cut-off was set to 520 eV. In modeling CeO_2 crystal, an 8×8×8 Monkhorst-Pack k-point mesh was used. The calculated lattice parameters of the CeO_2 cubic unit cell (Figure 4.1a) with Fm-3m space group, a=5.37 Å, agree with the experimental lattice vectors (a= 5.41 Å) within $\sim$1 %.

Our calculations of GB adsorption and decomposition were limited to modeling reactions on the most stable surfaces, including (110) and (111) surfaces (Figure 4.1 b and c), observed in our experiments. The model slab of (110) surface contained 252 atoms with the supercell lattice vectors of a = 16.23 Å, b = 14.92 Å, and c =31.61 Å. The model slab of (111) surface contained 240 atoms with the supercell lattice vectors of a = b = 15.03 Å, and c =34.37 Å. A vacuum layer of 20 Å placed on top of the CeO_2 surfaces served to minimize interactions between the supercells in the z-direction and to avoid any significant overlap between wave functions of periodically translated cells. All surface calculations were performed at G-point only. Kinetic energy cut-offs in modeling CeO_2 (110) and (111) surfaces were set to 520 eV. The convergence criterion for electronic steps was set to 10^{-5} eV, and the maximum force acting on any atom was set not to exceed 0.03 eV/Å.

Minimal energy paths in the VASP periodic calculations were obtained with the standard nudged elastic band method[100] . Atomic positions were relaxed using conjugate gradient and quasi-Newtonian methods within a force tolerance of 0.05 Å/eV. The convergence criterion for electronic steps was set to 10^{-5} eV.

4.2.3 Experimental Results and Discussion

4.2.3.1 Material Characterizations

The material used here is from the same batch of mesoporous CeO_2 that we used for the DMMP study, as is displayed in Figure 4.2 and Figure 4.3.

4.2.3.2 High reactivity of Mesoporous CeO_2 under high vacuum conditions

High vacuum experiments with live agent, sarin (also known as GB), were performed on the as synthesized mesoporous CeO_2 at room temperature. The sample was placed in high vacuum for 24h and then heated in the presence of oxygen to obtain a relatively hydroxylation-free and oxygen vacancy-free surfaces on mesoporous CeO_2 before the experiments. the GB gas was then introduced into the high vacuum chamber for 60 min at a constant flow of 10^{-4} Torr. Figure 4.12 displays the in-situ difference IR spectrum of the surfaces of mesoporous CeO_2 during the GB exposure (scans are taken every 5 minutes). The major peaks are assigned accordingly on the figure as well as listed in Table 4.2. Vibration modes of σ_a(C-CH_3), σ_s(C-CH_3), σ(P-CH_3), v(P=O), v(C-O) and v(P-F) exist in the structure of intact GB molecule. The gradual increase of these bands upon initial GB dosing indicates that intact GB molecules are readily adsorbed onto the surfaces of mesoporous CeO_2. The vibration bands of intact GB molecule stop growing at 20 minutes as the GB adsorption reaches the saturation on surfaces of CeO_2.

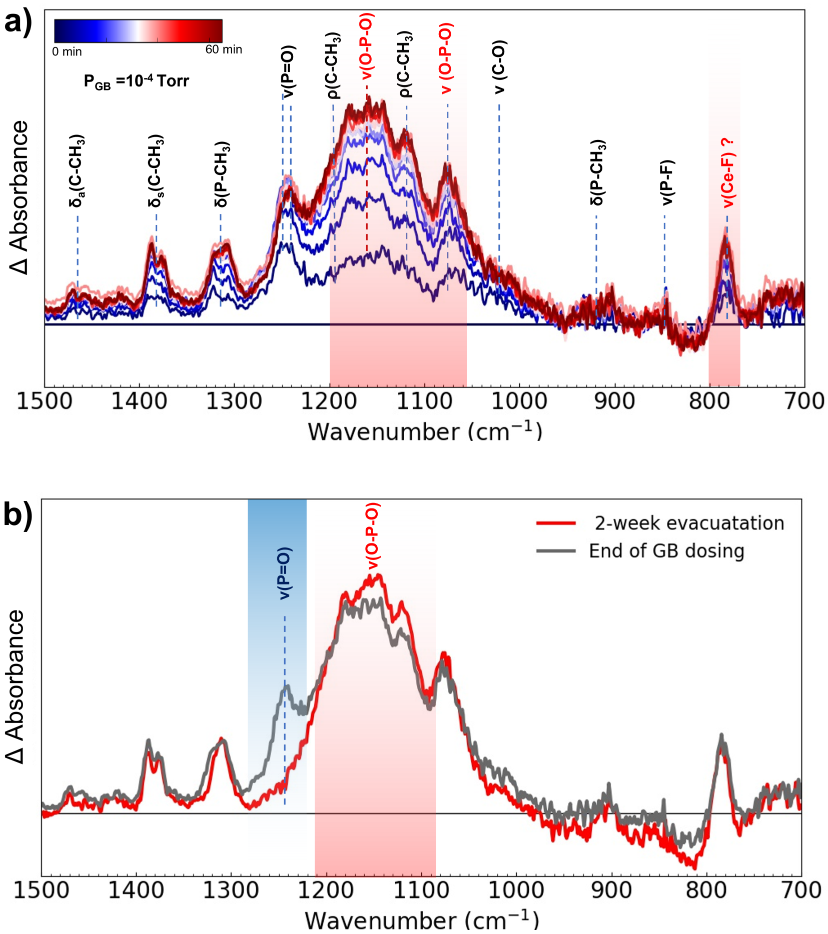

Figure 4.12: a) In situ difference IR spectrum of the surfaces of mesoporous CeO_2 upon GB exposure in the high vacuum. b) IR spectra of surfaces of mesoporous CeO_2 after GB exposure and after 2-week evacuation following the GB exposure.

Besides its intact form, the dissociation of GB molecule is also evidenced in the IR spectrum. A very broad band containing several peaks between 1100-1200 cm^{-1} are also growing upon the GB dosing. 1100-1200 cm^{-1} region is the signature region for the stretching vibration of O-P-O groups and is generally regarded as the strong indication of the GB decomposition[62, 58, 80, 109, 110, 111]. We realize ρ(C-CH_3) modes from intact GB molecules also appear in this region (1180 cm^{-1} and 1120 cm^{-1}), however, the intensity of ρ(C-CH$_3$) is relatively weak in IR spectrum according to various previous studies[62, 58, 80, 110, 111]on DMMP and GB molecules. therefore, ρ(C-CH$_3$) modes are not major contribution for the growing intensity of this region and we are confident that O-P-O groups form on the surfaces of CeO$_2$. The very broad and multi-peak nature of v(O-P-O) in the spectrum indicates there might be multiple O-P-O configurations on the surfaces of mesoporous CeO$_2$. As the as synthesized mesoporous CeO$_2$ is characterized to have both (110) and (111) surfaces exposed. It is possible GB decomposition of the GB on different surfaces leads to different O-P-O configurations. In addition, GB can either lose F or OCH(CH$_3$)$_2$ to form different O-P-O configurations on the surfaces, or even lose both F and OCH(CH$_3$)$_2$ to form RP(-O)$_3$ with three P-O bonds, as presented in Figure 4.13. Even though here we are not clear which O-P-O configuration(s) contribute to the broad band, there is no doubt they all come from the degradation of GB.

GB vapor phase (cm^{-1})	Vacuum IR (cm^{-1})	DRIFTS (cm^{-1})	IR band assignments
1468	1460, 1470		σ_a(CH$_3$C)
1380	1375,1388	1370,1380	σ_s(CH$_3$C)
1328	1310, 1320	1322	σ(P–CH$_3$)
1303	1240, 1245	1245, 1277	v(P=O)
1183/1111	1190/1120	1190/1120	ρ(CH$_3$C)
	1100–1200	1100-1200	v$_a$(O–P–O)
	1080		v$_s$(O–P–O)
1020	1020-1038	1030	v(C–O)
928	920		σ(P–CH$_3$)
845	845		v(P–F)
	780		v(M-F)?

Table 4.2: IR Frequencies (cm^{-1}) of GB in the Vapor Phase, GB Adsorbed on CeO$_2$ characterized by vacuum IR and ambient DRIFTS.

We are not confident on the assignment of the gradually growing band at around 760-

800 cm^{-1}. It seems to be the Ce-F stretching mode, as M-F stretching modes usually locate at 200-800 cm^{-1} region[112, 113, 114]. The appearance of band might indicate the P-F bond breaking mechanism for GB dissociation. The dissociation of GB molecules is also evidenced by the splitting bands of σa (C-CH$_3$), σs (C-CH$_3$), σ(P-CH$_3$). As shown in Figure 4.12a, doublets separated by $\sim$ 10cm^{-1} are all visible for σa (C-CH$_3$), σs (C-CH$_3$), σ(P-CH$_3$) modes. It is reported that cleavage of the P-F bond or the leaving of -OCH(CH$_3$)$_2$ group from GB molecules can lead to the red shift of these bending modes[110, 111, 79, 58].

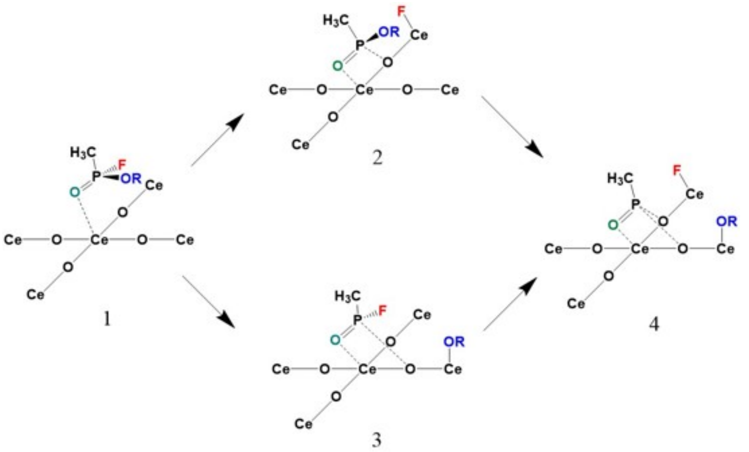

Figure 4.13: Possible pathway for Sarin (GB) decomposing on the CeO$_2$ Surface.

After the final GB exposure, the sample was evacuated under the base pressure of 7x10^{-9} torr for 2 weeks. The sample was re-scanned with IR and the comparison with final scan under GB exposures is presented in Figure 4.12b. Most notably, v(P=O) mode at 1240 cm^{-1}, completely disappeared. While the bands (1100-1200 cm^{-1}) associated with v(O-P-O) increased significantly. This means the adsorbed GB molecules continues to dissociate on the surfaces of CeO$_2$, leading to the breaking of P=O bonds to form O-P-O. We also observed the intensities of other major bands in the spectrum remain nearly unchanged after 2-week ultra-high vacuum evacuation, implying extremely strong non-reversible adsorption of the decomposition species from GB on the surfaces of mesoporous CeO_2.

4.2.3.3 Mesoporous CeO_2 interacting with GB under ambient conditions

The activity of mesoporous CeO_2 towards GB under ambient condition is also explored via diffuse reflectance infrared Fourier transform spectroscopy (DRIFTS). The flow line set-up in the DRIFTS cannot fully eliminate the moisture (H_2O) both from the gas flow and samples. Thus, different from the high vacuum IR experiment mentioned previously, the mesoporous CeO_2 tested in the DRIFTS is more or less hydroxylated, which more resembles the practical situations when materials are put into applications. Figure 4.14 displays the difference DRIFTS spectra of the surface of mesoporous CeO_2 under flow of GB vapor for 6 min (Figure 4.14a) and 90 min (Figure 4.14b). Most IR bands appearing here resemble what we have observed in the vacuum IR experiment (Figure 4.12) and can be assigned based on Table 4.2.

A notable difference is that a shoulder peak at 1277 cm^{-1} is observed in the DRIFTS spectra but not in the high vacuum IR spectra. This peak most likely belongs to v(P=O) mode of the GB when GB is adsorbed on the surface through the hydrogen bond interaction with surface hydroxyl groups[23, 68, 109] The v(P=O) mode when GB interacts with pristine CeO_2 surfaces is observed at $\sim$ 1230 cm^{-1}. We made such attribution because v(P=O) mode at 1230 cm^{-1} appears also at the high vacuum IR experiment (Figure 4.12). The two distinct v(P=O) modes observed in the DRIFTS measurement indicates that the mesoporous CeO_2 possesses both hydroxylated regions and pristine (dry) regions on the surfaces. Compared with the v(P=O) mode when GB interacts with pristine surface, a significant blueshift ($\sim$ 40 cm^{-1}) is observed for the v(P=O) mode when GB interaction with surface hydroxyl groups, implying a weaker

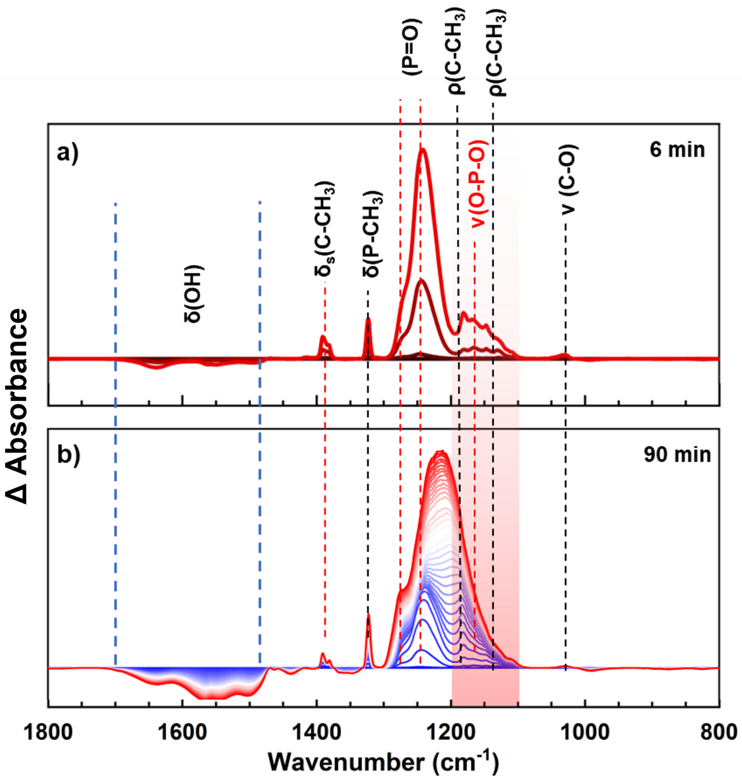

Figure 4.14: DRIFTS measurement spectrometry of mesoporous CeO_2 upon GB dosing under ambient conditions with He flow.

adsorption strength of GB on hydroxylated surfaces than the pristine surfaces. The weaker adsorption strength of GB on hydroxylated surfaces can be attributed to the different dominating interaction forces between pristine and hydroxylated surfaces. Pristine CeO_2 surfaces have under-coordinated Ce atoms exposed, which can provide empty f orbitals for lone pairs elections of P=O from GB molecules to coordinate, forming relative stronger covalent interactions. While on the hydroxylated surfaces, hydroxyl group (-OH) rather than under-coordinated Ce atoms are exposed, thus hydrogen bond (P=O—-HO), which is weaker than covalent interaction, instead will dominate when GB interact with the surfaces. The interaction between hydroxylated surfaces and GB are also evident by the gradual decrease of σ(OH) bands between $1500\sim1700$ cm^{-1}. The decrease of σ(OH) bands implies the surface OH or H_2O was consumed through hydrogen bond formation or being replaced by adsorbed GB molecules. The very broad nature of σ(OH) bands implies there are different configurations of OH groups available on the surfaces.

Similar to the high vacuum IR spectra (Figure 4.12), the rise of v(O-P-O) bands at 1100-1200 cm^{-1} is observed in the DRIFTS measurement (Figure 4.14), an indication of the GB degradation. However, unlike high vacuum IR spectra, the relative intensities of v(O-P-O) is never comparable to v(P=O) throughout the whole GB flow period. We thus conclude the activity of the mesoporous CeO_2 is more reactive in the high vacuum environment than in the ambient conditions. A likely cause can be that the hydroxylation of the surfaces in the ambient conditions is less reactive than the pristine surfaces. Our previous modeling study show hydroxylated CeO_2 surfaces is less reactive than the pristine surfaces towards DMMP dissociation as hydroxyl groups can block active undercoordinated Ce sites for the stabilization of dissociated methoxy species[60]. Given the structural similarity between GB and DMMP (GB also contains alkoxy group), hydroxyl groups on the CeO_2 might prevent the GB to dissociate into stable species on the surfaces as well.

As GB flow continues, most of the IR modes from intact GB molecules continue growing while the v(O-P-O) becomes less obvious in the spectra, as shown in Figure 4.14b. The plateau of the v(O-P-O) modes in the DRIFTS spectra implies that the active sites of CeO_2 surfaces for GB degrading is saturated and cannot be spontaneously regenerated or reused. Therefore, the degradation of GB on the surfaces of CeO_2 is more of a heterogenous surface-molecule reaction rather than a catalytic reaction. The surfaces of CeO_2 behave as a reactant instead of a catalyst when interacting with GB molecules.

4.2.3.4 Understanding the high activity of CeO_2 via DFT Modeling

Both high vacuum IR measurement and ambient DRIFTS measurement show GB can actively dissociate on the mesoporous CeO_2. While the measurements imply the high reactivity mainly come from the dry pristine surfaces as the CeO_2 show decreased activity at ambient conditions with hydroxylated surfaces available. Thus here, we performed DFT modeling to understand the high activity of pristine surfaces of mesoporous CeO_2 towards GB dissociation. The CO adsorption IR characterization of CeO_2 mesoporous materials (Figure 1c) indicates that the as-synthesized mesoporous CeO_2 possesses both (110) and (111) surfaces. Thus, we modeled the GB adsorption and decomposition on the (110) and (111) CeO_2 surfaces to obtain better understanding of GB interaction with mesoporous ceria and provide interpretation of our experimental observations. In this work, we focus on the interaction of GB with pristine dry CeO_2 surfaces.

a. GB Adsorption on (110) and (111) CeO_2 Surfaces.

GB is strongly adsorbed on pristine (110) and (111) surface through its phosphoryl oxygen (Figure 4.5a-f). For CeO_2 (101) surface, adsorption energy varies from 136 to 171.5 kJ mol^{-1}. Adsorption on CeO_2 (111) is weaker than on the (110) surface with adsorption energy 124-147.5 kJ mol^{-1}. Similar trends were observed for DMMP apportion on CeO_2 (110) and (111) surfaces[60]. Inspection of Figure 4.15 indicates relatively large contribution of hydrogen bonding in energies of GB adsorption on CeO_2. Thus, adsorption configurations M2 and M4 have adsorption energies -135.9 kJ mol^{-1} and -133.5 kJ mol^{-1} and correspond to structures with the lowest absorption energy on (110) and (111) surface, respectively. In configuration M2, GB forms hydrogen bond with lattice oxygens trough one of its hydrogen atoms. In configuration M4, the molecule is orientated on the (111) surface in such a way that no hydrogen bonds can be formed. On the contrary, in configuration M3, GB forms hydrogen bonds with lattice oxygen on CeO_2 (110) surface through at least two of its hydrogens. As a result, configuration M3 corresponds to structure with the highest calculated adsorption energy -171.5 kJ mol^{-1}. On the (111) surface, configuration M6, in which GB forms hydrogen bond with one of the lattice oxygens, corresponds to the structure with the highest adsorption energy -147.5 kJ mol^{-1}. We have noted effect of hydrogen bonding on GB adsorption on metal oxides, including ZnO[44], MoO_2[115] and TiO_2[58]. In terms of strength of adsorption, CeO_2, particularly (110) surface, demonstrates stronger adsorption than ZnO (10-10) surface (-171.5 vs -133 kJ mol^{-1}1) [44] and TiO_2 anatase surface (101) surface (-171.5 vs -129 kJ mol^{-1})[58]. Energy of GB adsorption of rutile (110) surface (-171 kJ mol^{-1})22 is close to GB adsorption on CeO_2 (110) surface. Considerably stronger adsorption was calculated for GB adsorption on CeO_2 (011) surface (200-230 kJ mol^{-1})[115]. Comparison of energies of energies of GB adsorption on different materials shows that CeO_2 demonstrates attractive properties.

b. GB Decomposition on (110) and (111) CeO_2 Surfaces.

In studying GB decomposition on CeO_2 (110) and (111) surfaces, we modeled three most plausible, from our point of view, mechanisms: 1) P-OC_3H_7 bond scission and 2) P-F bond scission (Figure 4.16a and b). Propene elimination through P-OC_3H_7 bond breaking is also considered for comparison as such a mechanism generally happens at higher temperatures[116]. Elimination of propene (A1-A2) on the (110) surface requires 81.1 kJ mol^{-1}. Reaction is exothermic and proceeds with the energy release of 130 kJ mol^{-1}. Elimination of propene on the (111) surface (B1-B2) requires noticeably higher energy 120 kJ mol^{-1}. In addition, the reaction mechanism has reaction energy of only -3.6 kJ mol^{-1}. Scission of P-OC_3H_7 bond requires 59.3 kJ mol^{-1} which

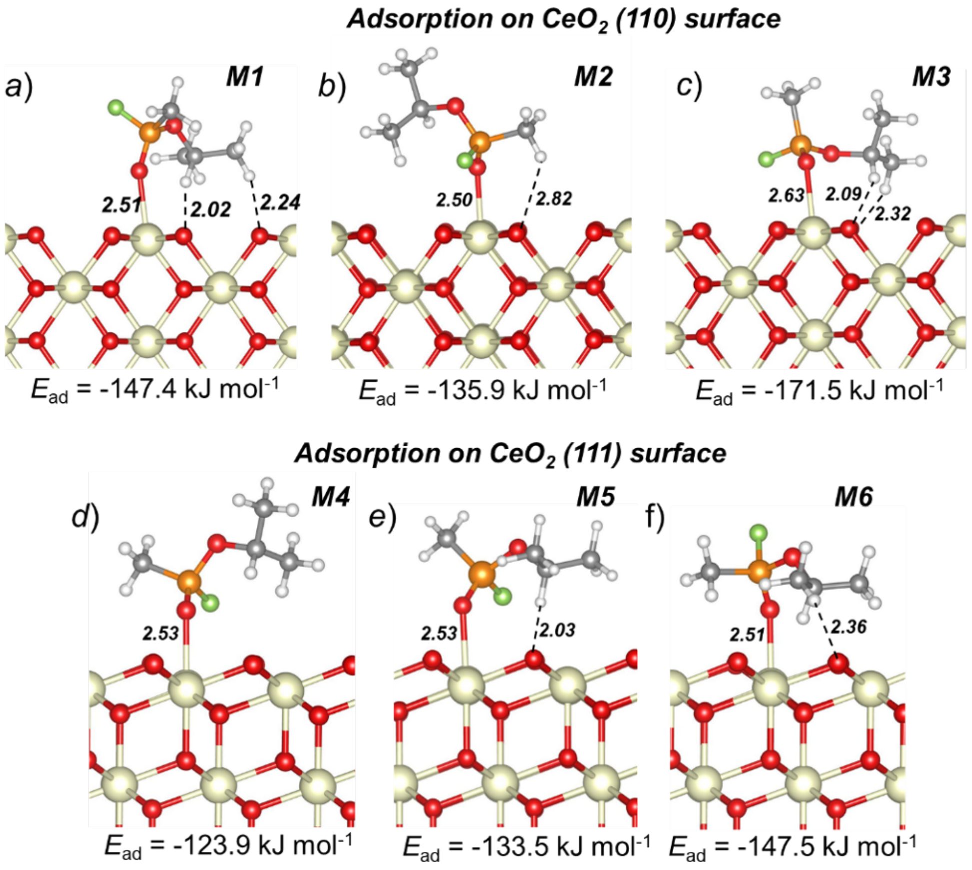

Figure 4.15: Adsorption of GB molecule on CeO$_2$ (a)-(c) (110) and (d)-(f)

is 40 kJ mol^{-1} lower than activation barrier of P-OC$_3$H$_7$ bond cleavage on (111) surface (B1-B2, 100.9 kJ mol^{-1}). Relative high reaction energy (-91.9 kJ mol^{-1}) corresponds to high exothermicity of the reaction on the (110) surface. Reaction on the (111) surface, unlike (110) surface, is endothermic process with reaction energy 51.7 kJ mol^{-1}. Breaking of P-F bond has the lowest activation energy on (110) and (111) surfaces. Thus, on the (110) surface, breaking of P-F bond (A1-A3) requires 44.4 kJ mol^{-1}. On the (111) P-F bond scission (B1-B3) requires 24.4 kJ mol^{-1} higher energy (69.2 kJ mol^{-1}) than on (110) surface. Results of our calculations shows that P-F bond scission is exothermic reaction on both (110) and (111) surface, with decomposition on (110) surface being 65.4 kJ mol^{-1} more exothermic than on (111) surface (-103.1 vs -37.7 kJ mol^{-1}).

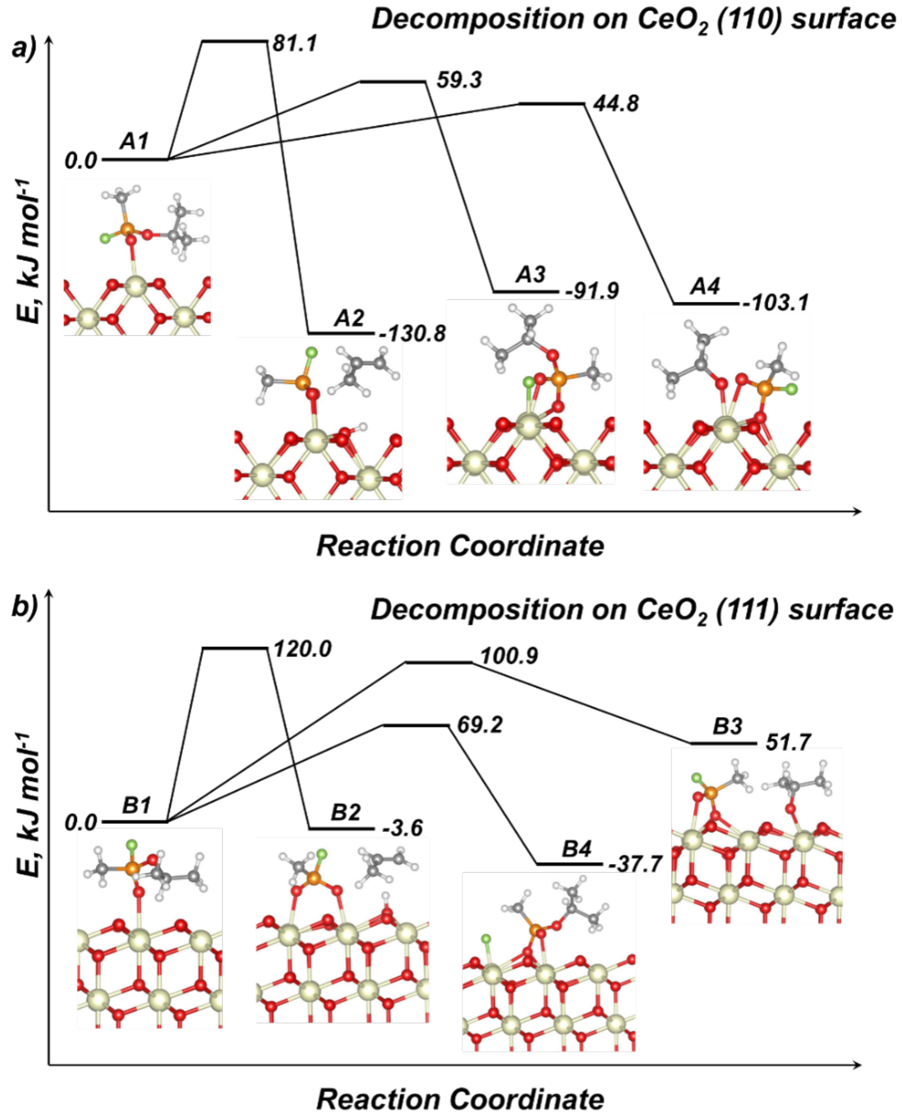

Figure 4.16: GB decomposition on CeO_2 a) (110) and b) (111) surfaces.

Our calculation indicates propene elimination mechanism for GB dissociation requires significant higher activation energy compared with P-OC_3H_7 bond scission or P-F bond scission mechanism on both (110) and (111) surfaces. Thus, propene elimination is unlikely to be the dominant GB dissociation pathways on the surfaces of CeO_2 at room temperature. Comparison of activation energies and reaction energies indicates that decomposition of GB on CeO_2 (110)

surfaces via P-F bond scission and P-OC_3H_7 bond scission and are both likely, as two mechanisms require similar activation energies (59.3 vs 44.8 kJ mol^{-1}) and proceed with similar energy release (-91.9 vs –103.1 kJ mol^{-1}). The slight lower activation energy and higher energy release imply P-OC_3H_7 bond scission mechanism is slightly favored on (110) surfaces. While decomposition of GB on CeO_2 (111) surfaces via P-F bond scission and P-OC_3H_7 bond scission shows significant energy differences, P-F bond scission are much favored both kinetically (activation energy) and thermodynamically (energy release) on (111) surfaces. We suspect such a huge preference of P-F bond scission than P-OC_3H_7 bond scission is a result of the steric effect on the (111) surfaces. Compared with (110) surface, Ce atoms are more embed below the oxygen atoms on (111) surface. thus (111) surface poses a stronger steric repulsion force from the top oxygen atoms when the species interact with the Ce atoms on the surfaces. The P-F bond scission requires F of the GB molecule positioned close to undercoordinated Ce atoms and will lead to attachment of F onto Ce atoms. While P-OC_3H_7 bond scission requires -OC_3H_7 of the GB molecule positioned close to undercoordinated Ce atoms will lead to attachment of -OC_3H_7 onto Ce atoms. -OC_3H_7 is a much larger group than F thus will experience larger steric repulsion force when it moves close or attached onto Ce atoms on (111) surfaces, leads to the rising of the activation energy and destabilizing the final dissociation products if reaction proceed via P-OC_3H_7 bond breaking. In conclusion, P-OC_3H_7 bond breaking are slightly favored on (110) surfaces while P-F bond breaking is strongly favored (111) surfaces when GB molecules decompose on the CeO_2.

Comparison of results obtained in this work with previously published papers shows that GB decomposition on CeO_2 requires considerably lower energies than on other metal oxides. Thus, decomposition of GB on ZnO proceeds via elimination of propene and requires 113 kJ mol^{-1}[44]. Similarly, elimination of propene on is energetically most favorable pathway for

GB decomposition on TiO_2 rutile (110) and anatase (101) surfaces with activations calculated energies 108 and 122.6 kJ mol^{-1}[58], respectively. Considerably lower activation barrier for propene elimination is required on TiO_2 (101) surface with oxygen vacancy 81.6 kJ mol^{-1}[117]. Breaking of P-F bond on ZnO (10-10) surface, TiO_2 anatase (101) surface, TiO_2 rutile (110) surface and MoO_2 (011) surface requires 113.679, 142.822, 191.322, and 121.4 kJ mol^{-1} 80, respectively. Breaking of P-F bond on TiO_2 anatase (101) surface requires 106.2 kJ mol^{-1}[117].

Results of our current study and comparison with previously reported activations barriers of GB decomposition shows that decomposition of GB on CeO_2 (110) and (111) surfaces will proceed via scission of P-F bond and will require activation energies as low as 45-70 kJ mol^{-1}, which is considerably lower than on other metal oxides.

4.2.4 Conclusion

In agreement with the reported high reactivity of CeO_2 materials to dissociate the nerve agent simulants, the high activity of mesoporous CeO_2 to degrade the real nerve agent sarin was verified in this study. The high vacuum IR measurement shows that GB molecules can effectively adsorb on the mesoporous CeO_2 and react with the surfaces at room temperature without any assistance of moisture or photo excitement. Our DFT modeling find available low-activation-energy pathways for GB to dissociate on both CeO_2 pristine (110) and (111) surfaces, which explains the high reactivity of CeO_2 observed in the experiment. The dissociated species of GB can be greatly stabilized through binding the surfaces. Our modeling also implies GB dissociation via P-OC_3H_7 bond scission and P-F bond breaking are not equally favored on (110) and (111) surfaces due to the different surface structures. We also utilized DRIFTS to investigate the activities of CeO_2 towards GB under ambient conditions. The active dissociation of GB on mesoporous CeO_2 is observed under ambient conditions while the activity is lower than in the high vacuum case, suggesting the moisture or hydroxylation might show a negative influence on the activity of CeO_2 surfaces. Though our experiments and modeling show exciting results on the high reactivity of CeO_2 materials towards GB decomposition, there will be existence of O_2(Air) in a more practical case for GB to interact with filter materials, which is not considered in the current study. Future studies should further explore the activity of CeO_2 materials under existence of O_2 (Air) to validate their potential to combat nerve agents, as oxygen can interact with CeO_2[118] and might significantly interference the interaction between CeO_2 surfaces and GB molecules.

Chapter 5: Influence of Alio doping of Mesoporous CeO_2 on its Activity toward DMMP Decomposition

The research described within this chapter was published in *J. Phys. Chem. C* 2022. Algrim, L.; Mcentee, M.; Tsyshevsky, R.; Leonard, M., Durke, E. M.; Karwacki, C.; and Kuklja, M. M. Zachariah, M. R. and Rodriguez, E. E. were contributing authors on the manuscript. I designed experiments, synthesized and characterized the materials, performed the DMMP dosing DRIFTS and solid-state NMR experiments, performed the data analysis and interpretation, and wrote the manuscript draft.

5.1 Introduction

Metal oxides are among the potential materials for protection against CWAs and the interactions between metal oxides and DMMP have been constantly studied[119, 62, 45, 23, 68, 120, 28, 81, 80, 25, 22, 3, 82, 59, 24]. It is believed that surface polarity, as well as diverse surface chemistry towards different molecules of metal oxides, can lead to a great performance on DMMP adsorption and decomposition. In addition, fabrication of the mesoporous metal oxides can overcome the low-surface-area nature of conventional metal oxide materials as adsorbers.

Another advantage that metal oxides bear is their promising tunability. Doping is a commonly used strategy to adjust the physical and chemical properties of various metal oxides. While extensive categories of pure phase metal oxide materials have been studied on their interactions with DMMP, little effort has been made on tuning the metal oxide materials to alter their activities towards DMMP.

Fluorite-structure CeO_2 draws extensive attention due to its great performance in extensive catalytic reactions and ionic conductivity[121, 122, 84, 70, 123]. The previous study on single crystal surface CeO_2 and our study on mesoporous CeO_2 also proved their profound decomposition activity towards DMMP and other phosphorus containing compounds at room temperature[100, 107, 85, 108, 60, 54, 86, 63]. CeO_2 is among the most tunable metal oxides due to its structure tolerance. Not only can rare earth metal elements (such as Gd and La) neighboring Ce be doped into CeO_2 structure in great portion, but also CeO_2 shows strong tolerance on doping of alkaline-earth or even transition metal elements. Doping has been proved to be an extremely effective way to adjust various properties of CeO_2. Doping can modulate the band gap of CeO_2 through adjusting lattice parameters or introducing impurity (donor or acceptor) bands, altering the electronic properties and photocatalytic/electrocatalytic activities[124, 125, 126, 127, 84, 70]. Lattice distortion or oxygen vacancies can also be introduced to CeO_2 through doping, leading to a change of ionic conductivity[123, 128, 71]. What interests us most is that doping also strongly influences the surface properties of CeO_2. Different dopants can lead to different stability of various surfaces of CeO_2[129, 130], which might lead to different surface exposures in the synthesis of CeO_2 materials. Doping can change the absorption strength of water and thus the hydrophilic behavior of CeO_2[131, 132, 133, 134]. What's more, the dissociation energy barrier of some molecules such as H_2O and CO on the CeO_2 surfaces can be greatly modulated via doping[135, 136, 137, 138, 139, 130]. The great tolerance for various dopants and the strong influence of doping on different properties of CeO_2 implies that doping can be an effective strategy to achieve greater surface activities of CeO_2 for DMMP adsorption and decomposition. Extensive research needs to be conducted to find the best doping strategy for the application of DMMP adsorption and decomposition.

Here, we aimed at understanding how a general alio-doping (low valence doping) influences the interaction between CeO_2 and DMMP. Thus, we synthesized mesoporous CeO_2 doped with various amounts (10%, 20% and 30%) of Y^{3+}, Gd^{3+}, and La^{3+}. Y, Gd, and La are neighboring Ce in the periodic table thus Y^{3+}, Gd^{3+}, and La^{3+} show similar ionic radius and chemical activity to Ce^{4+}. We focused our study on the Y^{3+} doped samples. We systematically studied the interaction between Y3+ doped CeO_2 materials and DMMP with mass spectroscopy, diffuse reflectance infrared Fourier transform spectroscopy (DRIFTS), and 31P solid-state NMR. All measurements consistently indicate Y3+ doping decreases the activity of DMMP decomposition compared with pure mesoporous CeO_2. Similarly, we also observed such a trend for Gd^{3+} and La^{3+} doped mesoporous CeO_2. The consistency on Y^{3+}, Gd^{3+}, and La^{3+} doped CeO_2 implies a relatively general effect of alio-doping of CeO_2 on DMMP decomposition activity. We argue that the reactivity difference of alio-doped mesoporous CeO_2 to the surface hydroxylation and preferred surface exposure leads to the difference of reactivity.

5.2 Experimental Section

5.2.1 Synthesis of Templated Mesoporous CeO_2

Mesoporous CeO_2 was synthesized via a nanocasting method which is previously reported[88, 89]. The silica template KIT-6 was first prepared via a reported method[49], on which 85 °C was used as the aging temperature during the KIT-6 synthesis. In our typical synthesis of mesoporous

CeO_2, 0.5000g as-prepared KIT-6 silica was initially dispersed in 20.0 mL 95% ethanol. Then 1.302g $Ce(NO_3)_3 \cdot 6H_2O$ (0.003 mol) was also dissolved in the same solution. Such mixture was under stirring at room temperature until all the solvents inside evaporated and the mixture became dry powder. The powder was later transferred to a glass vial (diameter $\sim$5 mm) and under calcination at 560 °C for 6h (ramping rate 1°C /min) to form CeO_2/KIT-6 composite. The CeO_2/KIT-6 composite was soaked in 2M NaOH solution 3 times at 80 °C overnight to fully remove the silica template. After being washed with distilled water 3 times and with ethanol 2 times, the final mesoporous CeO_2 product was dried in air at 80°C overnight and 150°C for another day. For the synthesis of Y^{3+}, La^{3+}, Gd^{3+} substituted samples, all the procedures are same as the synthesis of pure mesoporous CeO_2, except the 10%, 20%, 30% mol ratio of cerium nitrate salt was replaced by the same moles of Y, La, Gd nitrate salt.

5.2.2 Material Characterization

Transmission electron microscopy (TEM) image was taken using JEOL JEM 2100 LaB6 TEM equipment. X-ray Small angle scattering (SAXS) patterns were collected with a Xenocs Xeuss SAXS/WAXS/ GISAXS small angle system. The nitrogen adsorption isotherms were measured by Micromeritics ASAP 2020 Porosimeter Test Station. The surface area was calculated by applying Brunauer-Emmett-Teller (BET) equation on adsorption data obtained at P/P_0 between 0.05 and 0.35. The pore size distributions were calculated by analyzing the adsorption branch of the N_2 sorption isotherm using the Barret-Joyner-Halenda (BJH) method. Powder XRD patterns were recorded on the Bruker D8 Advance diffractometer, with Cu Kα/Kβ radiation. 10%, 20%, 30% Y^{3+} doped mesoporous CeO_2 were also examined by Time-of-flight (TOF) neutron diffraction. The Neutron diffraction patterns were collected at 300 K on the nanoscale-ordered materials diffractometer (NOMAD) at the Spallation Neutron Source (SNS), Oak Ridge National Laboratory (ORNL). Rietveld refinement was performed on the diffraction patterns using TOPAS 5[140]. Ce 3d and O 1s X-ray photoelectron spectroscopy (XPS) was collected on a Kratos Axis 165 X-ray photoelectron spectrometer operating in hybrid mode using Al Kα monochromatic X-rays at 280 W. For the Y, Gd, La doped CeO_2 samples, Y 3d, Gd 3d and La 3d spectra were also collected on corresponding samples. All XPS spectra were calibrated to the C 1s peak at 284.80 eV. All spectra fittings were performed using CasaXPS. Shirley background was used for background subtracting. 30% Gaussion +70% Lorentz is applied as the peak shape profile for the fitting.

5.2.3 CO Adsorption TIR

CO adsorption studies on doped CeO_2 were performed in a high vacuum chamber with a base pressure at $3x10^{-9}$ Torr. A more detailed description of the vacuum chamber is provided elsewhere[20]. Each sample was pressed into a 0.004" thick W-grid and attached to the sample mount via stainless steel clamps connected to copper rods. The copper rods were attached to a power supply allowing for resistive heating of the sample up to $\sim$1000 K at a resolution of ±0.1 K. Before introducing CO into the vacuum chamber, the sample was heated up to 450 K for 30 minutes in order to remove H_2O and hydrocarbon impurities. After heating, the surface was cooled down with liquid nitrogen ($\sim$140 K) and an IR spectrum was taken of the CeO_2 sample. An IR spectrum was taken of the W-grid without any CeO_2 powder and used as the background. Each IR spectrum contains an average of 256 interferograms at a resolution of 2

cm^{-1}. Subsequently, 10^{-2} Torr of CO vapor was introduced into the vacuum chamber. An IR spectrum was taken and was subtracted from the IR spectrum of CeO_2 prior to CO exposure. The subtracted spectrum represents a difference spectrum showing the CO adsorption on the CeO_2 surface.

5.2.4 In situ DRIFTS Measurement of DMMP Adsorption/Decomposition on Doped Mesoporous CeO_2 at Room Temperature

A Harrick Scientific Praying Mantis DRA optical accessory was used with an associated Harrick Scientific high-temperature reaction chamber HVC-DRP-5 and temperature controller unit (110 V, ATC-024-3) for the diffuse reflectance infrared Fourier transform spectroscopy (DRIFTS) measurements. Before the DMMP exposure experiment, mesoporous CeO_2 powder was heated under the 25 mL/min Ar flow at 200°C for 2 hours to remove as much physisorbed water as possible and then cooled to the room temperature. We were mainly interested in the interaction between mesoporous CeO_2 and strongly adsorbed DMMP molecules. In addition, we wanted to minimize the DMMP contamination on our DRIFTS system. Thus, we applied a swift injection approach to introduce DMMP into the DRIFTS cell containing mesoporous CeO_2 powder. In our typical experiment, mesoporous CeO_2 powder in the cell was under constant 25 mL/min Ar flow all the time, 2 mL saturated DMMP vapor carried by N_2 was quickly injected into the system using a delay controlled electronic injector. the illustration of such a system is provided in the supplementary information. The injections happened every 20 min. During the 20 min gap, DRIFTS spectra scans were collected every 30s, allowing the strong interaction between the substrate (CeO_2) and molecules (DMMP) to be observed. Totally 10 DMMP injections were performed.

5.2.5 Ex-situ Solid State 31P NMR Measurement of DMMP Adsorption/Decomposition on Doped Mesoporous CeO_2 at Room Temperature

For the ex-situ measurement, 50 mg of each powder sample (dried in Ar flow at 150 °C for 2 hours) was exposed under saturated DMMP vapor for 30 minutes at room temperature, followed by evacuation under vacuum for 10 minutes to remove the non-adsorbed or loosely adsorbed DMMP in the material. Right after the ex-situ DMMP experiment, 31P solid-state magic angle spinning (MAS) NMR spectra were collected for the material. Bruker AV NEO solid-state 500 MHz was used for performing NMR experiments. Magic angle spinning speed was set at 8000 Hz. The sample was measured for around 1 hour and 1024 scans were averaged to get the final 31P spectra. 85% H_3PO_4 was used as a reference (0ppm).

5.2.6 Detection of DMMP Decomposition on Doped Mesoporous CeO_2 via Mass Spectrometry

Mass spectrometry was used to detect reaction products (majorly methanol) from the interaction of doped mesoporous CeO_2 and DMMP. The measurements made with a mass spectrometer used an experimental setup described in the previous work[52], but again briefly described here. Before analysis with the mass spectrometer, the CeO_2 sample was heated to 200°C to remove any potential surface contaminants. Three mass flow controllers regulate the flow of dry argon, argon saturated with water, and DMMP, all of which are combined to produce a 35 mL/ min total flow that is 0.4 P/P0 DMMP and 4% relative humidity at room temperature. The combined flow is passed into a 4.7625 mm (3/16”) ID quartz tube which holds the CeO_2 sample, supported by inert glass wool. The quartz tube is heated at 10 °C/min to 325 °C and held for 3 hours before cooling to room temperature, where it dwells for approximately 7 hours before heating again. This temperature cycle was repeated multiple times. Downstream from the material, a capillary line samples the gas mixture into the Quadrupole Mass Spectrometer. Methanol signal (m/z 31) is monitored. All-time traces are normalized to m/z 36 (an isotope of Argon) to minimize the effects of signal drift.

5.3 Experimental Results and Discussion

5.3.1 Characterization

To exclude the possible influence of pore structure and surface area on the interaction between DMMP and CeO_2 samples, we used the same batch of KIT-6 silica template for all the synthesis of doped and pure mesoporous CeO_2, making sure all the samples to be tested possess very similar morphologies in the nanoscale. Such similarity was confirmed through TEM, SAXS, as well as nitrogen adsorption measurement. As shown in TEM (Figure B.1-B.3), all the mesoporous samples display very similar ordered porous structures. Clear diffraction peaks are visible in the SAXS measurement (Figure 5.1b for Y^{3+} doped, Figure B.4 and B.5 for Gd^{3+} and La^{3+} doped), confirming that ordered pore structures were preserved for pure and doped mesoporous CeO_2. No major diffraction pattern changes or peak shift is observed through the SAXS, indicating doping with Y^{3+}, La^{3+} and Gd^{3+} do not have a strong impact on the pore structure formation. Nitrogen adsorption isotherms and the corresponding pore size distribution curve (inset) for all samples are shown in Figure B.6-B.8. The extracted surface area and mean pore size of CeO_2 samples are listed in Table B.1. Doped, as well as pure mesoporous CeO_2, displayed relatively high and similar surface area (around 130±20 m^2/g). The mean pore size also deviates very little from each sample (∼3 nm).

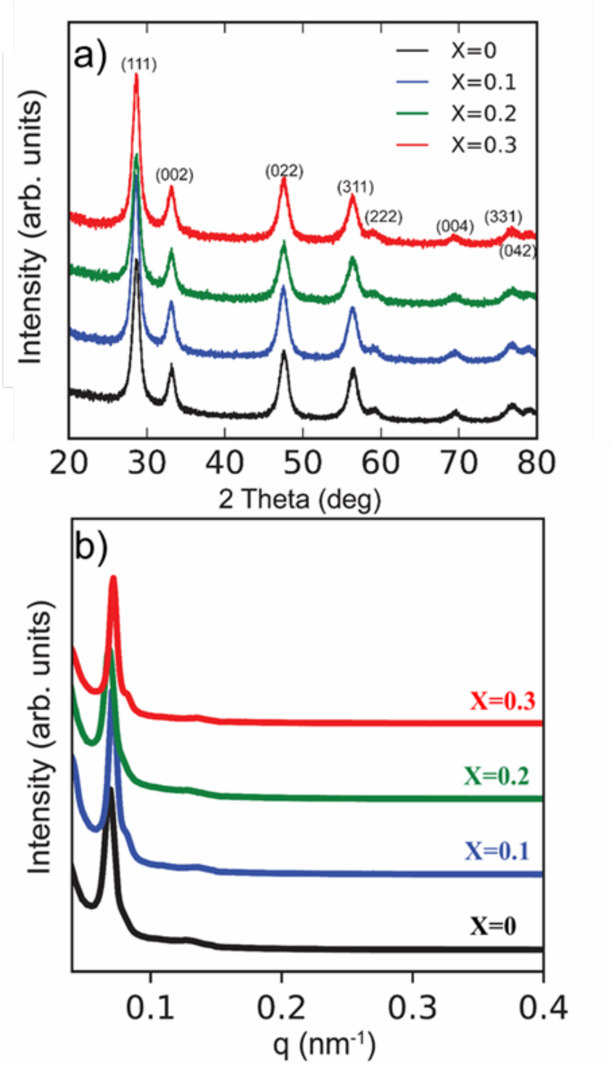

Figure 5.1: a) XRD and b) SAXS characterizations Mesoporous $Ce_{1-x}Y_xO_{2-\delta}$ (x=0, 0.1, 0.2, 0.3).

Figure 5.3a and Figure B.9 presents the XRD patterns of as-synthesized mesoporous samples. A pure phase of Fm-3m cubic fluorite CeO_2 structure is observed for all the samples. The broadened diffraction peak is the indication of low crystallinity and nano-scale crystal grain size. The refined Lorentz grain sizes are very similar for each sample, ranging from 8∼12 nm.

Theoretically, the lattice parameter will alter upon substituting/doping cations in the CeO_2 system due to the ionic size difference between Ce^{4+} and other cations[141]. Studies have shown that 10% doping of Y^{3+}, La^{3+} or Gd^{3+} is enough to see a lattice parameter deviation from the pure CeO_2 in the samples with very high crystallinity[141]. While in our systems, the extremely broadened diffraction peaks wiped out the difference between doped and pure CeO_2 samples, due to the low crystallinity as well as possible strain in our mesoporous system. The refined lattice parameter for each sample is nearly the same when the error is considered.

10%, 20%, 30% Y^{3+} doped mesoporous CeO_2 were selected to be examined with neutron diffraction since neutron diffraction is much more precise and sensitive to oxygen atoms. The neutron diffraction patterns are shown in Figure B.10. No impurity phase was observed for neutron patterns. Even for neutron diffraction, low crystallinity also causes a severe peak broadening, posing difficulty in data analysis. Our Rietveld refinement results on neutron diffraction show a decreasing trend of lattice parameters upon the increasing amount of Y^{3+} doping, which resembles what was reported in a previous study[142]. During the refinement, we deliberately fixed the oxygen occupancy at 100% and watched the change of atomic displacement (ADP) of Ce and O atoms for each sample. As shown in Figure B.10, as Y^{3+} doping increases, the ADPs of Ce and O both increase, indicating the increase of disordering of the sample because of the increase of oxygen vacancies in the crystals[142]. Thus, as expected, alio-doping Y^{3+} into our mesoporous CeO_2 system increases the concentration of oxygen vacancies in the bulk. As more Y^{3+} doped into CeO_2 lattice, our neutron diffraction measurement can detect the increase of oxygen vacancies in the bulk. Gd^{3+} and La^{3+} are very similar to Y^{3+} in terms of valence and chemical reactivity. We therefore infer, increasing Gd^{3+} and La^{3+} doping will also increase the concentration of oxygen vacancies in the bulk for mesoporous CeO_2, just as Y^{3+} does in mesoporous CeO_2, based on our neutron measurement on Y^{3+} doped CeO_2 and the reported study on doped CeO_2 with high crystallinity[141, 143].

XPS measurements were performed to understand the elemental valence states and ratio on the surface. Ce 3d XPS is displayed in Figure B.11 and B.12. The spectra are fitted by strictly following the reported fitting parameters[103]. The Ce 3d spectra can well be fitted with just Ce^{4+} components for pure and all doped mesoporous CeO_2 samples, implying that doping of Y^{3+}, La^{3+} or Gd^{3+} does not influence the valence state of CeO_2 in our mesoporous system and that Ce^{4+} instead of Ce^{3+} dominates on the surface for all the samples. O 1s XPS (Figure B.13 and B.14) shows two major types of oxygen exist, namely lattice oxygen (O^{2-}) at 529.3 eV and surface oxygen(-OH) at 531.5 eV, common for metal oxides. The statistics of the ratio between surface oxygen (-OH) and total oxygen fitted from XPS O1s spectra are displayed in Figure 5.1a. We observed an increasing trend of hydroxylating level (ratio of OH) on the surface as the doping level rises for the mesoporous CeO_2 samples. Such a trend exists for all Y^{3+}, La^{3+}, Gd^{3+} doped systems. While it is also clear low level of doing (10%) shows little difference with pure CeO_2 in terms of OH ratio on the surface. We attribute the increase of hydroxylating level upon doping to the stabilization of oxygen vacancies on the surface. We learned bulk oxygen vacancies rise upon alio-doping level increases, which should be also the case on the surface. However, in the ambient synthetic conditions, surface oxygen vacancies are not stable and will be stabilized by surrounding molecules such as CO_2 and H_2O[131, 132, 133, 134, 136, 137, 139]. In our case, the defective surface is stabilized by environment H_2O and the OH groups will be formed. In a low doping level case, the destabilization energy of oxygen vacancies is not high enough to allow the formation of OH groups. Thus, 10% doping does not alter the hydroxylating level in our mesoporous CeO_2 system. From Figure 5.3a, we also found different dopants have different levels of impact on surface hydroxylating level, with Y^{3+} having the strongest influence and Gd^{3+} the weakest. Such variation of the impact of dopants on surface hydroxylation results from different destabilization energies of dopants on the crystal lattices[131]. The XPS 3d spectra of dopants (Y^{3+}, La^{3+}, Gd^{3+}) were also recorded (Figure S15) and we looked at the dopant/Ce^{4+} ratio change as the increase of doping level (Figure 5.2b). As is expected the dopant ratio (Y^{3+}, La^{3+} and Gd^{3+}) on the surface rises when the doping level increases in bulk. However, for each of the doping levels, the dopant ratio on the surface exceeds the dopant ratio that we added in the CeO_2 during the synthesis(bulk). The dopant ratio on the surface is more than 2 times that in the bulk. Since we observed no impurity phases in our diffraction measurement, we exclude the phase separation of bulk as the cause. In the alio-doping metal oxides, enrichment of dopants is not rare and has been reported on some metal oxide systems[144, 145, 146, 147, 148, 149, 150]. The dopant enrichment on the surface is usually driven by lowering the surface energy[145] (stabilization).

5.3.2 Influence of Y^{3+} Doping on the Activity of Mesoporous CeO_2 towards DMMP Decomposition

The understanding on how alio-doping influences the interaction between DMMP and mesoporous CeO_2 at room temperature is focused on Y^{3+} doped mesoporous CeO_2 samples. We first performed DRIFTS study and made direct comparisons within mesoporous CeO_2 doped with different amount of Y^{3+}. Figure 5.3 shows the in-situ DRIFTS spectra of pure and Y^{3+} doped mesoporous CeO_2, which was taken instantly following the first injection of DMMP onto the materials. The assignment of the IR bands is shown in Table 5.1. Bands at locations 1-4,6-

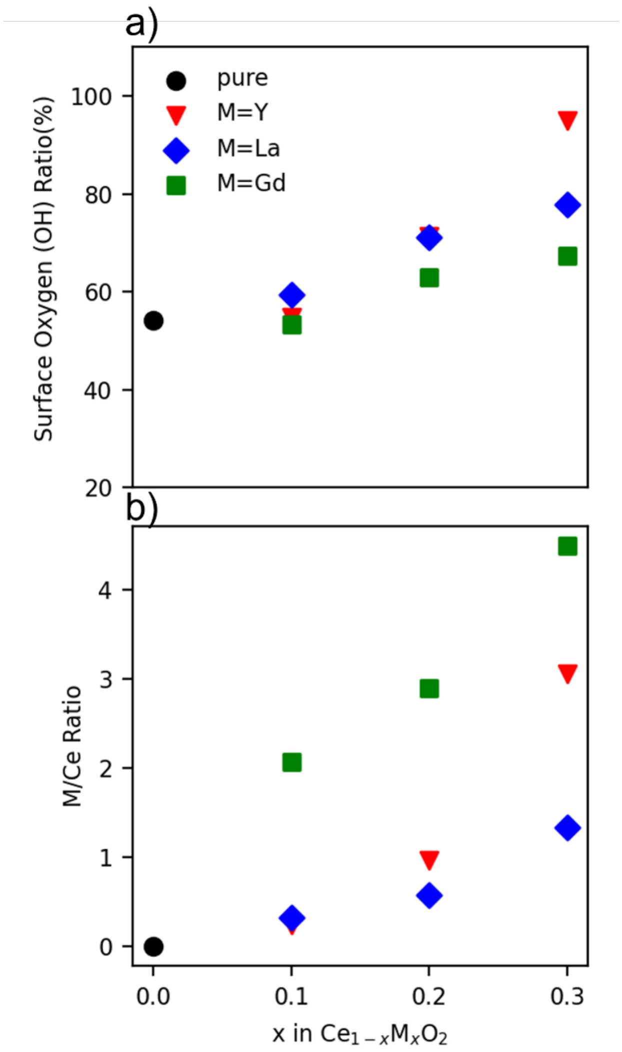

Figure 5.2: a) Surface oxygen/lattice oxygen ratio b) Dopant/Ce ratio of mesoporous $Ce_{1-x}M_xO_{2-\delta}$ (x=0, 0.1, 0.2, 0.3) extracted from XPS measurement.

10,12-13 belong to the different vibration modes of intact DMMP[62, 23, 63]. Band 5 ($\sim$2810 cm^{-1}) corresponds to C-H stretching modes of the OCH_3 group when OCH_3 group directly bonds to a metal center[151, 23, 68]. Band 11(1096 cm^{-1}) and part of broad band 14(1116 -1170 cm^{-1}) stretching modes of OPO species[68, 151, 80]. The appearance of Band 5, 11 and 14 is the indication of dissociation of DMMP on the surface. The dissociation is believed to go through a P-OCH_3 bond breaking[151, 63, 62]. Interestingly, as shown in Figure 5.3, we observed that the relative intensities of Band 5, 11 and 14 undergo a significant decrease as the doping level increase compared with other bands. Such a decrease of intensity indicates the decay of decomposition activity of DMMP on the surface as the doping level increases.

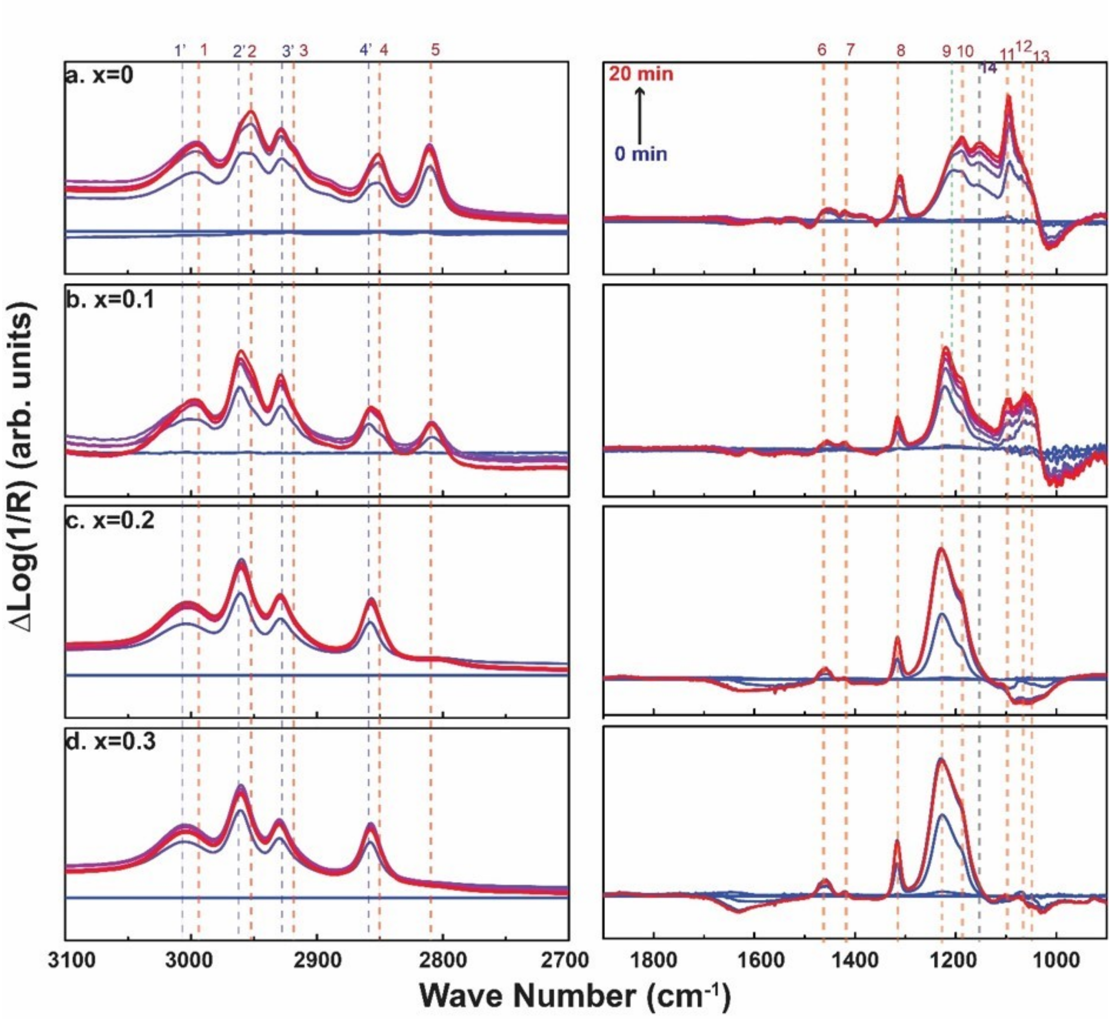

Figure 5.3: In situ DRIFTS measurement of $Ce_{1-x}Y_xO_{2-\delta}$ (x=0, 0.1, 0.2, 0.3) upon DMMP injections.

Band 9 at around 1204 cm^{-1} correlates the P=O stretching mode of adsorbed intact DMMP. For all the doped series, we found this band 9 undergoes a blue shift (to high wavenumber) as the doping level rises, as is shown in Figure 5.3 and Table 5.1. It is commonly believed that DMMP adsorbed on the surface through P=O bond[81, 80, 22, 3, 152, 49]. The P=O can contribute some of its electron density during the adsorption, leading to a less polar or weaker P=O bond[153, 154]. A blue shift of P=O stretching modes means a less polar P=O bond, implying a weaker DMMP adsorption. Thus, we conclude that the alio-dopant not only leads to a decreased activity of DMMP decomposition but weaker DMMP adsorption on the surface of mesoporous CeO_2.

vibration mode	position	x=0	x=1	x=2	x=3
$v_a(PCH_3)$	1	2996	2996	/	/
$v_a(PCH_3)$	1’	3003	3004	3003	3004
$v_a(OCH_3)$	2’	2952	2952	/	/
$v_a(OCH_3)$	2’	2960	2959	2960	2960
$v_s(PCH_3)$	3	2905	2905	/	/
$v_s(PCH_3)$	3’	2928	2928	2929	2929
$v_s(OCH_3)$	4	2851	2851	/	/
$v_s(OCH_3)$	4’	2856	2856	2857	2857
$v_s(MOCH_3)$	5	2811	2808	/	/
$\sigma_a(OCH_3)$ and $\sigma_s(OCH_3)$	6	1467	1467	1467	1467
$\sigma_a(P–CH_3)$	7	1421	1421	1421	1421
$\sigma_s(P–CH_3)$	8	1314	1314	1314	1314
v(P=O)	9	1204	1220	1228	1228
$\rho(OCH_3)$	10	1188	1190-1192	/	/
v(O–P-O)	11	1096	1100	/	/
v_a(C–O))	12	1070	1069	/	/
v_s(C–O))	13	1047	1047	/	/
v(O–P-O)	14	1116-1170	1116-1170	/	/

Table 5.1: Assignment of IR peaks upon DMMP dosing onto mesoporous $Ce_{1-x}Y_xO_{2-\delta}$ (x=0, 0.1, 0.2, 0.3) from DRIFTS characterization.

Bands 1-4 are the C-H stretching modes of $-CH_3$ part of DMMP molecule. Through the comparison with doped samples, we found these bands are all accompanied by a “sideband” in the lower wavenumber region (indicated as 1’, 2’, 3’ and 4’, redshift) as shown in Figure 5.3 and Table 5.1. And interestingly, those sidebands gradually fade as the concentration of dopants increases, like what has happened on band 5, 12 and 14. We did not find any mentioning of similar observation in other DMMP adsorption studies. we speculate those side bands may come from the C-H stretching modes of decomposition product of DMMP (such as MMP). Another possibility would be the C-H stretching modes of stronger adsorbed DMMP molecule. Like P=O bond, stronger interaction (adsorption) of DMMP on the surface might also activate the C-H bonds (weaker bonding), leading to a redshift of the IR bands[153, 154].

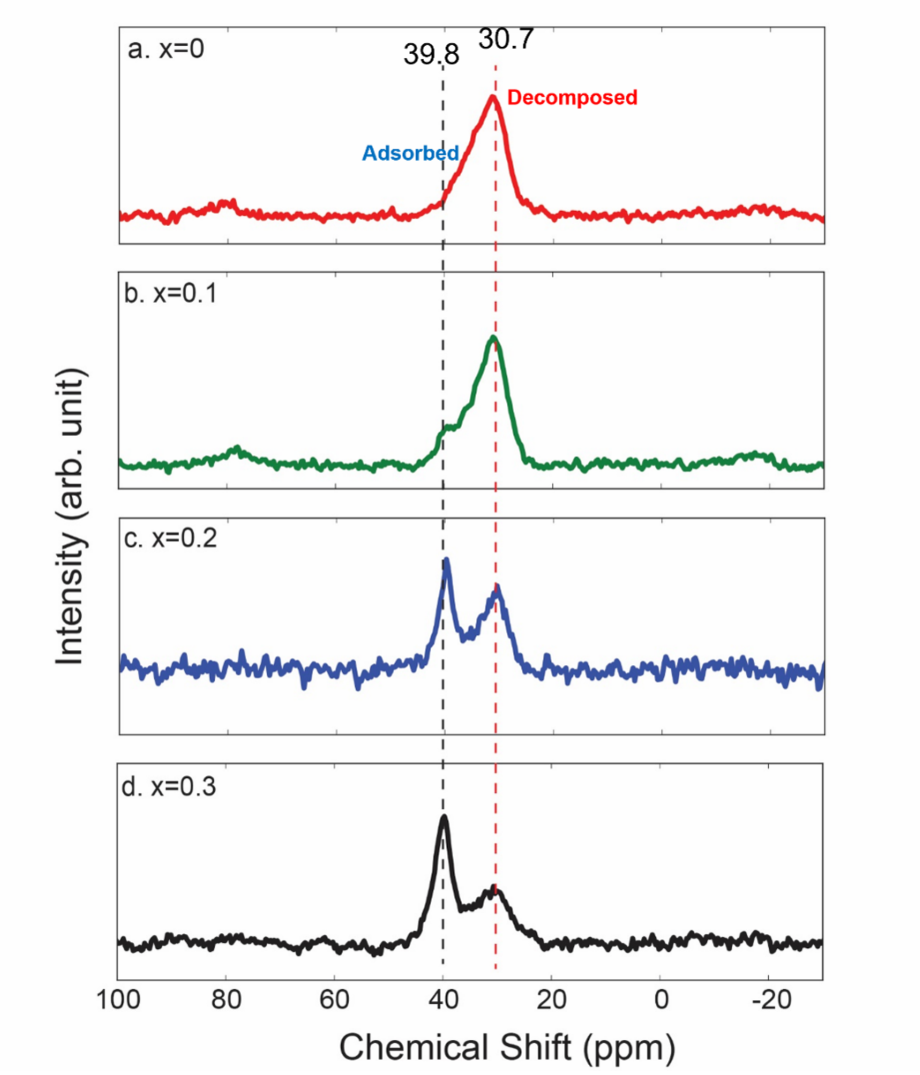

Figure 5.4: Ex situ 31P Solid State NMR measurement of mesoporous $Ce_{1-x}Y_xO_{2-\delta}$ (x=0, 0.1, 0.2, 0.3) after DMMP dosing.

31P Solid State NMR provides an alternative to looking at the decomposition activity of DMMP on the mesoporous CeO_2. We examined the 31P NMR spectra of the mesoporous CeO_2

series after their interaction with gas-phase DMMP for 30 min. The NMR spectra of Y^{3+} doped series are shown in Figure 5.4. We were able to identify three major peaks based on the previous solid state NMR study on DMMP interacting solids[155, 156, 157, 158]. The peak located at 39.8 ppm corresponds to DMMP adsorbed through hydrogen bond. The peak located at 34 ppm is from DMMP adsorbed on the surface. And it was reported the peak around 30.7 pm is adsorbed MMP or MPA, which is the dissociation product of DMMP after -OCH_3 is cleaved from DMMP. The relative intensity between 39.8 ppm and 30.7 ppm increases as the doping level increases, implying that less DMMP dissociates on the alio-doped mesoporous CeO_2, confirming what we have observed in the DRIFTS measurement.

DRIFTS and 31P Solid State NMR are only capable to look at the surface species upon DMMP interacting with CeO_2 materials. While it is possible the reaction products between CeO_2 surface and DMMP leave the CeO_2 surface and then it leads to the decrease of signal of dissociation species in DRIFTS and NMR measurement. To further confirm that Y^{3+} doping leads to the decreased activity of CeO_2. Mass spectrometry was used to detect reaction products. As is discussed earlier and reported previously, DMMP dissociation on CeO_2 surfaces (or other metal oxides) is through a P-OCH_3 bond breaking, leaving O-P-O species and -OCH_3(or methanol if surface is hydroxylated)[63, 59, 82, 25, 68]. O-P-O species adsorbs strongly and irreversibly on the surface of metal oxides, while -OCH_3 (or methanol) can easily desorbed through heating. Thus, methanol signal was monitored upon heating cycles under the DMMP vapor flow. Figure 5.5 displays the production of methanol (normalized by surface area) of mesoporous CeO_2 materials integrated at each heating cycle. For pure and all the doped CeO_2, a gradual decrease in methanol production was noted upon each heating cycle, indicating DMMP decomposition on the CeO_2 is a surface reaction instead of a hetero-catalytic reaction and doping does not alter such a behavior.

It is common that the interaction between DMMP and metal oxides are mostly non catalytic reactions[28]. Most importantly, through all the heating cycles, we observed that methanol production from pure mesoporous CeO_2 far exceeds doped CeO_2. As the doping level increases, the production of methanol gradually decreases in very first cycles. In the later cycles, methanol production from doped CeO_2 is very close to each other and their differences are within the range of error. Again, the decreased of methanol production on doped CeO_2 compared with pure CeO_2 further supports that surface activity of mesoporous CeO_2 for DMMP degradation are impeded through Y^{3+} doping.

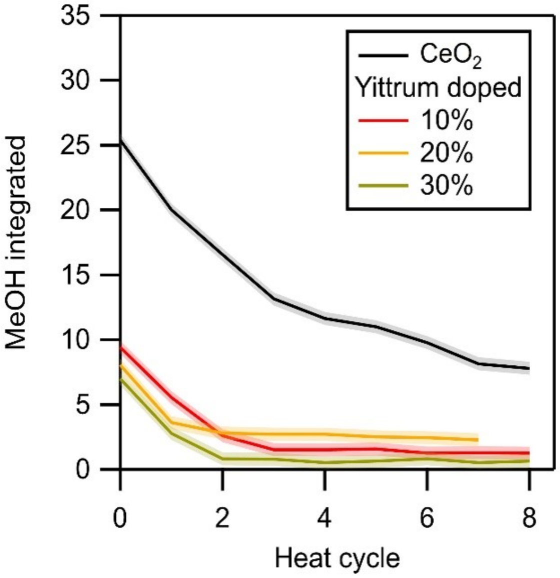

Figure 5.5: Mass Spectrometry measurement of Methanol production during heating cycles upon flowing DMMP through mesoporous $Ce_{1-x}Y_xO_{2-\delta}$ (x=0, 0.1, 0.2, 0.3).

5.3.3 Origin of Decreased Activity of Mesoporous CeO_2 upon Y^{3+} Doping

All three different measurements (DRIFTS, Solid State NMR and Mass Spectrometry) consistently show doping with Y^{3+} gradually decreases the surface activity of mesoporous CeO_2 for DMMP degradation. We exclude that the activity decrease is caused by the change of crystal structure, porosity, or pore structure, as the XRD, nitrogen adsorption and SAXS characterizations do not diverge among pure and doped mesoporous CeO_2 samples. As previous IR study indicates Y_2O_3 nanoparticle is reactive towards DMMP dissociation at room temperature[68], it is not likely the doped Y site on mesoporous CeO_2 behave as inactive site and decrease the activity. The change of the surfaces of mesoporous CeO_2 upon doping must play a role in deactivating the activity towards DMMP dissociation.

5.3.3.1 Hydroxylation Level and Active sites

We believe the first factor leading to the decreased the activity is the increased hydroxylation level of surfaces upon doping. Our previous modeling of DMMP interacting with CeO_2 implies DMMP decomposition on the hydroxylated surfaces of CeO_2 (both (110) and (111)) require higher activation energy barrier than on the pristine surfaces[60], which here we summarized in Figure 5.6. The under-coordinated Ce atoms on the pristine surfaces provide sites for a stronger interaction with DMMP molecules either through P=O or P-OCH_3. While on the hydroxylated surfaces, OH group will bind to under-coordinated Ce atoms, leading to a much less exposure of those active under-coordinated Ce atoms.

As mentioned previously, the XPS results (Figure 5.2) clearly shows the increased weight percent of surface oxygen (OH) upon Y^{3+} doping (except that 10% doping remains nearly unchanged), which might be the result of stabilization of oxygen vacancies due to alio-doping. Purely based on the different hydroxylation level, we should expect at least for 20% and 30% doped mesoporous CeO_2 show a decreased activity towards DMMP dissociation, which actually agrees well with what we have observed experimentally.

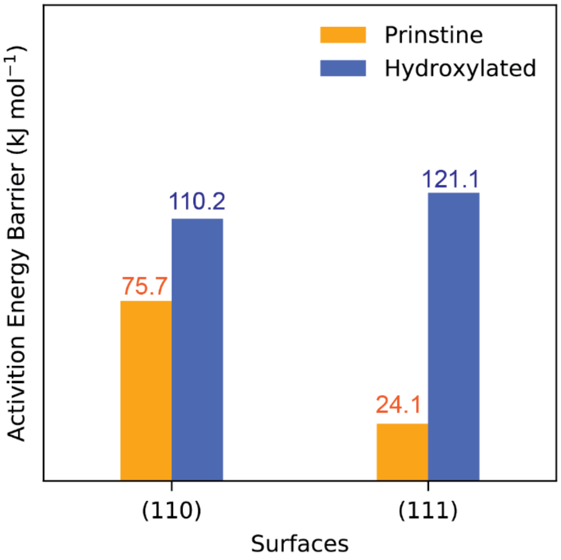

Figure 5.6: Summarized activation energy barrier for DMMP dissociation on pristine and hydroxylated (110) and (111) surfaces of CeO_2. The results are based on DFT calculation reported previously[4]

Our previous study shows that using CO as probe molecules to characterize the surfaces of CeO_2 with IR is an outstanding approach to gain more insight on the surfaces of mesoporous CeO_2. Thus, here we used the same method to characterize the surfaces of Y^{3+} doped mesoporous CeO_2. Pure mesoporous CeO_2 and all Y^{3+} doped CeO_2 are dosed with CO and then IR spectroscopy was applied to detect CO stretching modes. The CO adsorption IR results are shown on Figure 5.7a. Two major characteristic peaks are observed for pure and Y^{3+} doped mesoporous CeO_2, which represent CO stretching modes when CO is adsorbed on (110) and (111) surfaces[104, 105]. These two stretching peaks implies the major exposed surfaces for pure and doped mesoporous CeO_2 remain (110) and (111) surfaces. In addition, we observed a decreased intensity of the spectra upon Y^{3+} doping (except 10%). The integrated area of the CO stretching spectra is presented in Figure 5.7b, which can be also interpreted as the concentration of under-coordinated Ce atoms on the surfaces. The concentration of under-coordinated Ce atoms deceased upon doping, which is due to the increased OH group binded to those sites, as indicated from XPS. The decrease of active sites should lead to a weakened activity towards DMMP decomposition, which again agrees well with the experimental observations. The increased hydroxylation level can also explain the weaker adsorption of DMMP on mesoporous CeO_2 observed in DRIFTS measurement (red shift of v(P=O) modes in Figure 5.3). The adsorption through P=O coordinating onto the under-coordinated Ce atoms (P=O–Ce) is stronger than through P=O forming Hydrogen bond with surface hydroxyl groups(P=O—HO-Ce). As the level of surface hydroxylation increases, DMMP tends to adsorb more through forming P=O—HO-Ce rather than P=O–Ce on the surface of CeO_2, leading to a weakened adsorption.

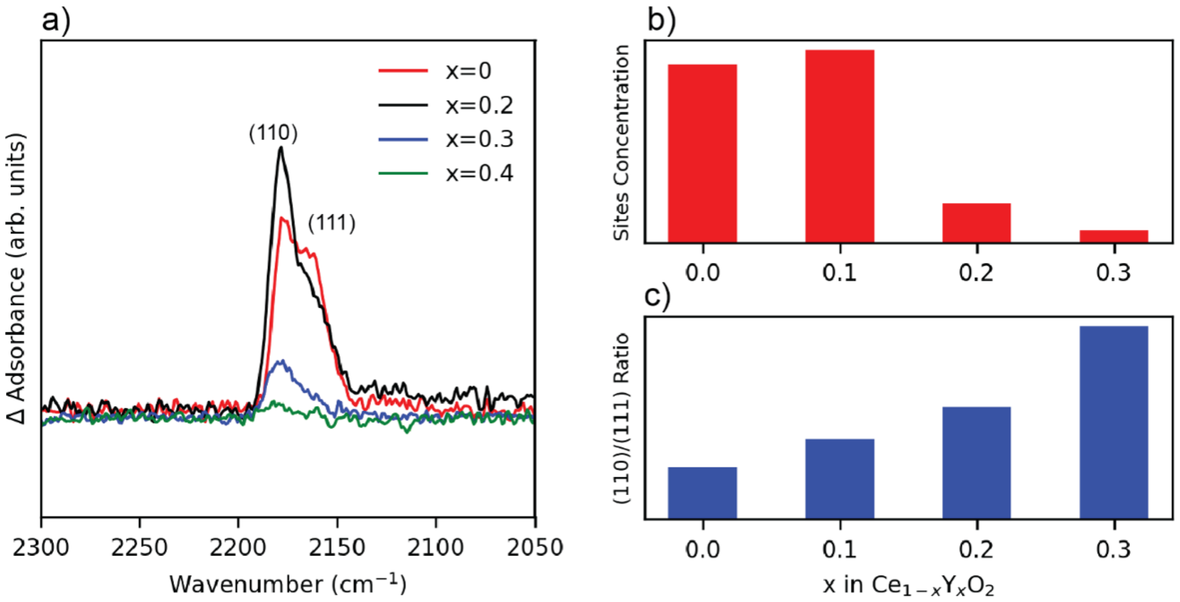

Figure 5.7: a) IR characterization of CO stretching mode when CO is adsorbed on mesoporous $Ce_{1-x}Y_xO_{2-\delta}$ (x=0, 0.1, 0.2, 0.3). b) Undercoordinated Ce site concentration of mesoporous $Ce_{1-x}Y_xO_{2-\delta}$ (x=0, 0.1, 0.2, 0.3). c) (110)/(111) surface ratio of mesoporous concentration $Ce_{1-x}Y_xO_{2-\delta}$ (x=0, 0.1, 0.2, 0.3). graph b) and c) are extracted from a).

5.3.3.2 (110) and (111) Surfaces

The increased hydroxylation level and declining amount of active under- coordinated Ce/Y sites can well explain the observed gradually declined activity of 20% and 30% Y^{3+} doped mesoporous CeO_2 for DMMP dissociation. While for 10% doped mesoporous CeO_2, the hydroxylation level (shown in Figure 5.2a) as well as the concentration of active under- coordinated Ce sites (presented in Figure 5.7b) does not show significant deviations from the pure mesoporous CeO_2, even the concentration of active under-coordinated Ce sites of 10% doped mesoporous CeO_2 slightly exceeds the pure mesoporous CeO_2. Still, we observed a profoundly degrading activity of 10% doped mesoporous CeO_2 towards DMMP decomposition. Clearly, the decreased activity of 10% doped mesoporous CeO_2 cannot be attributed to hydroxylation level and amount of active under- coordinated Ce sites. What leads to the decreased activity of 10% doped mesoporous CeO_2? Our previous modeling of DMMP interacting with CeO_2 not only indicates the hydroxylation level show great influence on the surface activity of CeO_2, but also suggests that the activity is strongly surface (facet)-dependent[60]. As also summarized in Figure 5.6, the pristine (111) surface requires significant lower activation energy for DMMP dissociation (through P-OCH_3 cleavage) than the pristine 100 surface (24.1 vs. 75.7 kJ mol^{-1}). So one would expected high ratio of exposed pristine (111) surface than (110) surface in the CeO_2 materials can lead to an improved activity for DMMP decomposition. We realize the hydroxylation level as well as the concentration of active under- coordinated Ce sites are similar between 10% doped and pure mesoporous CeO_2, but the exposed surfaces are composed of higher ratio of (110) surface rather than (111) surface 10% doped mesoporous CeO_2, as is shown in Figure 5.7a and summarized in Figure 5.7c. Thus, we postulate the decrease of the ratio of pristine (111) surface is the major cause for the declined activity of 10% doped mesoporous CeO_2. It turns out (110) surface rather than (111) surface is more exposed as the doping level grows (Figure 5.7c). This decrease exposure of (111) surfaces can also be part of the cause of declined activity of 20% and 30% Y^{3+} doped mesoporous CeO_2. Trenque et al.[85] also reported (111) surfaces of CeO_2 nanocrystals have outstanding activity towards the DMNP (which has similar structure with DMMP) dissociation. As for the reason why Y^{3+} doping leads to a change of the ratio of exposed (110) and (111) surfaces, we suspect the doping changed the stability of the surfaces (surface energy) and this change varies from surface to surface. Theoretical work suggest doping is able to weaken the surface polarity thus lower the surface energy and stabilize polar surfaces on ZnO[159, 160]. Doping might work in a similar way on CeO_2 surfaces. It seems the Y^{3+} doping changed surface energy of (110) and (111) surfaces in different degrees. Such a change leads to a larger difference in surface energy between (110) and (111) surfaces. After doping, (110) surface seems to have a much lower surface energy than (111) surface. Thus, (110) surface is easier to be stabilized and is more exposed in the materials. (110) CeO_2 surface is corrugated and expose either Ce or O atoms thus is a polar surface while (111) surface consists of both Ce and O atoms in a single plane thus is a non-polar surface[161, 162]. Dopant induced surface stabilization is more prominent in polar (110) rather than non-polar (111) surface in CeO_2, leading to more exposure of (110) surface upon Y^{3+} doping. Such hypothesis needs to be further confirmed experimentally and theoretically.

5.3.4 Consistency with La and Gd Doped Mesoporous CeO_2

The decreased decomposition activity of DMMP on mesoporous CeO_2 upon alio doping not only applies on Y^{3+} doped CeO_2 as discussed above but is also observed on La^{3+} and Gd^{3+} doped samples. DRIFTS measurements of DMMP on La^{3+} and Gd^{3+} shows nearly identical trend upon increasing doping level, as is presented in Figure B.16 and B.17. 31P Solid State NMR La^{3+} doped series shows similar results with Y^{3+} doped CeO_2, as is presented in Figure B.18. We cannot get any 31P NMR signal in the Gd^{3+} series due to the strong magnetic interaction of Gd^{3+}. Since Gd^{3+} doped CeO_2 series show a similar trend with Y^{3+} and La^{3+} doped series in the DRIFTS measurements, the 31P solid state NMR would not show significant deviation should the signal be observed. Both La^{3+} and Gd^{3+} doped mesoporous CeO_2 were also tested with temperature dependent mass spectrometry upon DMMP dosing. Consistent trends are also observed (displayed in Figure SB.19): the methanol generated at whole temperature range dramatic decreases upon the doping, indicating the degrading of the activity. As different dopants and various testing techniques shows a consistent trend, we are convinced to say alio-doping with 3+ valence ions (the ion has to show similar property with Ce^{4+}) will generally deactivate the surfaces of mesoporous CeO_2 towards DMMP dissociation. Since the characterizations show that different dopants have similar effect on the surfaces of mesoporous CeO_2, we speculate similar factors caused by alio-doping leads to the decreased activity towards DMMP decomposition.

5.4 Conclusion

Pure mesoporous CeO_2 possesses excellent activity to decompose DMMP at room temperature while our study shows a general alio-doping on CeO_2 will impede such an activity. alio-doping can introduce oxygen vacancies in the bulk CeO_2. However, the scenario becomes complicated on the surfaces. Surface oxygen vacancies introduced through alio-doping may be stabilized through hydroxylation in the ambient conditions. Preferred surface orientations can also be adjusted due to the change of the surface energy on different facets. We argued the increased hydroxylation level as well as the change of preferred surface exposure are the major cause of degradation of the surface activity of mesoporous CeO_2 upon alio-doping. Our study provides important directions to design better CeO_2 (or possibly other metal oxides) materials for DMMP (or Sarin) decomposition: control of surface hydroxylation and preferred surface exposures. Besides alio-doping, CeO_2 can bear other categories of doping (e.g., isovalent, transition metals). Those types of doping might change the surfaces of mesoporous CeO_2 in a totally different way. Thus, though our alio-doping attempt did not improve the activity of mesoporous CeO_2 towards DMMP dissociation, other types of doping strategies might lead to the enhancement of the activity of CeO_2 and should be explored in the future.

Chapter 6: Interaction of Sarin With Mesoporous TiO_2 in Comparison with Commercial TiO_2 Nanomaterials

The research described within this chapter was published in *ACS Appl. Nano Mater.* 2022, 6670. Tsyshevsky, R.; Mcentee, M.; Durke, E. M.; Karwacki, C.; Rodriguez, E. E. and Kuklja, M. M. were contributing authors on the manuscript. I designed experiments, synthesized and characterized the materials, performed the data analysis and interpretation, and wrote the manuscript draft.

6.1 INTRODUCTION

GB (sarin), a chemical warfare agent (CWA), due to its extreme fatal toxicity and the involvement in a few terrorist and battle attacks, has been becoming an ever-increasing concern for the national, international, civilian, and military safety. Hence, developing reliable and efficient filter materials that can strongly adsorb and quickly decompose sarin attracts growing research interest[6, 12, 13, 1, 14],. Understanding the relationship between the structure of a material and its reactivity is essential for the design of new materials with targeted properties, including the filter materials for protection against chemical attacks. Filter materials used for absorption and destruction of CWAs should satisfy several key requirements, such as a high surface area and high chemical stability[13, 1]. Over many years, carbon materials impregnated with metal oxide particles were used as a filter media in gas masks and protection gear[163]. In this type of composite, carbon materials with high surface areas are responsible for adsorption of CWAs, whereas metal oxide particles react with those agent vapors that are ineffectively adsorbed by the activated carbon. While impregnated carbon materials perform well against a wide range of chemical agents, they possess several shortcomings, e.g., limited capacity for agents that are removed by a chemical reaction and/or weakly adsorbed7.

A great diversity of metal oxides and their abundant surface chemistry suggest an appealing opportunity and vast potential to find suitable filter materials among metal oxides[1, 24, 28]. In the past decades, a wide range of metal oxides have been explored for the application of GB (its simulant DMMP as well) adsorption and decomposition[80, 26, 82, 22, 59, 57, 49, 68, 63, 60, 61, 3]. TiO_2 is one of the most studied metal oxides in this application[80**?** **?** , 56, 23, 37**?** **?** , 76**?** , 47, 41, 167] because of its wide popularity in other applications[164, 165], as well as its high tunability in the atomic and nano scale[166]. Recent impressive advances in nano synthesis and characterization lead to the attempt to probe TiO_2 nanomaterials for GB or DMMP decomposition. Besides the high surface area that can greatly increase adsorption capacity and promote the decomposition activity of GB, TiO_2 nanomaterials can potentially tolerate high concentrations of special surface structures (e.g., hydroxylation, defects), which can lead to a higher reactivity. It is widely believed that the dissociation of GB/DMMP on TiO_2 is through losing -OR group or F group (GB only)[56, 23, 167, 168, 58, 169]. The dissociated products need to bond to TiO_2 surface to form a stable structure. Several theoretical and experimental studies imply the dissociation of GB or DMMP on the dry clean surfaces of the TiO_2 is not a favorable process at least at room temperature[169, 167, 23, 56, 168, 58]. Special sites on the surface structure, like bridge oxygen, adsorbed oxygen, intact or dissociated water, and

hydroxylation, might promote the decomposition by lowering the activation energy barriers of the dissociation reaction, triggering unusual or co-existing decomposition mechanisms, or stabilize the dissociated products
[169, 167, 23, 56].

As most studies related to TiO_2 combating GB were performed with the simulant molecule DMMP (sarin simulant), it is necessary to examine the true performance and reaction mechanisms with the real GB molecule on the TiO_2 materials. This remains an extremely challenging task. In this research, we perform joint experimental and theoretical study of fundamental interactions between GB and three different TiO_2 nanomaterials to reveal details of surface chemistry. Experimentally, we study the adsorption and decomposition of GB on commercial P25, anatase TiO_2 nanoparticles and synthesized mesoporous anatase TiO_2 at room temperature. We found that the as-synthesized mesoporous anatase TiO_2 exhibits the highest activity towards GB decomposition despite it has the same crystalline structure and similar surface area as the anatase TiO_2 nanopowder. Density functional theory (DFT) was employed to explore mechanisms of adsorption and decomposition of GB on a pristine TiO_2 surface and surface containing defects to establish factors that govern the reaction and ensure high reactivity of mesoporous TiO_2. A comparison of experimental data with results of DFT modeling suggests that high reactivity of mesoporous materials is correlated with surface hydroxylation. We find that mesoporous TiO_2 adsorbs more water than P25 and anatase nanoparticles, and the water and OH groups facilitate the P—F bond cleavage of sarin on the surfaces of TiO_2.

This work demonstrates new opportunities for the design and synthesis of new nanomaterials for destruction of CWAs. High reactivity combined with relatively easy and inexpensive synthesis make mesoporous TiO_2 an attractive candidate material for using in gas masks and other protective equipment.

6.2 EXPERIMENTAL PROCEDURES

6.2.1 Preparation and Synthesis of TiO_2 nanomaterials

P25 TiO_2 (21 nm primary particle size, $\geq$99.5% trace metals basis) and pure anatase TiO_2 nanopowder ($<$ 25 nm particle size, 99.7% trace metals basis) were both purchased from Sigma-Aldrich. Mesoporous TiO_2 was synthesized via a reported evaporation-induced self-assembly (EISA) method[170, 171]. This method was adjusted so that the synthesized mesoporous TiO_2 has a surface area which is comparable to the commercially available TiO_2 samples. Typically, 4.0 g of triblock copolymer Pluronic P127 was first added into 60 mL of anhydrous ethanol (EtOH), followed by the addition of 6 g acetic acid and 6 g concentrated hydrochloric acid (HCl 37%). After stirring for 0.5 h at room temperature, 25 mmol ($\approx$ 8 ml) Titanium isopropoxide ($Ti(OCH(CH_3)_2)_4$) was slowly added to the solution dropwise. The above solution was vigorously stirred for approximately 3 h. The resulting sol solution was transferred in an open glass container (diameter 2 inch) and was later placed in 40 °C environment and 60 °C environment each for 24 h, allowing the evaporation of the solvent to form gel. The Mesoporous TiO_2 powder was obtained by calcinating the formed gel at 350 °C for 4h (1°C /min ramping) with enough air provided.

6.2.2 Characterization of titania nanomaterials

Powder XRD patterns were recorded on the Bruker D8 Advance diffractometer, with Cu $K\alpha/K\beta$ radiation. Rietveld refinement was performed using TOPAS 5[140]. The nitrogen adsorption isotherms were measured on a Micromeritics ASAP 2020 Porosimeter Test Station. Surface areas were calculated by applying the Brunauer-Emmett-Teller (BET) equation on adsorption data obtained at P/P0 between 0.05 and 0.35. The pore size distributions were calculated by analyzing the adsorption branch of the N_2 sorption isotherm using the Barret-Joyner-Halenda (BJH) method.

Ti 2p and O 1s X-ray photoelectron spectroscopy (XPS) was collected on a Kratos Axis 165 X-ray photoelectron spectrometer operating in hybrid mode using Al Kα monochromatic X-rays at 280 W. All XPS spectra were calibrated to the C 1s peak at 284.80 eV. All spectra fittings were performed using CasaXPS. Shirley background was used for background subtracting. 30% Gaussion+70% Lorentz is applied as fitted peak shape profile. Thermogravimetric analysis (TGA) was conducted using an SDT Q600 equipped with a TA Discovery MKS104-S0212004 Micron Vision 2 Mass Spectrometer. The samples were heated to 800 °C in air with ramping rate of 10 °C/min and gas flow rate of 10 mL/min.

6.2.3 IR Detection of GB on TiO_2 Nanomaterials under Vacuum

(CAUTION! Experiments performed with ultra-toxic CWAs require extreme care, highly trained operators, and a secure government-regulated facility.) Experimental GB adsorption studies on TiO_2 nanomaterials were performed in a high vacuum chamber with a base pressure at 3×10^{-9} Torr. Detailed description of the vacuum chamber is provided elsewhere[20, 172]. The as-received TiO_2 nanomaterials were pressed into a 0.004" thick W-grid and attached to the sample mount via stainless steel clamps. An IR spectrum of the W-grid without any TiO_2 powder was taken and used as the background. Each IR spectrum contains an average of 256 interferograms at a resolution of 2 cm^{-1}. Subsequently, 10^{-4} Torr of GB vapor was introduced into the vacuum chamber. An IR spectrum was taken and was subtracted from the IR spectrum of TiO_2 before GB exposure. The subtracted spectrum represents a difference spectrum showing the GB adsorption changes on the TiO_2 surface. Positive IR bands represent adsorbed GB vibrations, and negative peaks represent TiO_2 surface sites interacting with GB via adsorption or reactivity. After GB exposure, the vacuum chamber was evacuated for 24 h, and the base pressure returned to 3×10^{-9} Torr. Another IR spectrum was then taken after evacuation to determine what was left on the surface. In another experiment to determine the impact of surface water and OH species on GB adsorption and decomposition on the as-synthesized mesoporous TiO_2, the mesoporous TiO_2 was first heated up to 450 K for 30 min before introducing GB vapor into the vacuum chamber in order to remove H_2O, hydrocarbon impurities, and as many isolated OH sites as possible from the TiO_2 sample. After cooling down to room temperature (300 K), IR detection of GB on mesoporous TiO_2 under vacuum with same procedure was performed.

6.2.4 XPS Characterization on surfaces of TiO_2 Nanomaterials upon GB Exposure

(CAUTION! Experiments performed with ultra-toxic CWAs require extreme care, highly trained operators, and a secure government-regulated facility.) The adsorption and possible decomposition of GB on the TiO_2 surfaces was supported by XPS data recorded following the IR experiments. Sample powders were transferred and packed into small wells of a copper XPS sample plate. The XPS system utilized for these studies was comprised of a dual anode (AlKα and MgKα) X-ray source (DAR 400, Omicron Nanotechnology) and was equipped with a Z translation stage with 5° X-Y tilt for alignment with the sample. Detection of photoelectrons was achieved with an Omicron Sphera hemispherical analyzer with a five-channel detector mounted at a 45° angle relative to the X-ray source. Energy calibration was performed using the C 1s peak observed from the carbon tape used as the mounting substrate at 285.0 eV.

6.2.5 Ambient diffuse reflectance infrared Fourier transform spectroscopy (DRIFTS)

(CAUTION! Experiments performed with ultra-toxic CWAs require extreme care, highly trained operators, and a secure government-regulated facility.) The activity of mesoporous TiO_2 for GB degradation was also characterized in an in situ environmental DRIFTS reaction cell maintained at 25 °C. Caution! Experiments using chemical agents should only be performed by trained personnel using the appropriate safety procedures. Approximately 15–20 mg of the sample was loaded into a 6 mm porous ceramic cup.

The cell was configured as a continuous-flow setup where the inlet vapor stream flows from the bottom of the porous ceramic cup through the packed sample bed before exiting the cell. Helium (Airgas, 99.999% purity) was used as the carrier gas.The carrier gas streams were passed through the inline hydrocarbon and water vapor traps prior to their introduction to the reaction chamber.

The mesoporous TiO_2 was dosed with the agent vapor (GB) for 1 h by diverting the carrier gas flow through a microsaturator cell containing a liquid reservoir of the agent situated in a temperature-controlled water-circulating chamber (Glassblowers.com, Turnersville, NJ) that was maintained at 20 °C. DRIFTS IR spectra were recorded with a Thermo Fisher Scientific 6700 FTIR spectrometer. The background scan was collected by averaging 1024 scans (726.96 s duration) prior to beginning the dosing experiment. During the dose, 128 spectra were averaged over 60 s with a 2 cm^{-1} resolution at a gain of 2 from 4200.27 to 599.76 cm^{-1} and a data spacing of 0.96 cm^{-1}.

6.2.6 Gas Chromatography-Mass Spectrometry

(CAUTION! Experiments performed with ultra-toxic CWAs require extreme care, highly trained operators, and a secure government-regulated facility.) The surface products of mesoporous TiO_2 after DRIFTS experiment were examined via Gas Chromatography-Mass Spectrometry. Following the completion of simulant or agent vapor exposed sample, sample was transferred immediately to a 20 mL scintillation vial. 1.5 mL of acetonitrile was added to chemical-exposed powder within the 20 mL scintillation vial and vortexed for sixty (60) seconds. Entire liquid contents were drawn into a 2 mL Luer-slip plastic syringe (National S7510-3) and pushed entire extract through a (0.45 μm x 13 mm diameter) nylon membrane syringe filter into a clear silanized screw top 2 mL vial (Agilent Technologies Part # 5183-2070). Subsequently, added N,O-Bis(trimethylsilyl)trifluoroacetamide (BSTFA) derivativizing agent into 2 mL vial and placed into a Agilent GC autosampler and flowed by the GC-mass spec measurement.

6.2.7 DFT modeling

Solid state periodic calculations of crystalline TiO_2 samples were performed with DFT using GGA PBE[93] functional and projector augmented-wave (PAW) pseudo-potentials[94], as implemented in the VASP code[95, 96, 97]. In simulating ideal bulk crystals, atomic coordinates and lattice constants were allowed to relax simultaneously without any symmetry constraints. The convergence criterion for electronic steps was set to 10^{-5} eV, and the maximum force acting on any atom was set not to exceed 0.01 eV/Å. Kinetic energy cut-off was set to 520 eV. In simulating an ideal bulk TiO_2 anatase crystal (Figure 6.1b), a 12×12×6 Monkhorst-Pack k-point mesh was used. The calculated lattice parameters of the TiO_2 anatase tetragonal unit cell with I41/amd space group, a= b= 3.81 Å and c= 9.73 Å, agree with the experimental lattice vectors (a=b= 3.78 Å and c= 9.51 Å)[173] within 2 %.

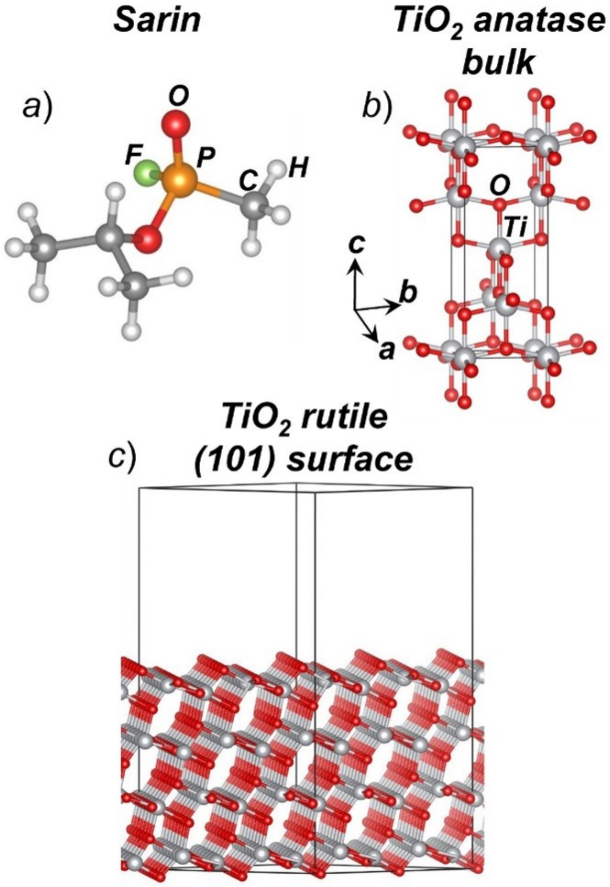

Figure 6.1: The model structure of a) a sarin molecule, b) TiO_2 anatase ideal bulk crystal, and c) TiO_2 anatase (101) supercell surface slab.

Our calculations of adsorption and decomposition were limited to modeling reactions on the pristine (101) surface (Figure 6.1c) and surface containing defects, including an oxygen vacancy (Figure 6.2 a and b), a step (Figure 6.2c), and a hydrated surface (Figure 6.2d). In the TiO_2 anatase (101) surface calculations, the model surface slab contained 288 atoms with the supercell lattice vectors of a = b =15.47 Å, and c =32.98 Å. In modeling the oxygen vacancy, one of the oxygen atoms was removed from the surface (Figure 2 a and b). A model of TiO_2 anatase (101) surface with a step (Figure 6.2c) was adopted from existing literature[174, 175]. The model surface slab representing a step on the TiO_2 anatase (101) surface contained 432 atoms with the supercell lattice vectors of a = 15.69 Å, b = 22.23 Å, and c =36.52 Å. A monolayer of intact water molecules was added to the (101) surface to model GB decomposition on the hydroxylated surface (Figure 6.2d). A vacuum layer of 20 Å placed on top of the TiO_2 (101) surface served to minimize interactions between the supercells in the z-direction and to avoid any significant overlap between wave functions of periodically translated cells. All surface calculations were performed at G-point only. Kinetic energy cut-off was set to 520 eV. The convergence criterion for electronic steps was set to 10^{-5} eV, and the maximum force acting on any atom was set not to exceed 0.03 eV/Å. PBE+D functional, which includes corrections for weak van der Waals interactions[176], was used to calculate adsorption energies. Minimal energy paths in the VASP periodic calculations were obtained with the standard nudged elastic band method[177]. Atomic positions were relaxed using conjugate gradient and quasi-Newtonian methods within a force tolerance of 0.05 Å/eV. The convergence criterion for electronic steps was set to 10^{-5} eV.

6.3 RESULTS AND DISCUSSION

6.3.1 Characterization

The phase composition of three TiO_2 materials was confirmed from XRD. Structural refinements to the XRD patterns are shown in Figure 6.3a-c. Pure anatase TiO_2 nanopowder as well as synthesized mesoporous TiO_2 were confirmed to consist pure anatase phase. P25 TiO_2 shows

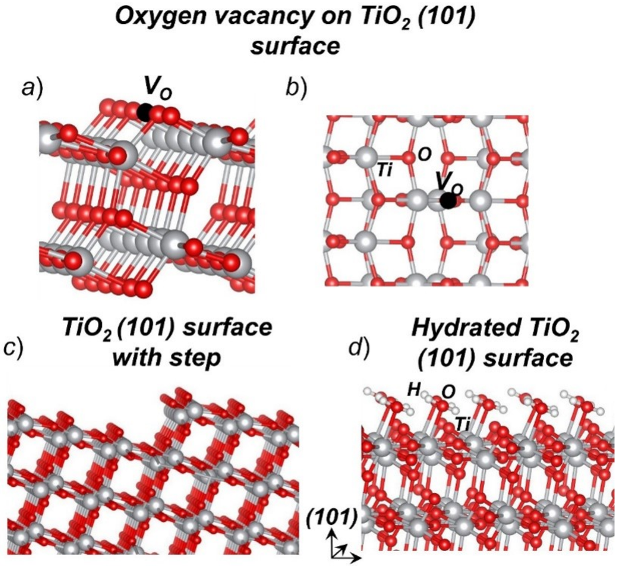

Figure 6.2: The model structure of a) a sarin molecule, b) TiO_2 anatase ideal bulk crystal, and c) TiO_2 anatase (101) supercell surface slab.

a mix phase of 17% rutile and 83% anatase, similar to what was previously reported[178, 179]. The refined crystalline sizes from XRD are listed in Table 6.1. P25 TiO_2 has largest crystallite size (36 nm) while the mesoporous TiO_2 has the smallest crystallite size (13 nm).

Nitrogen adsorption isotherms of three samples are displayed in Figure 6.4 and the calculated surface area the porosity information is also included in Table 6.1. P25 TiO_2 has the lowest surface area and pore volume, while the anatase TiO_2 nanopowder and mesoporous TiO_2 are comparable in terms of both surface area and pore volume. Mesoporous TiO_2 has a very narrow pore size distribution which is centered at 11 nm.

XPS was used to investigate the surface composition of three TiO_2 materials. The full energy scans (Figure 6.3d) show all TiO_2 sample surfaces to be clean and consist of predominantly C, O, and Ti. Ti 2p, O 1s and C 1s XPS spectra are displayed in Figure 6.5, 6.6 and 6.7. For all three samples, the Ti 2p 3/2 spectra are located at 458.7 eV[180], which belong to Ti^{4+}. Ti 2p 3/2 for Ti^{4+} is reported to be located at 457.3 eV[180], while we did not observe any features at

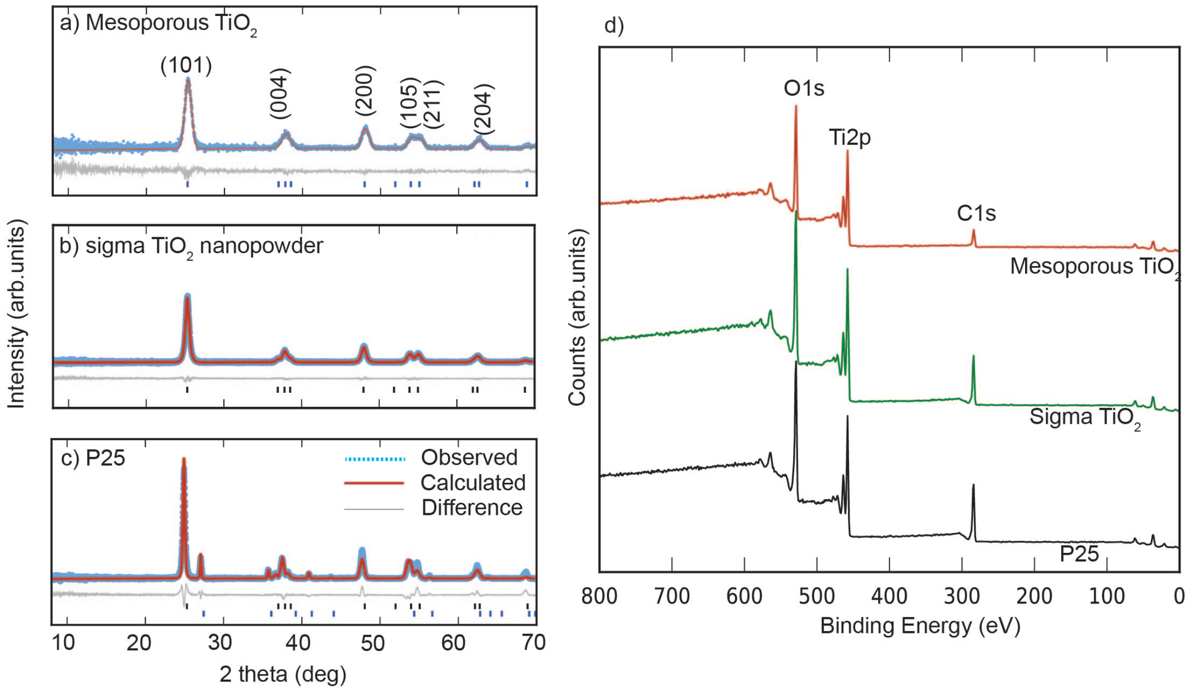

Figure 6.3: The model structure of a) a sarin molecule, b) TiO_2 anatase ideal bulk crystal, and c) TiO_2 anatase (101) supercell surface slab.

this location for all three samples, indicating there is no Ti^{3+} on the surfaces of all the samples, as shown in Figure 6.5. O1s and C 1s spectra are also nearly identical for all 3 samples, as shown in Figure 6.6 and Figure 6.7. TGA are used to characterize the amount of water and OH group in the materials and the results are plotted in Figure 6.8. The mesoporous TiO_2 displays greatest mass loss (7%) during heating, implying it contains largest amount of water and OH groups among samples, which is possibly due to the water condensation in its narrow mesopores. Following mesoporous TiO_2 (4.5%) is the anatase nanopowder with P25 TiO_2 displaying the least mass loss (3%).

Sample	Phase	Crystalline size(nm)	Surface Area(m^2/g)	Pore volume (cm^3/g)	Mean Pore size (nm)
P25 TiO_2	17% rutile, 83% anatase	36.0	50.71	0.11	/
Sigma TiO_2	anatase	21.4	92.25	0.26	/
Meso TiO_2	anatase	13.3	116.19	0.28	11

Table 6.1: Summary of surface and pore characteristics of TiO_2 nanomaterials.

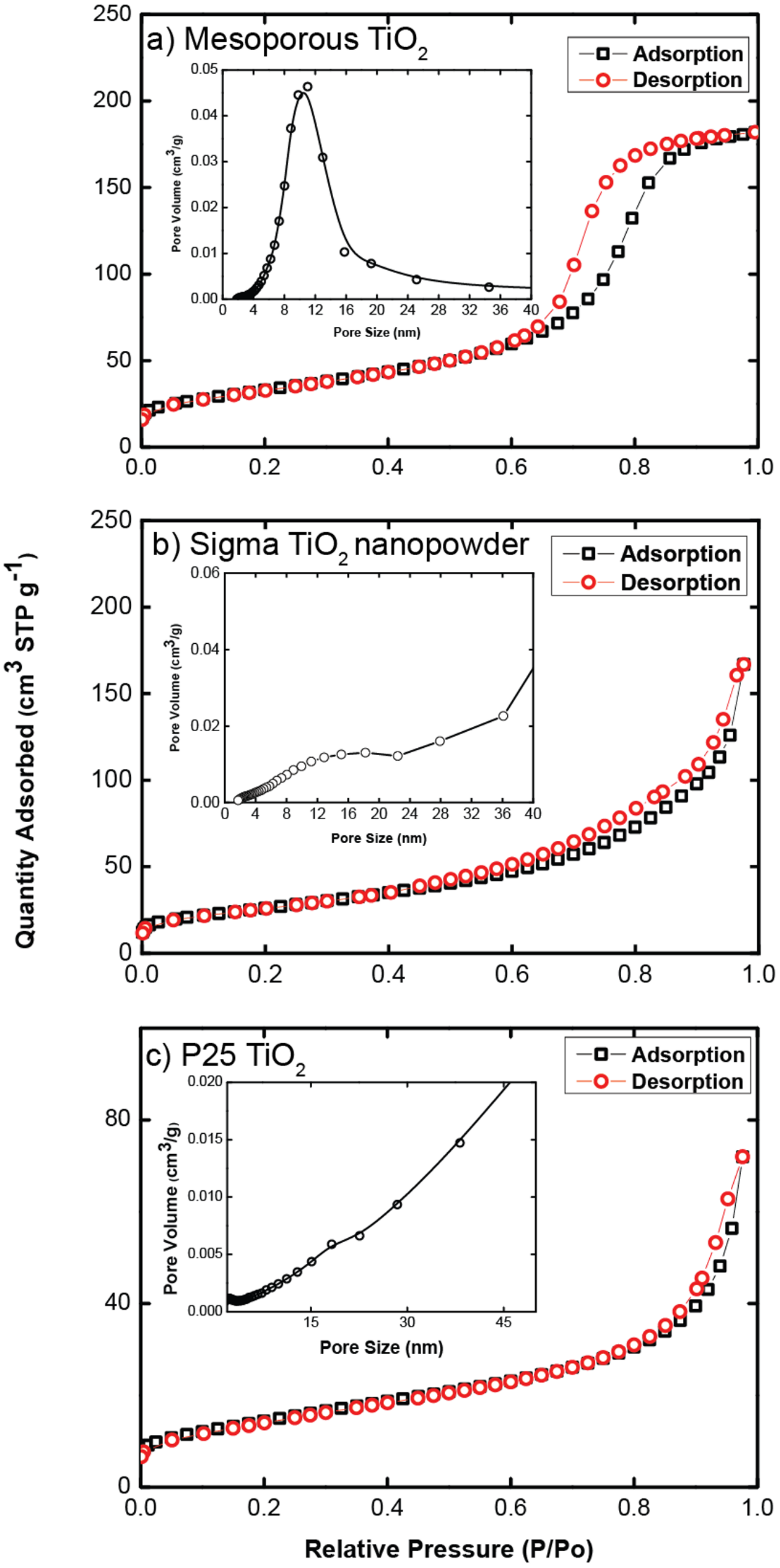

Figure 6.4: Nitrogen Adsorption isotherms and pore size distributions of TiO_2 materials.

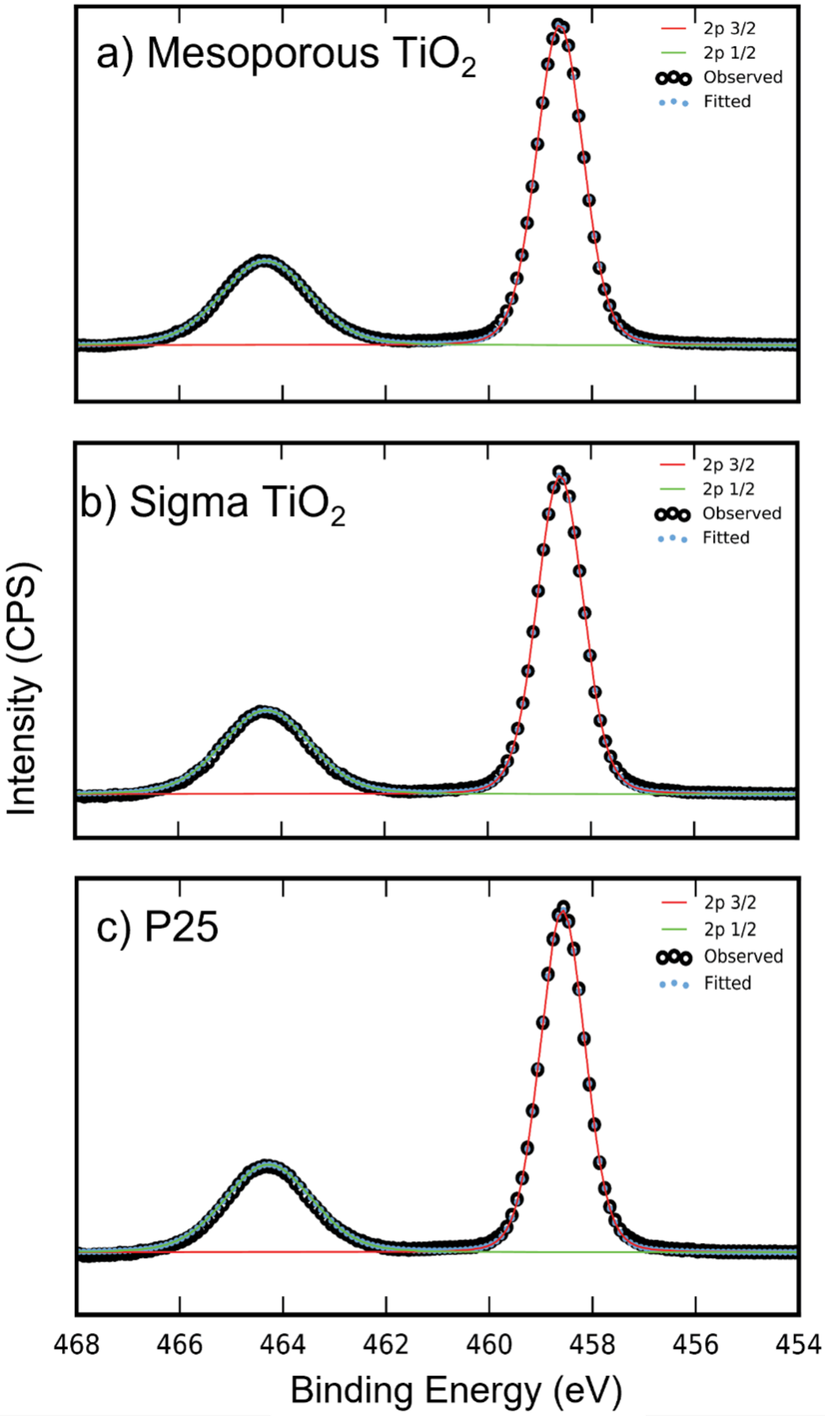

Figure 6.5: Ti 2p XPS spectra of TiO_2 materials

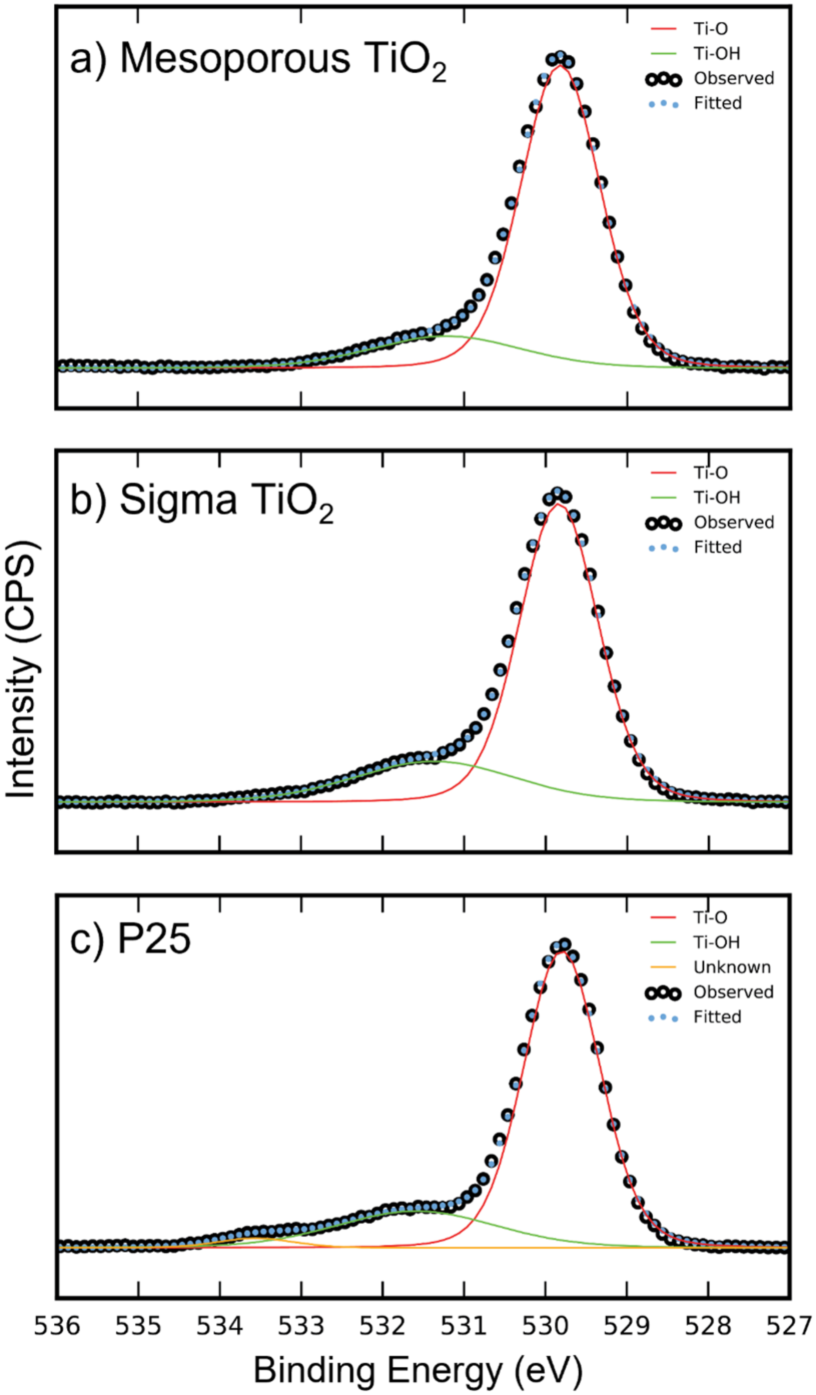

Figure 6.6: O 1s XPS spectra of TiO_2 materials.

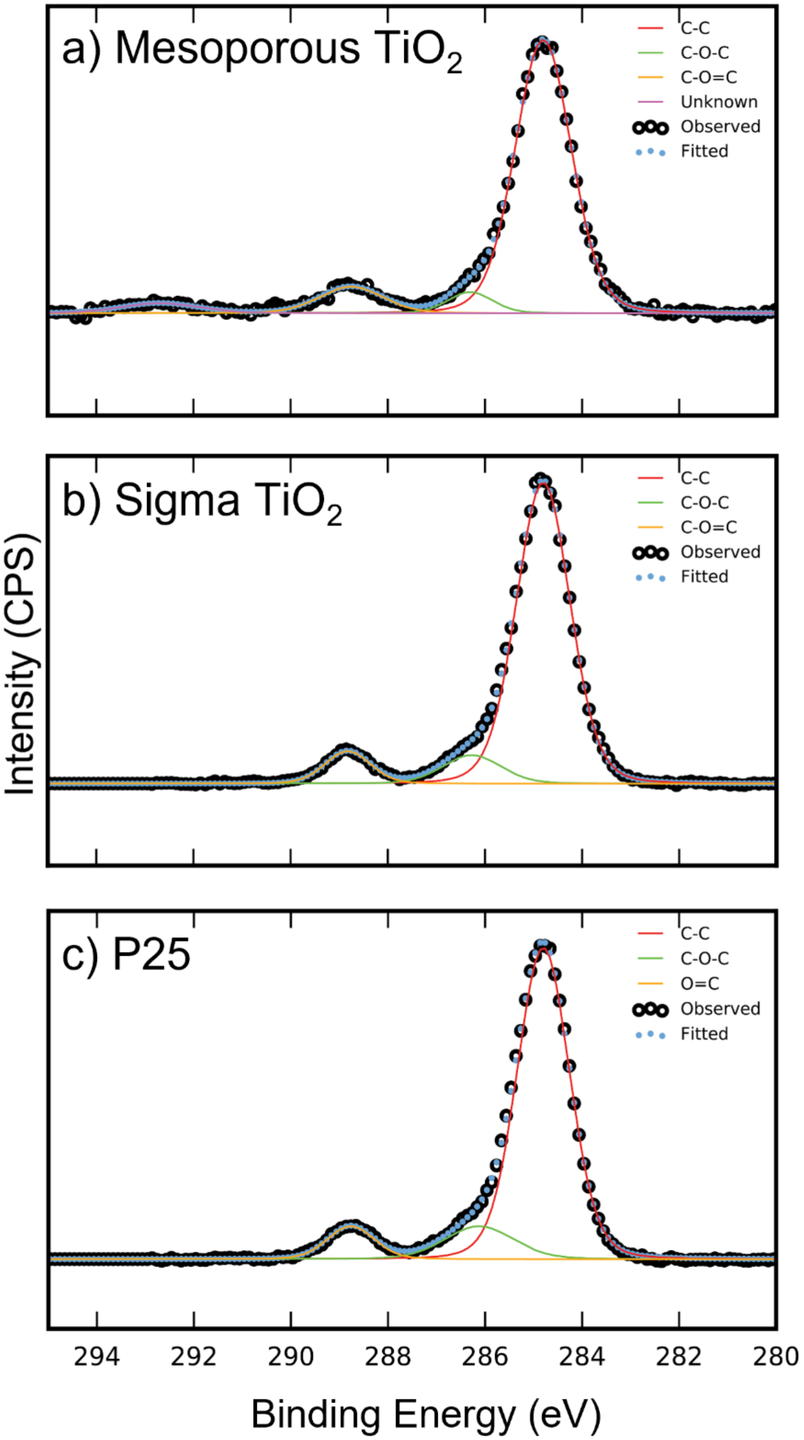

Figure 6.7: C 1s XPS spectra of TiO_2 materials.

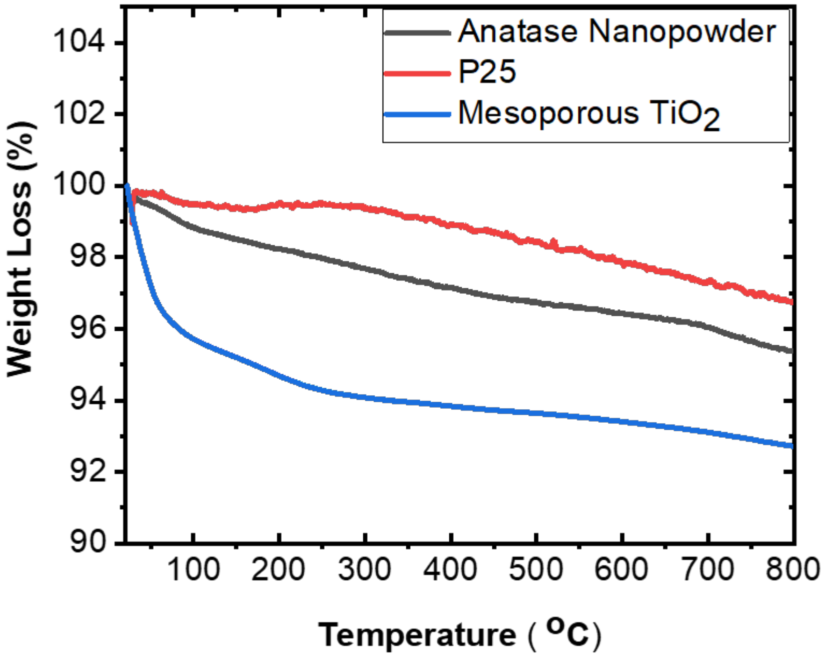

Figure 6.8: TGA curves for TiO_2 samples under air.

6.3.2 GB reactivity on titania nanomaterials

In order to compare the activity of three types of TiO_2 nanomaterials toward decomposition of live agent, sarin, we utilized IR detection of GB on as-received mesoporous anatase TiO_2, anatase TiO_2 from Sigma and P25 TiO_2 under vacuum. Figure 6.9 shows the difference IR spectrum of the surfaces of TiO_2 nanomaterials upon GB exposure. IR spectrum of gaseous GB was given (Figure 6.9a) for comparison. Black curves represent the spectrum after GB dosing with GB is still in the environment. Red curves stand for the spectrum after GB dosing with GB evacuated from the environment for 24h. A detailed IR assignment is shown in Table 6.2. For all three TiO_2 nanomaterials, all of the IR vibrational modes of GB vapor are present on the GB-exposed TiO_2 surface with multiple IR modes shifted, which is commonly seen as result of GB adsorption or condensation[181]. Two new IR bands observed at 1145 and 1090 cm^{-1} (indicated by the blue arrows), which possibly corresponds to v$_a$(O-P-O) and v$_s$(O-P-O) respectively, are the indication of GB degradation[110, 111, 109, 58, 23, 80]. After the GB evacuation, bands from intact GB remain, implying a very strong GB adsorption on the surfaces. We also observe the growth of v$_a$(O-P-O) and v$_s$(O-P-O) bands from the continuous dissociation of GB.

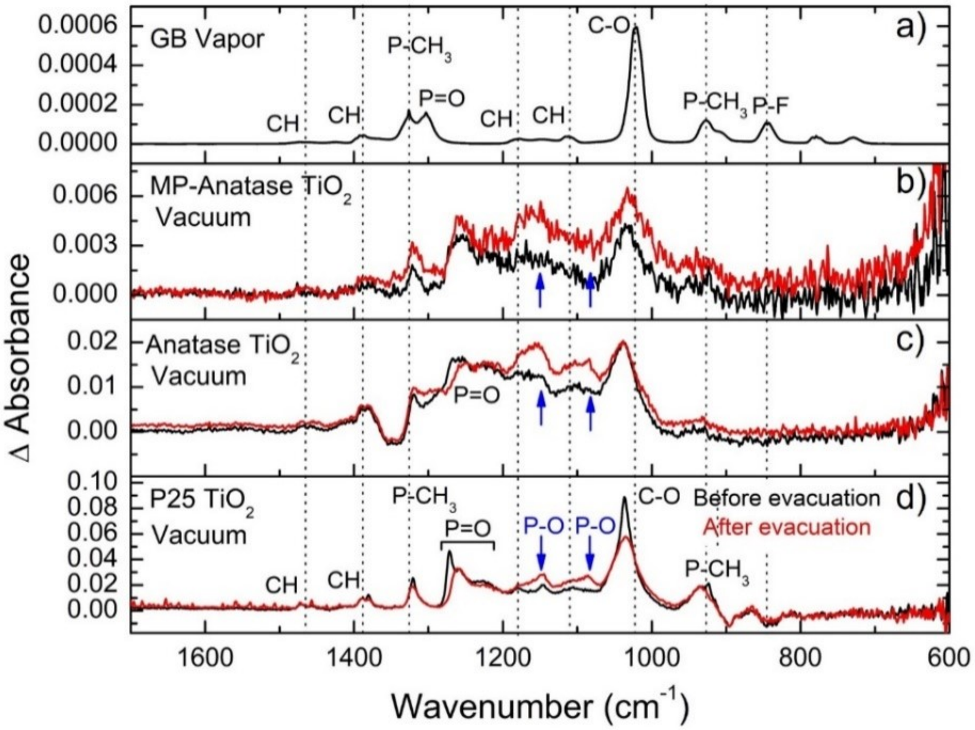

Figure 6.9: IR detection of surfaces of TiO$_2$ materials after sarin (GB) dosing. Scans were taken before and after GB evacuation from the chamber when dosing is finished.

Though GB decomposition is observed on all TiO$_2$ nanomaterials, the decomposition activities vary considerably among the three. We use the intensity ratio between O-P-O bands (1145 and 1090 cm^{-1}) and P=O bands (1271–1200 cm^{-1}) to compare the surface reactivities for GB degradation. For GB dosing on P25 TiO$_2$, as is shown on Figure 6.9d, intensity of O-P-O bands are minimal compared with P=O bands even after long time GB evacuation. Thus, we conclude the activity of P25 TiO$_2$ towards GB dissociation is rather weak. While for the anatase

TiO_2 nanopowder (Figure 6.9c) and mesoporous TiO_2 (Figure 6.9b), intensity of O-P-O bands is comparable to the intensity of the P=O bands, implying a much stronger activity towards GB dissociation. The intensity ratios of O-P-O bands and P=O bands are very close for the nanopowder and mesoporous samples. Our IR instrument, however, is not sensitive enough to conclude which one represents higher activity between anatase nanopowder and mesoporous TiO_2 as the relative intensities of O-P-O bands are in the similar level for both samples.

GB vapor phase (cm^{-1})	GB adsorbed on TiO_2 (cm^{-1})	IR band assignments
1468	1472	$\sigma_{as}(CH_3C)$
1380	1380	$\sigma_s(CH_3C)$
1328	1320	$\sigma(P–CH_3)$
1303	1270	v(P=O)
1183/1111	1183/1111	$\rho(CH_3C)$
	1145–1135	$v_{as}(O–P–O)$
	1095–1075	$v_s(O–P–O)$
1020	1038	v(C–O–(P))
928	928	$\sigma(P–CH_3)$
845		v(P–F)

Table 6.2: IR Frequencies (cm^{-1}) of GB in the Vapor Phase, GB Adsorbed on TiO_2.

To further investigate the reaction activity of the anatase nanopowder and mesoporous TiO_2 samples towards GB dissociation. we conducted XPS characterization on their surfaces before and after GB exposure. F 1s, C 1s and P 2p spectrum are collected to track the change of the surfaces upon GB exposure, which are presented in Figure 6.10. The P 2p spectrum for the nanopowder and mesoporous samples after GB exposure (Figure 6.10a) effectively resemble each other. Only a component centered at around 133 eV appears in P 2p spectrum, commonly observed for GB, or DMMP (a simulant for GB) adsorption[110, 182, 183, 184, 81, 3, 59]. Figure 6b displays F 1s spectrum. Two characteristic components appear in F 1s region for both samples after GB dosing. The peak appearing at higher binding energy (687.4 eV) is known to come from organic fluorine[185, 186, 187]. We attribute this high-binding-energy component as the signal of intact GB molecules. The peak at a lower binding energy (683.7 eV) typically belongs to ionic F$^-$ in metal fluoride species (M-F)[188, 189, 190]. Clearly, the observation of formation of metal fluoride species (M-F) after GB exposure is a strong indication of GB dissociation. The formation of metal fluoride species also implies that the dissociation of GB on TiO_2 surfaces involves the breakage of P-F bonds and subsequent formation of Ti-F bonds on the surfaces, as is illustrated on Figure 6.10d. Several theoretical works have proposed the dissociation of GB on TiO_2 surface proceeds through either P-F bond breaking or P-OR bond breaking, with P-F bonding favored based on energetic considerations[58, 56, 47]. Our results constitute the first experimental evidence supporting a mechanism of P-F bonding breaking. Metal fluoride species are observed on both samples; however, it is obvious the ratio of organic fluorine and metal fluoride species are different between the two, which indicates varied reactivities. For the nanopowder, the fitted ratio of organic fluorine and metal fluoride is 51:49 (Figure 6.10b bottom), and for the mesoporous TiO_2, the ratio is 66:33 (Figure 6.10b middle). Our observation indicates that the surfaces of mesoporous TiO_2 are more efficient in promoting the P-F bond breaking in GB molecules. The C 1s spectra (Figure 6.10c) shows that a carbon species such as hydrocarbons naturally exist on the original materials (Figure 6.10c top). Nevertheless the interpretation of the C 1s spectra is more difficult and ambiguous. The highest binding region at 284.8 eV corresponds to naturally existing hydrocarbons. No obvious change is observed in this region between the nanopowder and mesoporous TiO_2. The rise in the region between 280-290 eV corresponds to the adsorbed GB[110**?**], observed on both TiO_2 materials. Interestingly, two components between 292-295 eV arise only for the mesoporous anatase TiO_2. Due to the very limited XPS study on GB, we are not able to identify what carbon species these two components belong to. Studies show such a high binding energy of C 1s usually belongs to carbon that is directly bonded to the fluorine (C-F)[191]. We speculate that the rise of this region comes from the product of the reaction between dissociated F group and carbon species on the surface (e.g., propanol): HF + HOR→ RF+ H_2O. It is certain that they are a result of the GB degradation. The fact that these two components are lacking on the surfaces of the nanopowder also indicates surfaces of mesoporous TiO_2 are much more reactive toward GB decomposition. We now employ DFT modeling to further study the possible mechanisms of GB decomposition on TiO_2 anatase.

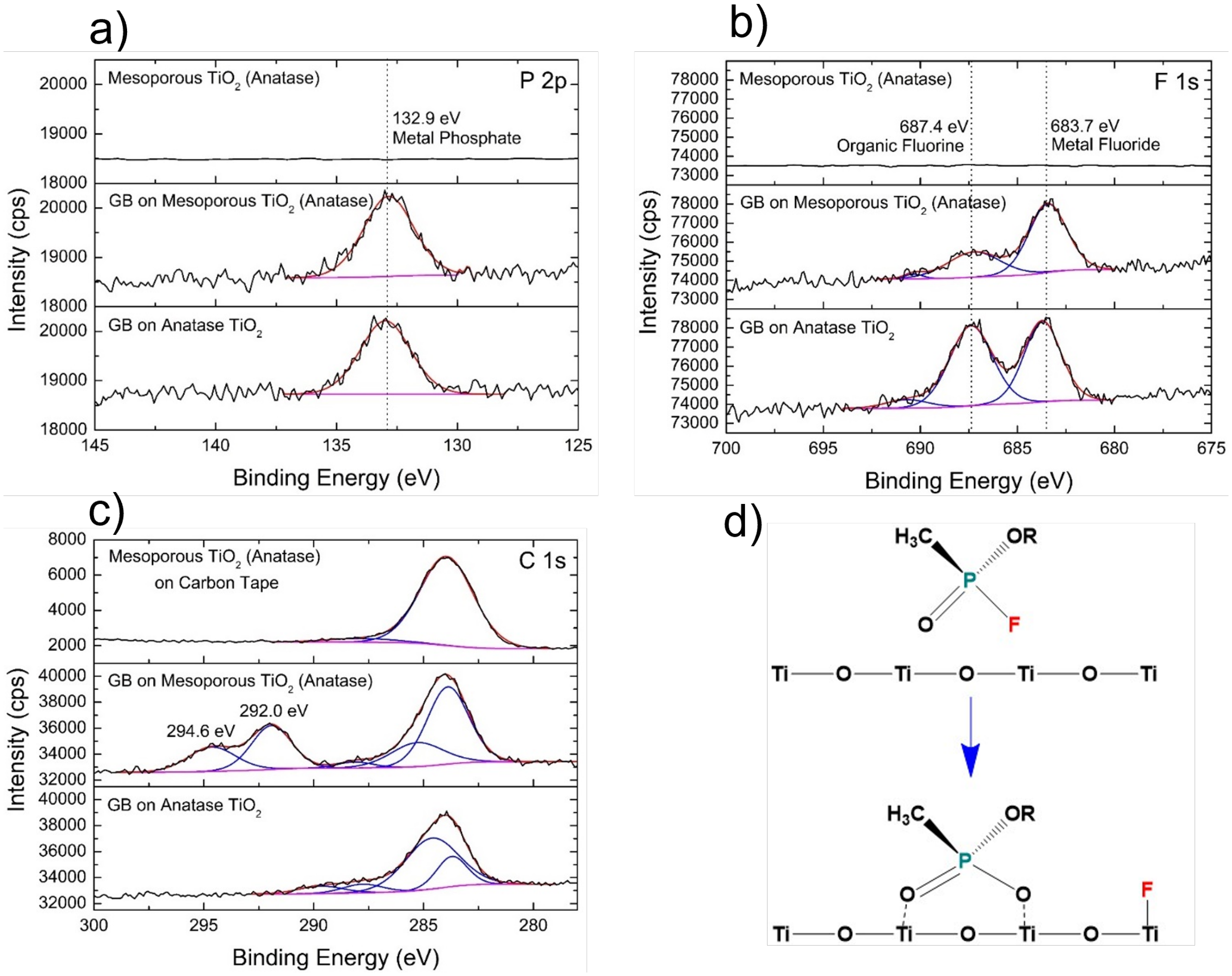

Figure 6.10: XPS a) P 2p. b) F 1s. c) C 1s spectra of mesoporous TiO_2 and anatase nanopowder after GB dosing and d) proposed mechanism for the dissociation of GB on the surface of TiO_2.

6.3.3 DFT modeling of GB on TiO_2 anatase (101) surface.

We conclude that the as-synthesized mesoporous TiO_2 is the most reactive sample towards GB dissociation as F 1s XPS clearly shows that surfaces of mesoporous TiO_2 are more effective on breaking P-F bonds. The lower activity of P25 TiO_2 might be attributed to a much smaller surface area and the existence of rutile phases. Contrastingly, the anatase nanopowder and as-synthesized mesoporous anatase are nearly identical in their crystalline phase composition and have comparable surface areas. Therefore, a reasonable question is what are the factors that lead to such a considerable difference between activities of GB dissociation between the two forms of TiO_2? We speculate that defects on the TiO_2 surfaces might contribute to the varied activities towards sarin decomposition. We thus turn to DFT calculations and further explore mechanisms of adsorption and decomposition of GB on a pristine TiO_2 surface and surface with defects to reveal factors that governs high reactivity of mesoporous TiO_2. We chose the (101) anatase surface in our modelling as (101) it is known to be the most stable surface of anatase TiO_2. Besides the pristine (101) surface, we also consider three common defects on the (101) surfaces: oxygen vacancies, surface steps, and hydroxylation.

We first explore the adsorption of GB on different TiO_2 (101) surfaces. Adsorption of GB on the pristine TiO_2 (101) surface is rather a straightforward process. GB interacts with one of the under-coordinated surface Ti atoms through its phosphoryl oxygen (Figure 6.11a). A relatively high adsorption energy of -129.1 kJ mol^{-1} indicates strong binding of the molecule to the pristine surface. These findings are consistent with results of a recent theoretical study[41], which also shows sarin adsorption on TiO_2 (101) anatase surface through its phosphoryl oxygen. According to Le et al energy of sarin adsorption on TiO_2 (101) anatase surface is -76.1 kJ mol^{-1}. However, we note that this estimate was obtained using standard PBE functional without including corrections for van der Waals interactions. This explains why the adsorption energy reported by Le and co-authors is noticeably lower than our estimate. Considerably higher adsorption is observed on the TiO_2 (101) surface containing an oxygen vacancy, as the GB molecule is strongly bonded to the reduced Ti atom (Figure 6.11b). The calculated energy of GB adsorption on the surface with the oxygen vacancy is -212.3 kJ mol^{-1}. The energy of GB adsorption on the surface with a step is -146.3 kJ mol^{-1} (Figure 6.11c), which is 17.2 kJ mol^{-1} higher than that on the pristine surface. When adsorbed on the hydrated TiO_2 (101) surface covered with a monolayer of water molecules, GB interacts with hydrogens of water molecules through its phosphoryl oxygen atom (Figure 6.11d). The calculated energy of GB adsorption on a hydrated TiO_2 (101) surface is -97.8 kJ mol^{-1}. This indicates strong adsorption on the GB molecule on the surface covered with a monolayer of water, even though the adsorption energy on the hydrated surface is noticeably lower than the energies of GB adsorption on both the pristine TiO_2 (101) surface and surface with structural defects.

Mechanisms of GB decomposition on pristine TiO_2 anatase (101) surface have been reported in our recent paper38. Our study revealed that a dry TiO_2 anatase surface is relatively inactive toward GB dissociation at room temperature. Breaking of the P-F bond on a dry TiO_2 surface requires a relatively high activation energy of 142.8 kJ mol^{-1}[58]. In addition, the P-F bond breaking is an endothermic process with the reaction energy of 60.7 kJ mol^{-1} (Figure 6.12a). The high activation energy and endothermicity of the reaction are due to the structure of the TiO_2 (101) surface. A relatively large distance between under-coordinated Ti atoms 3.8 Å prevents interactions of the GB molecule with multiple surface metal atoms through its different functional groups. The structure of the TiO_2 (101) surface also affects the activation energy and

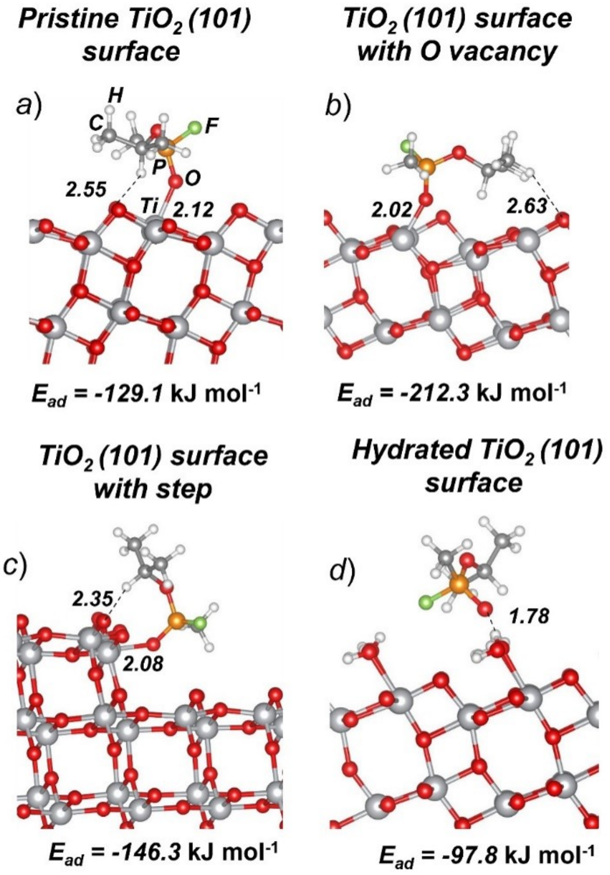

Figure 6.11: Adsorption of GB molecule on a) pristine TiO_2 anatase (101) surface; b) TiO_2 (101) surface with oxygen vacancy; c) TiO_2 (101) surface with a step, and d) hydrated TiO_2 (101) surface.

reaction energy of propene elimination from GB. Usually an exothermic reaction, the elimination of propene on the TiO_2 anatase (101) surface turned out to be an endothermic process with the reaction energy of 18.6 kJ mol^{-1} (Figure 6.12a).

The observation that GB decomposes on the TiO_2 nanomaterials at room temperature clearly deviates from the results of our modeling of GB interaction with a dry pristine TiO_2 surface. Thus, we further studied an effect of structural defects and water on GB adsorption and decomposition on the TiO_2 (101) surface.

The presence of the surface oxygen vacancy leads to additionally reduced (under-coordinated) Ti atoms. This facilitates GB decomposition via a propene elimination reaction (Figure 6.12b), as the GB molecule interacts with under-coordinated Ti atoms through its phosphoryl oxygen atom and that of the alkoxy (-OC_3H_7) group. According to our calculations, an elimination of propene from GB on the surface vacancy requires 81.6 kJ mol^{-1} and proceeds with the energy release of 25 kJ mol^{-1}. Unlike the propene elimination, the oxygen vacancy formation precludes decomposition via P-F bond breaking, as the surface lacks oxygen atoms essential for this reaction. Tesvara et al. computationally studied the DMMP (a GB simulant molecule) and GB interactions with oxygen vacancies on rutile TiO_2 (110) surfaces[47]. They also found that oxygen vacancies on the surface promote the cleavage of the alkoxy (-OR) group with minimal impact on the P-F bond breaking, which is consistent with our conclusion.

The TiO_2 (101) surface with a step represents a favorable structure for GB decomposition via the P-F bond cleavage (path C1-C2, Figure 6.12c), i.e., providing access to surface oxygen and under-coordinated Ti atom. At the beginning of the reaction, GB coordinates to the surface oxygen atom through the phosphorus atom. Once the bond between the surface oxygen and the phosphorus atom of the molecule is formed, the P-F bond becomes broken, and the fluorine atom forms a bond with the Ti atom. The calculated activation barrier of the P-F bond scission on the surface step is 106.2 kJ mol^{-1}, which is 36.6 kJ mol-1 lower than that on the pristine surface (path A1-A2, Figure 6.12a). Furthermore, the P-F bond breaking on the surface step is an exothermic process with the calculated reaction energy of -45.5 kJ mol^{-1}. Unlike the P-F bond cleavage, the surface step has little effect on the propene elimination. Thee calculated activation barrier of propene elimination on TiO_2 (101) surface step is only 0.9 kJ mol^{-1} lower than the same reaction on the pristine surface (141.9 vs 142.8 kJ mol^{-1}, Figure 6.12a and c). The propene elimination on the surface step remains endothermic although the calculated reaction energy is small (2.8 kJ mol^{-1}, Figure 6.12c) and 15.8 kJ mol^{-1} lower than the reaction energy on the pristine surface

(Figure 6.12a).

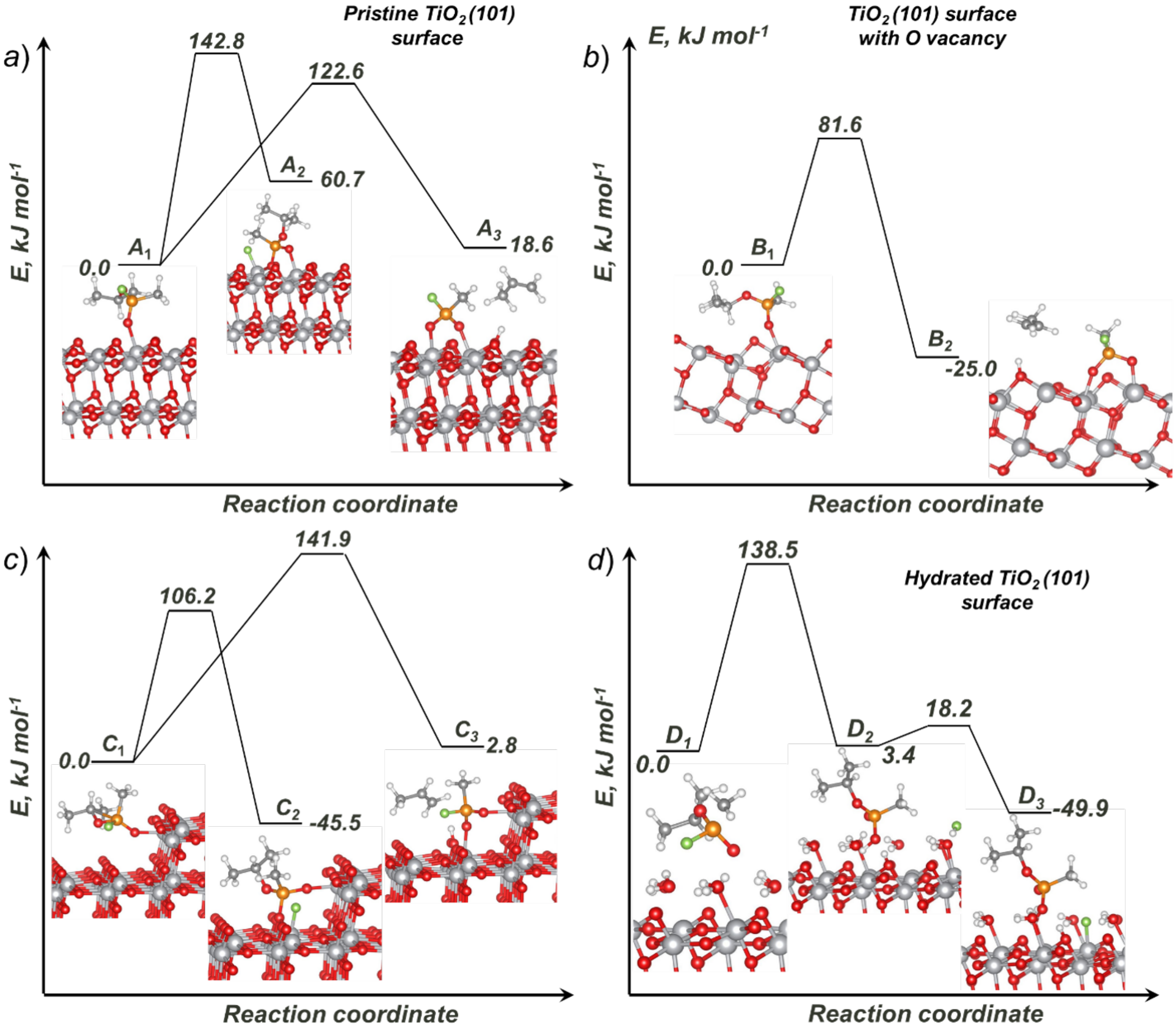

Figure 6.12: Potential energy diagram depicting GB decomposition on a) pristine TiO_2 anatase (101) surface; b) surface with oxygen vacancy; c) surface with a step; and d) hydrated TiO_2 (101) surface.

Our modeling shows that the monolayer of water molecules precludes decomposition of GB via the propene elimination pathway as the molecule has no access to under-coordinated Ti atoms on the surface. On the other hand, our calculations revealed that GB decomposes via the P-F bond cleavage on the hydrated TiO_2 (101) surface (Figure 6.12d). The reaction proceeds in two stages. The first stage (D1-D2) is associated with the P-F bond cleavage and the HF molecule formation. GB coordinates to the oxygen atom of one of the water molecules via its phosphorus atom. This stage requires 138.5 kJ mol^{-1} and has the reaction energy of 3.4 kJ mol^{-1}. The second stage of the reaction (D2-D3) involves dissociation of the HF molecule. In the final configuration, fluorine is bonded to the Ti atom and remains on the surface. The activation barrier and reaction energy of the second stage are 14.8 and -53.3 kJ mol^{-1}, respectively. Thus, the overall activation barrier and reaction energy of a D1-D2-D3 mechanism are 138.5 and -49.9 kJ mol^{-1}, respectively.

Summing up, our DFT modeling shows that only the presence of defects (a surface step and a monolayer of water) on the TiO_2 anatase (101) surface can facilitate decomposition of GB via the P-F bond cleavage. While reactions on the pristine surface are endothermic and require relatively high activation energies, introducing an oxygen vacancy facilitates the propene elimination, but precludes decomposition via the P-F bond cleavage.

6.3.4 IR detection on surface hydration effects on GB reactivity on mesoporous TiO_2

Our DFT model implies that common defects (oxygen vacancies, surface stepped structure and hydroxylation) can all promote the GB decomposition compared with pristine dry surface. However, surfaces with oxygen vacancies mainly facilitate the cleavage of $-OC_3H_7$ group while stepped structures and hydroxylation instead benefit the P-F bond breaking. Our XPS experiment indicates more P-F bonds breaking on the mesoporous TiO_2. In addition, the Ti 2p XPS spectra (Figure S2) shows there is no significant difference of the oxygen vacancy levels among three TiO_2 materials (formation of oxygen vacancies will lead to the reduction of Ti^{4+} to Ti^{3+}, which should be evident from XPS). Both pieces of evidence suggest that the oxygen vacancies might not be cause for the enhanced activity of mesoporous TiO_2. For the stepped surface, it is possible the mesoporous TiO_2 can have higher concentration of stepped structures on the surfaces because mesopore might lead to more curved surfaces. However experimentally, we currently do not have the capability to measure the concentration of stepped structures within the mesopores.

DFT modeling also reveals that surface hydroxylation can promote the P-F bond breaking through a new reaction pathway, which is exothermic and requires a lower activation barrier. This finding and conclusion are supported by another theoretical study of sarin on TiO_2[56]. Similarly, both experimental and theoretical studies of DMMP (sarin simulant) suggest that a favored decomposition pathway on TiO_2 is due to the involvement of surface hydroxylation[56, 23, 169, 32]. We also note the most significant difference between the two TiO_2 materials is that the surface hydration level (OH group or water on the surface) of mesoporous TiO_2 is higher than in the nanopowder, as indicated by TGA (Figure 3). The DFT modeling and TGA characterization seem to imply that hydroxylation plays a significant role in enhancing the reactivity of mesoporous TiO_2 towards the GB dissociation.

To further validate the computational results and our reasoning, we performed GB dosing experiment on the as received and "dried" mesoporous TiO_2. The "dried" mesoporous TiO_2 was prepared by first heating up to 450 K for 30 min before introducing GB vapor into the vacuum chamber to remove H_2O and as many isolated OH sites as possible from the surfaces. After the heat treatment and cooling, the level of surface H_2O and OH groups greatly decreased, as indicated by the IR characterization on the preheated and as received mesoporous TiO_2, shown in Figure 6.13b. The IR characterization of GB dosing is presented on Figure 6.13a. Here again, we use the intensity ratio between O-P-O bands (1145 and 1090 cm^{-1}) and P=O bands (1271–1200 cm^{-1}) to qualitatively compare the surface reactivities for GB degradation. The relative intensity of O-P-O bands compared with P=O vibration bands on the preheated mesoporous TiO_2 is significantly lower than in the untreated TiO_2, implying a decreased reactivity after removing surface H_2O and OH groups. This result further strengthens our argument that high reactivity of mesoporous TiO_2 comes from high level of hydroxylation on the surfaces.

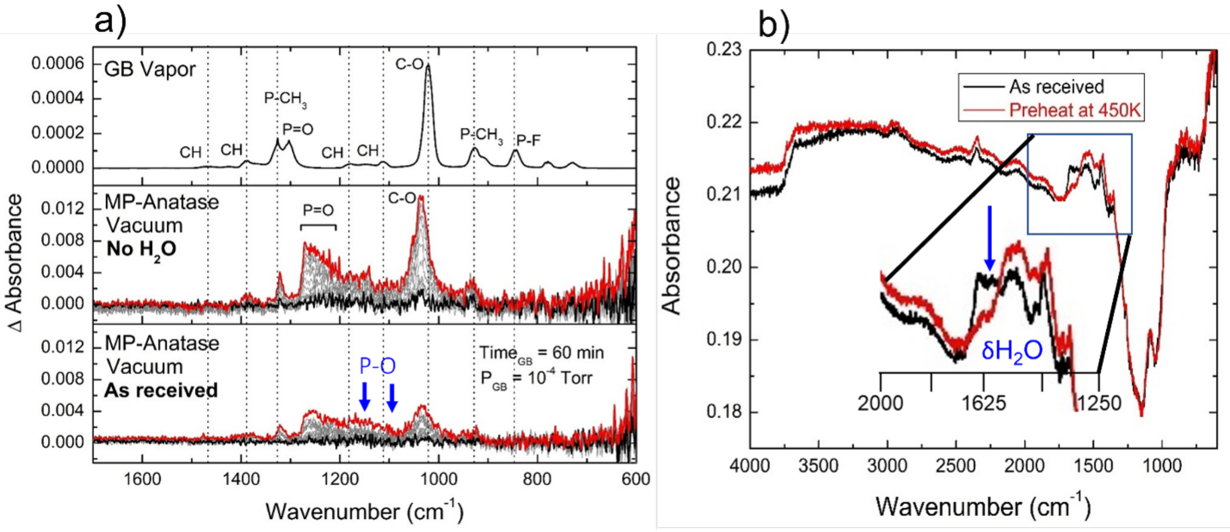

Figure 6.13: a) IR characterization of as dried mesoporous TiO_2 and as received mesoporous TiO_2 after GB exposure. b) IR characterization of OH region of as dried mesoporous TiO_2 and as received mesoporous TiO_2.

6.3.5 GB reactivity on mesoporous TiO_2 at ambient conditions

Based on spectroscopic studies under vacuum, we conclude that mesoporous TiO_2 is highly active for GB decomposition. While in the practical case, a potential material to combat GB must also function in the ambient conditions. Thus, ambient diffuse reflectance infrared Fourier transform spectroscopy (DRIFTS) measurements were conducted on the mesoporous TiO_2 under the GB exposure to examine its performance to decompose GB under ambient conditions. Figure 6.14a shows the difference DRIFTS spectra of the surface of mesoporous TiO_2 under flow of GB vapor for 60 min. The IR bands appearing here resemble what we have observed in the vacuum IR

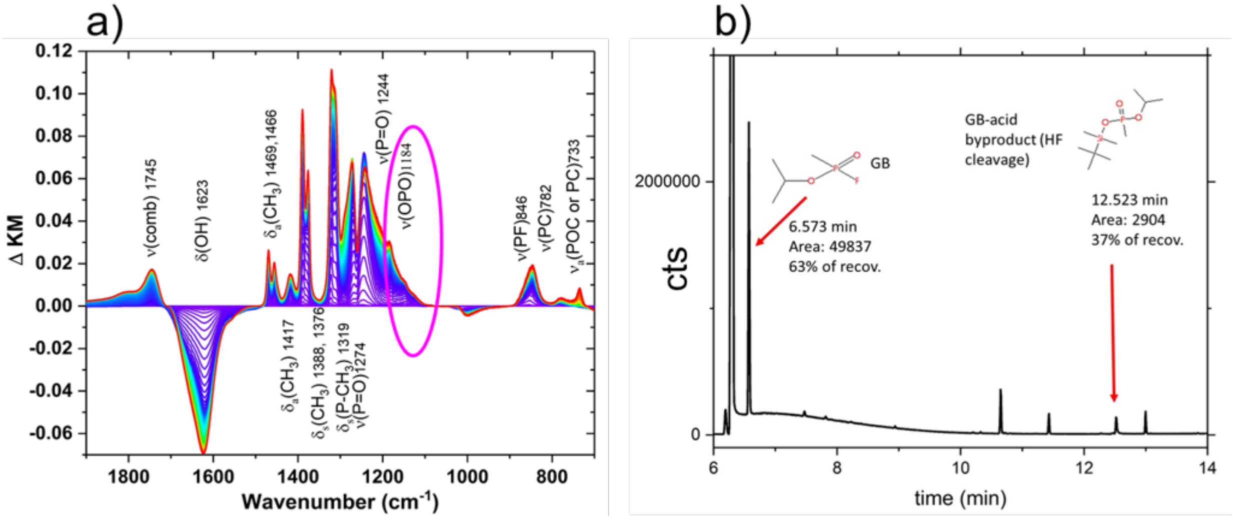

Figure 6.14: a) DRIFTS measurement and b) Gas Chromatography-Mass Spectrometry of mesoporous TiO_2upon GB dosing under ambient conditions.

experiment (Figure 5) and can be assigned based on Table 6.2. Under the constant GB flow, most of GB molecules are readily absorbed onto the mesoporous TiO_2, as indicated by the gradually growing bands of $\sigma_{as}(CH_3C)$ at 1472 cm^{-1} , $\sigma_s(CH_3C)$ at 1380 cm^{-1} , σ(P–CH_3) at 1320 cm^{-1}, v(P=O) at 1270 cm^{-1} and v(P–F) at 845 cm^{-1}. The v(O-P-O) bands at 1100-1200 cm^{-1} are the indication of GB decompositions. The v(O-P-O) bands increase very quickly at early stage of GB dosing, implying effective GB dissociation. However, v(O-P-O) bands then plateaus when the other bands belonging to intact GB still grows, suggesting the active surface of mesoporous TiO_2 is saturated and the physisorption instead of decomposition of GB dominates. It is also worth noting, we observed a significant gradual decrease of σ(OH) bands at 1630cm^{-1} upon GB dosing. The decrease of σ(OH) bands implies the surface OH and H_2O was consumed by either involving in GB dissociation reaction or being replaced by adsorbed GB molecules.

The surface product on the mesoporous TiO_2 after GB dosing for 1h was extracted by N,O-Bis(trimethylsilyl)trifluoroacetamide (BSTFA). The extracted liquid was examined with Gas

Chromatography -Mass Spectrometry (GC-Mass Spec). The result is shown on Figure 6.14b. Except the signal from intact GB, the GB dissociation product after P-F bond breading was also observed (in the form of IMPA binded with BSTFA), also suggesting a P-F cleavage mechanism for GB dissociation on mesoporous TiO_2. Overall, GC-Mass Spec shows around 63% intact GB is physiosorbed and 37% GB is decomposed.

6.4 CONCLUSIONS

In exploring sarin decomposition on titania nanomaterials, we performed extensive surface characterization on three different TiO_2 samples under GB exposure to evaluate their potentials as filter materials for combating GB. In our vacuum IR and XPS studies, we found that mesoporous TiO_2 displays strong activity towards GB degradation at room temperature. For the first time, we provided experimental evidence for GB dissociation on TiO_2 surfaces through the P-F bond cleavage. Combining experimental observations with computational modeling, we argue that a high level of surface H_2 O and OH groups facilitates the dissociation of GB on the mesoporous TiO_2 by providing new pathways for P-F bond breaking with low energy activation barriers. Finally, our study suggests the high reactivity combined with relatively easy and inexpensive synthesis make mesoporous TiO_2 an attractive candidate material for using in gas masks and other protective equipment.

Chapter 7: Overall conclusions & future work

7.1 Conclusion

Throughout the work presented in this thesis, we made attempt to make correlations between the structure of metal oxides and their activity towards Sarin/DMMP adsorption and decomposition. Based on simple solid-state chemistry and molecular chemistry, simple models were come up to predict adsorption behaviors and dissociation behaviors on the metal oxides. For the detailed experiments and DFT calculations, we focus on two systems - mesoporous CeO_2 and mesoporous TiO_2, to examine our proposed native and qualitative model.

When it comes to the adsorption interaction between the Sarin/DMMP and metal oxides, we consider the interaction between electronic band and molecular orbitals. Our qualitative model suggests the energy difference between the conduction band of metal oxides and HOMO of the molecule can dictate the which attractive force (covalent or dipole-dipole) dominate the interactions. We then went further to predict the influence of the hydroxylation based on the change of the interaction force. Out qualitative prediction on CeO_2 and TiO_2 seems to match well with the experimental and theoretical observations.

The non-electronic decomposition of Sarin/DMMP on metal oxides tends to form similar decomposition products on the surfaces. The atom distance on the metal oxides should determine the activation energy barrier for the dissociation and the stability of the decomposition. A favored atomic distance should match the molecular geometry to achieve high reactivity. For the case of TiO_2 and CeO_2, their atomic distances match differently with the molecular geometry of Sarin/DMMP, thus should pose different activities towards Sarin/DMMP decomposition and different response to the hydroxylation, which our experiment and DFT modelling also suggest.

Though the qualitative model we came up with to predict the interaction between Sarin/DMMP and metal oxides are native and oversimplified, it turns out to be effective on matching the experiment and computation results. While such a problem is an interest of application, the fundamental principle of molecular chemistry and solid-state chemistry can still help in understanding the problem and facilitating the searching of candidate materials.

7.2 Future Work

Though efforts are made to build intuitive model to qualitatively understand and predict the interactions between the metal oxides and DMMP/Sarin, and we see success that the model matches with some experimental and computational results. The reality is the prediction is rather rough. For example, we made claim that the adsorption strength should correlate to the energy match between conduction band of the metal oxides and HOMO of DMMP/Sarin. The relative energy level of the conduction band can be roughly estimated and compared based on the periodicity and electronegativity of the metal elements, and we would expect the similar trend for the adsorption strength. However, our model failed to make such correlations both computationally and experimentally. The reason for the failure lies on that different metal oxide materials can have very different surface structures and surface orientations. The real-space determines the physical interaction between molecules and metal oxides. The surface structure can show critical impact on how close the surfaces and molecules can be and their interaction strength. The decomposition activity of the metal oxides can also be greatly impacted by the surface structures. Thus, using binary metal oxides to verify our model is not a good choice. Another metal oxide system with better control on the surface structure, metal elements, bond distance should be used as a model system to gain better understanding of the interaction and examine our model. Perovskite oxides seems to be a perfect candidate system. The perovskite ABO_3 is highly tunable. Their energy band and atomic distance can be easily tuned and controlled through A site or B site substitution. In addition, their crystal structure frame works are very similar to each other, thus their surface structure should not deviate much from each other. Though the perovskite oxides might not be a good candidate for the real filter materials due to the difficulty to make the perovskite high-surface-area, but their controllable bands, atomic distance and surface structure can make them a excellent to gain better understanding on the interaction and help us perfect the intuitive model.

Going back to the practical. Any materials that can be used for the filter materials to combat nerve agent should be able to keep their surface activity (adsorption and decomposition) as it is not realistic to have freshly made filter materials in the masks or protective equipment. While long-term activity study on all kinds of candidate materials is lacking. The atmospheric CO_2 can play a major role in deactivating the surfaces of the metal oxides, as long period interaction between metal oxides and CO_2 will lead to the formation of carbonates. CO_2 as an interference gas is studied on some of the materials. In those experiments, CO_2 and Sarin/DMMP are co dosed on to materials. It turns out CO_2 interact with most of solids less strongly than sarin/DMMP as CO_2 has much lower vapor pressure, thus CO_2 does not really change the interaction between DMMP/sarin and filter materials. However, once the carbonates forms, activation energy barrier to dissociate carbonates into CO_2 and metal oxides are high. in such a case, DMMP/Sarin will primarily interact with metal carbonates rather than metal oxides. Such situation should also be considered when evaluating the potential of the materials. Two focuses in the future studies. First, the tendency of formation of carbonates of the materials should be systematically explored on all the candidate materials. How soon the carbonates can form from the freshly made materials under the ambient environment should be documented. Second, the interaction behavior between and DMMP/Sarin and some carbonates should be systematically studied like metal oxides to fully evaluate their influences on the surface activities.

Appendix A: Instrument setup

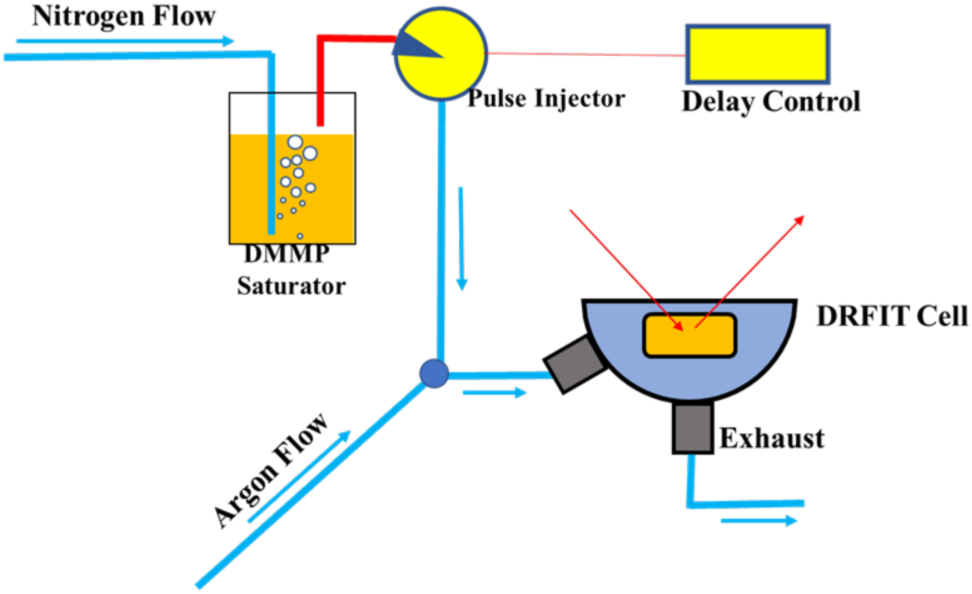

Figure A.1: DFRIFTS flow line setup for DMMP dosing (used For experiments in Chapter 4 and Chapter 5).

Appendix B: Characterizations of doped mesoporous CeO2 and their activities towards DMMP dissociation

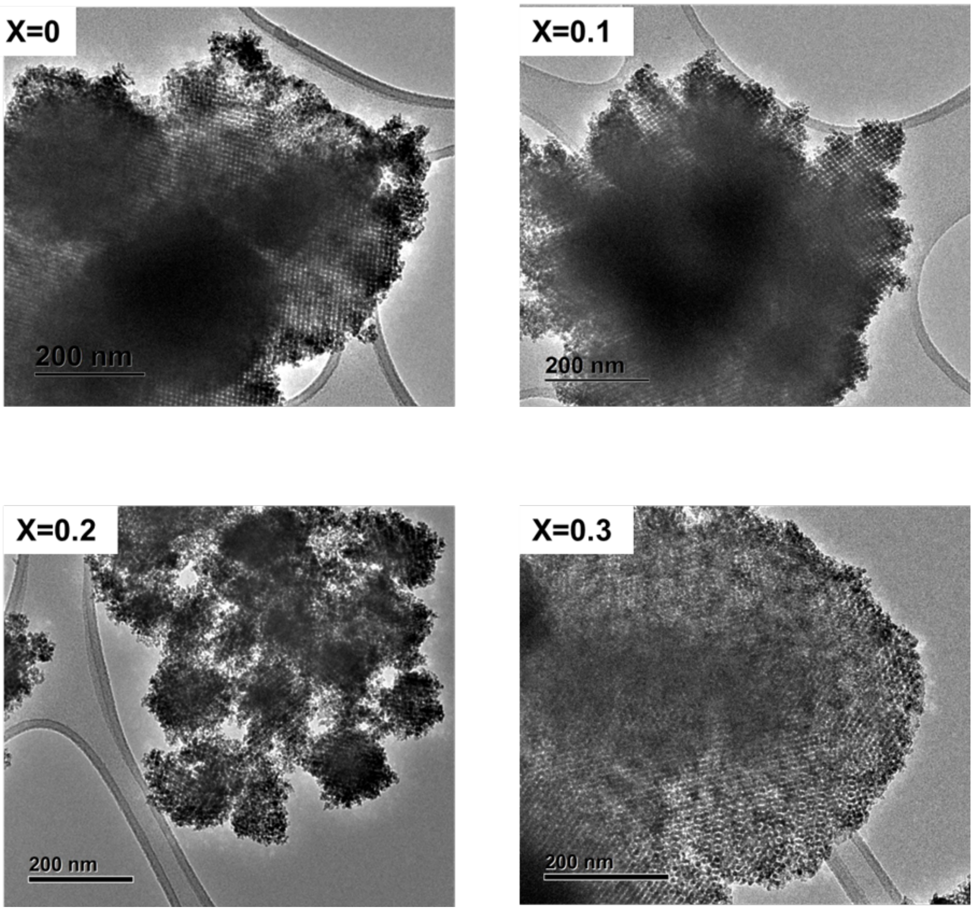

Figure B.1: TEM Images of Mesoporous $Ce_{1-x}Y_xO_{2-\delta}$(x=0, 0.1, 0.2, 0.3)

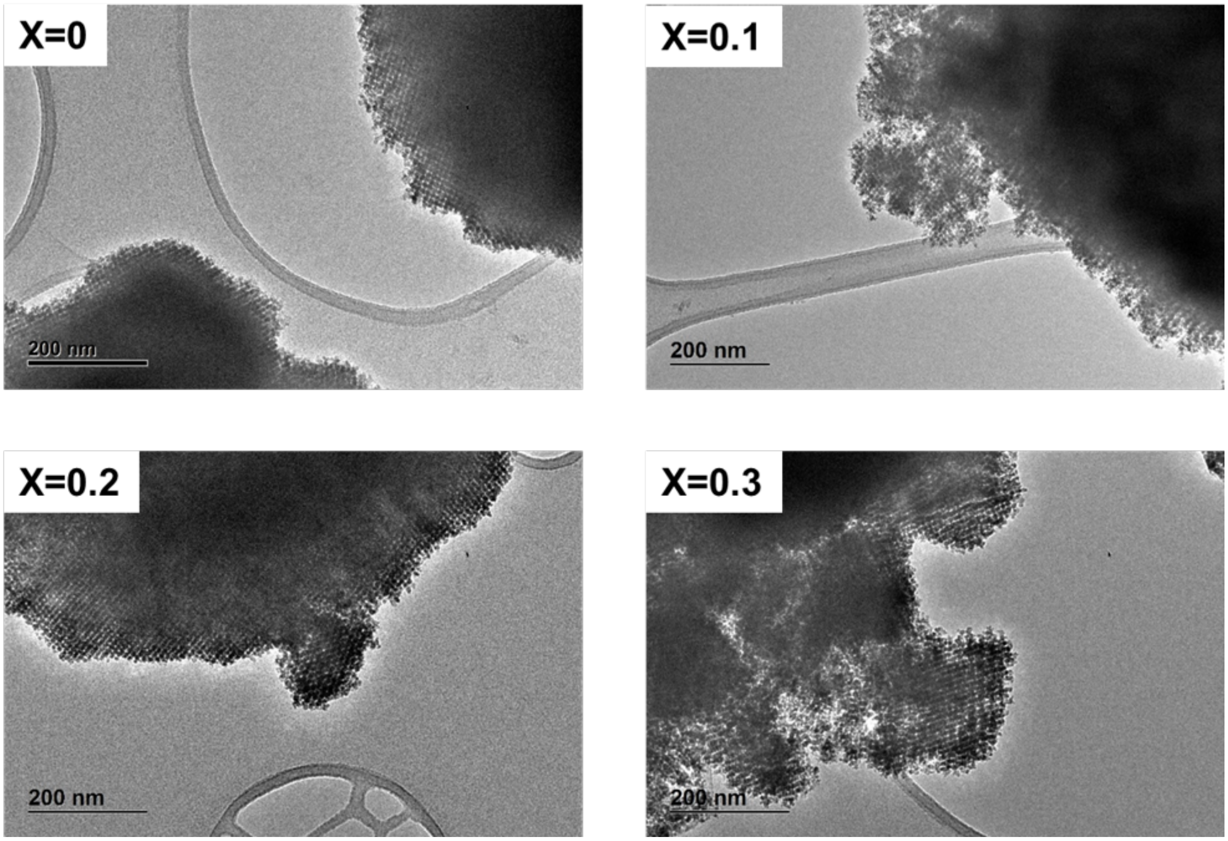

Figure B.2: TEM Images of Mesoporous $Ce_{1-x}Gd_xO_{2-\delta}$ (x=0, 0.1, 0.2, 0.3).

Sample	Surface Area(m^2/g)	Mean Pore Size(nm)
Mesoporous CeO_2	130.4	2.9
$Ce_{1-x}Gd_xO_{2-\delta}$ (x= 0.1)	133.8	3.6
$Ce_{1-x}Gd_xO_{2-\delta}$ (x= 0.2)	128.6	3.6
$Ce_{1-x}Gd_xO_{2-\delta}$ (x= 0.3)	134.7	3.1
$Ce_{1-x}Y_xO_{2-\delta}$ (x= 0.1)	111.4	3.1
$Ce_{1-x}Y_xO_{2-\delta}$ (x= 0.2)	108.6	2.9
$Ce_{1-x}Y_xO_{2-\delta}$ (x= 0.3)	157.8	2.9
$Ce_{1-x}La_xO_{2-\delta}$ (x= 0.1)	126.4	3.6
$Ce_{1-x}La_xO_{2-\delta}$ (x= 0.2)	139.8	3.4
$Ce_{1-x}La_xO_{2-\delta}$ (x= 0.3)	134.7	4.1

Table B.1: Surface Area and Pore size information of pure as well as Y^{3+}, Gd^{3+} and La^{3+} doped mesoporous CeO_2

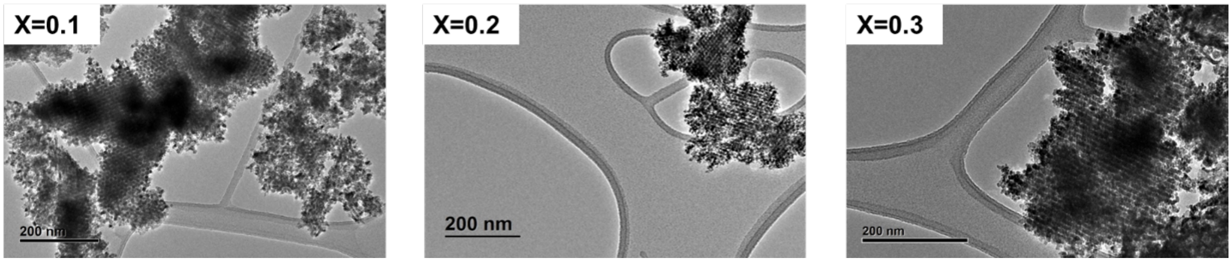

Figure B.3: TEM Images of Mesoporous $Ce_{1-x}La_xO_{2-\delta}$ (x= 0.1, 0.2, 0.3).

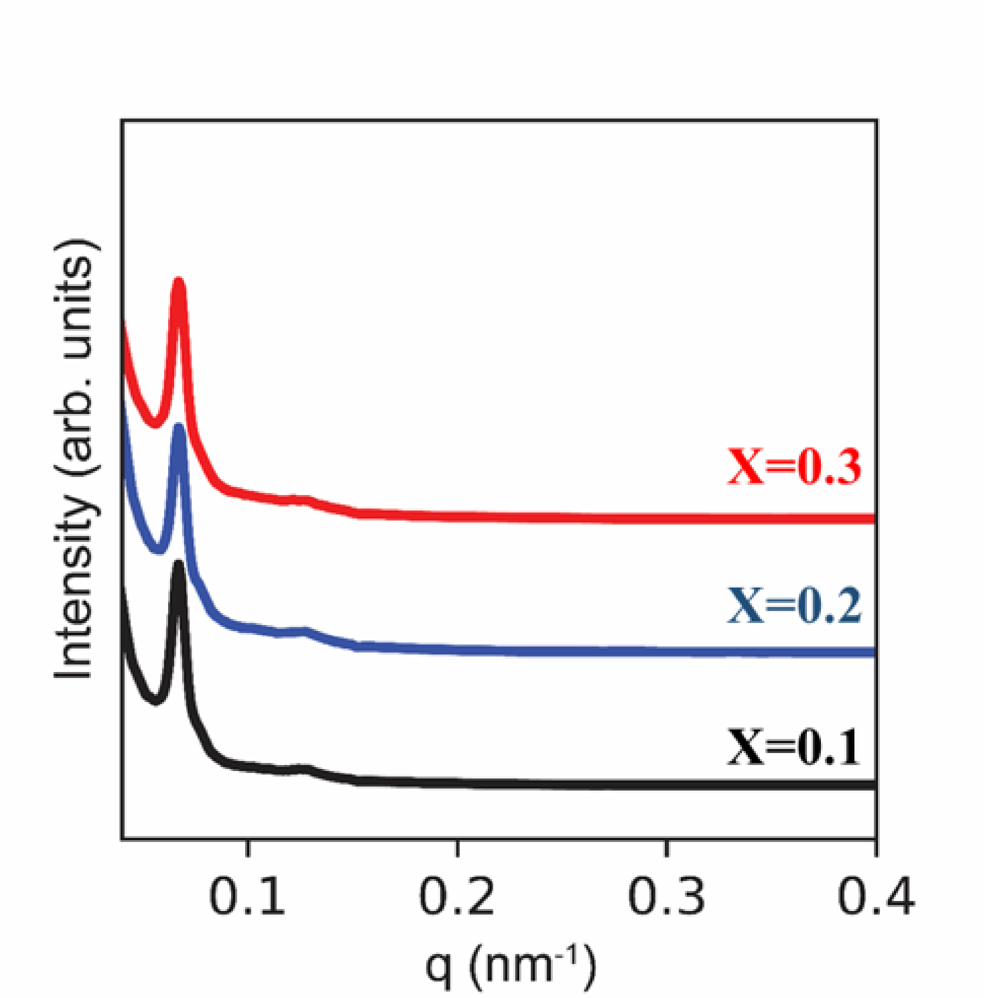

Figure B.4: Small Angle Scattering X-Ray (SAXS) Characterization of Mesoporous $Ce_{1-x}Gd_xO_{2-\delta}$ (x= 0.1, 0.2, 0.3)

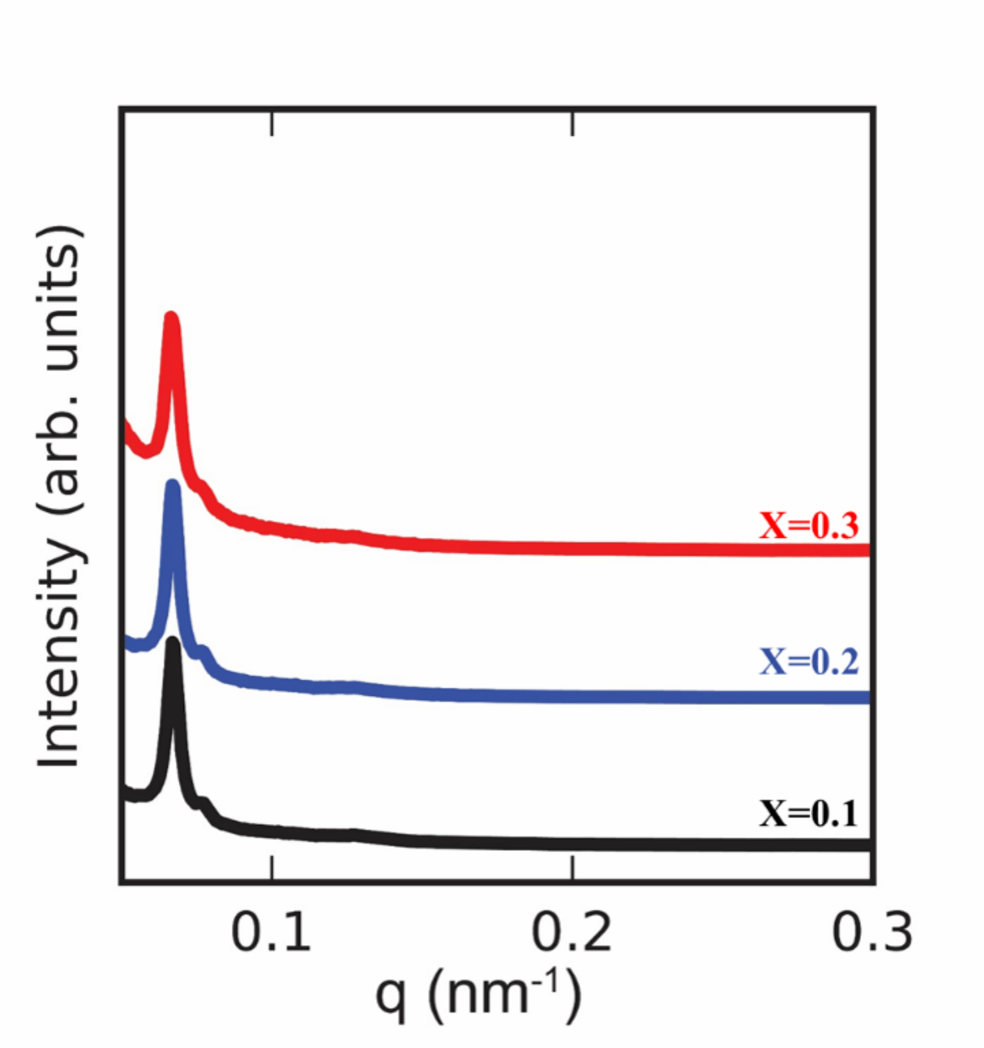

Figure B.5: Small Angle Scattering X-Ray (SAXS) Characterization of Mesoporous $Ce_{1-x}La_xO_{2-\delta}$ (x=0.1, 0.2, 0.3)

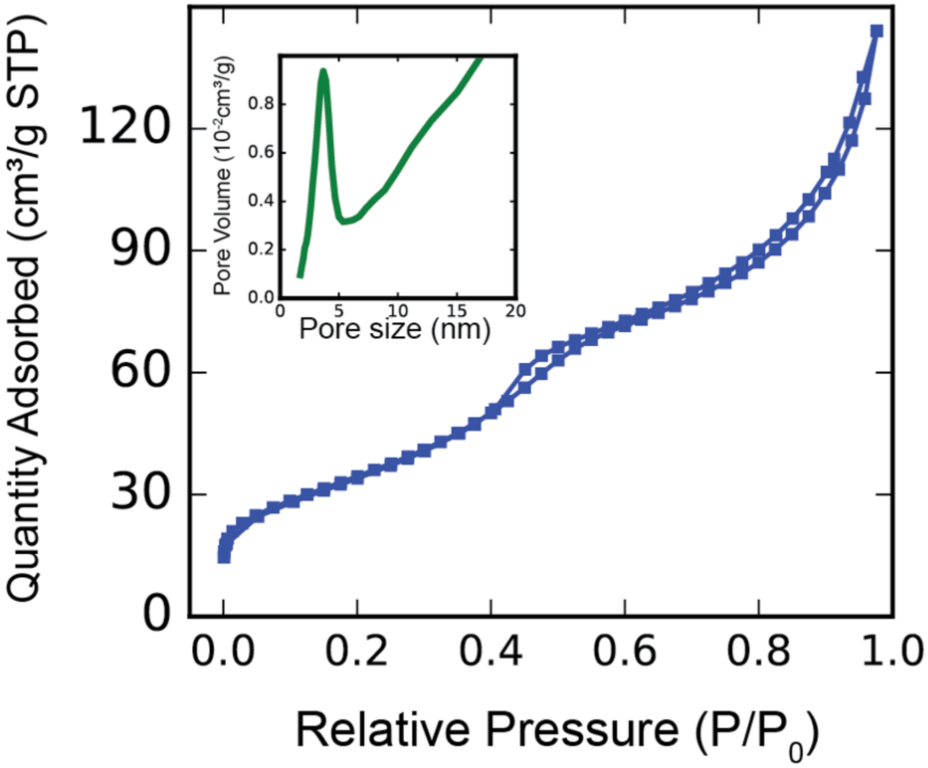

Figure B.6: Nitrogen Adsorption/Desorption of Mesoporous CeO_2

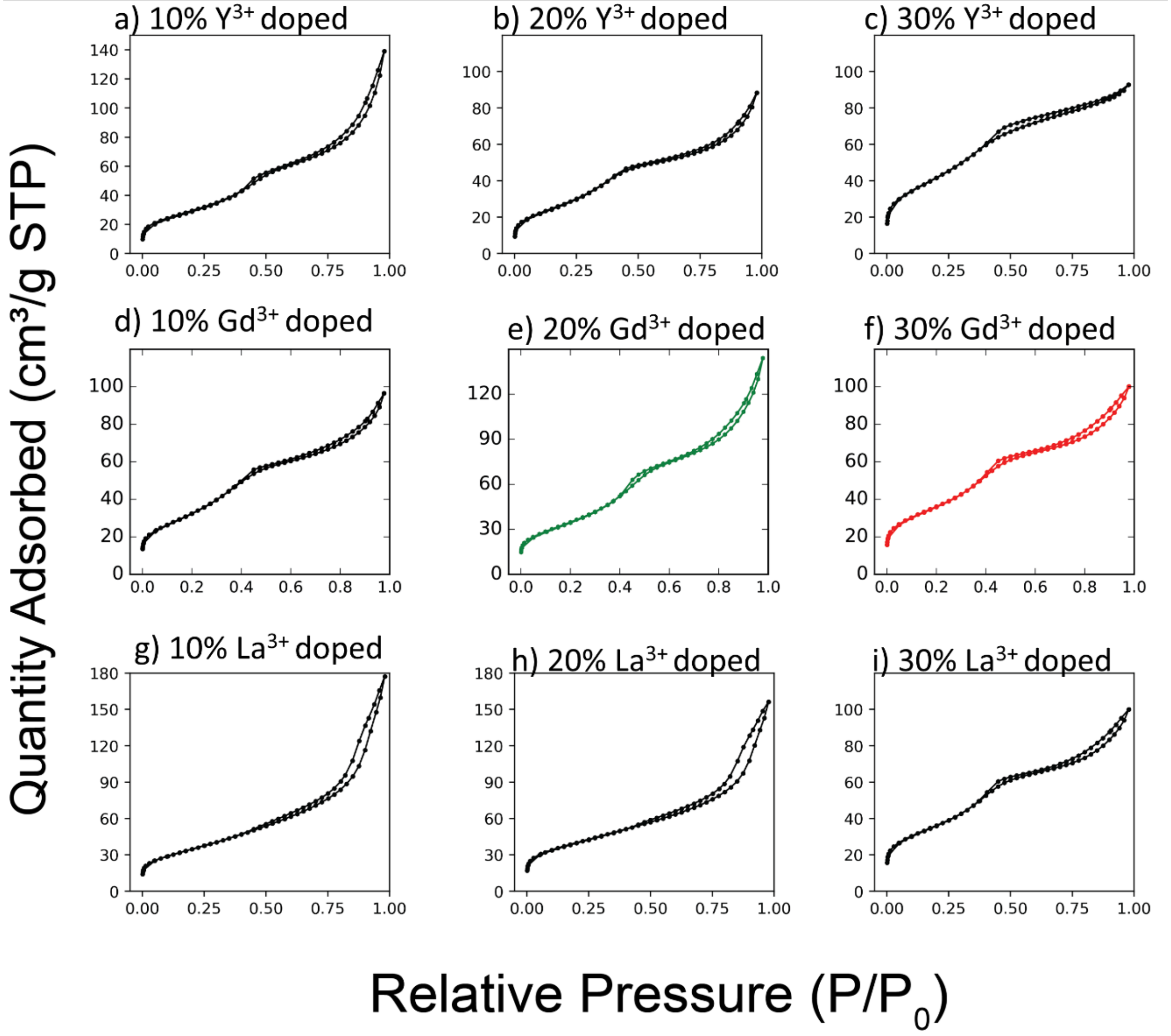

Figure B.7: Nitrogen Adsorption/Desorption isotherms of Y^{3+}, Gd^{3+} and La^{3+} doped mesoporous CeO_2.

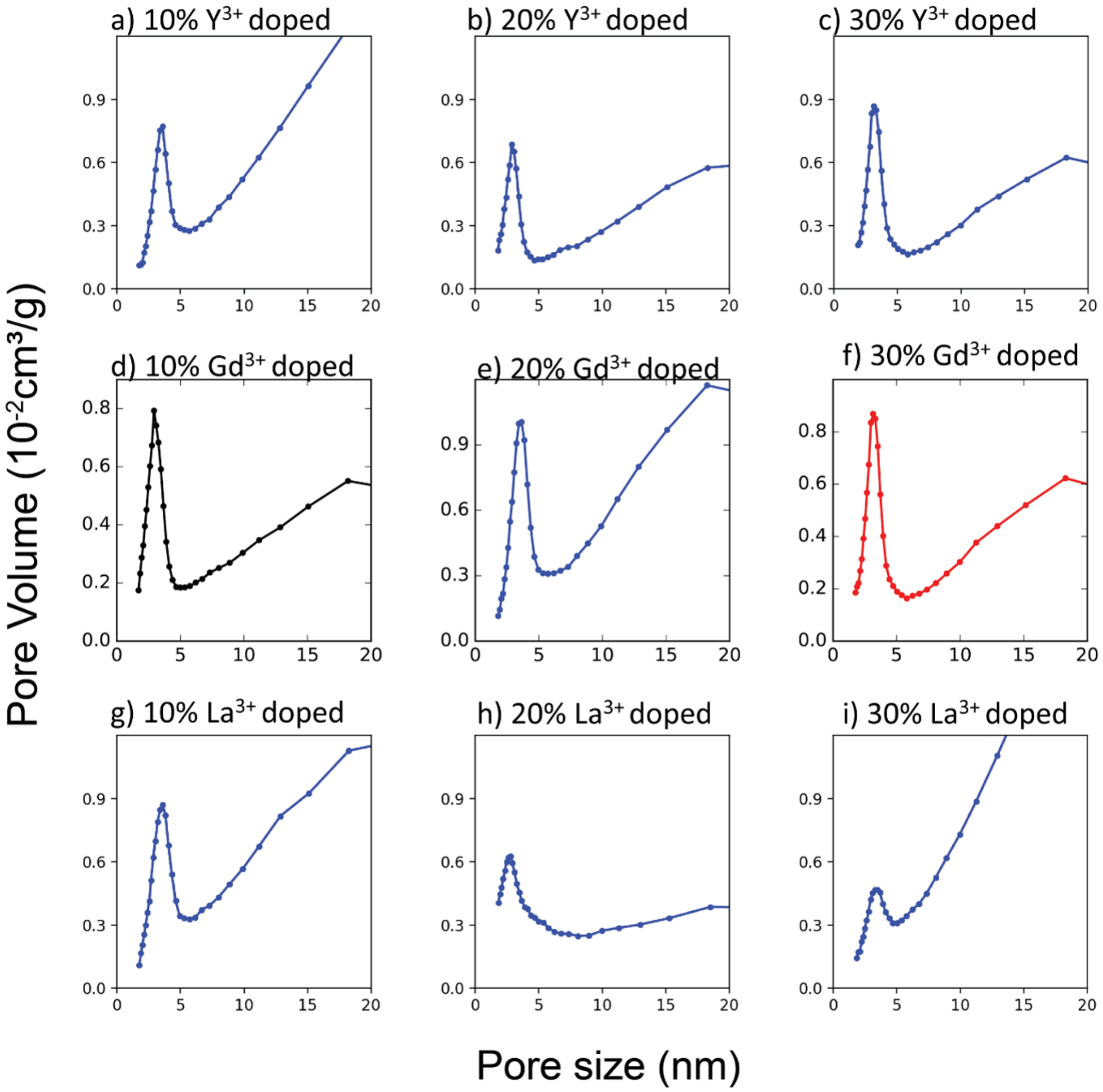

Figure B.8: Pore size distribution of Y^{3+}, Gd^{3+} and La^{3+} doped mesoporous CeO_2.

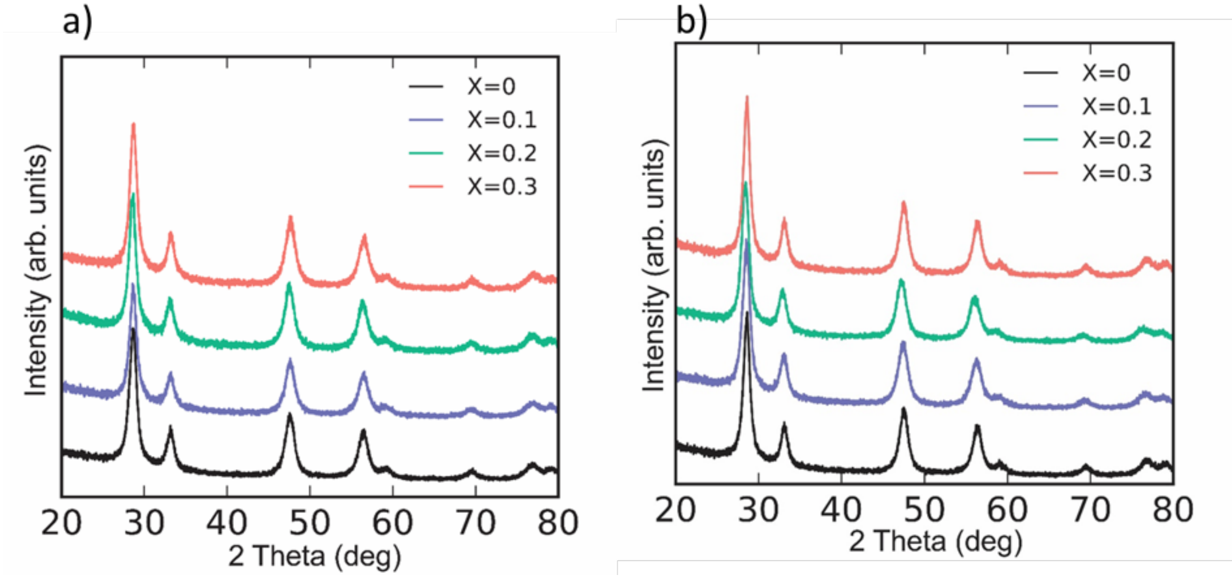

Figure B.9: XRD of Mesoporous a) Ce_{1-x}GdxO$_{2-\delta}$ and Mesoporous $Ce_{1-x}La_xO_{2-\delta}$ (x=0, 0.1, 0.2, 0.3).

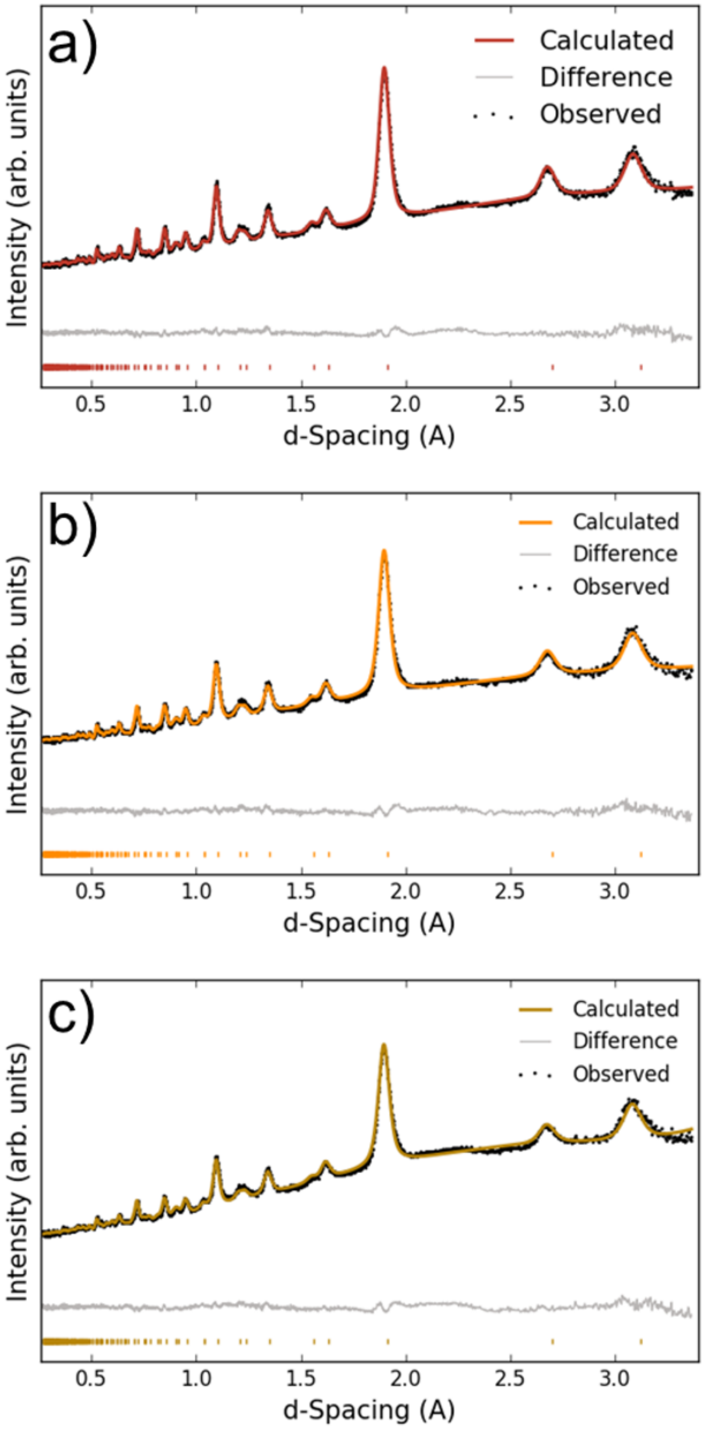

Figure B.10: Neutron Diffraction patterns of Mesoporous $Ce_{1-x}Y_xO_{2-\delta}$: a) x=0.1, b) x=0.2, c) x=0.3.

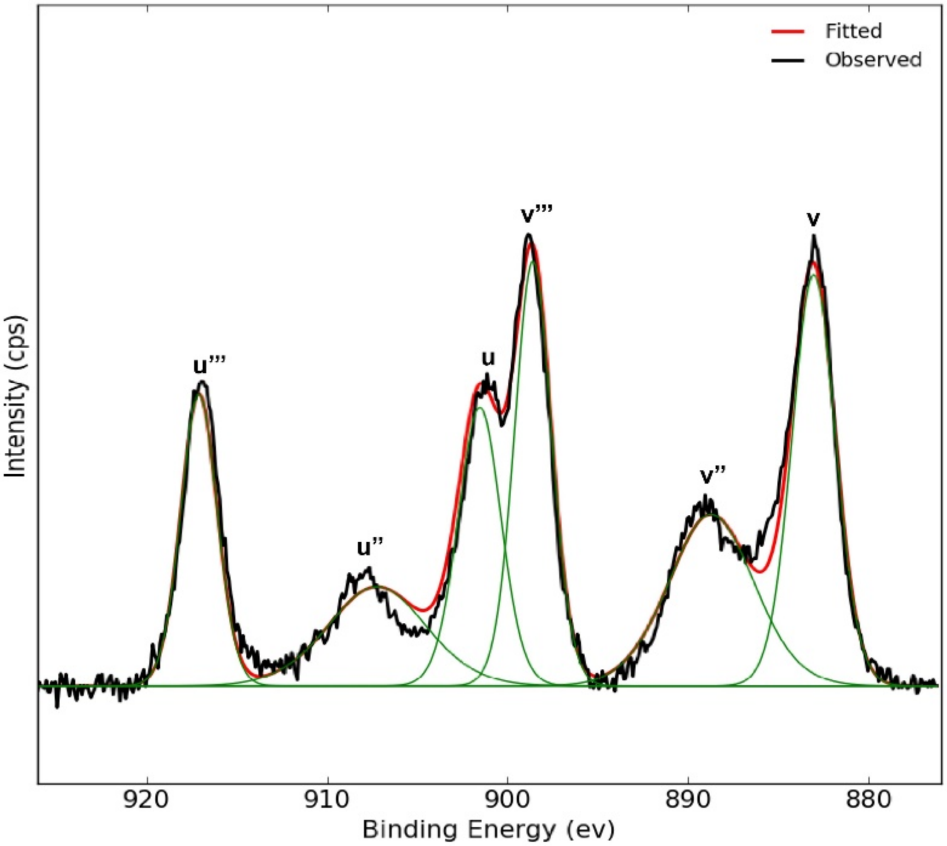

Figure B.11: Ce 3d XPS spectra for pure mesoporous CeO_2.

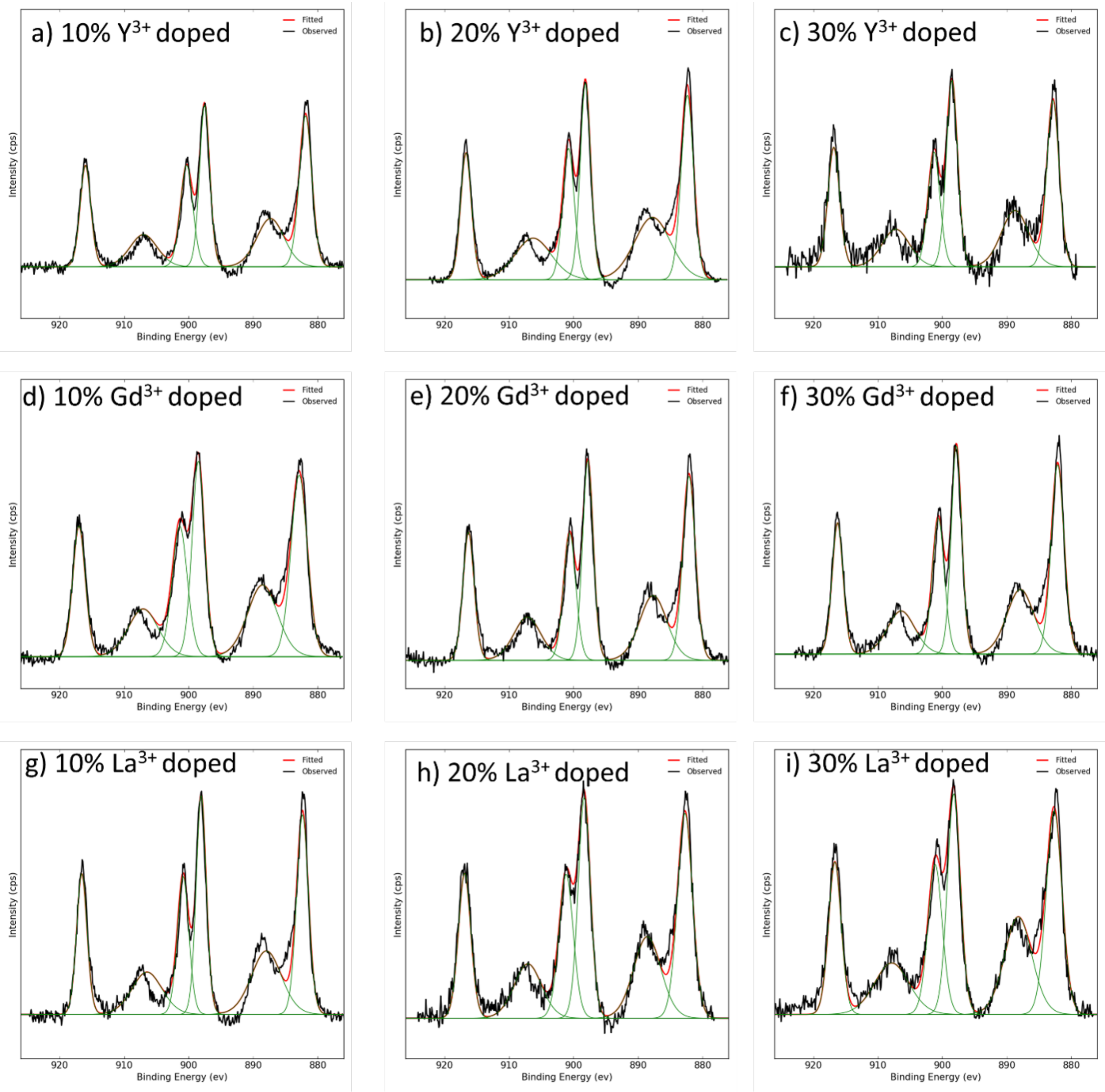
a) 10% Y^{3+} doped

b) 20% Y^{3+} doped

c) 30% Y^{3+} doped

d) 10% Gd^{3+} doped

e) 20% Gd^{3+} doped

f) 30% Gd^{3+} doped

g) 10% La^{3+} doped

h) 20% La^{3+} doped

i) 30% La^{3+} doped

Figure B.12: Ce 3d XPS spectra for Y^{3+}, Gd^{3+} and La^{3+} doped mesoporous CeO_2.

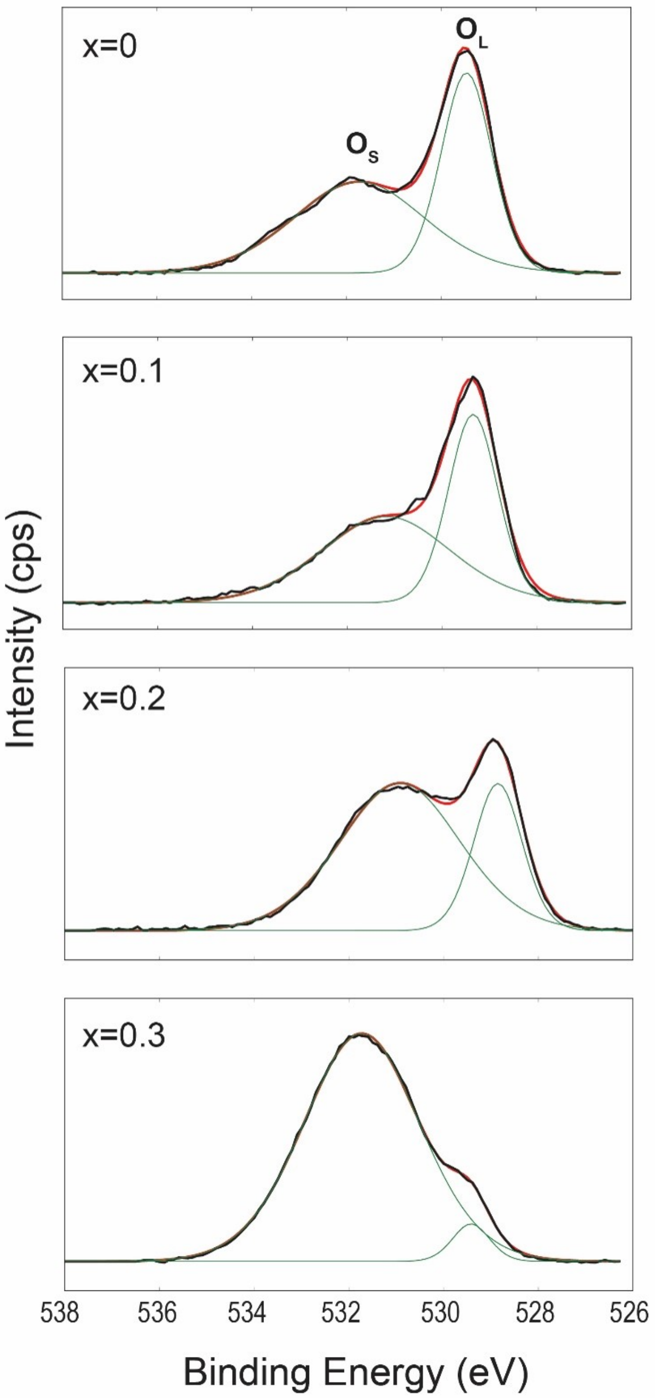

Figure B.13: O 1s XPS spectra for Y^{3+} doped and pure mesoporous CeO_2. High binding energy corresponds to "surface oxygen" (OH group). Low binding energy corresponds to "lattice oxygen".

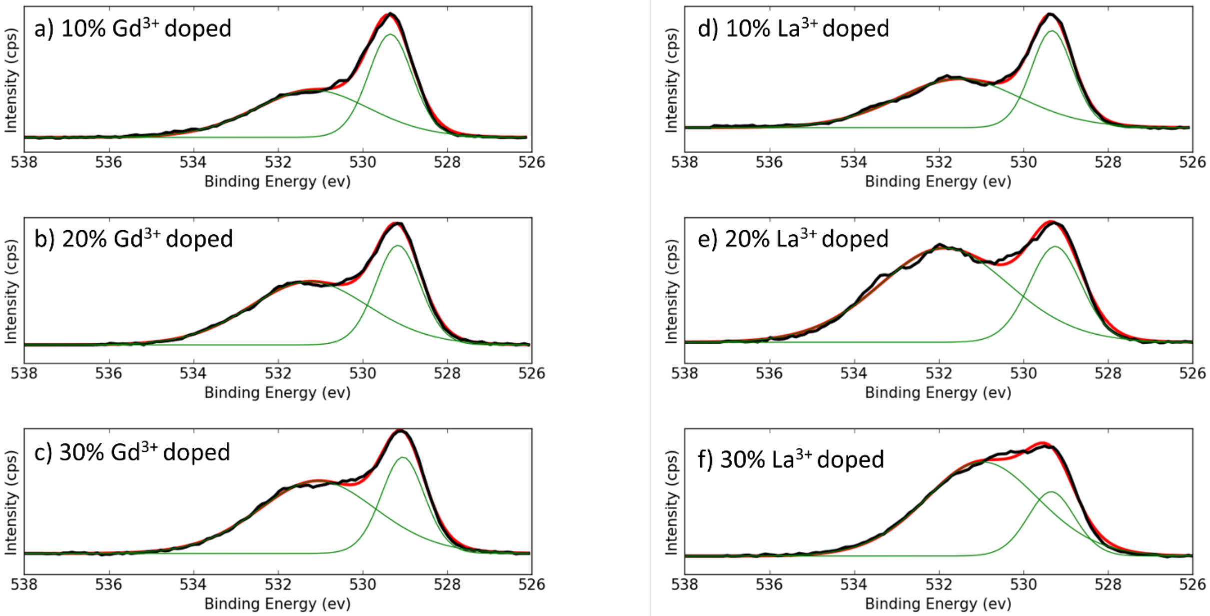

Figure B.14: O 1s XPS spectra for Gd^{3+} and La^{3+} doped mesoporous CeO_2. High binding energy corresponds to “surface oxygen” (OH group). Low binding energy corresponds to “lattice oxygen”.

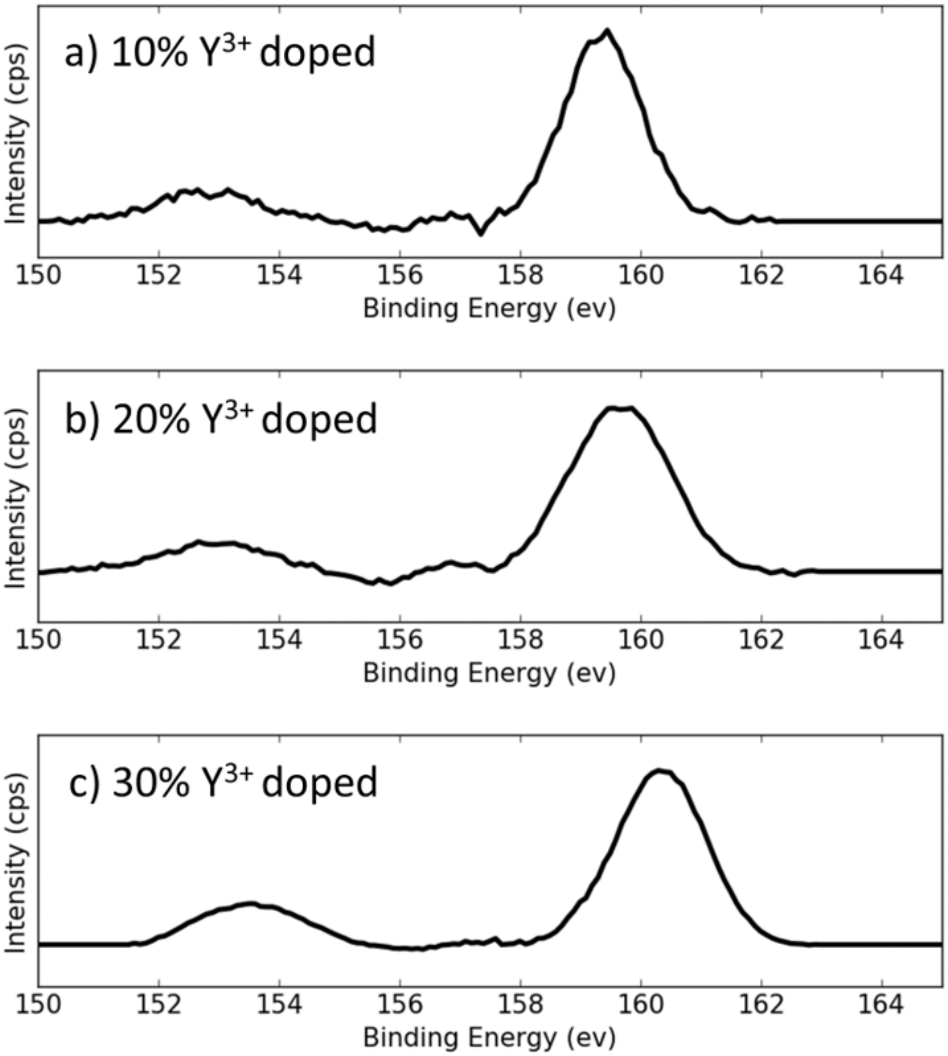

Figure B.15: Y 3d XPS spectra for Y^{3+} doped mesoporous CeO_2.

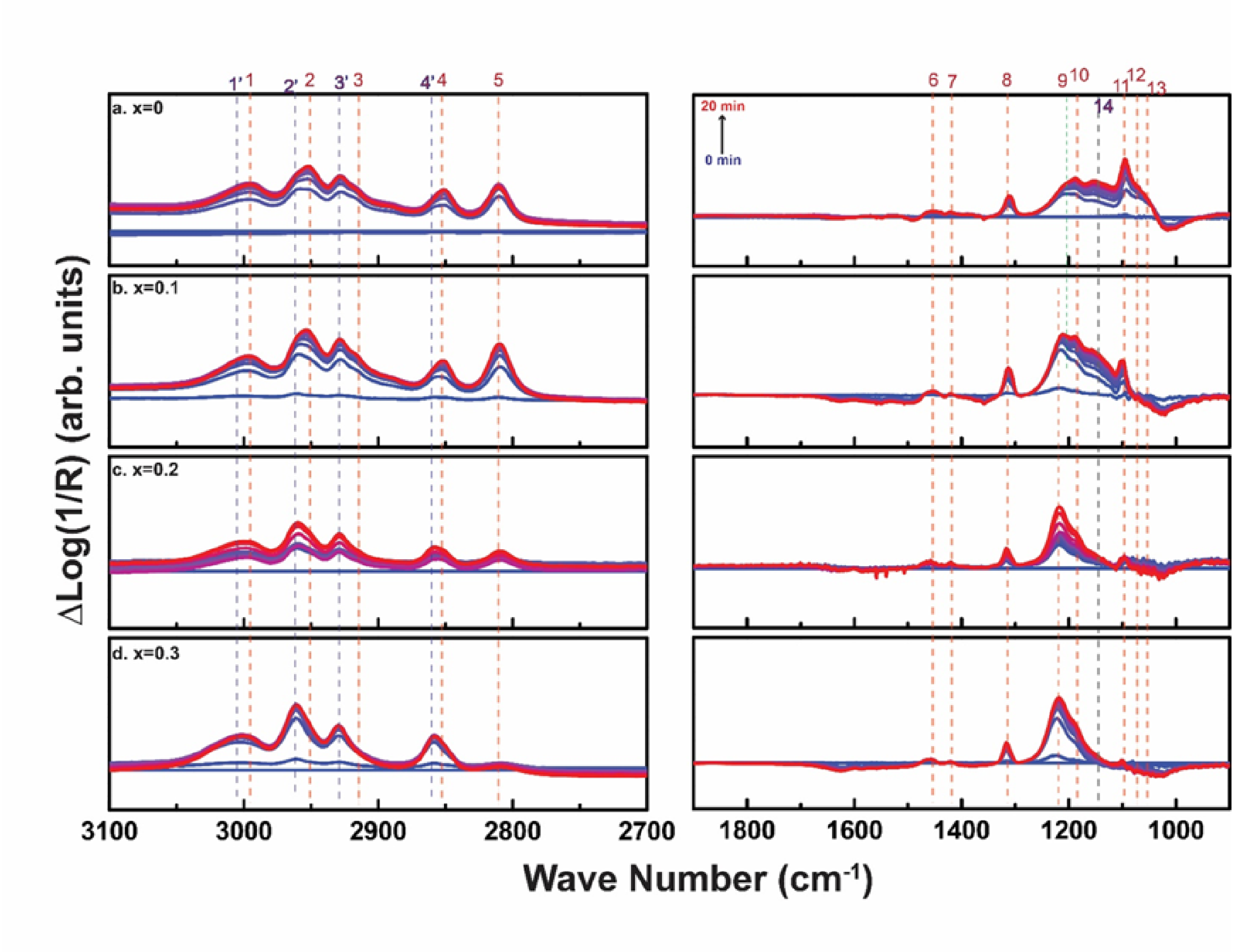

Figure B.16: In situ DRIFTS measurement of $Ce_{1-x}Gd_xO_{2-\delta}$ (x=0, 0.1, 0.2, 0.3) upon DMMP injections.

vibration mode	position	x=0	x=1	x=2	x=3
$v_a(PCH_3)$	1	2996	2996	/	/
$v_a(PCH_3)$	1’	3003	3004	3004	3003
$v_a(OCH_3)$	2’	2952	2952	/	/
$v_a(OCH_3)$	2’	2960	2960	2959	2959
$v_s(PCH_3)$	3	2905	2910	/	/
$v_s(PCH_3)$	3’	2928	2928	2929	2929
$v_s(OCH_3)$	4	2851	2851	/	/
$v_s(OCH_3)$	4’	2856	2856	2857	2858
$v_s(MOCH_3)$	5	2811	2809	/	/
$\sigma_a(OCH_3)$ and $\sigma_s(OCH_3)$	6	1467	1467	1467	1467
$\sigma_a(P–CH_3)$	7	1421	1421	1421	1421
$\sigma_s(P–CH_3)$	8	1314	1314	1316	1316
v(P=O)	9	1204	1212	1216	1216
$\rho(OCH_3)$	10	1188	1188	1189	1189
v(O–P-O)	11	1096	1103	1096	/
v_a(C–O))	12	1070	1069	/	/
v_s(C–O))	13	1047	/	/	/
v(O–P-O)	14	1116-1170	1116-1170	/	/

Table B.2: Assignment of IR peaks upon DMMP dosing onto mesoporous Ce$_{1-x}$Gd$_x$O$_{2-\delta}$ (x=0, 0.1, 0.2, 0.3) from DRIFTS characterization.

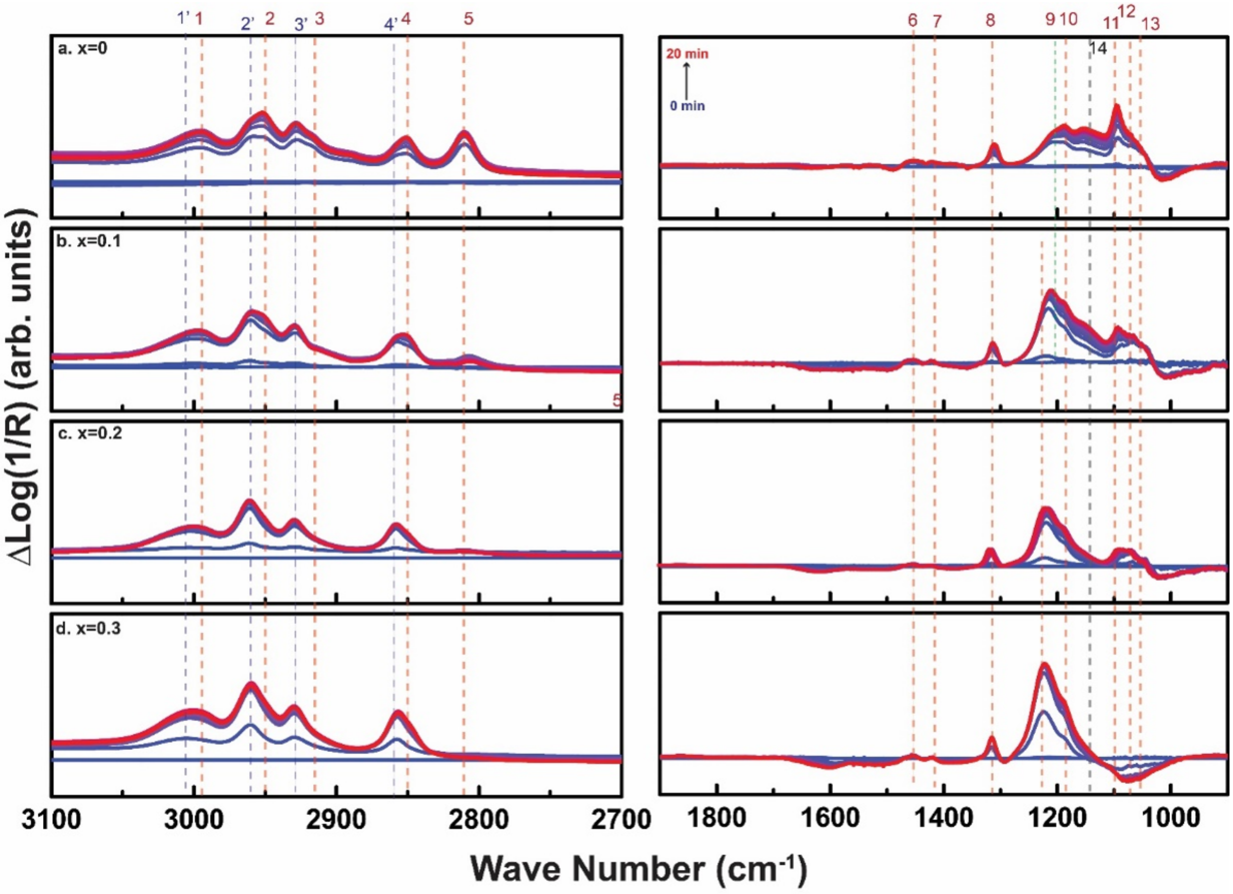

Figure B.17: In situ DRIFTS measurement of $Ce_{1-x}La_xO_{2-\delta}$ (x=0, 0.1, 0.2, 0.3) upon DMMP injections.

vibration mode	position	x=0	x=1	x=2	x=3
$v_a(PCH_3)$	1	2996	2997	/	/
$v_a(PCH_3)$	1’	3003	3004	3002	3003
$v_a(OCH_3)$	2’	2952	2952	/	/
$v_a(OCH_3)$	2’	2960	2960	2961	2961
$v_s(PCH_3)$	3	2905	2910	/	/
$v_s(PCH_3)$	3’	2928	2929	2929	2930
$v_s(OCH_3)$	4	2851	2850	/	/
$v_s(OCH_3)$	4’	2858	2858	2857	2858
$v_s(MOCH_3)$	5	2811	2807	/	/
$\sigma_a(OCH_3)$ and $\sigma_s(OCH_3)$	6	1467	1467	1467	1467
$\sigma_a(P\text{–}CH_3)$	7	1421	1421	1421	1421
$\sigma_s(P\text{–}CH_3)$	8	1314	1315	1315	1315
v(P=O)	9	1204	1213	1216	1223
$\rho(OCH_3)$	10	1188	1188	1188	1188
v(O–P-O)	11	1096	1093	1090	/
v_a(C–O))	12	1070	1071	1071	/
v_s(C–O))	13	1047	1047	1044	/
v(O–P-O)	14	1116-1170	1116-1170	/	/

Table B.3: Assignment of IR peaks upon DMMP dosing onto mesoporous $Ce_{1-x}La_xO_{2-\delta}$ (x=0, 0.1, 0.2, 0.3) from DRIFTS characterization.

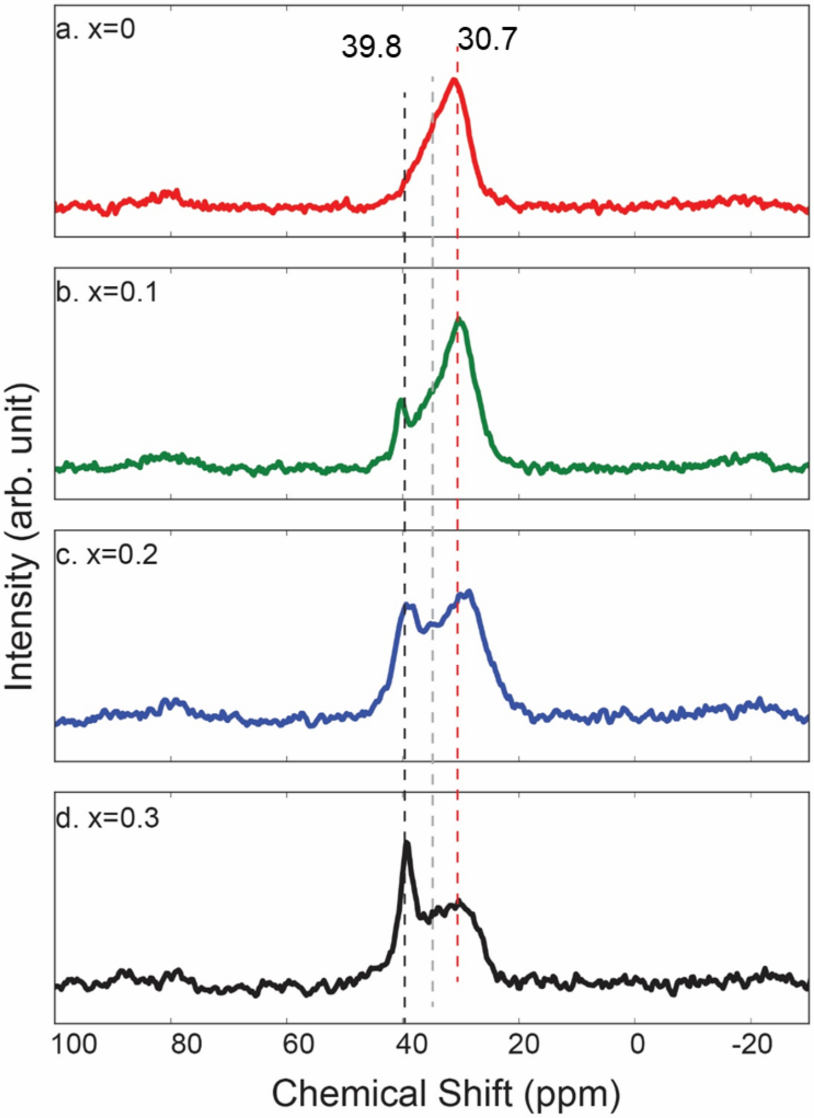

Figure B.18: Ex situ 31P Solid State NMR measurement of mesoporous $Ce_{1-x}La_xO_{2-\delta}$ (x=0, 0.1, 0.2, 0.3) after DMMP dosing.

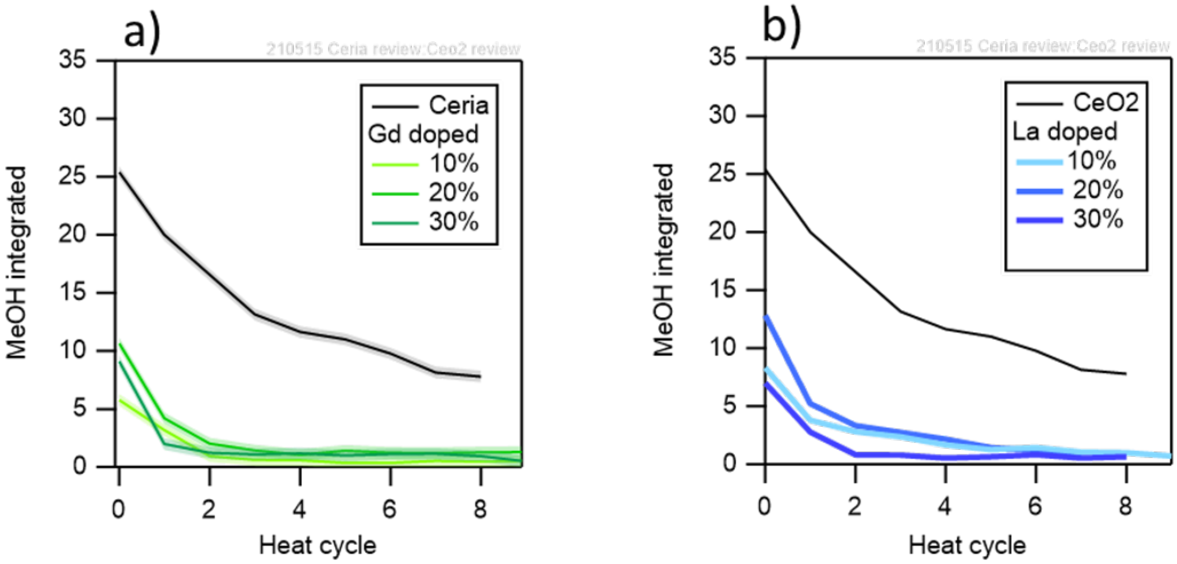

Figure B.19: Mass Spectrometry measurement of Methanol production during heating cycles upon flowing DMMP through mesoporous a) $Ce_{1-x}Gd_xO_{2-\delta}$ and b) $Ce_{1-x}La_xO_{2-\delta}$ (x=0, 0.1, 0.2, 0.3).

Appendix C: Particle size and pore pize selection on ordered mesoporous silica

The research described within this appendix was preprinted in *ChemRxiv* 2022.

Since Prof. Galen Stucky developed the method to synthesize ordered mesoporous silica[33], the research on synthesizing ordered mesoporous materials has increased explosively. Because of the high surface area and favored mass transport, ordered mesoporous materials attract great interest in the field of catalyst and energy conversions[34, 192, 193]. Besides practical applications, the ordered mesoporous silica are also good model systems for the fundamental understanding of host-gust interactions in the mesopores. The universal pore size and pore structure of countless pores in the materials will show collective response and thus can 'magnify' an event happening in the nanoscale, which allows for characterizing nano-scale event with statistical scattering and spectroscopic measurement. Those fundamental studies include gas adsorption[194, 195], fluid transport[196] and interfacial behaviors[197, 198] within the mesopores. To make the ordered mesoporous silica better candidates as model systems for fundamental studies, achieving pore size and particle size selections are crucial. From the point of view of synthetic chemistry, it is possible to control pore size or particle size once a time, while it is challenging to synthesize the ordered mesoporous materials with precise pore size and particle size control at the same time, as controlling pore size and particle size both require the adjustment of the surfactants (or templates) during synthesis. A good strategy to achieve the pore size and particle size selections is that we first synthesize the mesoporous materials with controllable pore size, and then use physical methods to perform particle size selections. Pore size selection on the ordered mesoporous silica can be easily achieved by adjusting the aging temperature during the synthesis[101]. Here we synthesized KIT-6 silica with 3 different pore sizes (4 nm, 7nm, and 9 nm) with reported method[101]. Both Nitrogen Adsorption Isotherm (Figure C.1) and Small Angle Scattering (SAXS) (Figure C.2) indicate the different pore sizes among three samples. And SEM image (Figure C.3) suggests that the as synthesized mesoporous silica materials display a huge particle size range, from hundreds of nanometers to hundreds of microns.

Our goal is to select three different particle size ranges corresponding to three different pore sizes for the future fundamental study on the influence of particle size and pore size on the gas transport and adsorption behaviors. The way we perform the size selection is through sediment of the silica particles in the liquid (we choose water here). The process is illustrated in the Figure C.4. We first disperse the as synthesized mesoporous silica powder in the water. No doubt the silica particles will start to sediment once the liquid mixture stands still. According to the Stokes' Law[199], the velocity of a sphere falling in a fluid can be described as :

$$v = \frac{D^2\left(\rho_p - \rho_f\right)g}{18\mu}$$

Where g is the gravitational field strength, D is the diameter of the spherical particle, ρ_p is the mass density of the particle, ρ_f is the mass density of the fluid, and μ is the dynamic viscosity. Figure C.5 shows the simulated sentiment time vs. falling length curve of the silica particles with different size in water. Clearly, it will take different time for particles with different sizes to sediment onto the bottom from the liquid mixture. By collecting the mesoporous silica particles with different sediment time, narrow particle size selections should be achieved. Our particle size selection process follows as:

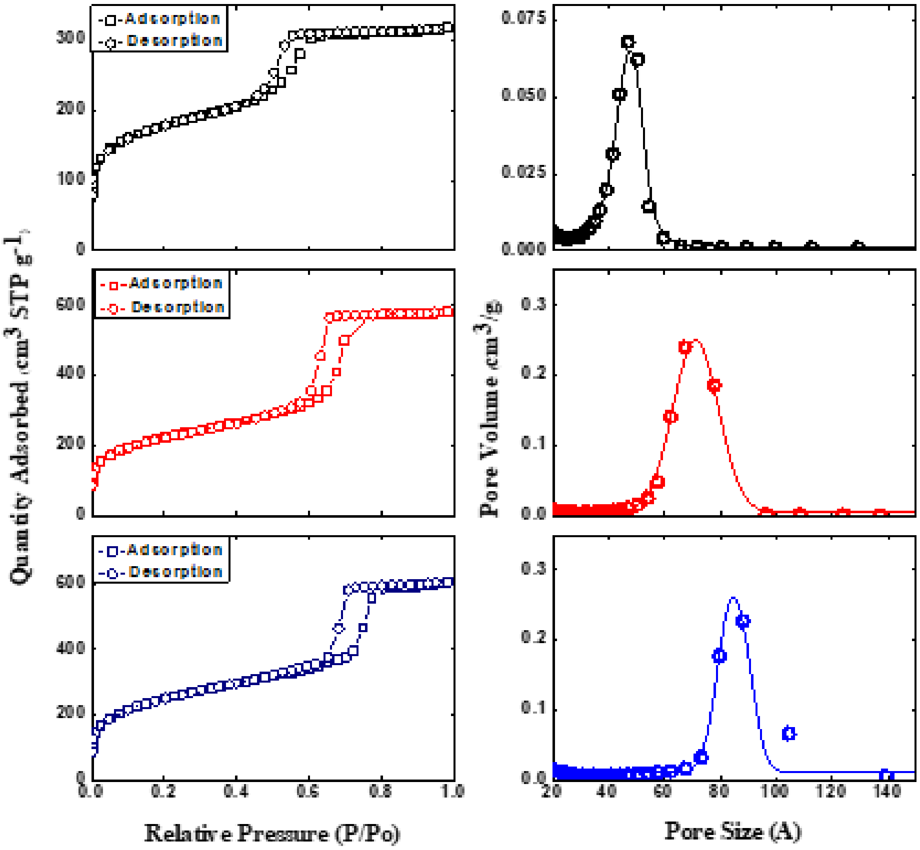

Figure C.1: Nitrogen adsorption/desorption isotherm and pore size distribution of KIT-6 mesoporous silica aged at different temperature (black: 35 °C, red: 80 °C, blue: 120 °C), which have different pore sizes (9 nm, 7 nm, and 4 nm).

1. We mix the silica powder with water in a test-tube to prepare a 10 cm height liquid mixture
2. We let the liquid mixture to stand still for certain duration from (t1-t2)
3. We collect the particles (p1) in the bottom of the tube by removing the liquid part (l2)
4. We mix the particles p1 with water again and reaped step 2 and step 3
5. Repeat step 2-4 for several times to totally get rid of the smaller particles
6. We let the left liquid part (l2) to stand for t3 (t3>t2) and remove the particles on the

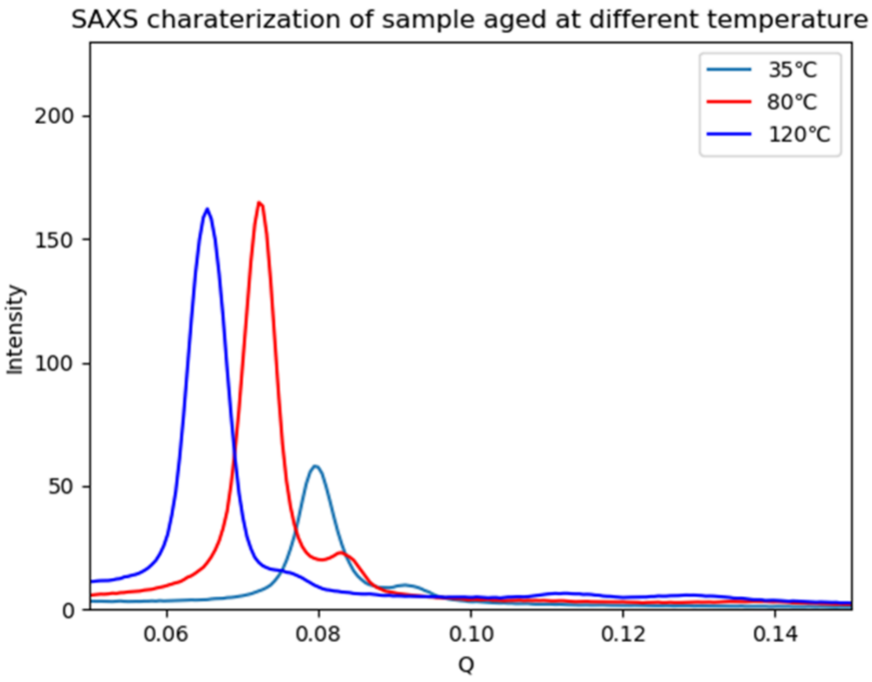

Figure C.2: Small Angle Scattering (SAXS) of KIT-6 mesoporous silica aged at different temperature.

bottom to get liquid (l3)

7. We use liquid l3 to repeat 2-5 to get particles (duration: t4-t5, t4>t3) with smaller size (p2) and the new left liquid (l4)

8. Repeat step 6-7 to get smaller and smaller particle size

In our first trial, we used 9 nm pore size silica for the size selection. We picked 6 different standing duration period: 0-10 s, 45-60 s, 2-3 min, 5-6 min, 9-10 min, 500r/min centrifuge for 3 min. We use centrifuge for the last one because last one takes too long to sediment with only gravity force. The SEM images of size-selected samples are shown in Figure C.6. It is very clear a narrow particle size selection was achieved. We then pick the 0-10 s, 45-60 s and 500r/min centrifuge for 3 min to select the 200 um, 30-40 um and ¡1 um particles for 4 nm, 7nm, and 9 nm pore size mesoporous silica. Figure C.7-C.8 display the SEM images of size selected samples

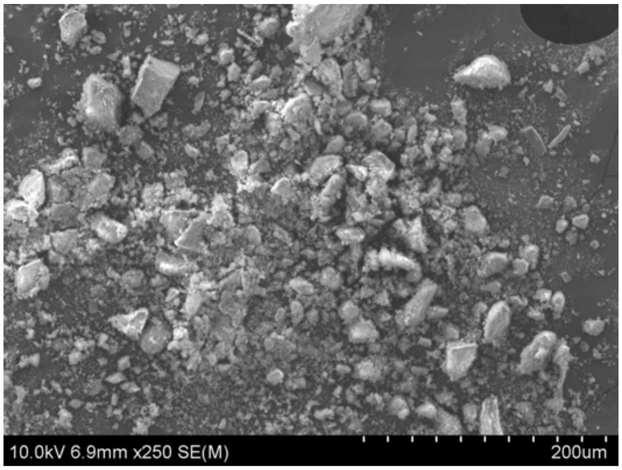

Figure C.3: SEM image of as synthesized KIT-6 mesoporous silica.

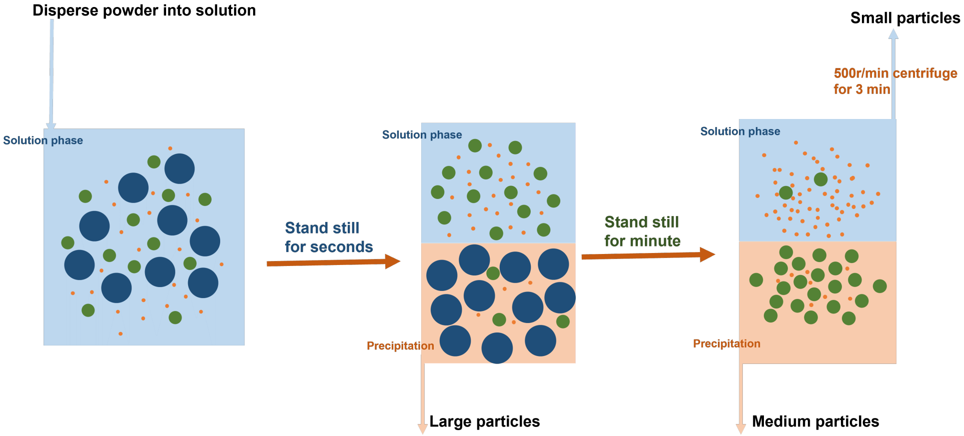

Figure C.4: Illustration of particle size selection of mesoporous silica through sediment in water.

with different pore size. We performed the SAXS on all size select samples. After the size selection, the samples from the same batch of as synthesized samples show identical diffraction patterns, suggesting the pore size remains after the size selection.

In summary, because the large particle size range of the as synthesized ordered mesoporous silica, traditional centrifuge method is not suitable for the particle size selection. Realizing that different sizes of particles fall at different speeds in the liquid, we achieve a narrow particle size selection through sediment of the mesoporous silica in water. Combining the pore size control during the synthesis and particle size selection method that we developed here, we are able to make the ordered mesoporous silica a much more controllable system, suitable for the future studies where the influence of both pore size and particle size need to be considered.

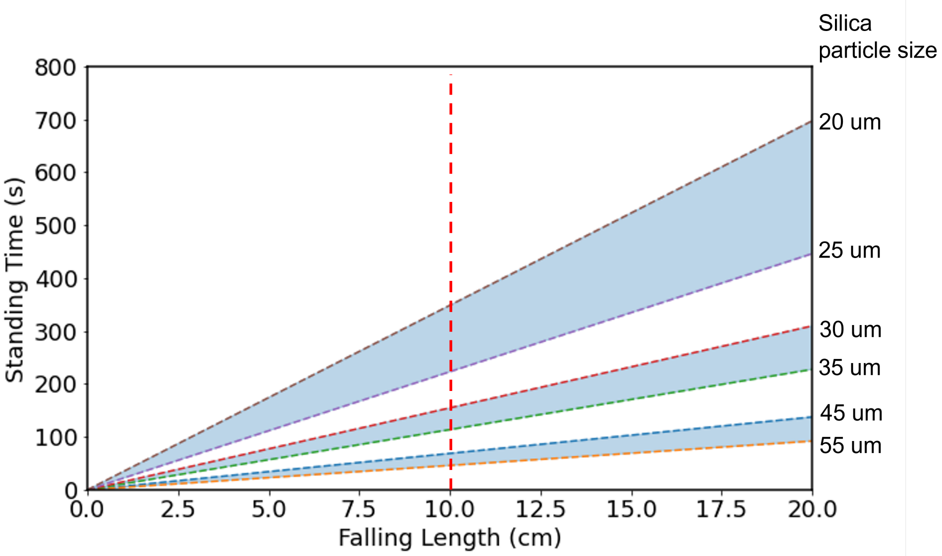

Figure C.5: Simulated falling time of silica particles with different particle sizes. By picking suitable falling length and standing time duration, narrow particle size selection is achievable.

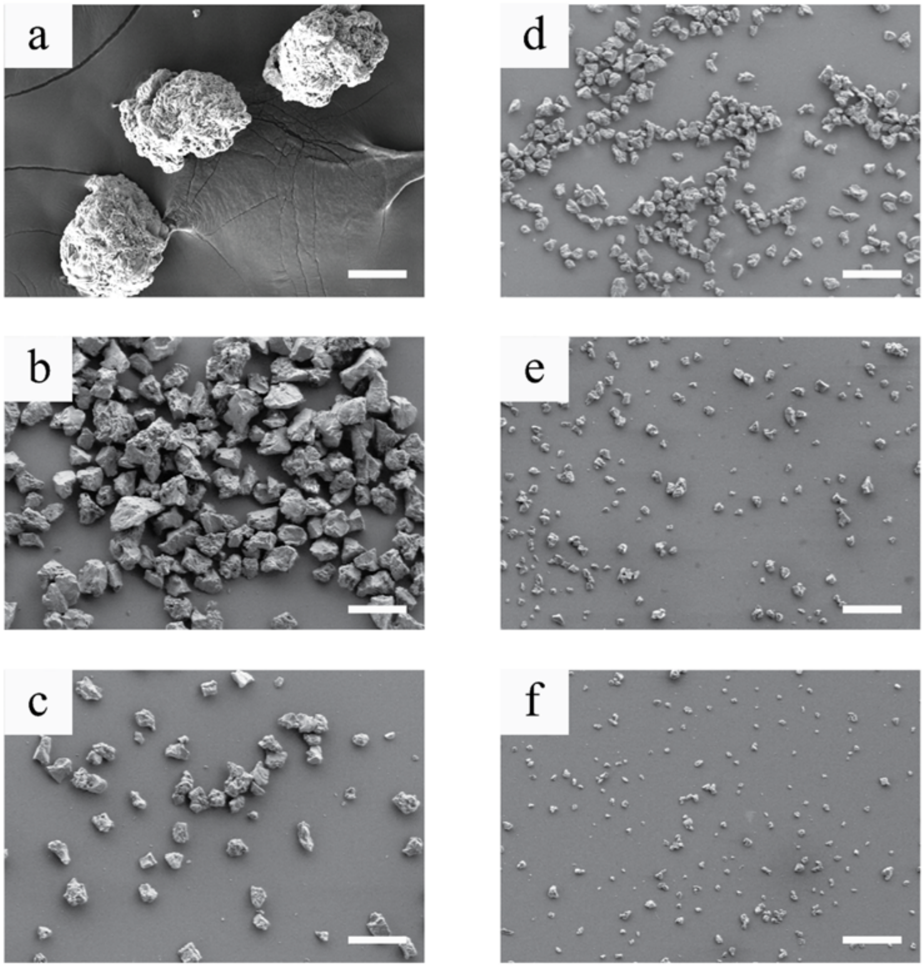

Figure C.6: SEM image of size selected mesoporous KIT-6 with different standing time: (a) 0-10 s, (b) 45-60 s, (c) 2-3 min, (d) 5-6 min, (e) 9-10 min, (f) 500r/min centrifuge for 3 min. 100 um scale bar.

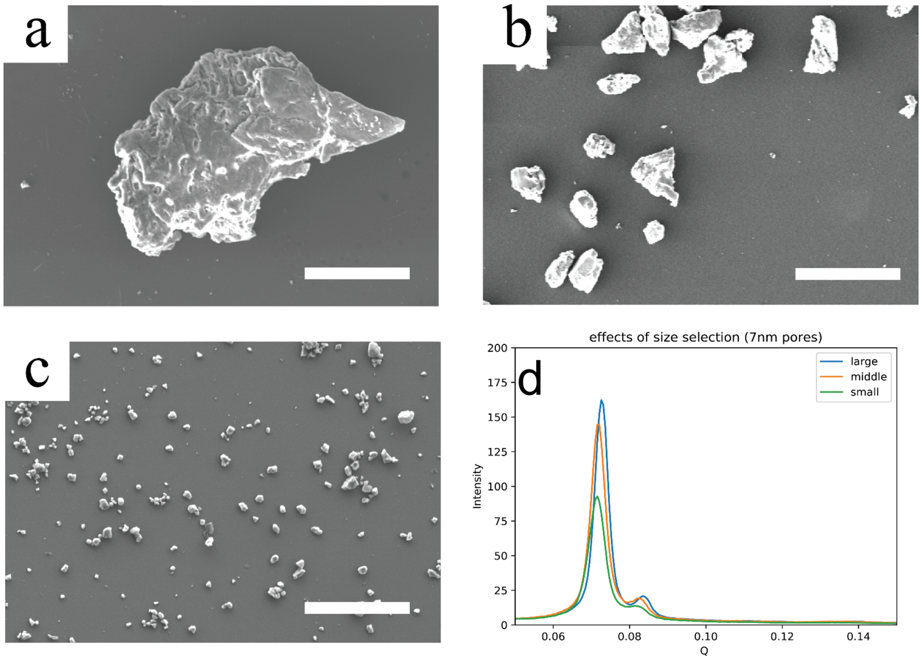

Figure C.7: SEM image of size selected mesoporous KIT-6 (pore size is 9 nm) with different standing time: (a) 0-10 s, (b) 45-60 s and (c) 500r/min centrifuge for 3 min. 100 um scale bar. (d) SAXS measurement of size selected samples.

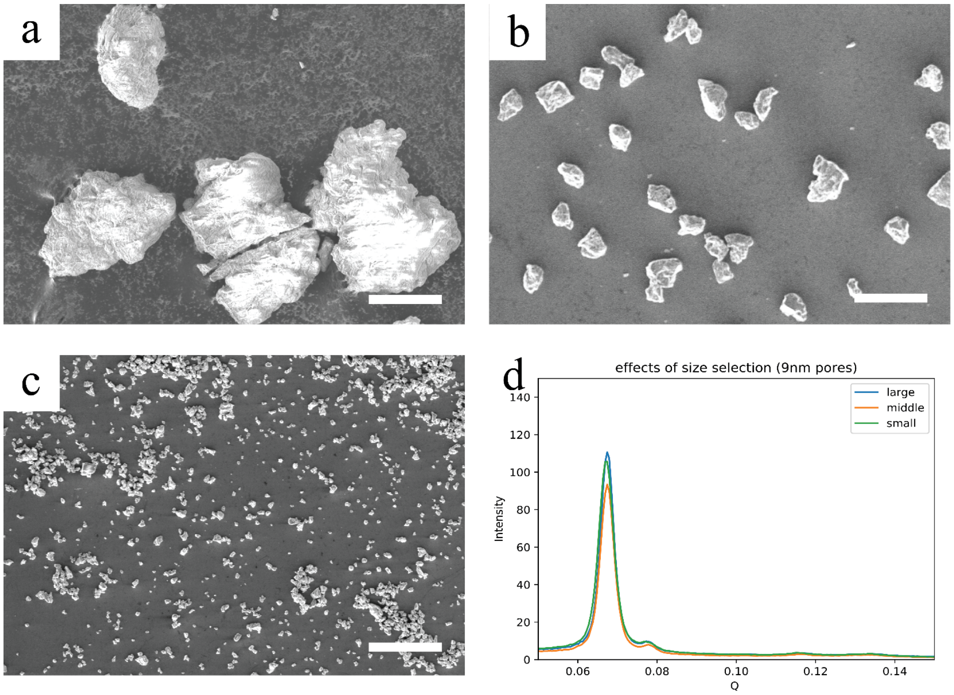

Figure C.8: SEM image of size selected mesoporous KIT-6 (pore size is 7 nm) with different standing time: (a) 0-10 s, (b) 45-60 s and (c) 500r/min centrifuge for 3 min. 100 um scale bar. (d) SAXS measurement of size selected samples.

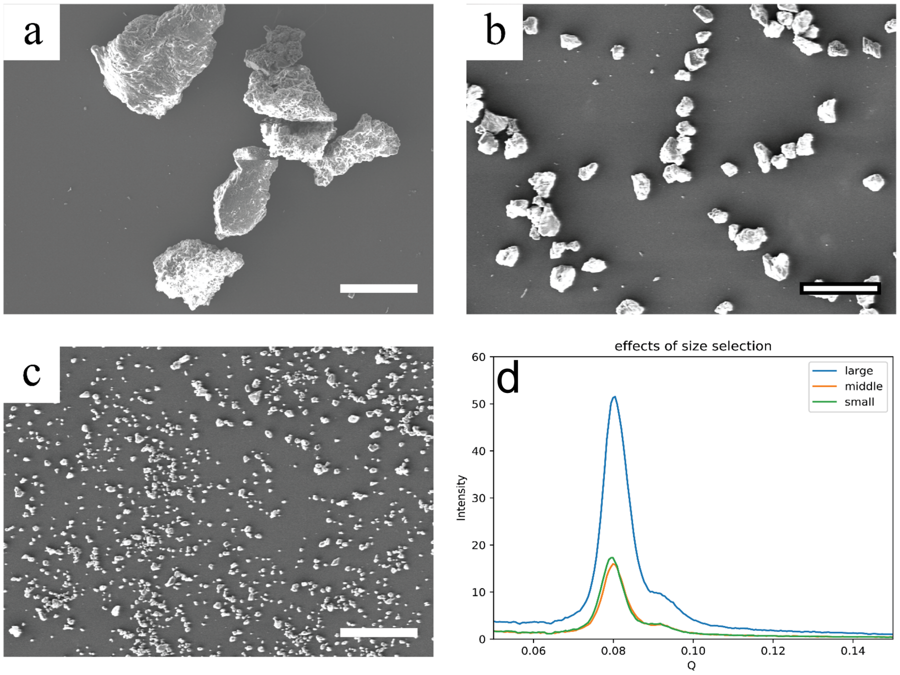

Figure C.9: SEM image of size selected mesoporous KIT-6 (pore size is 4 nm) with different standing time: (a) 0-10 s, (b) 45-60 s and (c) 500r/min centrifuge for 3 min. 100 um scale bar. (d) SAXS measurement of size selected samples.

Appendix D: Mesoporous Metal Oxides Synthesized

Mesoporous Materials	Doped?
CeO_2	Pure, 5%, 10%, 15% Y, La, Gd doped; %5 Mg, Ca, Mn, Fe, Co, Ni, Cu, Zn, Sr, Zr doped
Al_2O_3	Pure, 0.5%, 5%, 10%, 15% Mn, Fe, Cu, Zn, Ce doped
TiO_2	Pure, 0.5%, 5%, 10%, 15% Mn, Fe, Cu, Zn, Ce doped
Fe_2O_3	
Mn_2O_3	
Co_3O_4	
Co_3O_4	
$SrTiO_3$	Pure,0.5% Mn, Fe, Co, Ni, Ce doped
$BaTiO_3$	Pure,0.5% Mn, Fe, Co, Ni, Ce doped
$LiTiO_3$	
$LaFeO_3$	
$LaMnO_3$	
$LaCoO_3$	
$LaNiO_3$	

Table D.1: Mesoporous Metal Oxides Synthesized

Bibliography

[1] Kibong Kim, Olga G. Tsay, David A. Atwood, and David G. Churchill. Destruction and Detection of Chemical Warfare Agents. *Chemical Reviews*, 111(9):5345–5403, sep 2011.

[2] Reinaldo T. Delfino, Tatiana S. Ribeiro, and José D. Figueroa-Villar. Organophosphorus compounds as chemical warfare agents: A review. *Journal of the Brazilian Chemical Society*, 20(3):407–428, 2009.

[3] Ashley R. Head, Roman Tsyshevsky, Lena Trotochaud, Yi Yu, Line Kyhl, Osman Karslloğlu, Maija M. Kuklja, Hendrik Bluhm, Osman Karslıoğlu, Maija M. Kuklja, and Hendrik Bluhm. Adsorption of Dimethyl Methylphosphonate on MoO3: The Role of Oxygen Vacancies. *Journal of Physical Chemistry C*, 120(51):29077–29088, dec 2016.

[4] T. Li, R.S. Jayathilake, D.D. Taylor, and E.E. Rodriguez. Structural studies of the perovskite series La¡inf¿1-:X¡/inf¿Sr¡inf¿x¡/inf¿CoO¡inf¿3- δ¡/inf¿ during chemical looping with methane. *Chemical Communications*, 55(34), 2019.

[5] På Aas. The Threat of Mid-Spectrum Chemical Warfare Agents. *Prehospital and Disaster Medicine*, 18(4):306–312, 2003.

[6] K. Ganesan, S. K. Raza, and R. Vijayaraghavan. Chemical warfare agents. *Journal of Pharmacy and Bioallied Sciences*, 2(3):166, 2010.

[7] L. Szinicz. History of chemical and biological warfare agents. *Toxicology*, 214(3):167–181, oct 2005.

[8] Lichen Liu. Multiscale structural characterization of shaped catalysts. *Trends in Chemistry*, 3(11):898–901, nov 2021.

[9] Jeanne Mager Stellman, Steven D. Stellman, Richard Christian, Tracy Weber, and Carrie Tomasallo. The extent and patterns of usage of Agent Orange and other herbicides in Vietnam. *Nature 2003 422:6933*, 422(6933):681–687, apr 2003.

[10] Opcw. *CHEMICAL WEAPONS CONVENTION Convention on the Prohibition of the Development, Production, Stockpiling and Use of Chemical Weapons and on their Destruction*.

[11] Alain Friboulet, François Rieger, Danièle Goudou, Gabriel Amitai, and Palmer Taylor. Interaction of an organophosphate with a peripheral site on acetylcholinesterase. *Biochemistry*, 29(4):914–920, jan 2002.

[12] S. Chauhan, S. Chauhan, R. D'Cruz, S. Faruqi, K. K. Singh, S. Varma, M. Singh, and V. Karthik. Chemical warfare agents. *Environmental Toxicology and Pharmacology*, 26(2):113–122, sep 2008.

[13] Hans Jürgen Altmann and André Richardt. Decontamination of Chemical Warfare Agents. *Decontamination of Warfare Agents: Enzymatic Methods for the Removal of B/C Weapons*, 92:83–115, 2008.

[14] Gregory W. Peterson, Tracee Whitfield, and Omar Farha. Nanomaterial Development, Characterization, and Integration Strategies for Chemical Warfare Defense. *ACS Applied Materials Interfaces*, 12(13):14629–14630, apr 2020.

[15] Sidra Shaoor Kiani, Amjad Farooq, Masroor Ahmad, Naseem Irfan, Mohsan Nawaz, and Muhammad Asim Irshad. Impregnation on activated carbon for removal of chemical warfare agents (CWAs) and radioactive content. *Environmental Science and Pollution Research*, 28(43):60477–60494, nov 2021.

[16] Martijn C. De Koning, Marco Van Grol, and Troy Breijaert. Degradation of Paraoxon and the Chemical Warfare Agents VX, Tabun, and Soman by the Metal-Organic Frameworks UiO-66-NH2, MOF-808, NU-1000, and PCN-777. *Inorganic Chemistry*, 56(19):11804–11809, oct 2017.

[17] Dennis T. Lee, Junjie Zhao, Christopher J. Oldham, Gregory W. Peterson, and Gregory N. Parsons. UiO-66-NH2 Metal-Organic Framework (MOF) Nucleation on TiO2, ZnO, and Al2O3 Atomic Layer Deposition-Treated Polymer Fibers: Role of Metal Oxide on MOF Growth and Catalytic Hydrolysis of Chemical Warfare Agent Simulants. *ACS Applied Materials and Interfaces*, 9(51):44847–44855, dec 2017.

[18] Linna Song, Tianyu Zhao, Dongzhi Yang, Xuejiao Wang, Xinmin Hao, Yaxin Liu, Shiyi Zhang, and Zhong Zhen Yu. Photothermal graphene/UiO-66-NH2 fabrics for ultrafast catalytic degradation of chemical warfare agent simulants. *Journal of Hazardous Materials*, 393:122332, jul 2020.

[19] Joseph E. Mondloch, Michael J. Katz, William C. Isley, Pritha Ghosh, Peilin Liao, Wojciech Bury, George W. Wagner, Morgan G. Hall, Jared B. Decoste, Gregory W. Peterson, Randall Q. Snurr, Christopher J. Cramer, Joseph T. Hupp, and Omar K. Farha. Destruction of chemical warfare agents using metal–organic frameworks. *Nature Materials 2014 14:5*, 14(5):512–516, mar 2015.

[20] Jacob A Harvey, Monica L. McEntee, Sergio J. Garibay, Erin M. Durke, Jared B. DeCoste, Jeffery A. Greathouse, and Dorina F. Sava Gallis. Spectroscopically Resolved Binding Sites for the Adsorption of Sarin Gas in a Metal-Organic Framework: Insights beyond Lewis Acidity. *The journal of physical chemistry letters*, 10(17):5142–5147, sep 2019.

[21] Dahee Jung, Pradipta Das, Ahmet Atilgan, Peng Li, Joseph T. Hupp, Timur Islamoglu, Julia A. Kalow, and Omar K. Farha. Reactive Porous Polymers for Detoxification of a Chemical Warfare Agent Simulant. *Chemistry of Materials*, 32(21):9299–9306, nov 2020.

[22] Scott Holdren, Roman Tsyshevsky, Kenan Fears, Jeffrey Owrutsky, Tao Wu, Xizheng Wang, Bryan W. Eichhorn, Maija M. Kuklja, and Michael R. Zachariah. Adsorption and Destruction of the G-Series Nerve Agent Simulant Dimethyl Methylphosphonate on Zinc Oxide. *ACS Catalysis*, 9(2):902–911, dec 2018.

[23] Dimitar A. Panayotov, John R. Morris, Dimitar A. Panayotov, and John R. Morris. Uptake of a Chemical Warfare Agent Simulant (DMMP) on TiO2: Reactive Adsorption and Active Site Poisoning. *Langmuir*, 25(6):3652–3658, feb 2009.

[24] B. Aurian-Blaieni and M. M. Boucher. Interaction of Dimethyl Methylphosphonate with Metal Oxides. *Langmuir*, 5(1):170–174, 1989.

[25] Scott R. Segal, Lixin Cao, Steven L. Suib, Xia Tang, and Sunita Satyapal. Thermal Decomposition of Dimethyl Methylphosphonate over Manganese Oxide Catalysts. *Journal of Catalysis*, 198(1):66–76, feb 2001.

[26] Mark B. Mitchell, Viktor N. Sheinker, Aron B. Tesfamichael, Enid N. Gatimu, Maya Nunley, Mark B. Mitchell, Viktor N. Sheinker, Aron B. Tesfamichael, Enid N. Gatimu, and Maya Nunley. Decomposition of Dimethyl Methylphosphonate (DMMP) on Supported Cerium and Iron Co-Impregnated Oxides at Room Temperature. *The Journal of Physical Chemistry B*, 107(2):580–586, dec 2003.

[27] Teweldemedhin M. Tesfai, V. N. Sheinker, Mark B. Mitchell, Teweldemedhin M. Tesfai, V. N. Sheinker, and Mark B. Mitchell. Decomposition of Dimethyl Methylphosphonate (DMMP) on Alumina-Supported Iron Oxide. *The Journal of Physical Chemistry B*, 102(38):7299–7302, aug 1998.

[28] Shomik Mukhopadhyay, Mirko Schoenitz, and Edward L. Dreizin. Vapor-phase decomposition of dimethyl methylphosphonate (DMMP), a sarin surrogate, in presence of metal oxides. *Defence Technology*, 17(4):1095–1114, aug 2021.

[29] Mark Kalaj, Michael S. Denny, Kyle C. Bentz, Joseph M. Palomba, and Seth M. Cohen. Nylon–MOF Composites through Postsynthetic Polymerization. *Angewandte Chemie*, 131(8):2358–2362, feb 2019.

[30] Denghui Ma and Zexing Cao. Adsorption and Decomposition of Sarin on Dry and Wet Cu2O(111) and CuO(111) Surfaces: Insight from First-Principles Calculations. *Journal of Physical Chemistry C*, 125(44):24396–24405, nov 2021.

[31] Ruili Liu, Yingjie Ren, Yifeng Shi, Fan Zhang, Lijuan Zhang, Bo Tu, and Dongyuan Zhao. Controlled synthesis of ordered mesoporous C-TiO2 nanocomposites with crystalline titania frameworks from organic-inorganic-amphiphilic coassembly. *Chemistry of Materials*, 20(3):1140–1145, feb 2008.

[32] Amani M. Ebrahim, Anna M. Plonka, Yiyao Tian, Sanjaya D. Senanayake, Wesley O. Gordon, Alex Balboa, Hui Wang, Daniel L. Collins-Wildman, Craig L. Hill, Djamaladdin G. Musaev, John R. Morris, Diego Troya, and Anatoly I. Frenkel. Multimodal Characterization of Materials and Decontamination Processes for Chemical Warfare Protection. *ACS Applied Materials Interfaces*, 12(13):14721–14738, apr 2019.

[33] Dongyuan Zhao, Jianglin Feng, Qisheng Huo, Nicholas Melosh, Glenn H. Fredrickson, Bradley F. Chmelka, and Galen D. Stucky. Triblock copolymer syntheses of mesoporous silica with periodic 50 to 300 angstrom pores. *Science*, 279(5350):548–552, jan 1998.

[34] Dong Gu and Ferdi Schüth. Synthesis of non-siliceous mesoporous oxides. *Chemical Society Reviews*, 43(1):313–344, jan 2014.

[35] Charles Kittel and Paul McEuen. *Introduction to solid state physics*. John Wiley & Sons, 2018.

[36] Y. Paukku, A. Michalkova, and J. Leszczynski. Adsorption of dimethyl methylphosphonate and trimethyl phosphate on calcium oxide: an ab initio study. *Structural Chemistry 2008 19:2*, 19(2):307–320, feb 2008.

[37] V. M. Bermudez and V. M. Bermudez*. Computational Study of the Adsorption of Trichlorophosphate, Dimethyl Methylphosphonate, and Sarin on Amorphous SiO2. *Journal of Physical Chemistry C*, 111(26):9314–9323, jul 2007.

[38] V. M. Bermudez and V. M. Bermudez†. No Title. *Journal of Physical Chemistry C*, 111(9):3719–3728, mar 2007.

[39] A. Michalkova, M. Ilchenko, L. Gorb, J. Leszczynski, † A. Michalkova, ‡ M. Ilchenko, , ‡ L. Gorb, and ‡ J. Leszczynski*. Theoretical Study of the Adsorption and Decomposition of Sarin on Magnesium Oxide. *Journal of Physical Chemistry B*, 108(17):5294–5303, apr 2004.

[40] Scott Holdren, Roman Tsyshevsky, Kenan Fears, Jeffrey Owrutsky, Tao Wu, Xizheng Wang, Bryan W. Eichhorn, Maija M. Kuklja, Michael R. Zachariah, Bryan W. Eichhorn, Maija M. Kuklja, and Michael R. Zachariah. Adsorption and Destruction of the G-Series Nerve Agent Simulant Dimethyl Methylphosphonate on Zinc Oxide. *ACS Catalysis*, 9(2):902–911, dec 2018.

[41] Nam Q. Le, Chinedu E. Ekuma, Brett I. Dunlap, and Daniel Gunlycke. First-Principles Calculations of Sarin Adsorption on Anatase Surfaces. *Journal of Physical Chemistry C*, 122(5):2832–2839, feb 2018.

[42] Tamalika Ash, Tanay Debnath, Soumadip Banerjee, Avik Ghosh, and Abhijit K. Das. Theoretical study of gas-phase detoxication of DMMP and DMPT using ammonia-borane and its analogous compound. *Journal of Molecular Graphics and Modelling*, 109:108037, dec 2021.

[43] Daniel Waffel, Eko Budiyanto, Thomas Porske, Julia Büker, Tobias Falk, Qi Fu, Stefan Schmidt, Harun Tüysüz, Martin Muhler, and Baoxiang Peng. Investigation of Synergistic Effects between Co and Fe in Co3-xFexO4 Spinel Catalysts for the Liquid-Phase Oxidation of Aromatic Alcohols and Styrene. *Molecular Catalysis*, 498, dec 2020.

[44] Roman Tsyshevsky, Scott Holdren, Bryan W. Eichhorn, Michael R. Zachariah, and Maija M. Kuklja. Sarin Decomposition on Pristine and Hydroxylated ZnO: Quantum-Chemical Modeling. *The Journal of Physical Chemistry C*, 123(43):26432–26441, oct 2019.

[45] Ran Yoo, Somi Yoo, Dongmei Lee, Jeongmin Kim, Sungmee Cho, and Wooyoung Lee. Highly selective detection of dimethyl methylphosphonate (DMMP) using CuO nanoparticles /ZnO flowers heterojunction. *Sensors and Actuators B: Chemical*, 240:1099–1105, mar 2017.

[46] V. M. Bermudez. No Title. *Journal of Physical Chemistry C*, 113(5):1917–1930, feb 2009.

[47] Celine Tesvara. *Modeling the Reactivity of Chemical Warfare Agents on Metal Oxides Using Computational Chemistry Methods*. PhD thesis, University of California, Los Angeles, 2021.

[48] Roald Hoffmann. How Chemistry and Physics Meet in the Solid State. *Angewandte Chemie International Edition in English*, 1987.

[49] Seokmin Jeon, Igor V. Schweigert, Pehr E. Pehrsson, and Robert B. Balow. Kinetics of Dimethyl Methylphosphonate Adsorption and Decomposition on Zirconium Hydroxide Using Variable Temperature in Situ Attenuated Total Reflection Infrared Spectroscopy. *ACS Applied Materials and Interfaces*, 12(13):14662–14671, feb 2020.

[50] Stephan Lany. Band-structure calculations for the 3d transition metal oxides in GW. *Physical Review B - Condensed Matter and Materials Physics*, 87(8):085112, feb 2013.

[51] Elijah Thimsen, Subhashis Biswas, Cynthia S. Lo, and Pratim Biswas. Predicting the Band Structure of Mixed Transition Metal Oxides: Theory and Experiment. *Journal of Physical Chemistry C*, 113(5):2014–2021, feb 2009.

[52] J. B. Goodenough and J. S. Zhou. Localized to Itinerant Electronic Transitions in Transition-Metal Oxides with the Perovskite Structure. *Chemistry of Materials*, 10(10):2980–2993, 1998.

[53] Suman Bhasker-Ranganath, Chuanlin Zhao, and Ye Xu. Theoretical analysis of the adsorption of phosphoric acid and model phosphate monoesters on CeO2(111). *Surface Science*, 705:121776, mar 2021.

[54] Chuanlin Zhao and Ye Xu. Theoretical investigation of dephosphorylation of phosphate monoesters on CeO2(111). *Catalysis Today*, 312:141–148, aug 2018.

[55] V. M. Bermudez. No Title. *Langmuir*, 26(23):18144–18154, dec 2010.

[56] Yenny Cardona Quintero and Ramanathan Nagarajan. Molecular and dissociative adsorption of DMMP, Sarin and Soman on dry and wet TiO2(110) using density functional theory. *Surface Science*, 675:26–35, sep 2018.

[57] Mohammad Reza Housaindokht and Nasser Zamand. A DFT study of associative and dissociative chemical adsorption of DMMP onto SnO2(110) surface nano-cluster. *Structural Chemistry 2014 26:1*, 26(1):87–96, jul 2014.

[58] Roman Tsyshevsky, Monica McEntee, Erin M. Durke, Christopher Karwacki, and Maija M. Kuklja. Degradation of Fatal Toxic Nerve Agents on Dry TiO2. *ACS Applied Materials and Interfaces*, 13(1):696–705, jan 2021.

[59] Lena Trotochaud, Roman Tsyshevsky, Scott Holdren, Kenan Fears, Ashley R. Head, Yi Yu, Osman Karslloğlu, Sven Pletincx, Bryan Eichhorn, Jeffrey Owrutsky, Jeffrey Long, Michael Zachariah, Maija M. Kuklja, and Hendrik Bluhm. Spectroscopic and Computational Investigation of Room-Temperature Decomposition of a Chemical Warfare Agent Simulant on Polycrystalline Cupric Oxide. *Chemistry of Materials*, 29(17):7488–7496, sep 2017.

[60] T. Li, R. Tsyshevsky, L. Algrim, M. McEntee, E.M. Durke, B. Eichhorn, C. Karwacki, M.R. Zachariah, M.M. Kuklja, and E.E. Rodriguez. Understanding Dimethyl Methylphosphonate Adsorption and Decomposition on Mesoporous CeO¡inf¿2¡/inf¿. *ACS Applied Materials and Interfaces*, 13(45), 2021.

[61] Constantin A. Walenta, Fang Xu, Celine Tesvara, Christopher R. O'Connor, Philippe Sautet, and Cynthia M. Friend. Facile Decomposition of Organophosphonates by Dual Lewis Sites on a Fe3O4(111) Film. *Journal of Physical Chemistry C*, 124(23):12432–12441, jun 2020.

[62] Dimitar A. Panayotov and John R. Morris. Thermal decomposition of a chemical warfare agent simulant (DMMP) on TiO2: Adsorbate reactions with lattice oxygen as studied by infrared spectroscopy. *Journal of Physical Chemistry C*, 113(35):15684–15691, aug 2009.

[63] Donna A. Chen, Jay S. Ratliff, Xiaofeng Hu, Wesley O. Gordon, Sanjaya D. Senanayake, and David R. Mullins. Dimethyl methylphosphonate decomposition on fully oxidized and partially reduced ceria thin films. *Surface Science*, 604(5-6):574–587, 2010.

[64] Robert B. Balow, Jeffrey G. Lundin, Grant C. Daniels, Wesley O. Gordon, Monica McEntee, Gregory W. Peterson, James H. Wynne, and Pehr E. Pehrsson. Environmental Effects on Zirconium Hydroxide Nanoparticles and Chemical Warfare Agent Decomposition: Implications of Atmospheric Water and Carbon Dioxide. *ACS Applied Materials and Interfaces*, 9(45):39747–39757, nov 2017.

[65] Ingmar Persson, Mylène Trublet, and Wantana Klysubun. Structure Determination of Phosphoric Acid and Phosphate Ions in Aqueous Solution Using EXAFS Spectroscopy and Large Angle X-ray Scattering. *Journal of Physical Chemistry A*, 122(37):7413–7420, sep 2018.

[66] Benjamin Gamoke, Diane Neff, and Jack Simons. Nature of PO Bonds in Phosphates. *Journal of Physical Chemistry A*, 113(19):5677–5684, may 2009.

[67] Ashley R. Head, Roman Tsyshevsky, Lena Trotochaud, Yi Yu, Osman Karslıoğlu, Bryan Eichhorn, Maija M. Kuklja, and Hendrik Bluhm. Dimethyl methylphosphonate adsorption and decomposition on MoO 2 as studied by ambient pressure x-ray photoelectron spectroscopy and DFT calculations. *Journal of Physics: Condensed Matter*, 30(13):134005, apr 2018.

[68] Wesley O. Gordon, , Brian M. Tissue, and John R. Morris*. Adsorption and Decomposition of Dimethyl Methylphosphonate on Y2O3 Nanoparticles. *Journal of Physical Chemistry C*, 111(8):3233–3240, mar 2007.

[69] T. Li, R. Tsyshevsky, M. McEntee, E.M. Durke, C. Karwacki, E.E. Rodriguez, and M.M. Kuklja. Titania Nanomaterials for Sarin Decomposition: Understanding Fundamentals. *ACS Applied Nano Materials*, 5(5), 2022.

[70] Alessandro Trovarelli. Catalytic properties of ceria and CeO2-Containing materials. *Catalysis Reviews - Science and Engineering*, 38(4):439–520, 1996.

[71] Toshiyuki Mori, John Drennan, Jong Heun Lee, Ji Guang Li, and Takayasu Ikegami. Oxide ionic conductivity and microstructures of Sm- or La-doped CeO2-based systems. *Solid State Ionics*, 154-155:461–466, dec 2002.

[72] Shuohan Yu, Yiyang Lu, Fei Gao, and Lin Dong. Study on the crystal plane effect of CuO/TiO2 catalysts in NH3-SCR reaction. *Catalysis Today*, 339:265–273, jan 2020.

[73] Dawei Su, Xiuqiang Xie, Shixue Dou, and Guoxiu Wang. CuO single crystal with exposed 001 facets - A highly efficient material for gas sensing and Li-ion battery applications. *Scientific Reports 2014 4:1*, 4(1):1–9, aug 2014.

[74] Peter C.K. Vesborg, Brian Seger, and Ib Chorkendorff. Recent development in hydrogen evolution reaction catalysts and their practical implementation. *Journal of Physical Chemistry Letters*, 6(6):951–957, mar 2015.

[75] Ali Eftekhari. Electrocatalysts for hydrogen evolution reaction. *International Journal of Hydrogen Energy*, 42(16):11053–11077, apr 2017.

[76] Kevin E. O'Shea, Shawn Beightol, Ivelitza Garcia, Martha Aguilar, David V. Kalen, and William J. Cooper. Photocatalytic decomposition of organophosphonates in irradiated TiO2 suspensions. *Journal of Photochemistry and Photobiology A: Chemistry*, 107(1-3):221–226, jul 1997.

[77] K. E. O'Shea, I. Garcia, and M. Aguilar. TiO2 photocatalytic degradation of dimethyl- and diethyl- methylphosphonate, effects of catalyst and environmental factors. *Research on Chemical Intermediates 1997 23:4*, 23(4):325–339, 1997.

[78] Yi Chuan Chen, Alexandre V. Vorontsov, and Panagiotis G. Smirniotis. Enhanced photocatalytic degradation of dimethyl methylphosphonate in the presence of low-frequency ultrasound. *Photochemical Photobiological Sciences 2003 2:6*, 2(6):694–698, jun 2003.

[79] Paul A. DeSario, Wesley O. Gordon, Alex Balboa, Ashley M. Pennington, Catherine L. Pitman, Monica McEntee, and Jeremy J. Pietron. Photoenhanced Degradation of Sarin at Cu/TiO 2 Composite Aerogels: Roles of Bandgap Excitation and Surface Plasmon Excitation. *ACS Applied Materials Interfaces*, 13(10):12550–12561, mar 2021.

[80] Camelia N. Rusu, John T. Yates, Camelia N. Rusu, and John T. Yates. Adsorption and Decomposition of Dimethyl Methylphosphonate on TiO2. *The Journal of Physical Chemistry B*, 104(51):12292–12298, dec 2000.

[81] Ashley R. Head, Xin Tang, Zachary Hicks, Linjie Wang, Hannes Bleuel, Scott Holdren, Lena Trotochaud, Yi Yu, Line Kyhl, Osman Karslıoğlu, Kenan Fears, Jeffrey Owrutsky, Michael Zachariah, Kit H. Bowen, and Hendrik Bluhm. Thermal desorption of dimethyl methylphosphonate from MoO3. *https://doi.org/10.1080/2055074X.2017.1278891*, 3(1-2):112–118, apr 2017.

[82] Teweldemedhin M. Tesfai, V. N. Sheinker, and Mark B. Mitchell. Decomposition of dimethyl methylphosphonate (DMMP) on alumina-supported iron oxide. *Journal of Physical Chemistry B*, 102(38):7299–7302, sep 1998.

[83] Ran Ma, Sai Zhang, Tao Wen, Pengcheng Gu, Lei Li, Guixia Zhao, Fenlei Niu, Qifei Huang, Zhenwu Tang, and Xiangke Wang. A critical review on visible-light-response CeO2-based photocatalysts with enhanced photooxidation of organic pollutants. *Catalysis Today*, 335:20–30, sep 2019.

[84] Tiziano Montini, Michele Melchionna, Matteo Monai, and Paolo Fornasiero. Fundamentals and Catalytic Applications of CeO2-Based Materials, may 2016.

[85] Isabelle Trenque, Greta Camilla Magnano, Marie Alexandrine Bolzinger, Lucian Roiban, Frédéric Chaput, Isabelle Pitault, Stéphanie Briançon, Thierry Devers, Karine Masenelli-Varlot, Matthieu Bugnet, and David Amans. Shape-selective synthesis of nanoceria for degradation of paraoxon as a chemical warfare simulant. *Physical Chemistry Chemical Physics*, 21(10):5455–5465, mar 2019.

[86] Alicia Salerno, Isabelle Pitault, Thierry Devers, Jocelyne Pelletier, and Stéphanie Briançon. Model-based optimization of parameters for degradation reaction of an organophosphorus pesticide, paraoxon, using CeO2 nanoparticles in water media. *Environmental Toxicology and Pharmacology*, 53:18–28, jul 2017.

[87] Jiří Henych, Pavel Janoš, Martin Kormunda, Jakub Tolasz, and Václav Štengl. Reactive adsorption of toxic organophosphates parathion methyl and DMMP on nanostructured Ti/Ce oxides and their composites. *Arabian Journal of Chemistry*, 12(8):4258–4269, dec 2019.

[88] S. C. Laha and R. Ryoo. Synthesis of thermally stable mesoporous cerium oxide with nanocrystalline frameworks using mesoporous silica templates. *Chemical Communications*, 3(17):2138–2139, 2003.

[89] Pengfei Ji, Jinlong Zhang, Feng Chen, and Masakazu Anpoa. Ordered mesoporous CeO2 synthesized by nanocasting from cubic Ia3d mesoporous MCM-48 silica: Formation, characterization and photocatalytic activity. *Journal of Physical Chemistry C*, 112(46):17809–17813, 2008.

[90] William T. Gibbons, Scott Holdren, Junkai Hu, Bryan W. Eichhorn, and Michael R. Zachariah. Fixed Feed Temperature-Programmed Modulation - A Quantitative Method to Obtain Thermophysical Parameters: Application to Chemical Warfare Agent Adsorbents. *Journal of Physical Chemistry C*, 123(20):12694–12705, 2019.

[91] W. Kohn and L. J. Sham. Self-consistent equations including exchange and correlation effects. *Physical Review*, 140(4A):1133–1338, nov 1965.

[92] P. Hohenberg and W. Kohn. Inhomogeneous electron gas. *Physical Review*, 136(3B):864–871, nov 1964.

[93] John P. Perdew, Kieron Burke, and Matthias Ernzerhof. Generalized gradient approximation made simple. *Physical Review Letters*, 77(18):3865–3868, oct 1996.

[94] P. E. Blöchl. Projector augmented-wave method. *Physical Review B*, 50(24):17953–17979, dec 1994.

[95] G. Kresse and J. Hafner. Ab initio molecular dynamics for liquid metals. *Physical Review B*, 47(1):558–561, jan 1993.

[96] G. Kresse and J. Furthmüller. Efficiency of ab-initio total energy calculations for metals and semiconductors using a plane-wave basis set. *Computational Materials Science*, 6(1):15–50, jul 1996.

[97] G. Kresse and J. Furthmüller. Efficient iterative schemes for ab initio total-energy calculations using a plane-wave basis set. *Physical Review B - Condensed Matter and Materials Physics*, 54(16):11169–11186, oct 1996.

[98] S. Dudarev and G. Botton. Electron-energy-loss spectra and the structural stability of nickel oxide: An LSDA+U study. *Physical Review B - Condensed Matter and Materials Physics*, 57(3):1505–1509, jan 1998.

[99] Sergio Tosoni and Gianfranco Pacchioni. Trends in Adhesion Energies of Gold on MgO(100), Rutile TiO2(110), and CeO2(111) Surfaces: A Comparative DFT Study. *Journal of Physical Chemistry C*, 121(51):28328–28338, dec 2017.

[100] K. W. Adu, Q. Xiong, H. R. Gutierrez, G. Chen, and P. C. Eklund. Raman scattering as a probe of phonon confinement and surface optical modes in semiconducting nanowires. *Applied Physics A: Materials Science and Processing*, 3(85):287–297, 2006.

[101] Tae-Wan Kim, Freddy Kleitz, Blain Paul, and Ryong Ryoo. MCM-48-like Large Mesoporous Silicas with Tailored Pore Structure: Facile Synthesis Domain in a Ternary Triblock CopolymerButanolWater System. *Journal of the American Chemical Society*, 127(20):7601–7610, apr 2005.

[102] Giuseppe Faraci, Santo Gibilisco, Agata R. Pennisi, and Carla Faraci. Quantum size effects in Raman spectra of Si nanocrystals. *Journal of Applied Physics*, 109(7), 2011.

[103] Ernesto Paparazzo. Use and mis-use of x-ray photoemission spectroscopy Ce3d spectra of Ce ¡sub¿2¡/sub¿ O ¡sub¿3¡/sub¿ and CeO ¡sub¿2¡/sub¿. *Journal of Physics: Condensed Matter*, 30(34):343003, aug 2018.

[104] Chengwu Yang, Xiaojuan Yu, Stefan Heißler, Alexei Nefedov, Sara Colussi, Jordi Llorca, Alessandro Trovarelli, Yuemin Wang, and Christof Wöll. Surface Faceting and Reconstruction of Ceria Nanoparticles. *Angewandte Chemie - International Edition*, 56(1):375–379, 2017.

[105] Xiaoguang Wang, Emre Bukusoglu, and Nicholas L. Abbott. A practical guide to the preparation of liquid crystal-templated microparticles. *Chemistry of Materials*, 29(1):53–61, jan 2017.

[106] David R. Mullins. The surface chemistry of cerium oxide. *Surface Science Reports*, 70(1):42–48, 2015.

[107] Isabelle Trenque, Greta Camilla Magnano, Jan Bárta, Frédéric Chaput, Marie Alexandrine Bolzinger, Isabelle Pitault, Stéphanie Briançon, Karine Masenelli-Varlot, Matthieu Bugnet, Christophe Dujardin, Václav Čuba, and David Amans. Synthesis routes of CeO2 nanoparticles dedicated to organophosphorus degradation: a benchmark. *CrystEngComm*, 22(10):1725–1737, mar 2020.

[108] Jakub Ederer, Pavel Janoš, Martin Šťastný, Jiří Henych, Karel Ederer, Michaela Šrámová Slušná, and Jakub Tolasz. Nanocrystalline cerium oxide for catalytic degradation of paraoxon methyl: Influence of CeO2 surface properties. *Journal of Environmental Chemical Engineering*, 9(5):106229, oct 2021.

[109] Paul A. DeSario, Wesley O. Gordon, Alex Balboa, Ashley M. Pennington, Catherine L. Pitman, Monica McEntee, and Jeremy J. Pietron. Photoenhanced Degradation of Sarin at Cu/TiO 2 Composite Aerogels: Roles of Bandgap Excitation and Surface Plasmon Excitation. *ACS Applied Materials Interfaces*, 13(10):12550–12561, mar 2021.

[110] Robert B. Balow, Monica McEntee, Igor V. Schweigert, Seokmin Jeon, Gregory W. Peterson, and Pehr Pehrsson. Battling Chemical Weapons with Zirconium Hydroxide Nanoparticle Sorbent: Impact of Environmental Contaminants on Sarin Sequestration and Decomposition. *Langmuir*, 37(23):6923–6934, jun 2021.

[111] Anna M. Plonka, Qi Wang, Wesley O. Gordon, Alex Balboa, Diego Troya, Weiwei Guo, Conor H. Sharp, Sanjaya D. Senanayake, John R. Morris, Craig L. Hill, and Anatoly I. Frenkel. In Situ Probes of Capture and Decomposition of Chemical Warfare Agent Simulants by Zr-Based Metal Organic Frameworks. *Journal of the American Chemical Society*, 139(2):599–602, jan 2017.

[112] Doris Möncke and Hellmut Eckert. Review on the structural analysis of fluoride-phosphate and fluoro-phosphate glasses. *Journal of Non-Crystalline Solids: X*, 3:100026, sep 2019.

[113] Felix Brosi, Tobias Schlöder, Alexei Schmidt, Helmut Beckers, and Sebastian Riedel. A combined quantum-chemical and matrix-isolation study on molecular manganese fluorides. *Dalton Transactions*, 45(12):5038–5044, mar 2016.

[114] Tengfei Huang, Lijuan Zhao, Xuelian Jiang, Wenjie Yu, Bing Xu, Xuefeng Wang, W. H.Eugen Schwarz, and Jun Li. Metal Oxo-Fluoride Molecules O nMF2(M = Mn and Fe; N = 1-4) and O2MnF: Matrix Infrared Spectra and Quantum Chemistry. *Inorganic Chemistry*, 60(11):7687–7696, jun 2021.

[115] Roman Tsyshevsky, Ashley R. Head, Lena Trotochaud, Hendrik Bluhm, and Maija M. Kuklja. Mechanisms of Degradation of Toxic Nerve Agents: Quantum-chemical Insight into Interactions of Sarin and Soman with Molybdenum Dioxide. *Surface Science*, 700:121639, oct 2020.

[116] Elif Irem Senyurt, Mirko Schoenitz, and Edward L. Dreizin. Rapid destruction of sarin surrogates by gas phase reactions with focus on diisopropyl methylphosphonate (DIMP). *Defence Technology*, 17(3):703–714, jun 2021.

[117] Tianyu Li, Roman Tsyshevsky, Monica Mcentee, Erin M. Durke, Christopher Karwacki, Efrain E. Rodriguez, and Maija M. Kuklja. Titania Nanomaterials for Sarin Decomposition: Understanding Fundamentals. *ACS Applied Nano Materials*, 2022:6670, 2022.

[118] Y. M. Choi, Harry Abernathy, Hsin Tsung Chen, M. C. Lin, and Meilin Liu. Characterization of O2–CeO2 Interactions Using In Situ Raman Spectroscopy and First-Principle Calculations. *ChemPhysChem*, 7(9):1957–1963, sep 2006.

[119] Yong Xi. Li and Kenneth J. Klabunde. Nano-scale metal oxide particles as chemical reagents. Destructive adsorption of a chemical agent simulant, dimethyl methylphosphonate, on heat-treated magnesium oxide. *Langmuir*, 7(7):1388–1393, may 2002.

[120] Travis G. Novak, Paul A. DeSario, Jeffrey W. Long, and Debra R. Rolison. Designing Oxide Aerogels With Enhanced Sorptive and Degradative Activity for Acute Chemical Threats. *Frontiers in Materials*, 0:164, may 2021.

[121] Guilong Lu, Haiyan Zheng, Junjun Lv, Ge Wang, and Xiubing Huang. Review of recent research work on CeO2-based electrocatalysts in liquid-phase electrolytes, dec 2020.

[122] Nandini Jaiswal, Khagesh Tanwar, Rathod Suman, Devendra Kumar, Shail Uppadhya, and Om Parkash. A brief review on ceria based solid electrolytes for solid oxide fuel cells. *Journal of Alloys and Compounds*, 781:984–1005, apr 2019.

[123] Mogens Mogensen, Thomas Lindegaard, Uffe Rud Hansen, and Gurli Mogensen. Physical Properties of Mixed Conductor Solid Oxide Fuel Cell Anodes of Doped CeO2. *Journal of The Electrochemical Society*, 141(8):2122, aug 1994.

[124] Enrique Ruiz-Trejo. The optical band gap of Gd-doped CeO2 thin films as function of temperature and composition. *Journal of Physics and Chemistry of Solids*, 74(4):605–610, apr 2013.

[125] Anjalee D. Liyanage, Sanjaya D. Perera, Kui Tan, Yves Chabal, and Kenneth J. Balkus. Synthesis, characterization, and photocatalytic activity of Y-doped CeO2 nanorods. *ACS Catalysis*, 4(2):577–584, feb 2014.

[126] Lin Yue and Xiao Ming Zhang. Structural characterization and photocatalytic behaviors of doped CeO2 nanoparticles. *Journal of Alloys and Compounds*, 475(1-2):702–705, may 2009.

[127] Yuji Goto, Kazuyuki Takahashi, Takahisa Omata, and Shinya Otsuka-Yao-Matsuo. Synthesis of Y2O3-doped CeO2 nanocrystals and their surface modification. In *Journal of Physics: Conference Series*, volume 165, page 12041. Institute of Physics Publishing, may 2009.

[128] Hideaki Inaba and Hiroaki Tagawa. Ceria-based solid electrolytes. *Solid State Ionics*, 83(1-2):1–16, 1996.

[129] G. S. Otero, P. G. Lustemberg, F. Prado, and M. V. Ganduglia-Pirovano. Relative Stability of Near-Surface Oxygen Vacancies at the CeO2(111) Surface upon Zirconium Doping. *The Journal of Physical Chemistry C*, 2019.

[130] Bin Zhang, Lei Wang, and Feng Chen. Recent Advances in Femtosecond Laser Processing of LiNbO3 Crystals for Photonic Applications. *Laser Photonics Reviews*, 14(8):1900407, aug 2020.

[131] Kota Murakami, Shuhei Ogo, Atsushi Ishikawa, Yuna Takeno, Takuma Higo, Hideaki Tsuneki, Hiromi Nakai, and Yasushi Sekine. Heteroatom doping effects on interaction of H2O and CeO2 (111) surfaces studied using density functional theory: Key roles of ionic radius and dispersion. *Journal of Chemical Physics*, 152(1):14707, jan 2020.

[132] Anna Kossoy, Hagai Cohen, Tatyana Bendikov, Ellen Wachtel, and Igor Lubomirsky. Water adsorption at the surface of pure and Gd-doped ceria. *Solid State Ionics*, 194(1):1–4, jul 2011.

[133] Marco Fronzi, Simone Piccinin, Bernard Delley, Enrico Traversa, and Catherine Stampfl. Water adsorption on the stoichiometric and reduced CeO2(111) surface: A first-principles investigation. *Physical Chemistry Chemical Physics*, 11(40):9188–9199, oct 2009.

[134] Delfina García Pintos, Alfredo Juan, and Beatriz Irigoyen. Density functional theory study of water interactions on Mn-doped CeO 2 (1 1 1) surface. *Applied Surface Science*, 313:784–793, sep 2014.

[135] Alex Le Gal and Stéphane Abanades. Dopant incorporation in ceria for enhanced water-splitting activity during solar thermochemical hydrogen generation. *Journal of Physical Chemistry C*, 116(25):13516–13523, jun 2012.

[136] Jun Chen, Longlong Fan, Yang Ren, Zhao Pan, Jinxia Deng, Ranbo Yu, and Xianran Xing. Unusual transformation from strong negative to positive thermal expansion in PbTiO3-BiFeO3 perovskite. *Physical Review Letters*, 110(11):115901, mar 2013.

[137] Yuesheng Li, Haijun Liao, Zhen Zhang, Shiyan Li, Feng Jin, Langsheng Ling, Lei Zhang, Youming Zou, Li Pi, Zhaorong Yang, Junfeng Wang, Zhonghua Wu, and Qingming Zhang. Gapless quantum spin liquid ground state in the two-dimensional spin-1/2 triangular antiferromagnet YbMgGaO4. *Scientific Reports*, 5(1):1–8, nov 2015.

[138] Giulia Spezzati, Angelica D. Benavidez, Andrew T. DeLaRiva, Yaqiong Su, Jan P. Hofmann, Shunsuke Asahina, Ezra J. Olivier, Johannes H. Neethling, Jeffrey T. Miller, Abhaya K. Datye, and Emiel J.M. Hensen. CO oxidation by Pd supported on CeO2(100) and CeO2(111) facets. *Applied Catalysis B: Environmental*, 243:36–46, apr 2019.

[139] Noah Baumann, Jinggang Lan, and Marcella Iannuzzi. CO2adsorption on the pristine and reduced CeO2(111) surface: Geometries and vibrational spectra by first principles simulations. *Journal of Chemical Physics*, 154(9):94702, mar 2021.

[140] Robert W. Cheary and Alan Coelho. Fundamental parameters approach to x-ray line-profile fitting. *Journal of Applied Crystallography*, 2(2):109–121, apr 1992.

[141] J. R. McBride, K. C. Hass, B. D. Poindexter, and W. H. Weber. Raman and x-ray studies of Ce1-xRExO2-y, where RE=La, Pr, Nd, Eu, Gd, and Tb. *Journal of Applied Physics*, 76(4):2435–2441, aug 1994.

[142] M. Coduri, M. Scavini, M. Allieta, M. Brunelli, and C. Ferrero. Local disorder in yttrium doped ceria (Ce1-xYxO 2-x/2) probed by joint X-ray and neutron powder diffraction. In *Journal of Physics: Conference Series*, volume 340, page 012056. Institute of Physics Publishing, feb 2012.

[143] Ming Guo, Jiqing Lu, Yanni Wu, Yuejuan Wang, and Mengfei Luo. UV and visible Raman studies of oxygen vacancies in rare-earth-doped ceria. *Langmuir*, 27(7):3872–3877, apr 2011.

[144] Ethan J. Crumlin, Eva Mutoro, Zhi Liu, Michael E. Grass, Michael D. Biegalski, Yueh Lin Lee, Dane Morgan, Hans M. Christen, Hendrik Bluhm, and Yang Shao-Horn. Surface strontium enrichment on highly active perovskites for oxygen electrocatalysis in solid oxide fuel cells. *Energy and Environmental Science*, 5(3):6081–6088, mar 2012.

[145] Bonjae Koo, Kyeounghak Kim, Jun Kyu Kim, Hyunguk Kwon, Jeong Woo Han, and Woo Chul Jung. Sr Segregation in Perovskite Oxides: Why It Happens and How It Exists, aug 2018.

[146] Franziska Hess and Bilge Yildiz. Polar or not polar? the interplay between reconstruction, Sr enrichment, and reduction at the La0.75Sr0.25MnO3 (001) surface. *Physical Review Materials*, 4(1):015801, jan 2020.

[147] Yuesheng Li, Devashibhai Adroja, Robert I. Bewley, David Voneshen, Alexander A. Tsirlin, Philipp Gegenwart, and Qingming Zhang. Crystalline Electric-Field Randomness in the Triangular Lattice Spin-Liquid YbMgGaO4. *Physical Review Letters*, 118(10):107202, mar 2017.

[148] Tim T. Fister, Dillon D. Fong, Jeffrey A. Eastman, Peter M. Baldo, Matthew J. Highland, Paul H. Fuoss, Kavaipatti R. Balasubramaniam, Joanna C. Meador, and Paul A. Salvador. In situ characterization of strontium surface segregation in epitaxial La0.7Sr0.3MnO3 thin films as a function of oxygen partial pressure. *Applied Physics Letters*, 93(15):151904, oct 2008.

[149] Anne Katrin Huber, Mareike Falk, Marcus Rohnke, Bjoern Luerssen, Matteo Amati, Luca Gregoratti, Dietrich Hesse, and Jürgen Janek. In situ study of activation and de-activation of LSM fuel cell cathodes - Electrochemistry and surface analysis of thin-film electrodes. *Journal of Catalysis*, 294:79–88, oct 2012.

[150] Daniel G. Stroppa, Cleocir J. Dalmaschio, Lothar Houben, Juri Barthel, Luciano A. Montoro, Edson R. Leite, and Antonio J. Ramirez. Analysis of dopant atom distribution and quantification of oxygen vacancies on individual Gd-doped CeO2 nanocrystals. *Chemistry - A European Journal*, 20(21):6288–6293, 2014.

[151] John A. Moss, Steven H. Szczepankiewicz, Eleanor Park, and Michael R. Hoffmann. Adsorption and photodegradation of dimethyl methylphosphonate vapor at TiO 2 surfaces. *Journal of Physical Chemistry B*, 109(42):19779–19785, oct 2005.

[152] M. K. Templeton and W. H. Weinberg. Adsorption and decomposition of dimethyl methylphosphonate on an aluminum oxide surface. *Journal of the American Chemical Society*, 107(1):97–108, jan 1985.

[153] Jorly Joseph and Eluvathingal D. Jemmis. Red-, blue-, or no-shift in hydrogen bonds: A unified explanation. *Journal of the American Chemical Society*, 129(15):4620–4632, apr 2007.

[154] Ashley M. Wright, Austin A. Howard, J. Coleman Howard, Gregory S. Tschumper, and Nathan I. Hammer. Charge transfer and blue shifting of vibrational frequencies in a hydrogen bond acceptor. *Journal of Physical Chemistry A*, 117(26):5435–5446, jul 2013.

[155] Justin B. Sambur, David C. Doetschman, Szu Wei Yang, Jürgen T. Schulte, Barry R. Jones, and Jared B. DeCoste. Multiple effects of the presence of water on the nucleophilic substitution reactions of NaX Faujasite zeolite with dimethyl methylphosphonate (DMMP). *Microporous and Mesoporous Materials*, 112(1-3):116–124, jul 2008.

[156] Szu Wei Yang, David C. Doetschman, Jürgen T. Schulte, Justin B. Sambur, Charles W. Kanyi, Jack D. Fox, Chrispin O. Kowenje, Barry R. Jones, and Neesha D. Sherma. Sodium X-type faujasite zeolite decomposition of dimethyl methylphosphonate (DMMP) to methylphosphonate: Nucleophilic zeolite reactions I. *Microporous and Mesoporous Materials*, 92(1-3):56–60, jun 2006.

[157] Wei Che Hung, Je Chuang Wang, and Kuo Hui Wu. Adsorption and decomposition of dimethyl methylphosphonate (DMMP) on expanded graphite/metal oxides. *Applied Surface Science*, 444:330–335, jun 2018.

[158] Kevin Knagge, Matthew Johnson, Vicki H. Grassian, Sarah C. Larsen, Vicki H. Grassian, and Sarah C. Larsen. Adsorption and thermal reaction of DMMP in nanocrystalline NaY. *Langmuir*, 22(26):11077–11084, 2006.

[159] Simon Erker, Patrick Rinke, Nikolaj Moll, and Oliver T Hofmann. Doping dependence of the surface phase stability of polar O-terminated (0001) ZnO. *New Journal of Physics*, 19(8):083012, aug 2017.

[160] M. A. Lahmer. The effect of doping with rare earth elements (Sc, Y, and La) on the stability, structural, electronic and photocatalytic properties of the O-termintaed ZnO surface; a first-principles study. *Applied Surface Science*, 457:315–322, nov 2018.

[161] Hans F. Wardenga and Andreas Klein. Surface potentials of (111), (110) and (100) oriented CeO2x thin films. *Applied Surface Science*, 377:1–8, jul 2016.

[162] Thomas Désaunay, Armelle Ringuedé, Michel Cassir, Frédéric Labat, and Carlo Adamo. Modeling basic components of solid oxide fuel cells using density functional theory: Bulk and surface properties of CeO2. *Surface Science*, 606(3-4):305–311, feb 2012.

[163] Robert W. Morrison. NBC Filter Performance. Technical report, oct 2001.

[164] M. R. Al-Mamun, S. Kader, M. S. Islam, and M. Z.H. Khan. Photocatalytic activity improvement and application of UV-TiO2 photocatalysis in textile wastewater treatment: A review. *Journal of Environmental Chemical Engineering*, 7(5):103248, oct 2019.

[165] Zipeng Xing, Jiaqi Zhang, Jiayi Cui, Junwei Yin, Tianyu Zhao, Junyan Kuang, Ziyuan Xiu, Ning Wan, and Wei Zhou. Recent advances in floating TiO2-based photocatalysts for environmental application. *Applied Catalysis B: Environmental*, 225:452–467, jun 2018.

[166] Yan Wang, Yiming He, Qinghua Lai, and Maohong Fan. Review of the progress in preparing nano TiO2: An important environmental engineering material. *Journal of Environmental Sciences*, 26(11):2139–2177, nov 2014.

[167] Dmitry A. Trubitsyn and Alexander V. Vorontsov. Molecular and reactive adsorption of dimethyl methylphosphonate over (0 0 1) and (1 0 0) anatase clusters. *Computational and Theoretical Chemistry*, 1020:63–71, sep 2013.

[168] Yuki Yamaguchi, Yoshihiro Kanamaru, Minori Fukushima, Kenjiro Fujimoto, and Shigeru Ito. Preparation of Highly Crystallized Strontium Titanate Powders at Room Temperature. *Journal of the American Ceramic Society*, 98(10):3054–3061, oct 2015.

[169] Monica McEntee, Wesley O. Gordon, Alex Balboa, Daniel J. Delia, Catherine L. Pitman, Ashley M. Pennington, Debra R. Rolison, Jeremy J. Pietron, and Paul A. Desario. Mesoporous Copper Nanoparticle/TiO2 Aerogels for Room-Temperature Hydrolytic Decomposition of the Chemical Warfare Simulant Dimethyl Methylphosphonate. *ACS Applied Nano Materials*, 3(4):3503–3512, apr 2020.

[170] Wei Li, Zhangxiong Wu, Jinxiu Wang, Ahmed A. Elzatahry, and Dongyuan Zhao. A Perspective on Mesoporous TiO2 Materials. *Chemistry of Materials*, 26(1):287–298, jul 2013.

[171] Lars Robben, Adel A. Ismail, Sven Jare Lohmeier, Armin Feldhoff, Detlef W. Bahnemann, and Josef Christian Buhl. Facile synthesis of highly ordered mesoporous and well crystalline TiO 2: Impact of different gas atmosphere and calcination temperatures on structural properties. *Chemistry of Materials*, 24(7):1268–1275, apr 2012.

[172] Pam Basu and John T. Yates. An apparatus for temperature programmed desorption from high surface area solids: The adsorption and desorption of C2H4 from NaX-zeolite. *Surface Science*, 177(2):291–313, dec 1986.

[173] C. J. Howard, T. M. Sabine, and F. Dickson. Structural and thermal parameters for rutile and anatase. *Acta Crystallographica Section B*, 47(4):462–468, aug 1991.

[174] Sergio Tosoni, Hsin Yi Tiffany Chen, and Gianfranco Pacchioni. A DFT Study of the Reactivity of Anatase TiO2 and Tetragonal ZrO2 Stepped Surfaces Compared to the Regular (101) Terraces. *ChemPhysChem*, 16(17):3642–3651, dec 2015.

[175] Xue Qing Gong, Annabella Selloni, Olga Dulub, Peter Jacobson, and Ulrike Diebold. Small Au and Pt Clusters at the Anatase TiO2(101) Surface: Behavior at Terraces, Steps, and Surface Oxygen Vacancies. *Journal of the American Chemical Society*, 130(1):370–381, jan 2007.

[176] Stefan Grimme. Semiempirical GGA-type density functional constructed with a long-range dispersion correction. *Journal of Computational Chemistry*, 27(15):1787–1799, nov 2006.

[177] Graeme Henkelman, Blas P. Uberuaga, and Hannes Jónsson. Climbing image nudged elastic band method for finding saddle points and minimum energy paths. *Journal of Chemical Physics*, 113(22):9901–9904, dec 2000.

[178] D. M. Tobaldi, R. C. Pullar, M. P. Seabra, and J. A. Labrincha. Fully quantitative X-ray characterisation of Evonik Aeroxide TiO 2 P25®. *Materials Letters*, 122:345–347, may 2014.

[179] B Ohtani, O O Prieto-Mahaney, D Li, and R Abe. What is Degussa (Evonic) P25? Crystalline composition analysis, reconstruction from isolated pure particles and photocatalytic activity test. *Journal of Photochemistry and Photobiology A: Chemistry*, 216(2-3):179–182, 2010.

[180] Mark C. Biesinger, Leo W.M. Lau, Andrea R. Gerson, and Roger St C. Smart. Resolving surface chemical states in XPS analysis of first row transition metals, oxides and hydroxides: Sc, Ti, V, Cu and Zn. *Applied Surface Science*, 257(3):887–898, nov 2010.

[181] Nam Q. Le, Gloria Bazargan, Igor V. Schweigert, and Daniel Gunlycke. Vibrational Signatures of Sarin Adsorption on Anatase Surfaces. *Surface Science*, 705:121765, mar 2021.

[182] Michael A Denchy, Linjie Wang, Nicolas Blando, Lucas Hansen, Benjamin R Bilik, Xin Tang, Zachary Hicks, Gerd Gantefoer, and Kit H Bowen. Adsorption and decomposition of dimethyl methylphosphonate on size-selected zirconium oxide trimer clusters. *Journal of Physical Chemistry C*, 125(43):23688–23698, 2021.

[183] Gang Wang, Ganggang Li, Xin Xing, Zhongshen Zhang, and Zhengping Hao. Unraveling the adsorption and diffusion properties of hexamethyldisiloxane on zeolites by static gravimetric analysis. *Water Research*, 197, jun 2021.

[184] Xin Tang, Zachary Hicks, Linjie Wang, Gerd Ganteför, Kit H. Bowen, Roman Tsyshevsky, Jianwei Sun, and Maija M. Kuklja. Adsorption and decomposition of dimethyl methylphosphonate on size-selected (MoO3)3 clusters. *Physical Chemistry Chemical Physics*, 20(7):4840–4850, feb 2018.

[185] Ana Maria Ferraria, José Dias Lopes da Silva, and Ana Maria Botelho do Rego. XPS studies of directly fluorinated HDPE: problems and solutions. *Polymer*, 44(23):7241–7249, nov 2003.

[186] Y. M. Shulga, Ta Chang Tien, Chi Chen Huang, Shen Chuan Lo, V. E. Muradyan, N. V. Polyakova, Yong Chien Ling, R. O. Loutfy, and A. P. Moravsky. XPS study of fluorinated carbon multi-walled nanotubes. *Journal of Electron Spectroscopy and Related Phenomena*, 160(1-3):22–28, aug 2007.

[187] J F Moulder, W F Stickle, P E Sobol, and K D Bomben. Handbook of X-Ray Photoelectron Spectroscopy (Perkin-Elmer, Eden Prairie, MN, 1992). *Google Scholar*, page 128, 2002.

[188] Davide Barreca, Alberto Gasparotto, Chiara Maccato, Cinzia Maragno, and Eugenio Tondello. Cerium (III) Fluoride Thin Films by XPS. *Surface Science Spectra*, 13(1):87, oct 2007.

[189] Ankur Jain, Shivani Agarwal, Sanjay Kumar, Shotaro Yamaguchi, Hiroki Miyaoka, Yoshitsugu Kojima, and Takayuki Ichikawa. How does TiF4 affect the decomposition of MgH2 and its complex variants? – An XPS investigation. *Journal of Materials Chemistry A*, 5(30):15543–15551, aug 2017.

[190] John T. Wolan and Gar B. Hoflund. Surface characterization study of AgF and AgF2 powders using XPS and ISS. *Applied Surface Science*, 125(3-4):251–258, mar 1998.

[191] Andrei V. Shchukarev and D. V. Korolkov. XPS Study of group IA carbonates. *Open Chemistry*, 2(2):347–362, apr 2004.

[192] Yu Ren, Zhen Ma, and Peter G. Bruce. Ordered mesoporous metal oxides: Synthesis and applications. *Chemical Society Reviews*, 41(14):4909–4927, jun 2012.

[193] Chen Li, Qian Li, Yusuf Valentino Kaneti, Dan Hou, Yusuke Yamauchi, and Yiyong Mai. Self-assembly of block copolymers towards mesoporous materials for energy storage and conversion systems. *Chemical Society Reviews*, 49(14):4681–4736, jul 2020.

[194] Wei Shan Chiang, Emiliano Fratini, Piero Baglioni, Daniel Georgi, Jin Hong Chen, and Yun Liu. Methane Adsorption in Model Mesoporous Material, SBA-15, Studied by Small-Angle Neutron Scattering. *Journal of Physical Chemistry C*, 120(8):4354–4363, mar 2016.

[195] Li Zhou, Xiuwu Liu, Yan Sun, Jingwen Li, and Yaping Zhou. Methane Sorption in Ordered Mesoporous Silica SBA-15 in the Presence of Water. *Journal of Physical Chemistry B*, 109(48):22710–22714, dec 2005.

[196] Janika Hochstrasser, Artur Svidrytski, Alexandra Höltzel, Tatiana Priamushko, Freddy Kleitz, Wu Wang, Christian Kübel, and Ulrich Tallarek. Morphology–transport relationships for SBA-15 and KIT-6 ordered mesoporous silicas. *Physical Chemistry Chemical Physics*, 22(20):11314–11326, may 2020.

[197] Craig A. Bridges, Xiao Guang Sun, Jinkui Zhao, M. Parans Paranthaman, and Sheng Dai. In situ observation of solid electrolyte interphase formation in ordered mesoporous hard carbon by small-angle neutron scattering. *Journal of Physical Chemistry C*, 116(14):7701–7711, apr 2012.

[198] Hyunjin Moon, Ryan P. Collanton, Jacob I. Monroe, Thomas M. Casey, M. Scott Shell, Songi Han, and Susannah L. Scott. Evidence for Entropically Controlled Interfacial Hydration in Mesoporous Organosilicas. *Journal of the American Chemical Society*, 144(4):1766–1777, feb 2022.

[199] George Gabriel Stokes. On the Effect of the Internal Friction of Fluids on the Motion of Pendulums. In *Mathematical and Physical Papers*, pages 1–10. Cambridge University Press, aug 2010.